

SILICA SURFACE CHARACTERIZATION AS A FUNCTION OF
FORMATION AND SURFACE TREATMENT USING TRADITIONAL
METHODS AND PROTEINS AS SURFACE PROBES

BY

MICHELLE LYNN KORWIN-EDSON

A THESIS
SUBMITTED TO THE FACULTY OF

ALFRED UNIVERSITY

IN PARTIAL FULFILLMENT OF THE REQUIREMENTS
FOR THE DEGREE OF

DOCTOR OF PHILOSOPHY

IN

GLASS SCIENCE

ALFRED, NEW YORK

MAY, 2004

Alfred University theses are copyright protected and may be used for education or personal research only. Reproduction or distribution in any format is prohibited without written permission from the author.

SILICA SURFACE CHARACTERIZATION AS A FUNCTION OF
FORMATION AND SURFACE TREATMENT USING TRADITIONAL
METHODS AND PROTEINS AS SURFACE PROBES

BY

MICHELLE LYNN KORWIN-EDSON

B.S. ALFRED UNIVERSITY (1999)

SIGNATURE OF AUTHOR _____ (Signature on file)

APPROVED BY _____ (Signature on file)
ALEXIS G. CLARE, ADVISOR

(Signature on file)
THOMAS P. SEWARD III, ADVISORY COMMITTEE

(Signature on file)
ALAN H. GOLDSTEIN, ADVISORY COMMITTEE

(Signature on file)
WILLIAM C. LACOURSE, ADVISORY COMMITTEE

(Signature on file)
DOREEN D. EDWARDS, CHAIR, ORAL THESIS DEFENSE

ACCEPTED BY _____ (Signature on file)
ALASTAIR N. CORMACK, DEAN,
SCHOOL OF ENGINEERING

ACCEPTED BY _____ (Signature on file)
ALASTAIR N. CORMACK,
DIRECTOR OF THE GRADUATE SCHOOL,
ALFRED UNIVERSITY

Acknowledgements

I wish to dedicate this work to my parents, Roger and Kathy Korwin and I want to thank them for all the support and wisdom they have given me throughout the years. My father taught me the importance of quality in one's work and to take pride in everything I do. My mother taught me patience, to believe in myself and to never give up. I have been blessed to have been surrounded by many strong women in my life. Starting with my mom and sister, Terry. They both showed me that a woman can do anything she sets her mind to and having role models like them from the start of my life was a great advantage. Then to have come to college and find another role model in Alexis Clare, someone who works her fingers to the bone and always with cheer and optimism. Alix, you are a leader in your field, a terrific advisor and a true confidant. You helped me in ways that went far beyond the call of duty and I must thank you from the bottom of my heart for all you have done for me these past four years. My summer down at KSC NASA also bolstered my faith in women of science when I met Yai-Ping Mimi Shao and Patricia Currier. Mimi and Patty took me under their wings and were far more than unbelievable mentors, they were and are two of my best friends and people that I admire very much. During this time, I also met Rene' Elms, she and I worked together and played together and the four of us became an inseparable bundle of fun. I was also fortunate to have worked for Celia Merzbacher and Debra Rolison during my summer internships at the US Naval Research Laboratory. They both had a positive affect on my outlook towards being a scientist. So I have to say thank you to all the wonderful ladies I've worked with and for during my lifetime up to date.

My committee members have been very helpful in the creation of this thesis, thank you for your invaluable comments and suggestions. I have to individually thank Dr. Goldstein for all of his advice concerning the biological aspect of this thesis. I must admit that I had very little understanding of how to handle proteins at first and his patience in showing me the ropes was welcomed and is appreciated.

I wish to thank my siblings for their unique parts in molding me into the person I am today. Terry, my only sister, you taught me to be strong in who I am as an individual and that I should follow my dreams and never settle for anything less. Doug, it was you that I followed to Alfred and as a fellow glass scientist with all your wit and intelligence, you have helped me in so many ways, some of which you may not even be aware. Paul, you have been an inspiration to me, you have such charm and character and are one of the strongest people I know. I have to thank my nephew Kevin for reminding me what is truly important in life by making me roll down hills and laughing 'til I cry. To the newest addition to our family, Becky, Doug's wife, you are another strong woman that has come into my life, you are so brave and

thoughtful and I thank you for all of your advice. This family of mine is absolutely incredible, as the youngest of my siblings, I had some big shoes to fill. They are all very successful and I hope to one day be as successful, honorable, loving and hilarious as these four. They are all a part of me and I want to thank them for loving me and teaching me, the little sister.

Now, for my fellow graduate students, I want to express my thanks to Bryan Wheaton, Matt Hall, Doug Wing, Doug Rapp, Malin Charoenwongsa, Chris Tournour, Brian Luisi, Kevin Rowland and Liz Birtch. Thanks for all the laughs, happy hours, coffee breaks, and especially your friendships. Bryan and Matt were the most instrumental in helping me with my thesis work. Matt was always willing to answer my questions and show me how to use a piece of equipment. Since we had similar thesis topics, we shared literature and ideas, thank you Matt for your assistance and guidance. Bryan was literally a Godsend. If it weren't for him, a third of this thesis would not have been possible. He was able to provide access to Corning and spent countless hours teaching me the finer points of the AFM. He was also my sounding board for many of life's little problems, thank you for lending an ear and giving me so much advice.

To my soul mate and life partner. Daniel, as a fellow glass scientist, you have helped me study for countless exams, you've helped me with experiments and setting up equipment, and you have given me things to think about in my research. As a husband, you listened to my every concern, you calmed me when I was anxious and you urged me on when I was dismayed. You motivated me when I was lackadaisical, you gave me accolades when no one else cared, and you didn't let me quit when I was overwhelmed with failure. You are the reason I was able to keep going. You are the reason I am where I am today. You have unselfishly supported me in everything I wanted to do and for all of this I am forever grateful. I love you sweetheart for everything you are and I always will. Thank you!

Thank you to Coco, Liddy and Carmen for warming my lap and my heart.

Table of Contents

SECTION TITLE	PAGE
Acknowledgements	iii
Table of Contents	v
List of Tables	viii
List of Figures	x
Abstract	xxxii
1. Introduction	1
2. Literature Review	5
2.1. Former Work	5
2.2. Silica - Background and Forming	10
2.3. Silica Surface	21
2.3.1. Surface Species	21
2.3.2. Types of Surfaces	30
2.3.3. Silica and Water	32
2.3.4. Surface Treatments	35
2.3.4.1. "Cleaning"	35
2.3.4.2. Treatments on Multi-Component Glasses	39
2.3.4.3. Treatments on Silica Glass	44
2.3.4.4. Silanization of Silica Surfaces	48
2.4. Characterization	51
2.4.1. Common Surface Techniques for Powders	51
2.4.2. Surface Characterization on Bulk Samples	52
2.4.3. Atomic Force Microscopy	53
2.4.4. Fluorescence	61
2.5. Proteins	64
2.5.1. Protein Background	64
2.5.2. Proteins Used in this Study	69
2.5.2.1. Albumins	70

SECTION TITLE	PAGE
2.5.2.2. Streptavidin	70
2.5.2.3. Immunoglobulin G	73
2.6. Characterizing Proteins	75
2.6.1. Common Assays and Detection Methods	75
2.6.2. Gel-Electrophoresis	76
2.6.3. Fluorimetry of Proteins	77
2.6.4. Circular Dichroism	80
2.6.5. FTIR Spectroscopy of Proteins	83
2.7. Chemical Force Microscopy	86
2.8. Related Research	93
2.9. References	105
3. Experimental Procedure	143
3.1. Sample Preparation	143
3.2. Surface Treatments	147
3.3. Protein Solutions	148
3.4. Binding Procedure	150
3.5. Characterization Techniques	151
3.5.1. Electrophoresis	151
3.5.2. Fluorescence Spectroscopy	155
3.5.3. Bicinchoninic Acid (BCA) Assay	157
3.5.4. Glancing Incidence X-ray Analysis (GIXA)	159
3.5.5. Atomic Force Microscopy (AFM)	160
3.5.6. Chemical Force Microscopy (CFM) and Force Volume Imaging	162
3.6. Experimental Procedure References	164
4. Results	165
4.1. Gel Electrophoresis (SDS-PAGE)	165
4.1.1. Human Serum Albumin (HSA)	166

SECTION TITLE	PAGE
4.1.2. Streptavidin	172
4.1.3. Immunoglobulin G	188
4.2. Fluorescence Spectrometry	200
4.3. Bicinchoninic Acid Protein Assay	245
4.4. X-ray Analyses	252
4.5. Atomic Force Microscopy (AFM)	256
4.5.1. AFM References	295
4.6. Chemical Force Microcopy (CFM)	296
5. Discussion	350
5.1. Discussion of SDS-PAGE Results	350
5.2. Discussion of Fluorimetry Results	357
5.3. Discussion of BCA Assay Results	366
5.4. Discussion of X-ray Results	375
5.5. Discussion of AFM Results	375
5.6. Discussion of CFM Results	383
5.7. General Discussion	391
5.8. Discussion References	400
6. Conclusion	402
7. Thoughts for Future Work	408

List of Tables

TABLE	TITLE	PAGE
I	Eight Cleaning Methods Evaluated by Cras <i>et al.</i>	38
II	Spectroscopic Properties of the Aromatic Amino Acids at Neutral pH	68
III	Important IR Bands in the Study of Biological Molecules	84
IV	Molecular Properties of Proteins that May Influence Surface Activity	95
V	Surface Treatments Applied to Various Silica Forms	148
VI	Recipes for Common Chemicals Used in This Study	150
VII	Protein Band Quantification for the Gel in Figure 4.1.2.21 along with Calculated Binding Amounts	188
VIII	Primary and Secondary IgG Protein Binding Quantities Adsorbed to Surface Found Using Two Separate Methods for Binding Set One	193
IX	Primary and Secondary IgG Protein Binding Quantities Adsorbed to Surface Found Using Two Separate Methods for Binding Set Two	199
X	Concentration 0.01 mg/ml Streptavidin, Biotin, and FITC IgG Binding Amount Results from Binding Set Two Using Controls as the Starting Concentrations	240
XI	Concentration 0.1 mg/ml Streptavidin, Biotin, and FITC IgG Binding Amount Results from Binding Set Two Using Controls as the Starting Concentrations	240
XII	Concentration 0.01 mg/ml Streptavidin, Biotin, and FITC IgG Binding Amount Results from Binding Set Two Using Standards as the Starting Concentrations	241
XIII	Concentration 0.1 mg/ml Streptavidin, Biotin, and FITC IgG Binding Amount Results from Binding Set Two Using Standards as the Starting Concentrations	241

TABLE	TITLE	PAGE
XIV	BCA Assay Binding Results for Depleted Streptavidin Solutions from Binding Set One	247
XV	BCA Assay Binding Results for Depleted Mouse-IgG Solutions from Binding Set One	247
XVI	GIXA Model Values for the Data Simulation Shown in Figure 4.4.1	253
XVII	Force-Volume Collection Figure Array Reference List	301
XVIII	All of the Maximum and Minimum Forces Collected for the Entire Sample Set Along with the Variation in Forces.	347
XIX	Zhuravlev's Values for Silanol Concentration, Si Concentration and Si-O-Si Bridge Concentration as a Function of Heat Treatment Temperature.	365
XX	Binding Results Master Table Including Data from Fluorimetry, BCA assay and SDS-PAGE Using Controls.	374
XXI	Zhuravlev's Values for Silanol Concentration, Si Concentration and Si-O-Si Bridge Concentration as a Function of Heat Treatment Temperature.	391
XXII	Binding Capability Data for Fluorimetry, BCA Assay and SDS-PAGE for the Various Sample Forms and Surface Treatments.	399

List of Figures

FIGURE	DESCRIPTION	PAGE
2.1.1	The percent of CHO cell coverage on the seven types of glass substrates as a function of time.	7
2.1.2	The number of CHO cells growing as a function of time on glass substrates of different compositions.	8
2.1.3	The relative size of the CHO cells growing as a function of time on three glass substrates of different composition.	8
2.2.1	The silica tetrahedron. The silicon atom (at the center) is represented by the black circle and the oxygen atoms are the gray circles.	11
2.2.2	Heat treatment time-temperature-transformation diagram (T-T-T). To the left of the tangent to the nose temperature crystallization (at 10^{-6} volume fraction) is avoided.	12
2.2.3	The volume-temperature (V-T) diagram for glass or crystal formation from a liquid.	13
2.2.4	The X-ray powder diffraction patterns of α - and β -quartz, high and low temperature cristobalite, and amorphous silica.	14
2.2.5	Schematic of silicate bond angles giving definitions of the bond angle β in (a) and the torsion angles α_1 in (a and b) and α_2 in (a).	15
2.2.6	The correlation function for vitreous silica. I, II, and III indicate the extent of the various ranges of order.	16
2.3.1.1	Types of surface (hydroxyl) groups on the silica surface as postulated by Iler. (a) hydrated vicinal, (b) anhydrous vicinal, (c) dehydrated siloxane, (d) hydroxylated surface, (e) isolated, (f) geminal, (g) hydrogen bonded vicinal.	23

FIGURE	DESCRIPTION	PAGE
2.3.1.2	Reaction of two neighboring hydrogen bonded (indicated by the dotted line) hydroxyls to form molecular water and a siloxane bond. Dehydroxylation reaction.	26
2.3.1.3	Models of chemisorbed water and physisorbed water (with the molecular water encircled) that may evolve in dehydroxylation and dehydration respectively.	26
2.3.1.4	Lange's description of the two types of adsorbed water, hydrogen bonded (encircled) and physically bonded (everything above solid black line).	27
2.3.2.1	Various radii of curvature for silica surfaces. Typical examples of each extreme are noted and also the progression of crowding with changes in curvature. After Iler.	32
2.4.3.1	Schematic representation of an AFM. The right side of the schematic is an enlarged version of what occurs under the AFM head.	54
2.4.3.2	The five modes of the AFM.	55
2.4.3.3	A non-contact AFM image of a silica glass fracture surface, fractured under ultra-high vacuum (top) and imaged in vacuum (bottom). The insert from the upper image with possible O-O (solid lines, A,C) and Si-O (dashed lines,B) bonds.	60
2.4.4.1	A general energy band diagram for fluorescence. The excitation energy is typically in the ultraviolet and the emission energy is typically in the visible region of the electromagnetic spectrum.	63
2.5.1	All 20 amino acid structures (and names) that are the building blocks for proteins.	65
2.5.2	Two examples of protein motifs with loop regions indicated by arrows. (a) The hairpin beta motif and (b) the beta-alpha-beta motif.	67

FIGURE	DESCRIPTION	PAGE
2.5.2.2.1	Streptavidin amino acid sequence from Protein Data Bank file 1SLF.pdb. The Trp-Lys sequences at positions 79-80 and 120-121 are underlined.	71
2.5.2.2.2	Stereograms of (a) one monomer of streptavidin forms a β -barrel with extended hairpin loops and biotin (ball and stick molecule) is bound at the open end of the barrel. The asterisks denote the termini of the loop that folds over biotin. (b) A streptavidin tetramer.	71
2.5.2.3.1	A schematic diagram of the structural features of an IgG molecule (left). The constant region is identified by the crosshatches. A spacefill model of IgG (right) shows how the molecule structures twist around each other.	74
2.6.3.1	Common fluorophores used to label proteins, their absorption range and emission range. The arrow is pointing to fluorescein, a label used in the current study.	78
2.7.1	Basic function of a CFM setup.	87
2.7.2	Example of a force-distance curve. (1) Approach of tip to surface. (2) Jump-to-contact point. (3) Linear cantilever deflection under increasing force. (4) Retraction leads to a negative deflection of the cantilever. (5) Pull-off point.	88
2.7.3	Examples of CFM interactions and the force laws needed to interpret the corresponding curves.	90
2.8.1	Multiple adsorbed orientations of a protein due to multiple binding sites.	96
3.1.1	Photograph of the Heathway fiber redraw tower in room 106 of the Hall of Glass Science and Engineering.	145
3.5.1.1	Side view schematic of the XCell II Mini Cell used for gel electrophoresis.	153
3.5.1.2	Schematic drawing of a gel loading set-up.	154
3.5.2.1	Schematic diagram of SPEX 1680 fluorescence spectrometer.	156

FIGURE	DESCRIPTION	PAGE
3.5.3.1	A 96-well microtiter plate used for BCA assay. The more purple and deeper the color, the higher the protein concentration is in that well.	158
3.5.4.1	Schematic of the set-up for a glancing incidence X-ray analysis instrument.	160
4.1.1	Mark 12™ molecular weight marker in the lane of a 4-20% gradient tris-glycine gel in the unstained state.	166
4.1.1.1	A gel image of four HSA standards (at the arrow) with order of magnitude increases in concentration.	168
4.1.1.2	A gel image of five initial concentrations of HSA after being adsorbed for 30 minutes and then stripped from silica (Q) cane.	168
4.1.1.3	A gel image of four initial concentrations of HSA after being adsorbed for 30 minutes and then stripped from soda-lime silicate (SLS) cane.	169
4.1.1.4	A gel image of four initial concentrations of HSA after being adsorbed for 30 minutes and then stripped from borosilicate (BS) cane.	169
4.1.1.5	A gel image of the determined maximum required initial protein concentration for meeting binding capacity after being exposed to BS, Q, and SL cane with three internal standards.	171
4.1.1.6	Compare lanes export of the gel in Figure 4.1.1.5 with HSA on Silica (Q), SLS and BS glass rods including two HSA standards.	171
4.1.2.1	A gel image of streptavidin after binding to silica and SLS slides after no etch or 10 minutes of HF etching.	173
4.1.2.2	CLE of the gel in Figure 4.1.2.1 of streptavidin on HF etched or unetched Q and SLS slides.	173
4.1.2.3	A gel image of streptavidin after binding to silica and soda-lime silicate fibers with internal standards.	174

FIGURE	DESCRIPTION	PAGE
4.1.2.4	Compare lanes export of the gel in Figure 4.1.2.3 with streptavidin on Q and SLS fibers.	174
4.1.2.5	Image of a native gel created from HSA, BSA and streptavidin binding to SLS microspheres.	175
4.1.2.6	A gel image of 0.1 mg/ml streptavidin adsorbed to five silica forms. Stained with GelCode™.	176
4.1.2.7	A gel image of 0.1 mg/ml streptavidin adsorbed to five silica forms. Stained with SilverQuest™.	177
4.1.2.8	A CLE of the gel in Figure 4.1.2.7.	177
4.1.2.9	A gel image of 0.1 mg/ml streptavidin adsorbed to Q and SLS fibers. Binding was done on 6/22/01. Stained with SilverQuest™.	178
4.1.2.10	A gel image of 0.1 mg/ml streptavidin adsorbed to ethanol cleaned and H ₂ O plasma treated silica slides for 30 minutes. Stained with SilverQuest™.	179
4.1.2.11	A CLE of the gel in Figure 4.1.2.10.	179
4.1.2.12	Strept #1. A gel image of three streptavidin solution concentrations exposed to one Q or BS cane for 30 minutes. Stained with SilverQuest™.	180
4.1.2.13	Strept #2. A gel image of three concentrations of streptavidin exposed to one Q or BS cane each. The LSB-R used had no bromophenol blue.	181
4.1.2.14	Strept #3. A gel image of three concentrations of streptavidin exposed to one Q or BS cane each. Loading quantities were higher than previous gel.	182
4.1.2.15	Strept #4. A gel image of three streptavidin solution concentrations exposed to two Q or BS rods each with half as much LSB-R (no dye) for boiling.	183

FIGURE	DESCRIPTION	PAGE
4.1.2.16	Strept #5. A gel image of three concentrations of streptavidin exposed to two Q or BS rods each. Stained with SilverXpress™.	183
4.1.2.17	A gel image of 0.1 mg/ml streptavidin solutions exposed to either 3.7 mg of Stöber spheres or 1.85 mg of Stöber spheres. Stained with SilverXpress™.	184
4.1.2.18	A gel image from Binding Set #2 with 0.01 mg/ml streptavidin adsorbed to silica slides and cane with various surface treatments and three internal standards. The streptavidin band occurs at the arrow.	186
4.1.2.19	A gel image from Binding Set #2 with 0.1 mg/ml streptavidin adsorbed to silica slides and cane with various surface treatments and three internal standards. The streptavidin band occurs at the arrow.	186
4.1.2.20	A gel image from Binding Set #2 with 0.01 mg/ml streptavidin adsorbed to silica fiber and powders with various surface treatments and three internal standards. The streptavidin band occurs at the arrow.	187
4.1.2.21	A gel image from Binding Set #2 with 0.1 mg/ml streptavidin adsorbed to silica fiber and powders with various surface treatments and three internal standards. The streptavidin band occurs at the arrow.	188
4.1.3.1	A gel image of two concentrations of mouse IgG and anti-mouse IgG on silica fibers with either an HF etch treatment or an ethanol clean treatment.	190
4.1.3.2	A gel image of two concentrations of mouse IgG and anti-mouse IgG on silica slides with one of three surface treatments.	192
4.1.3.3	A gel image of two concentrations of mouse IgG and anti-mouse IgG on silica cane with one of three surface treatments.	192
4.1.3.4	A gel image of two concentrations of mouse IgG and anti-mouse IgG on either silica Cabosil™ or Stöber spheres.	193

FIGURE	DESCRIPTION	PAGE
4.1.3.5	A gel image of 0.01 mg/ml mouse IgG and anti-mouse IgG adsorbed to silica fiber, Cabosil™, or Stöber spheres with various surface treatments.	195
4.1.3.6	A CLE of 0.01 mg/ml mouse IgG and anti-mouse IgG adsorbed to silica fiber, Cabosil™, or Stöber spheres with various surface treatments.	195
4.1.3.7	A gel image of 0.1 mg/ml mouse IgG and anti-mouse IgG adsorbed to silica fiber, Cabosil™, or Stöber spheres with various surface treatments.	196
4.1.3.8	A CLE of 0.1 mg/ml mouse IgG and anti-mouse IgG adsorbed to silica fiber, Cabosil™, or Stöber spheres with various surface treatments.	196
4.1.3.9	A gel image of 0.01 mg/ml mouse IgG and anti-mouse IgG adsorbed to silica slides and cane with various surface treatments. Sample wells had 20 μ L loading.	197
4.1.3.10	A CLE of 0.01 mg/ml mouse IgG and anti-mouse IgG adsorbed to silica slides and cane with various surface treatments.	197
4.1.3.11	A gel image of 0.1 mg/ml mouse IgG and anti-mouse IgG adsorbed to silica slides and cane with various surface treatments. Samples wells had 20 μ L loading.	198
4.1.3.12	A CLE of 0.1 mg/ml mouse IgG and anti-mouse IgG adsorbed to silica slides and cane with various surface treatments.	198
4.2.1	Fluorescence emission spectra of three concentrations of streptavidin protein solutions and TBS excited at 280 nm.	201
4.2.2	Fluorescence emission spectra of three concentrations of streptavidin protein solutions and TBS excited at 295 nm.	201
4.2.3	Dual excitation and emission spectra of a 0.1 mg/ml streptavidin solution.	202

FIGURE	DESCRIPTION	PAGE
4.2.4	Fluorescence emission spectra of streptavidin protein solutions run in triplicate with the corresponding areas listed.	203
4.2.5	Fluorescence emission spectra of four depleted streptavidin solutions (originally 0.1mg/ml) after exposure to a section of silica slide or 2 pieces of silica cane each. Excited at 280 nm.	204
4.2.6	Fluorescence emission spectra of four depleted streptavidin solutions (originally 0.1mg/ml) after exposure to a section of silica slide or 2 pieces of cane each. Excited at 295 nm.	205
4.2.7	Fluorescence emission spectra of depleted streptavidin solutions (originally 0.1 mg/ml) after exposure to Cabosil™ or Stöber spheres. Excited at 280 nm.	206
4.2.8	Fluorescence emission spectra of streptavidin solution (originally 0.01 mg/ml) after incubation with either a slide, cane, Stöber spheres or Cabosil™. Excited at 280 nm.	207
4.2.9	Fluorescence emission spectra of streptavidin solutions after a 30 min exposure to HF etched silica slides. Excited at 280 nm with three standards.	208
4.2.10	Plot of the known micrograms for the standards in Figure 4.2.9 as a function of their corresponding areas. The equation provides quantity of protein in unknown sample solutions by knowing the area under their emission peaks.	208
4.2.11	Fluorescence emission spectra of streptavidin solutions after having been exposed to a water plasma treated slide. Excited at 280 nm with three standards.	209
4.2.12	Fluorescence emission spectra of FTIC IgG (originally 0.1 mg/ml) after exposure to a slide with the treatment indicated. Excited at 485 nm with two standards.	211
4.2.13	Standards plot for FITC labeled anti-mouse IgG for determining linear equation relating area under the emission peak to quantity of protein in cuvette.	211

FIGURE	DESCRIPTION	PAGE
4.2.14	Fluorescence emission spectra of FITC IgG (originally 0.01 mg/ml) after exposure to a slide with the surface treatment indicated. Excited at 485 nm with two standards.	212
4.2.15	Fluorescence emission spectra for streptavidin solutions (originally 0.1 mg/ml) after exposure to either an HF etched slide or a water plasma treated slide. Excited at 280 nm with two standards.	213
4.2.16	Fluorescence emission spectra of streptavidin solutions (originally 0.01 mg/ml) after exposure to either a HF etched slide or a water plasma treated slide. Excited at 280 nm with one standard.	214
4.2.17	Fluorescence emission spectra of FITC IgG (originally 0.1 mg/ml) after incubation with cane having the surface treatment indicated. Excited at 485 nm with two standards.	214
4.2.18	Fluorescence emission spectra of FITC IgG (originally 0.01 mg/ml) after incubation with cane having the surface treatment indicated. Excited at 485 nm with one standard.	215
4.2.19	Logarithmic plot of the quantity versus fluorescence emission peak area for the FITC IgG standards. Equation is shown with r-squared best fit value.	215
4.2.20	Fluorescence emission spectra of streptavidin protein solutions after incubation with ten fibers having the surface treatment indicated. Excited at 280 nm with two standards.	217
4.2.21	Fluorescence emission spectra of FITC IgG solutions after exposure to silica fibers with the treatment indicated and also an exposure to mouse IgG. Excited at 485 nm with two standards.	217
4.2.22	Fluorescence emission scan of a single 0.01 mg/ml streptavidin standard after three types of light exposure.	218
4.2.23	Fluorescence emission scan of a single 0.01 mg/ml FITC IgG standard after various light conditions.	219

FIGURE	DESCRIPTION	PAGE
4.2.24	Fluorescence emission spectra of a 0.01 mg/ml streptavidin standard after six “rinsing” steps. Excited at 280 nm.	220
4.2.25	Fluorescence emission spectra of a 0.01 mg/ml FITC IgG standard after six “rinsing” steps. Excited at 485 nm.	221
4.2.26	Fluorescence emission spectra of 1.0 mg/ml mouse IgG and anti-mouse IgG FITC labeled adsorbed to an ethanol cleaned silica slide for 30 minutes each. Legend follows graph top to bottom.	222
4.2.27	Fluorescence emission spectra of two silica slides with 0.1 mg/ml mouse IgG and FITC anti-mouse IgG adsorbed during drying in either light or darkness. Excited at 485 nm.	223
4.2.28	Fluorescence emission scan of three separate streptavidin solutions of 0.1 mg/ml concentration. Two solutions were standards and the other was created as a control. Excited at 280 nm.	224
4.2.29	Fluorescence emission spectra collected on various dates for 0.1 mg/ml streptavidin protein solution. Each day is a different solution.	225
4.2.30	Fluorescence emission spectra of streptavidin depleted solutions (originally 0.01 mg/ml) from Binding Set One. Excited at 280 nm.	226
4.2.31	Fluorescence emission spectra of streptavidin depleted solutions (originally 0.1 mg/ml) from Binding Set One. Excited at 280 nm.	227
4.2.32	Fluorescence emission spectra of FITC IgG depleted solutions (originally 0.01 mg/ml) from Binding Set One. Excited at 485 nm.	227
4.2.33	Fluorescence emission spectra of FITC IgG depleted solutions (originally 0.1 mg/ml) from Binding Set One. Excited at 485 nm.	228
4.2.34	Binding capacity bar chart for all silica slides in Binding Set One.	229

FIGURE	DESCRIPTION	PAGE
4.2.35	Binding capacity bar chart for all silica cane in Binding Set One.	229
4.2.36	Binding capacity bar chart for all silica fibers in Binding Set One.	230
4.2.37	Binding capacity bar chart for all silica Stöber spheres in Binding Set One.	230
4.2.38	Binding capacity bar chart for all silica Cabosil™ in Binding Set One.	231
4.2.39	Fluorescence emission spectra of five 0.01 mg/ml streptavidin solutions with different thermal and air exposure histories. Excited at 280 nm.	232
4.2.40	Fluorescence emission spectra of 0.01 mg/ml streptavidin solutions at various pHs. Half are controls and half have been exposed to silica cane.	233
4.2.41	Fluorescence emission spectra of streptavidin protein boiled in LSB-R, as well as two HF etched cane samples with adsorbed protein.	234
4.2.42	Fluorescence emission spectra of FITC IgG protein boiled in LSB-R, as well as two HF etched cane samples with adsorbed mouse IgG and FITC IgG.	234
4.2.43	Fluorescence emission spectra of streptavidin depleted solutions (0.01 mg/ml) from Binding Set Two.	235
4.2.44	Fluorescence emission spectra of depleted fluorescein biotin (originally 0.01 mg/ml) after exposure to streptavidin coated samples from Binding Set Two. Excited at 485nm.	236
4.2.45	Fluorescence emission spectra for depleted streptavidin solution (originally 0.1 mg/ml) from Binding Set Two.	237
4.2.46	Fluorescence emission spectra of depleted fluorescein biotin solutions (originally 0.1 mg/ml) after exposure to streptavidin coated samples from Binding Set Two.	237

FIGURE	DESCRIPTION	PAGE
4.2.47	Fluorescence emission spectra of FITC IgG (originally 0.01 mg/ml) after exposure to mouse IgG coated samples from Binding Set Two.	238
4.2.48	Fluorescence emission spectra of FITC IgG (originally 0.1 mg/ml) after exposure to mouse IgG coated samples from Binding Set Two.	239
4.2.49	Binding amounts for silica slides after FITC IgG and streptavidin from Binding Set Two.	242
4.2.50	Binding amounts for silica cane after FITC IgG and streptavidin from Binding Set Two.	242
4.2.51	Binding amounts for silica fiber after FITC IgG and streptavidin from Binding Set Two.	243
4.2.52	Binding amounts for silica Cabosil™ after FITC IgG and streptavidin from Binding Set Two.	243
4.2.53	Binding amounts for silica Stöber spheres after FITC IgG and streptavidin from Binding Set Two.	244
4.3.1	BCA assay binding results for silica slides from Binding Set Two using controls.	249
4.3.2	BCA assay binding results for silica cane from Binding Set Two using controls.	250
4.3.3	BCA assay binding results for silica fibers from Binding Set Two using controls.	250
4.3.4	BCA assay binding results for fumed silica Cabosil™ from Binding Set Two using controls.	251
4.3.5	BCA assay binding results for Stöber microspheres from Binding Set Two using controls.	251
4.4.1	GIXA data for untreated silica slide coated with streptavidin protein and the simulation fit.	253

FIGURE	DESCRIPTION	PAGE
4.4.2	X-ray data for quartz crystal. Powder diffraction data (top). Single crystal diffraction of natural quartz terminal (middle). PDF of synthetic quartz (bottom).	255
4.5.1	AFM tapping mode image of an as-received FFSLS slide showing crystal processing debris and organic film.	257
4.5.2	AFM tapping mode image of an FFSLS slide etched in HF acid for 2 minutes showing processing debris, but no surface film.	257
4.5.3	AFM tapping mode image of an as-received NCSLS slide showing heavy processing debris.	259
4.5.4	AFM tapping mode images of an as-received NCSLS slide. Left is topographical data and right is phase contrast data.	259
4.5.5	AFM tapping mode image of an NCSLS slide etched in HF acid for 10 minutes showing processing debris remains after etching.	260
4.5.6	AFM tapping mode image of another as-received NCSLS slide showing no processing debris.	260
4.5.7	AFM image of an NCSLS slide etched in 10% HF acid for 10 minutes showing a slight roughening of the surface.	261
4.5.8	AFM tapping mode image of two silica glass slides having been cleaned with ethanol.	262
4.5.9	AFM tapping mode image of a silica glass slide etched in 10% HF acid for (a) 10 minutes and (b) 2 minutes.	263
4.5.10	AFM tapping mode images of silica and SLS slides. (a) untreated silica, (b) 2 min HF etched silica, (c) untreated SLS, and (d) 2 min HF etched SLS.	264
4.5.11	3-D AFM tapping mode images of SLS slides (a) untreated and (b) etched in HF acid for 2 minutes.	265
4.5.12	AFM tapping mode image of a silica slide etched in 10% HF acid for 10 minutes.	265

FIGURE	DESCRIPTION	PAGE
4.5.13	AFM tapping mode topographical image of a 10-minute water plasma treated silica slide.	267
4.5.14	Section analysis of the line drawn in the lower left-hand image.	267
4.5.15	AFM topographical (left) and phase contrast (right) image of a 10-minute water plasma treated SLS slide.	268
4.5.16	AFM image of a SLS slide after a water plasma treatment for 5 minutes.	268
4.5.17	AFM tapping mode image of the natural quartz single crystal terminal with roughness analysis.	269
4.5.18	3-dimensional AFM tapping mode image of the natural quartz single crystal terminal showing planar steps.	270
4.5.19	AFM topographical image with height scale bar showing a rectangular depression on the natural quartz single crystal terminal.	270
4.5.20	3-dimensional AFM tapping mode image of the rectangular feature on natural quartz single crystal terminal.	271
4.5.21	AFM section analysis of a second rectangular feature on the natural quartz single crystal terminal.	271
4.5.22	AFM tapping mode image of natural quartz single crystal terminal at a 5-micron scan size with roughness analysis.	272
4.5.23	AFM topographical (left) and phase contrast (right) images for a 1-micron scan of the natural quartz single crystal terminal.	273
4.5.24	3-dimensional AFM tapping mode image of the natural quartz single crystal terminal at a 5-micron scan size.	273
4.5.25	3-dimensional AFM tapping mode image of an ethanol cleaned silica fiber surface.	274

FIGURE	DESCRIPTION	PAGE
4.5.26	AFM tapping mode image of a 1-micron section of an ethanol cleaned fiber surface with roughness analysis.	275
4.5.27	AFM topographical tapping mode image of a 10-minute HF etched fiber surface with height scale bar.	275
4.5.28	3-dimensional AFM tapping mode image of a 10-minute HF etched fiber surface.	276
4.5.29	AFM tapping mode topographical image of dried streptavidin protein adsorbed to an ethanol cleaned silica slide.	277
4.5.30	Section analysis of streptavidin on mica imaged using fluid cell tapping mode.	278
4.5.31	Fluid cell tapping topographical image (left) and phase contrast image (right) of streptavidin on mica.	279
4.5.32	AFM tapping mode images of a HF etched silica slide in (a) air and (b) using a fluid cell under a streptavidin solution.	280
4.5.33	AFM tapping mode 5-micron image of cane cleaned with ethanol.	281
4.5.34	AFM tapping mode 500 nm image of cane cleaned with ethanol.	281
4.5.35	AFM tapping mode 10-micron image of dried adsorbed mouse IgG on an ethanol cleaned cane.	282
4.5.36	AFM tapping mode 5-micron image of dried adsorbed mouse-IgG on ethanol cleaned silica cane.	282
4.5.37	AFM tapping mode 1-micron image of the small agglomerations of mouse-IgG on ethanol cleaned cane.	283
4.5.38	A 250 nm AFM topographical (left) and phase contrast image (right) of mouse-IgG adsorbed onto ethanol cleaned silica cane.	283
4.5.39	AFM tapping mode, 5-micron scan of a non-salt crystal area on IgG-coated ethanol-cleaned cane.	284

FIGURE	DESCRIPTION	PAGE
4.5.40	AFM tapping mode 5-micron image of adsorbed and dried streptavidin on ethanol cleaned silica cane.	285
4.5.41	A 1-micron AFM topographical (left) and phase contrast (right) image of streptavidin adsorbed to ethanol cleaned silica cane.	285
4.5.42	A 200 nm tapping mode AFM topographical (left) and phase contrast (right) image of streptavidin adsorbed to ethanol cleaned silica cane.	286
4.5.43	AFM tapping mode 5-micron image of a silica cane etched in HF for 10 minutes.	287
4.5.44	AFM tapping mode 500-nm image of HF etched silica cane.	288
4.5.45	AFM tapping mode 5-micron image of mouse-IgG adsorbed onto HF etched silica cane.	288
4.5.46	AFM tapping mode 1-micron image of mouse-IgG adsorbed onto HF etched silica cane.	289
4.5.47	AFM tapping mode 2-micron image of streptavidin adsorbed onto HF etched silica cane.	289
4.5.48	A topographical (left) and phase contrast (right) image of streptavidin adsorbed to HF etched silica cane.	290
4.5.49	AFM 1-micron section analysis of streptavidin adsorbed onto HF etched silica cane showing the height and diameter of the small protein agglomerations.	291
4.5.50	AFM tapping mode 5-micron image of water plasma treated silica cane.	292
4.5.51	3-dimensional AFM tapping mode 1-micron image of water plasma treated silica cane clearly showing surface impurities.	293
4.5.52	Dual topographical (left) and phase contrast (right) image of water plasma treated silica cane.	293

FIGURE	DESCRIPTION	PAGE
4.5.53	AFM tapping mode 500 nm image of water plasma treated silica cane.	294
4.5.54	AFM tapping mode 1-micron image of mouse-IgG adsorbed to water plasma silica cane.	294
4.6.1	Force-distance curve for a single point on a piece of water plasma treated silica cane using a plain silicon nitride tip in air.	298
4.6.2	Force-distance curve of a single point on a piece of water plasma treated silica cane using a streptavidin functionalized tip in air.	298
4.6.3	Force-distance curve of a single point on the natural quartz terminal using a streptavidin tip in air.	299
4.6.4	Force-distance curve of a single point on the natural quartz terminal using a streptavidin tip in TBS.	299
4.6.5	CFM FV image of the side of a natural quartz crystal using a –COOH functionalized tip.	309
4.6.6	CFM FV image of the side of a natural quartz crystal using a streptavidin functionalized tip.	310
4.6.7	CFM FV image of the side of a natural quartz crystal using a –CH ₃ functionalized tip.	311
4.6.8	CFM force-distance curve for the terminal of a natural quartz crystal using a –COOH functionalized tip.	312
4.6.9	CFM force-distance curve for the terminal of a natural quartz crystal using a streptavidin functionalized tip.	313
4.6.10	CFM FV image of the terminal of a natural quartz crystal using a –CH ₃ functionalized tip.	314
4.6.11	CFM FV image of an ethanol cleaned silica slide using a –COOH functionalized tip.	315

FIGURE	DESCRIPTION	PAGE
4.6.12	CFM FV image of an ethanol cleaned silica slide using a streptavidin functionalized tip.	316
4.6.13	CFM FV image of an ethanol cleaned silica slide using a –CH ₃ functionalized tip.	317
4.6.14	CFM FV image of a 20 minute HF etched silica slide using a –COOH functionalized tip.	318
4.6.15	CFM FV image of a 20 minute HF etched silica slide using a streptavidin functionalized tip.	319
4.6.16	CFM FV image of a 20 minute HF etched silica slide using a –CH ₃ functionalized tip.	320
4.6.17	CFM FV image of a 20 minute water plasma treated silica slide using a –COOH functionalized tip.	321
4.6.18	CFM FV image of a 20 minute water plasma treated silica slide using a streptavidin functionalized tip.	322
4.6.19	CFM FV image of a 20 minute water plasma treated silica slide using a –CH ₃ functionalized tip.	323
4.6.20	CFM FV image of a 16 hour 1000°C treated silica slide using a –COOH functionalized tip.	324
4.6.21	CFM FV image of a 16 hour 1000°C treated silica slide using a streptavidin functionalized tip.	325
4.6.22	CFM FV image of an ethanol cleaned silica cane using a –COOH functionalized tip.	326
4.6.23	CFM FV image of an ethanol cleaned silica cane using a streptavidin functionalized tip.	327
4.6.24	CFM FV image of an ethanol cleaned silica cane using a –CH ₃ functionalized tip.	328
4.6.25	CFM FV image of a 20 minute HF etched silica cane using a –COOH functionalized tip.	329

FIGURE	DESCRIPTION	PAGE
4.6.26	CFM FV image of a 20 minute HF etched silica cane using a streptavidin functionalized tip.	330
4.6.27	CFM FV image of a 20 minute HF etched silica cane using a $-CH_3$ functionalized tip.	331
4.6.28	CFM FV image of a 20 minute water plasma treated silica cane using a $-COOH$ functionalized tip.	332
4.6.29	CFM FV image of a 20 minute water plasma treated silica cane using a streptavidin functionalized tip.	333
4.6.30	CFM FV image of a 20 minute water plasma treated silica cane using a $-CH_3$ functionalized tip.	334
4.6.31	CFM FV image of a 16 hour 1000°C treated silica cane using a $-COOH$ functionalized tip.	335
4.6.32	CFM FV image of a 16 hour 1000°C treated silica cane using a streptavidin functionalized tip.	336
4.6.33	CFM FV image of a 16 hour 1000°C treated silica cane using a $-CH_3$ functionalized tip.	337
4.6.34	CFM FV image of an ethanol cleaned silica fiber using a $-COOH$ functionalized tip.	338
4.6.35	CFM FV image of an ethanol cleaned silica fiber using a streptavidin functionalized tip.	339
4.6.36	CFM FV image of an ethanol cleaned silica fiber using a $-CH_3$ functionalized tip.	340
4.6.37	CFM FV image of a 20 minute HF etched silica fiber using a $-COOH$ functionalized tip.	341
4.6.38	CFM FV image of a 20 minute HF etched silica fiber using a streptavidin functionalized tip.	342
4.6.39	CFM FV image of a 20 minute HF etched silica fiber using a $-CH_3$ functionalized tip.	343

FIGURE	DESCRIPTION	PAGE
4.6.40	CFM FV image of a 16 hour 1000°C treated silica fiber using a –COOH functionalized tip.	344
4.6.41	CFM FV image of a 16 hour 1000°C treated silica fiber using a streptavidin functionalized tip.	345
4.6.42	CFM FV image of a 16 hour 1000°C treated silica fiber using a –CH ₃ functionalized tip.	346
4.6.43	The variation in adhesion force in nN as a function of the silanol number as OH per square nanometer for the entire FV sample set.	348
4.6.44	Maximum adhesion force as a function of sample curvature for the entire FV sample set.	348
4.6.45	A CFM contact mode topographical image of a 16 hour 1000°C heat treated silica fiber collected using a –CH ₃ functionalized contact mode tip.	349
5.1.1	SDS-PAGE binding results for bulk samples displayed as a function of surface curvature.	357
5.3.1	BCA assay binding data and fluorimetry binding data for ethanol cleaned samples exposed to mouse-IgG and anti-mouse IgG FITC labeled, respectively.	367
5.3.2	BCA assay binding data and fluorimetry binding data for ethanol cleaned samples exposed to streptavidin protein.	368
5.3.3	BCA assay binding data and fluorimetry binding data for 10% HF etched samples exposed to mouse-IgG and anti-mouse IgG FITC labeled, respectively.	368
5.3.4	BCA assay binding data and fluorimetry binding data for 10% HF etched samples exposed to streptavidin protein.	369
5.3.5	BCA assay binding data and fluorimetry binding data for water plasma treated samples exposed to mouse-IgG and anti-mouse IgG FITC labeled, respectively.	369

FIGURE	DESCRIPTION	PAGE
5.3.6	BCA assay binding data and fluorimetry binding data for water plasma treated samples exposed to streptavidin protein.	370
5.3.7	BCA assay binding data and fluorimetry binding data for 1000°C treated samples exposed to mouse-IgG and anti-mouse IgG FITC labeled, respectively.	370
5.3.8	BCA assay binding data and fluorimetry binding data for 1000°C treated samples exposed to streptavidin protein.	371
5.3.9	BCA assay binding data and fluorimetry binding data for as-made powder samples exposed to mouse-IgG and anti-mouse IgG FITC labeled, respectively.	371
5.3.10	BCA assay binding data and fluorimetry binding data for as-made powder samples exposed to streptavidin protein.	372
5.3.11	BCA assay binding data and fluorimetry binding data for slide samples exposed to streptavidin or mouse-IgG and anti-mouse IgG FITC labeled.	372
5.5.1	Water plasma treated silica cane imaged as is (left) and after IgG adsorption and drying (right).	382
5.6.1	Adhesion forces of the three types of tip chemistry for the silica surface independent of surface treatment.	385
5.6.2	The percent variation of maximum adhesion force as a function of silanol number for the surface.	388
5.7.1	Proteins adsorbed to silica slides with various silanol concentrations.	393
5.7.2	Proteins adsorbed to silica cane with various silanol concentrations.	393
5.7.3	Proteins adsorbed to silica fiber with various silanol concentrations.	394

FIGURE	DESCRIPTION	PAGE
5.7.4	Proteins adsorbed to silica Stöber spheres with various silanol concentrations.	395
5.7.5	Proteins adsorbed to Cabosil™ fumed silica with various silanol concentrations.	395
5.7.6	IgG protein at a concentration 0.01 mg/ml binding capability for slides and cane comparing the three characterization techniques.	397
5.7.7	IgG protein at a concentration 0.01 mg/ml binding capability for cane and fiber comparing the three characterization techniques.	397
5.7.8	IgG protein at a concentration of 0.01 mg/ml binding capability for cane on a logarithmic scale showing the error associated with the three characterization techniques.	398

ABSTRACT

The motivation behind this work stems from Jedlicka's work on Chinese hamster ovary (CHO) cells and her observation that these cells proliferated differently depending on the glass chemistry on which the cells were growing. It is well established that proteins form the bonds between cells and glass substrates and so this work was aimed at discovering whether proteins also react differently to different glass surfaces. It is believed that the bond formed between glass and protein is a hydroxyl-amine interaction via hydrogen bonding. The scope of this work deals with silica glass in various forms including slides, cane, fiber, micron-sized spheres and Cab-o-Sil®. These forms are subjected to surface treatments such as ethanol cleaning, HF acid etching, water plasma treatments and 1000°C thermal treatments. A select few proteins are chosen as a tool to probe the surfaces of the silica glass and single crystal quartz surfaces. These proteins are human serum albumin (HSA), streptavidin, mouse immunoglobulin G (IgG), biotin, and anti-mouse IgG. A few characterization techniques are employed in an attempt to examine protein adsorption and its feasibility as a surface probe. These techniques include sodium dodecylsulfate-polyacrylamide gel electrophoresis (SDS-PAGE), bicinchoninic acid (BCA) assay, glancing incidence X-ray analysis (GIXA), fluorescence spectrometry, atomic force microscopy (AFM), and chemical force microscopy (CFM). The main goal of this work is to determine which of the above techniques in conjunction with protein adsorption is the most promising as a surface characterization technique.

It was determined that CFM is the most promising surface characterization technique utilizing proteins as surface probes. It is possible to attach a wide variety of molecules to a standard contact mode tip including proteins. Streptavidin, -COOH, and -CH₃ functionalized tips were utilized in the CFM study. The overall adhesion forces between silica and tip were greatest for -COOH, then streptavidin and least for -CH₃. This ordering is a broad generalization however, since the adhesion forces depend greatly on surface treatment and can either be very consistent across the surface or vary significantly. SDS-PAGE on streptavidin was preventatively difficult, but IgG electrophoresis was possible and did show some promising results. BCA assay and fluorimetry both utilized "depleted" protein solutions and thus it was very difficult to uncover trends in the data. GIXA showed that the protein layer thickness was monolayer in nature. AFM allowed proteins to be imaged while in the tris-buffered saline and the features were on the order of ten protein agglomerations. The GIXA and AFM data agree very well. CFM is able to discern between the various surface treatments. With the eventual development of carbon nanotube growth onto a contact mode tip and the subsequent application of a single chemical molecule onto the end of the tube, CFM will become an even stronger technique for surface characterization.

1. Introduction

Silica or silicon dioxide (SiO_2) is the most important constituent in the making of many commercial glasses. It is the structural basis of all traditional glass and is continually proving to be invaluable in the development of high-tech glasses. Single-component silica glass is one of the simplest glass systems in terms of composition, but some of its properties are far from simple. Vitreous silica behaves anomalously in many areas such as its volume-temperature relationship and its negative thermal expansion below room temperature. These properties lead one to consider the structure of the silica network.

The structure of vitreous silica may be one of the most highly debated issues in glass science of the past century. Scientists have gone from believing that silica was made of tiny crystallites, to proving that it definitely has no crystallites in a matter of a few years. The current knowledge is the generally accepted theory that glass consists of slightly distorted SiO_4 tetrahedra joined at the corners. Practically all of the oxygen atoms in silica are bridging to two silicon atoms. The angle between two neighboring tetrahedra (Si-O-Si) is the bond angle. This bond angle along with the torsion or rotation angles allow the tetrahedra to significantly alter their arrangement from a crystal such that no long-range order exists. Given the silica structure of the bulk, the surface structure is very different owing to the fact that the bonds are altered by the discontinuity. It is generally accepted that silica has various hydroxyl molecules on the surface. There are basically three forms of hydroxyls or silanols; geminal, vicinal and single. A single silanol is a silicon atom on the surface bound to a single OH molecule, a geminal silanol consists of two OH molecules bound to a single silicon atom on the surface, and a vicinal silanol has two OH molecules each bound to a

silicon atom on the surface with hydrogen bonding between the OH molecules.

The properties of many glasses depend on the condition of the surface. Clearly mechanical properties will depend on surface defects such as scratches or pits with fewer defects leading to stronger glasses. Several optical properties of glasses are highly dependent on the roughness of the surface, a smoother surface will reflect light more specularly. These properties are not intuitively affected by surface chemistry though. However, scratches on a glass surface will have unsatisfied bonds and these bonds will tend to react with water. This is why a scored glass piece breaks easier after having been wiped with water. On the chemical scale, glass properties are still affected by the surface. Liquid chromatography is a method by which organic molecules are separated in a column that usually contains silica gel. The chemical nature of the surface of the silica greatly affects the success of the separation in terms of time and resolution.

It is applications such as these that require scientists to understand the surface chemistry of silica. There are many instruments that can provide surface sensitive data, but these instruments often require silica forms that are not always utilized in application. Infrared spectroscopy often requires the powder form in order for the signal to be appreciable. The same can be said for BET nitrogen adsorption analysis or X-ray photoelectron spectroscopy. Bulk samples are usually required for glancing incidence X-ray techniques and microscopy techniques such as scanning electron microscopy and atomic force microscopy. Herein lies the problem though, how does one characterize the surface of a fiber or the inside of a capillary tube without altering the fundamental form of the glass and therefore the surface chemical structure?

The current work attempts to deal with this dilemma by utilizing small biological molecules to characterize surfaces that are otherwise difficult or impossible to characterize by conventional means. In order to accomplish

this goal, the work must begin with common surfaces and common characterization techniques to create a correlation between surface chemistries and observed reactions. The previous work that led to this study, suggested that Chinese hamster ovary cells can distinguish between glass surfaces where other characterization techniques cannot. It is known that proteins form the interface between glass and proliferating cells and so proteins were chosen as the surface probe in the current study. The hypothesis of this work is that proteins can be used to characterize glass surface. More specifically, that certain groups on a protein interact with the surface silanols of the silica. In this work, the following terms and their definitions will be employed. Silica is any material comprised essentially of SiO_2 . Vitreous silica is amorphous silica or silica glass. Crystalline silica refers to cristobalite, tridymite or quartz. Quartz is the low temperature crystalline form of silica. Quartz glass or fused quartz indicates vitreous silica formed by the melting of quartz.

The main proteins investigated are streptavidin and mouse immunoglobulin G (IgG). These proteins were selected because of their asymmetry and binding orientation sensitivity. Upon binding to a glass surface, these proteins may or may not present a binding site for a secondary protein, biotin and anti-mouse IgG, respectively. Unfortunately, this work did not achieve the stage whereupon the secondary protein binding capabilities were examined.

Silicon dioxide (SiO_2) was chosen as the composition to be studied and it was obtained in various forms. These forms include quartz single crystals, slides, cane, fiber, fumed Cab-o-Sil[®] and micron-sized spheres made via the Stöber process. The quartz single crystals were investigated because of their regular atomic arrangement. It was hypothesized that by using the known crystal structure of a given plane, one could correlate any repeated interaction of proteins to atomic groupings on the quartz surface. These specific interactions could then be correlated to the non-periodic structure of

amorphous silica and in so doing, determine the high affinity sites of proteins for silica.

The amorphous silica forms were exposed to various surface treatments, including, ethanol cleaning, HF acid etching, water plasma treatments, and 1000°C heat treatments. These surface treatments were intended to alter the surface chemistry of the silica by changing the type and population of surface silanols. The surfaces were characterized using a number of techniques, which included atomic force microscopy and chemical force microscopy. The proteins were then introduced to the various samples via incubation adsorption for 30 minutes. The adsorbed protein was analyzed either directly or indirectly using fluorescence spectroscopy, bicinchoninic acid protein assay, sodium dodecylsulfide polyacrylamide gel electrophoresis, atomic force microscopy and chemical force microscopy. The results were collected, analyzed, and conclusions were drawn as to the efficacy of utilizing proteins to characterize the surface of silica. This thesis deals with the interactions of proteins with the silica surface as a function of form and surface treatments.

2. Literature Review

“It is not enough to have a good mind; the main thing is to use it well.”

- Rene Descartes

2.1. Former Work

The current work was inspired by a previous study by Jedlicka on the variation in Chinese hamster ovary (CHO) cell growth on various glass substrates.¹ The objective of Jedlicka’s work was to systematically understand the effect of various amorphous materials on a model biological system. In essence, it was to understand how the glass structure affected the material’s biocompatibility. One of the most dangerous results of an adverse material-biological interaction is asbestosis. Asbestosis, a form of lung cancer, is practically a household word today due to the publication of the adverse affects of asbestos. Asbestosis is a lung disease that is common in the work place, arises from inhalation of airborne crystalline silicate fibers.² Asbestos contains crystalline silicate fibers and was a popular insulation material for many decades, but now is being stripped from ships, industrial, academic and private buildings and is being replaced with “safer” insulation materials. Asbestos and most crystalline silicate forms are very different from each other physically and chemically. It is not known whether the carcinogenic possibility of asbestos is caused by its crystallinity or the large aspect ratio inherent in the fiber form. Crystalline silica from any number of applications, such as sand from sand blasting, surface drilling, tunneling, silica flour milling and grinding have been reported to cause lung cancer. One study posed the hypothesis that it is the presence of the fiber form that causes cell mutation and eventual cancer.³ In terms of health, the safety of all fiber glass at one time was in question, with specific regard to their

carcinogenic possibilities.^{4,5} Asbestosis can be fatal and is often preceded by difficulty breathing and loss of lung function.² Therefore, the interactions involved in the development of this disease are important to understand by examining the various silica (surfaces) – biological systems.⁵

In her doctoral work, Jedlicka utilized CHO cells as a biological model because these cells are large, easily cultured, and reproducible yet sensitive to their environment.¹ The percent coverage of CHO cell growth varies significantly depending on the glass substrate composition. As shown in Figure 2.1.1, Bioglass® (BG) has a very high percentage of CHO cell coverage in a short amount of time, while at the other extreme, sodium silicate (NS) glass grows only to about a 12% coverage and then remains constant. The bioglass has a high calcium content, which promotes cell adhesion and spreading, and the bioactive nature of the BG surface aids in preventing cell disturbance. The cell behavior on the NS glass is attributed to the low chemical durability and corrosion of this type of glass. The percent coverage behavior of the CHO cells on three other glasses; silica (S with 100% SiO₂), soda-lime silicate (SL with 73% SiO₂, 14% Na₂O, 7% CaO, 4% MgO, and 2% Al₂O₃), and a high silica-containing fiber glass (FS with 63.6% SiO₂, 15.3% Na₂O, 5.76% CaO, 5.2% B₂O₃, 5.09% Al₂O₃, 2.7% MgO, 1.13% K₂O and 1.03% F₂) initially seems similar. However, upon further investigation, it was discovered that the cells grow differently on these three compositions even though their percent coverage is similar. The number of cells were counted in a given area as a function of time and as shown in Figure 2.1.2, cells reproduce more rapidly on the silica and the soda-lime silicate glasses than on the FS glass. In other words, more CHO cells form on silica and soda-lime silicate glasses in the same amount of time. The relative cell size of the CHO cells was also measured and it was observed that the high silica fiber glass substrate supports cells that are much larger than the other two compositions. Figure 2.1.3 shows this cell size relationship of the three glass compositions as a function of time. By microscopy, the cells on the FS glass

were observed to elongate and spread directionally across the surface tending towards a triangular morphology.

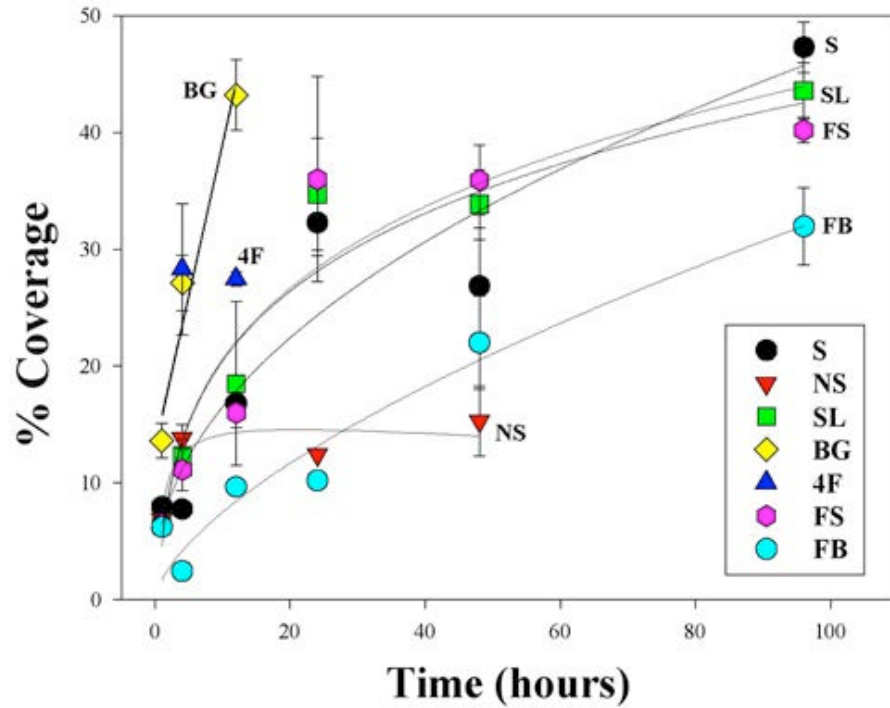


Figure 2.1.1. The percent of CHO cell coverage on the seven types of glass substrates as a function of time.¹

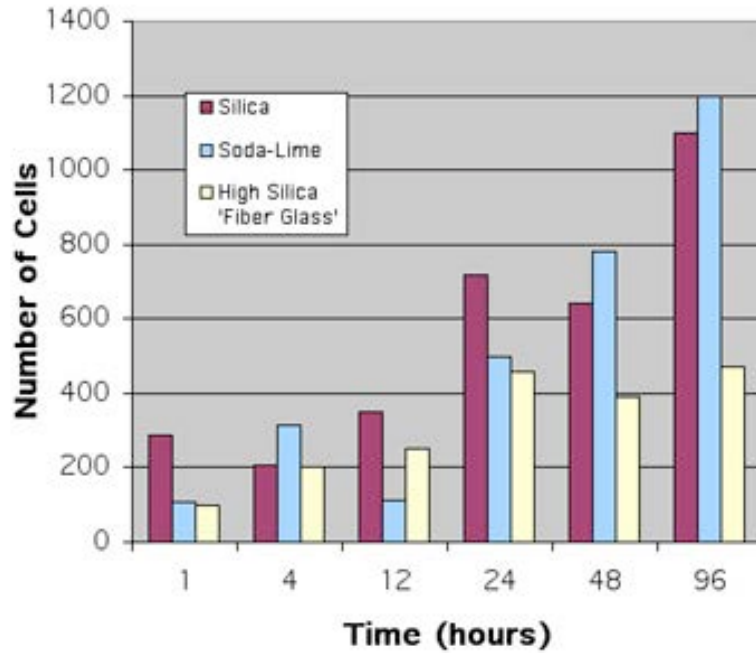


Figure 2.1.2. The number of CHO cells growing as a function of time on glass substrates of different compositions.

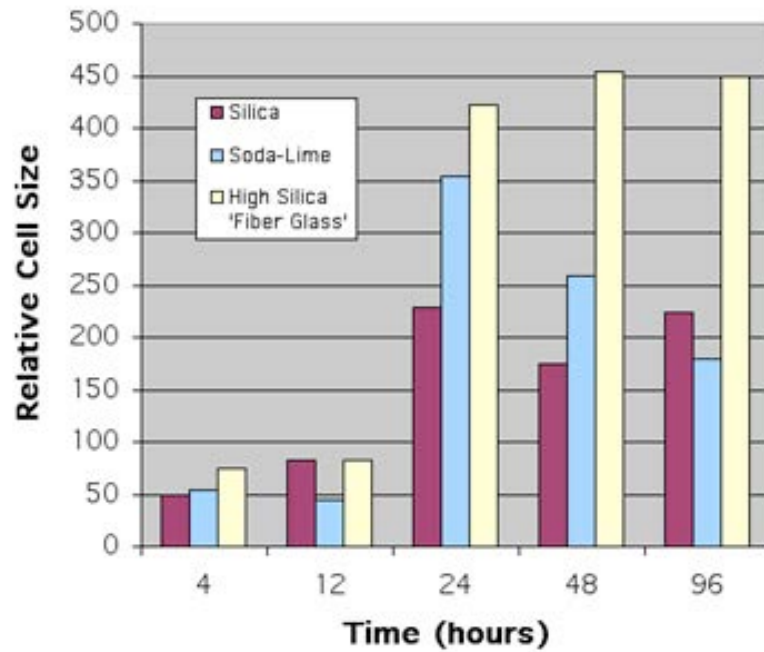


Figure 2.1.3. The relative size of the CHO cells growing as a function of time on three glass substrates of different composition.

It was observed that CHO cells are able to easily distinguish between the S, SL, and FS glasses when common characterization methods (dissolution analysis and DRIFT spectroscopy) can not. This observation logically leads one to believe that CHO cells can be used to provide a surface sensitive material characterization technique. However, a true surface characterization probe must be on the size order of the active surface species to reliably characterize a surface. Cells do not come in direct contact with a glass surface. Proteins form the bonds between material surfaces and cells.⁶⁻
¹¹ Although proteins are comprised of smaller entities called amino acids, proteins have functional groups that provide binding sites. To take this a step further, one could postulate that proteins, or even amino acids, can distinguish between surfaces of the same composition formed by different methods.

In a similar study to Jedlicka's, Elias *et al.*, examined the cytotoxic and transforming effects of silica particles with different surface properties in Syrian hamster embryo (SHE) cells.¹² The aim of this study was to gain information on the nature of the surface functionalities involved in the cytotoxic and transforming effects through the use of samples modified with controlled surface features. Several amorphous and crystalline silica dusts were utilized and the surfaces were modified by grinding, HF etching and heating. Their findings were many. Two biological responses were measured, cytotoxicity and neoplastic transformation, that are induced by silica and involve different mechanisms. Most of the dusts examined induce cytotoxicity and morphological transformations in the SHE cells in varying potencies. Even among the same silica polymorphs the degree of biological response varies indicating that the structure and the composition of the surface modulate the response. The cytotoxic effects appeared to be related to the distribution and abundance of silanol groups and to the presence of trace amounts of iron on the silica surface.¹² Induction of SHE cell transformation was accomplished on silica particles with fractured surfaces,

iron-active sites, and those able to generate reactive oxygen species. The effect of surface treatment on the biological response was evident in that heating, HF etching, and grinding in a wet atmosphere reduces the transforming potency. This again suggests that there may be more than one surface functionality involved in the reaction with the cells. It is believed that the specific surface functional groups involved in cell damage (and death) are the silanol groups and silicon based surface radicals, which both appear to play a role in cytotoxic effects.¹³⁻¹⁵ The presence of silanol appears to be a prerequisite for the attachment of the cell to silica particles.¹² This statement is supported by the reports by Nolan *et al.* and Shi *et al.* showing that the silanol groups form hydrogen bonds with some sites on the cell membrane.^{14,16} HF etching eliminates surface radicals, generally smoothes already smooth surfaces and creates pairs of surface silanols. Elias *et al.* found that HF etched quartz surfaces have patches of silanols that are arranged with a higher degree of order and occur in pairs. Quartz surfaces are more able to induce strong interactions with biomolecules than the disordered and isolated silanols on the amorphous layer of wet ground silica samples.¹² Amorphous silicas have different degrees of structural disorder and more variation in surface silanol arrangements than crystalline silicas.

2.2. Silica – Background and Forming

Vitreous silica and fused quartz are amorphous solids comprised of silicon and oxygen atoms in a ratio of 1:2. This ratio leads to a chemical formula of SiO_2 , which is commonly referred to as silica. Vitreous silica is typically formed through synthetic methods, whereas fused quartz is exactly that, quartz particles that have been melted and fused together. Silica also exists in crystalline forms where the silicon and oxygen atoms are arranged periodically. The basic building block of silica is the silica tetrahedron SiO_4^{4-} , which by definition is negatively charged with a value of 4. The silica

tetrahedron is shown in Figure 2.2.1. Each tetrahedron can bond with other tetrahedra (up to four) through the oxygen atoms by creating Si-O-Si bonds. When these tetrahedra link together, they can form either a crystal or an amorphous solid. The state and process of which depends on thermodynamic and kinetic principles.

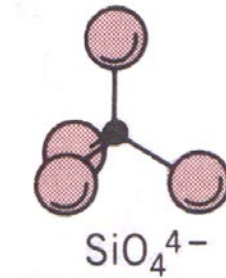


Figure 2.2.1. The silica tetrahedron. The silicon atom (at the center) is represented by the black circle and the oxygen atoms are the gray circles.

Silica can form by either natural or synthetic processes. Natural silica usually forms from a melt with many impurities or additives. For example, in nature, amorphous silica has been created in deserts when an area of sand is struck by lightning. The high temperature of the lightning melts the sand (mainly quartz) which then cools fairly quickly to form a glass, called fulgarites. These glasses are loaded with so many impurities, such as iron, that they appear black.

Crystalline silica, also found in nature, formed eons ago through geological processes too complicated to describe in detail, but mainly consists of the collision of land masses (with areas rich in silica), at high pressures and temperatures. Fused quartz made in a laboratory typically begins as quartz powder, which is heated to above 1723°C (1996 K), the melting temperature of the cristobalite form of SiO₂, and then cooled quickly enough to room temperature to prevent crystallization. A time-temperature-transformation diagram, such as the one shown in Figure 2.2.2, explains the cooling rate dependency of glass versus crystal formation. A general volume-

temperature diagram, such as the one shown in Figure 2.2.3, illustrates the variation in volume and thus arrangement of the atoms in a glass or crystal. This figure does not represent the behavior of silica, which has an anomalous U-shaped VT diagram. Figure 2.2.3 also shows the difference in cooling rate for two glasses and their resulting volumes. However, pure silica made in this way will almost always form a glass since it is difficult to cool it slowly enough to form a crystal. In fact, forming single crystal silica synthetically is very difficult and time consuming. Quartz single crystals are grown in a hydrothermal solution in large pressure vessels commonly known as autoclaves. Careful control of the temperature and pressure in the different areas of the autoclave result in the feed material, known as lascas, dissolving in the hotter portion. The material redeposits on seed crystals, located in the cooler portion, forming synthetic quartz crystals, which then grow. The process usually takes 30 to 60 days for the crystals to reach the desired size (~10cm).

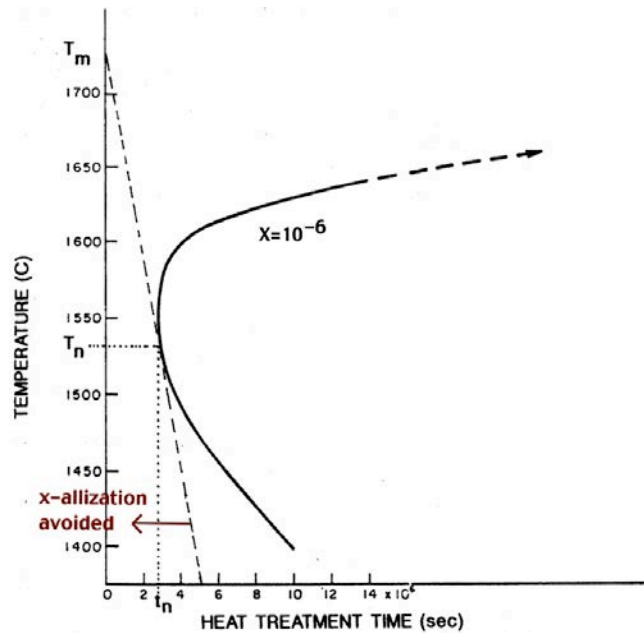


Figure 2.2.2. Heat treatment time-temperature-transformation diagram (T-T-T). To the left of the tangent to the nose temperature crystallization (at 10^{-6} volume fraction) is avoided.

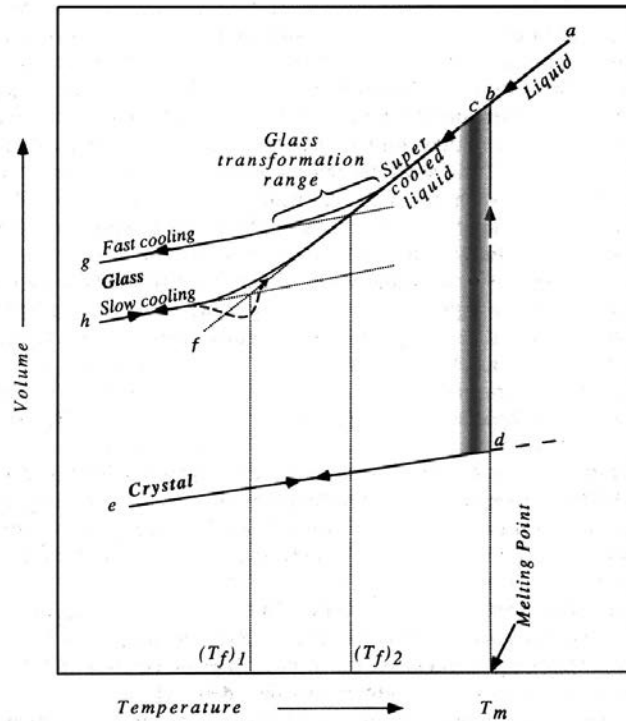


Figure 2.2.3. The volume-temperature (V-T) diagram for glass or crystal formation from a liquid.¹⁷

The exact structure of amorphous silica glass is not known. Of course, there have been a myriad of models and laws set forth in the history of glass science by very credible scientists. It is generally agreed upon that silica is composed of arrangements of silica tetrahedra that have short-range order, little to no medium-range order, and no long-range order. The various crystal structures of silica, namely cristobalite, tridymite, and quartz in both high and low forms have been proven by x-ray diffraction.^{18,19} The diffraction patterns of quartz and cristobalite, shown in Figure 2.2.4, have sharp peaks indicating the d-spacing and thus their crystal structures. Low quartz or α -quartz consists of Si atoms tetrahedrally coordinated by O atoms while the O atoms are surrounded by two Si atoms. The silica tetrahedra are arranged in a hexagonal array. A diffraction pattern of amorphous silica has a broad peak, much like a liquid, indicating no long-range periodicity, but the location of the broad peak being similar to that of the crystals indicates short-range

order similar to their crystal counterparts. This amorphous peak is also shown in Figure 2.2.4.²⁰

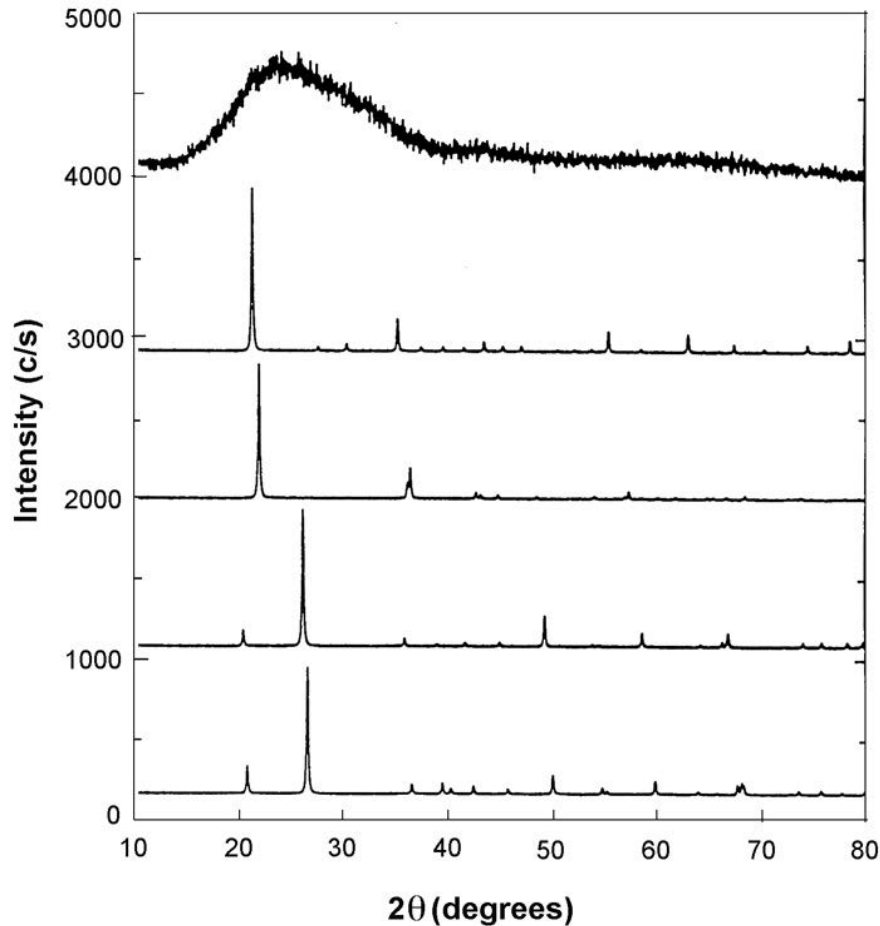


Figure 2.2.4. The X-ray powder diffraction patterns of α - and β -quartz, high and low temperature cristobalite, and amorphous silica.²⁰

The source of the structural differences between the crystalline and amorphous forms of silica lies in the variation in the bond angles, torsion angles and, to some extent, the variation in the bond distance.²¹ The disorder in the amorphous form itself can be ascribed to these differences as well.¹⁷ A schematic of the bond angles and torsion angles is shown in Figure 2.2.5. Mozzi and Warren created the pair distribution function that provides ion

pair distances such as Si-O, Si-Si, and O-O, in the first peaks and then describes the degree of randomness in the broadening of the further peaks.²² Neutron scattering studies of network glasses have shown that there are three ranges of order, range I being within the tetrahedra, range II being between neighboring tetrahedra and range III being between distanced tetrahedra, which shows some evidence of intermediate-range order.²³ The plot of the correlation function showing the three ranges of order found by Wright *et al.* is shown in Figure 2.2.6.

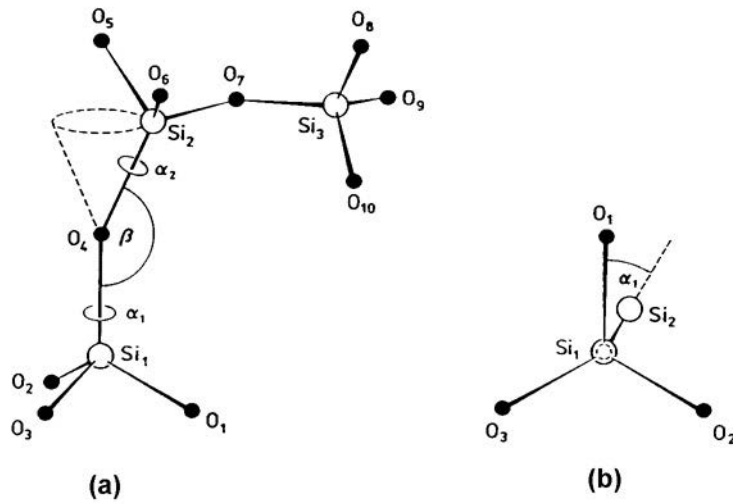


Figure 2.2.5. Schematic of silicate bond angles giving definitions of the bond angle β in (a) and the torsion angles α_1 in (a and b) and α_2 in (a).²¹

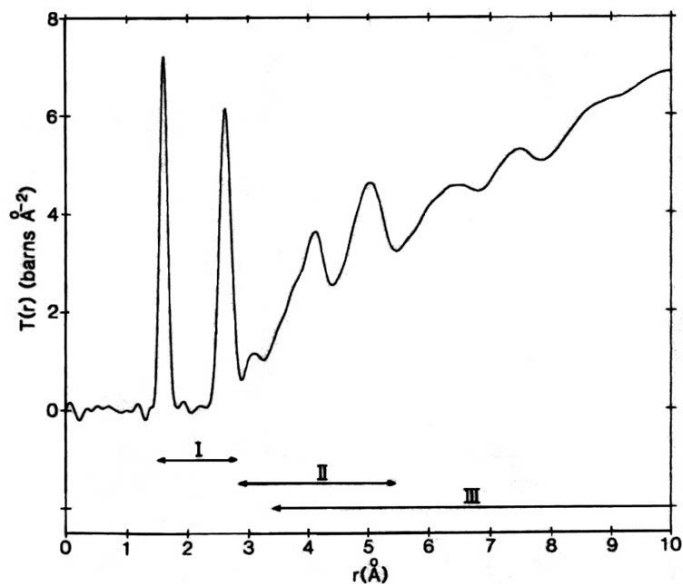


Figure 2.2.6. The correlation function for vitreous silica. I, II, and III indicate the extent of the various ranges of order.²³

Silica glass is one of the simplest glasses in terms of composition, but the production of high purity silica glass is not trivial. Numerous ways have been invented to create a pure form of silica. The earliest method was to simply filter quartz sand and melt in an inert crucible. Currently, someone wishing to make a fairly pure form of silica by a traditional fusion process can purchase “reagent-grade” raw materials from a chemical company and melt them in a suitable crucible. These “reagent-grade” silicas are typically purified through a washing process. The washing process, called froth flotation, removes refractory heavy mineral impurities by bringing them to the top of a wash in a froth and removing them.²⁴ The sand must then be subsequently dried for transport in the U.S..²⁴ Most of the glass-quality sand has a purity of 99.5% at this point. This silica is commonly used in the manufacture of commercially available glass, which consists of mainly soda-lime silicate glasses in the flat glass industry and container industry. The two other main categories of manufactured glass are fiberglass and specialty glasses, which may or may not use the silica sand mentioned above.²⁴

Wet chemical methods, of which there are approximately three varieties, result in very pure forms of silica. The three branches of chemical silicas are divided into gels, pyrogenic silicas, and precipitates.²⁵⁻²⁸ The gel type can produce hydrogels, xerogels and aerogels. The hydrogels are produced by adding a soluble silica to an acid creating a hydrosol, which with time will begin to gel into a hydrogel.²⁵ At this point, syneresis takes place where the gel structure contracts and pushes out liquid from its pores thus making it more dense and stronger. The hydrogel can be crushed and dried creating a fine pure powder or can be dried without crushing, which creates a xerogel or aerogel. A xerogel is a gel in which the porosity has been minimized by severe shrinkage during drying and typically a further sintering step to strengthen the gel.²⁹ Aerogels are hydrogels that have first been turned into an alcogel by replacing the water in the pores with alcohol and then dried under supercritical conditions such that the liquid in the structure is replaced by gas without shrinking the structure at all.^{25,30} Today most aerogels are made via the sol-gel route, where a metal alkoxide (such as tetraethylorthosilicate) reacts with water to create a sol and then condenses to form a gel.^{28,29} Carbon dioxide supercritical drying is much safer than alcohol drying in that the temperature and pressure required are much lower. In all of the gel processing methods there can be many variations creating a wide range of gels with various properties such as; large pores, varying degrees of crosslinking etc..

A variation on wet chemical processing is done at high temperature with the resulting silicas being termed pyrogenic. There are two primary methods of high temperature production; steam hydrolysis of silicon tetrachloride and fusion of sand in a plasma or arc. In the fumed silicas an oxygen and hydrogen flame is used to create the silica from the liquid building blocks SiCl_4 and H_2O . Fumed silica is very pure, airy and it has a very small particle size distribution. Some common trade-names are Cab-o-Sil® and Aerosil®. This method can be directed onto a bait rod to form silica

preforms for fiber drawing and is called modified chemical vapor deposition (MCVD). Aerosil 300 is made through the fuming technique and results in a chain-like structure, whereas Aerosil TK 800 is made by an arc technique and possesses more colloidal-type properties.

Arc silicas are made by the reduction of high purity sand to silicon monoxide in a furnace followed by oxidation in the vapor phase to form silica. Plasma silicas result in ultra-fine powders made via a direct volatilization of sand in a plasma jet. A plasma is an inert gas arc discharge and into which the fine sand is introduced. The sand is vaporized and then quenched to form pure silica powder. The pyrogenic silicas are manufactured in an anhydrous atmosphere, which may account for their lack of a chain structure. This structure probably results from hydrogen bonding in the gelation process.²⁵

The last type of pure silica are the precipitates, which do not vary too far from the gels in that the chemicals used are very similar. The main difference is in the solution conditions, mainly pH, that prevents the formation of a crosslinked gel. Instead, the silica building blocks form discrete particles that settle out of solution. The most familiar process for forming silica precipitates is the one created by Stöber *et al.*³¹ These scientists were able to create silica spheres with a highly controlled particle size distribution. This control was accomplished through hydrolysis of alkyl silicates and subsequent condensation of silicic acid in an alcoholic solution with ammonia as a morphological catalyst.³¹ Today these microspheres are being studied extensively for their potential as liquid chromatographic materials.³²⁻³⁸ Currently the most pure form of silica (99.9999% pure) is produced via the chemical vapor deposition technique, which typically is used to create silica preforms for telecommunications fiber.

Even the purest of silica glass made by vapor deposition techniques will contain trace impurities of chlorine or OH.³⁹ Other forms of silica are possible, but with ease of production commonly comes a loss of purity. Pure silica has a very high melting temperature (~1996 K) and adding very small

amounts of fluxes greatly reduces this temperature.^{40,41} The first glass forming processes were by hand. Workers would blow, press, shape and draw glass by hand, and today this is still done in artisan hot glass shops. The first automated processes of glass formation aimed to mimic hand processes. The ribbon machine (for light bulbs) and the float glass process (for flat glass) were the first to break from this tradition with highly automated and rapid production capabilities.⁴² Continuous glass flow operations start with a molten glass batch, which flows to the forming operation. Typical flowing processes produce glass such as; drawn, rolled, sheet, tubing, cane, bulb envelopes, and fiberglass.

The electric melting of glass is also an important process, especially for silica. Silica microscope slides are made via this process. The electric current is flowed through the container holding the silica sand. The resistivity of the container to the electric current creates heat. This heat in turn melts the sand into a molten glass state, which is then fined and homogenized with increasing heat. The advantage of electric melting is the reduction of volatilization losses that cause environmental and health hazards. The glass is then cooled and cut into sheets, followed by mechanical grinding and polishing.⁴³ Individual slides are then cut from a sheet.

Fiberglass fabrication can take on many forms as well. Glass wool for insulation is created in the rotary or spinner process. In this process, molten glass flows into a cylindrical container with holes in the walls through which glass flows via centrifugal force. The glass streams out of the holes and is then blown downward and collected. Fibers for textiles are formed by either the direct melt method or the marble melt method.⁴⁴ In the first, the molten glass is fed immediately into the forming mechanism and in the second method, glass marbles are fed into a melting tank and then formed. At the bottom of the tank there are forming bushings, which create glass filaments that are subsequently collected into a strand and then possibly chopped.⁴² Optical fibers are highly pure forms of silica and begin as MCVD preforms

produced by any variety of chemical deposition and then consolidated to form the glass.⁴⁵ The preforms are basically columns of glass with a cross-section exactly as desired in the final fiber. The preform is loaded into a holding device at the top of a draw tower and then lowered into a high temperature tube furnace. The glass begins as a stretched out gob, which is broken off until thin enough fiber is obtained to attach to a rotating tractor and then a collector wheel. The tractor provides the pulling force from the preform and the speed is controlled to determine the diameter of the fiber. Various other processes are applied to the fiber along the tower, such as coating with a polymer and UV curing for increased durability against handling.

Beyond the initial fabrication of the silica glass, there are subsequent treatments that the glass may undergo to induce various properties in the glass. The fracture strength of soda-lime silicate glass, for example, can be greatly increased by an ion exchange treatment whereby the sodium ions in the surface layers are replaced with larger potassium ions. The larger potassium ions create compression in the surface layers and thus lead to a strengthening of the glass. Since many properties are controlled by the state of the glass surface, surface treatments are very important in glass science. Surface treatments can range from a simple cleaning of the surface by wiping with ethanol to the much more complicated silanization of a surface.^{39,46-49} A silica surface can be dehydroxylated by thermal treatments, cleaned and/or rehydroxylated by various plasmas, freshly prepared from fracture or even coated with a polymer to protect it.^{48,50-62} More detail will be given in Section 2.3.4.

2.3. Silica Surface

2.3.1. Surface Species

Based upon what the scientific public has agreed to be the structure of silica, there have been numerous proposals as to the structure of the silica glass surface. This is an area about which we know even less, but are making great advances. Weyl stated that “because the tendency of the (glass) system (is) to keep its surface energy at a minimum, the structure and composition of the surface layer of a glass will be different from that of the interior.”⁶³ He was speaking of glasses that contain alkali in the mention of composition differences. It is also generally agreed that the physical properties of any glass are overwhelmingly controlled by the surface. The surface is the doorway through which other atoms must pass and the surface is where most strength limiting flaws will exist. Certainly, the surface is very important when dealing with colloidal powders or highly porous silicas such as aerogels. Most of the studies found in the literature on silica surface species investigated colloidal powders or gels. A scientific definition of a “surface” is the boundary of the nonporous solid phase, one that is impervious to nitrogen, since nitrogen is commonly used to measure surface area.²⁷ Another definition includes that the surface has a finite depth since no change in nature is instantaneous.⁶⁴ The depth is frequently determined by the nature of the analytical technique being used to study it and can range from an atomic layer to $\sim 50\mu\text{m}$.

Haber postulated that a surface contains “residual valences” since the atoms can only bond with its inner side.⁶⁵ The residual valences of the siloxane (Si–O–Si) surface of SiO_2 reacts with the atmosphere.²⁷ Primarily the water vapor in the atmosphere reacts with the siloxanes to create silanol groups (Si–OH) or hydroxyls. These ideas were first proposed by Kiselev in 1936 with Carman actually outlining the silanol formation reaction in 1940.^{66,67} Various types of hydroxyls are present on the surface of silica;

single, geminal and vicinal are the accepted types^{25,68-71} while trigonal has also been suggested.⁷² These types of surface hydroxyls are shown in Figure 2.3.1.1 in hydrated and dehydrated form. This surface chemistry easily lends itself to hydrogen bonding with species with which the surface may come into contact. Belyakova *et al.* showed that the surface silanol groups are responsible for binding to polar organic molecules through hydrogen bonds.⁷³ They found that all silica surfaces are alike (disregarding micropores) and that the concentration of OH groups is 6.6 per nm².⁷³ It is the hypothesis of this research that biological species can differentiate between various silicas based on their surfaces. The individual characterization techniques mentioned in the following text is described more fully in section 2.4.

D'Souza and Pantano conducted a study of amorphous fracture surfaces created under partial pressures of water vapor.^{60,74} These surfaces were analyzed using secondary ion mass spectroscopy (SIMS). It was found that immediately after fracture the following steps take place; dangling Si- and Si-O- bonds rearrange to form strained and unstrained siloxane bonds, then H₂O molecules react with the strained siloxane bonds to form silanol groups on the surface.^{60,74} Wood *et al.* performed static SIMS on crystalline silica surfaces to determine relative surface silanol concentrations.⁷⁵ They treated the quartz surfaces with water plasma or heat in vacuum and found a linear relationship of concentration with time.⁷⁵ SIMS and XPS were used by Hayashi *et al.* to successfully analyze surface silanol concentrations.⁷⁶ In contrast, it was stated by Dang *et al.* that ESCA is not a suitable method to evaluate surface silanol concentrations.⁷⁷

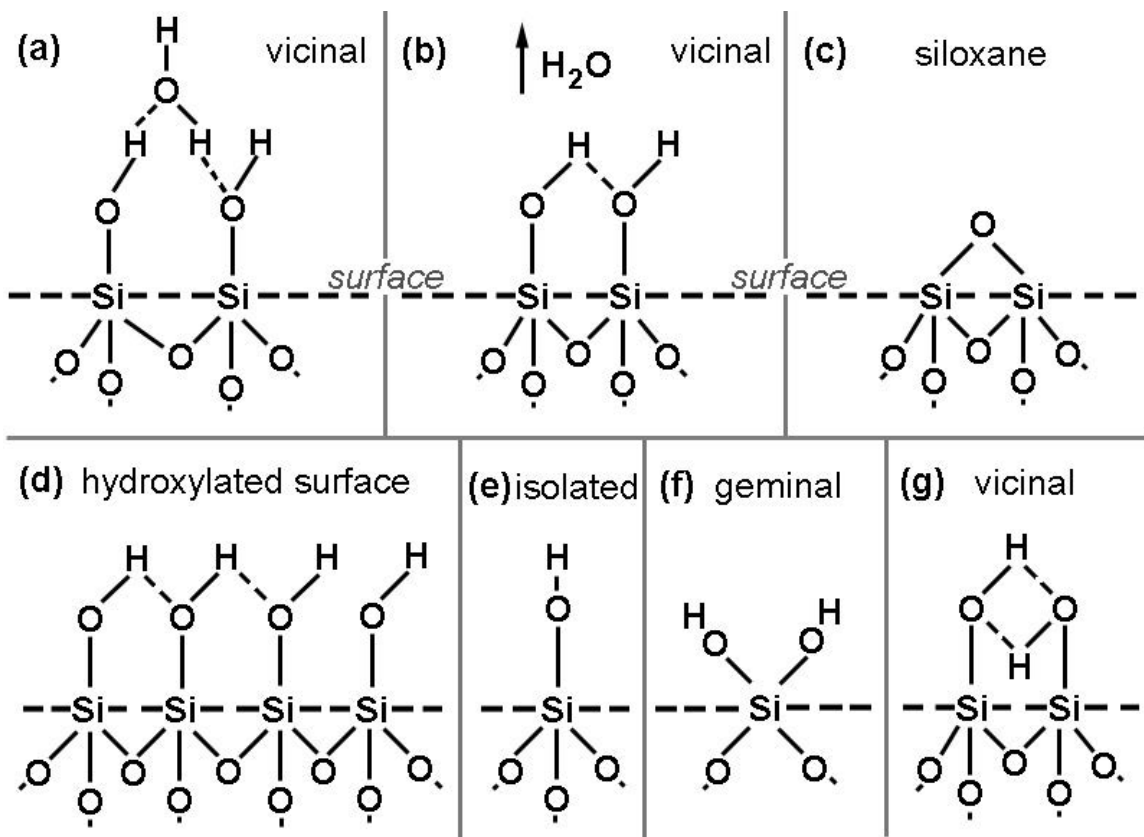


Figure 2.3.1.1. Types of surface (hydroxyl) groups on the silica surface as postulated by Iler. (a) hydrated vicinal, (b) anhydrous vicinal, (c) dehydrated siloxane, (d) hydroxylated surface, (e) isolated, (f) geminal, (g) hydrogen bonded vicinal.²⁷

Boehm in 1966 discussed surface groups on powdered carbon, silica, titania and alumina.⁷⁸ He compared experimentally found values for surface OH concentration with theoretical values. The theoretical values were based on quartz surface OH group concentration data and an adjustment was made for the lower density of amorphous silica. The calculated packing density of OH on the (001) face is 9.6 OH/100 Å² and that of the (101) face is 6.0 OH/100 Å².⁷⁸ The theoretical value of OH on the surface of amorphous silica was estimated to be ~5 OH/100 Å², but the experimental value was lower (2-4 OH/100 Å²).⁷⁸ He also conducted a dehydration/dehydroxylation study and found that dehydration is reversible below 450°C, but above 800°C the

rehydroxylation will not occur when cooled to room temperature.⁷⁸ He suggested that siloxane groups exist on the surface along with silanol groups based on the low experimental silanol surface concentrations.

Hair in 1967 authored a book about examining the surface chemistry of silica using infrared spectroscopy.⁷⁹ He discussed infrared absorption band changes in Cab-o-Sil® and precipitated silica with heat treatments. From data he deduced the following; dehydration is completely reversible up to ~400°C, but treatment above 400°C results in an inverse relationship of chemisorption capability with temperature.⁷⁹ Chemisorption refers to the strong chemical interaction between the monolayer of adsorbed molecules (OH) and the surface atoms. On the other hand, physisorption occurs when the interaction between molecules (H₂O) and surface atoms is weak and usually occurs in second layers.^{26,27,80} Hair also stated that above ~850°C the silica surface is hydrophobic and no chemisorption can occur. He is also one of the first to define the types of surface hydroxyls; geminal, vicinal, isolated, since they are distinguishable by infrared spectroscopy.⁷⁹ Above 400°C adjacent hydroxyl groups are eliminated leaving only isolated hydroxyls. Hair utilized silane coupling agents to further study the infrared bands of adsorbed water species.⁶⁹ In an earlier study (1964) by Davydov *et al.* deuterated water was implemented in conjunction with infrared spectroscopy to study surface hydroxyls.⁸¹ They claimed that the specific adsorption of D₂O (and silanes for that matter) is due to the free hydroxyl groups on the silica surface and not the bound groups.⁸¹ In a study by Morrow and McFarlan hydrogen sequestering agents were used successfully in conjunction with FTIR spectroscopy to determine the existence of various hydroxyl species on the surface of silica.⁸² Yoshinaga *et al.* also used a similar method to Hair in that silane coupling agents were bonded to silica surfaces and FTIR signals were analyzed to determine the surface hydroxyl group species and concentration.⁸³

Duval *et al.* used X-ray photoelectron spectroscopy (XPS) to evaluate silanols on the quartz surface as a function of pH.⁸⁴ XPS, AFM and contact angle measurements were conducted by Takeda *et al.*⁸⁵ They were able to correlate the OH group density on a glass surface as measured by XPS with the wettability as measured by contact angle. Also, the hydrophobicity that results from the adsorption of organic molecules onto the surface is dependent on the surface OH group density.⁸⁵

It should be defined that dehydration is the removal of molecular water (physisorbed) from the surface and that dehydroxylation is the removal of chemisorbed hydroxyl species by reacting two neighboring (hydrogen bonded) hydroxyls and leaving a siloxane bond (Figure 2.3.1.2), which occurs at a higher temperature than dehydration.⁷¹ This distinction of chemisorbed and physisorbed water, shown in Figure 2.3.1.3, is now accepted, but earlier was not shared by everyone.^{27,79,80} Lange made a distinction between two kinds of physisorbed water on the hydroxylated silica surface, “hydrogen bonded” water and “physically adsorbed” water. His definition of “hydrogen bonded” water is shown in Figure 2.3.1.4 and “physically adsorbed” water is again molecular water. He stated that the physically adsorbed water is removed during drying between 25-105°C and that the hydrogen bonded water is evolved between 105-180°C. Physically adsorbed water requires an activation energy of 6.6-8.2 kcal per mole and the hydrogen bonded water requires an activation energy of 10 kcal per mole for removal.⁸⁶ Today we do not make a distinction between the two “Lange” waters since it was probable that hydrogen bonded water was really only water adsorbed to silanol groups that were not close enough to each other to hydrogen bond to each other creating chemisorbed water.²⁷

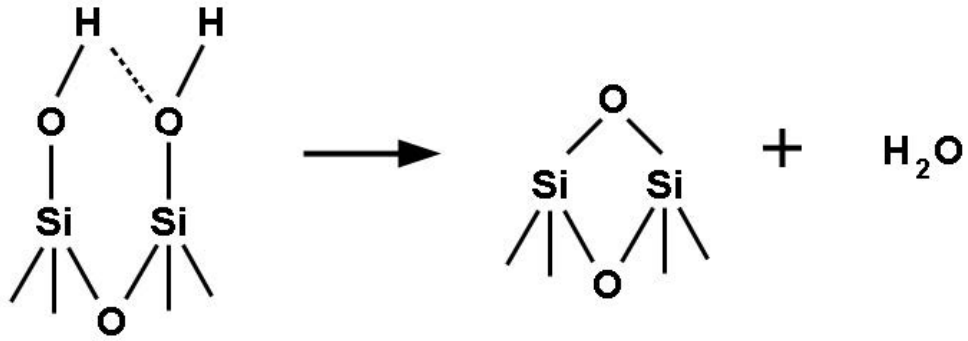


Figure 2.3.1.2. Reaction of two neighboring hydrogen bonded (indicated by the dotted line) hydroxyls to form molecular water and a siloxane bond. Dehydroxylation reaction.

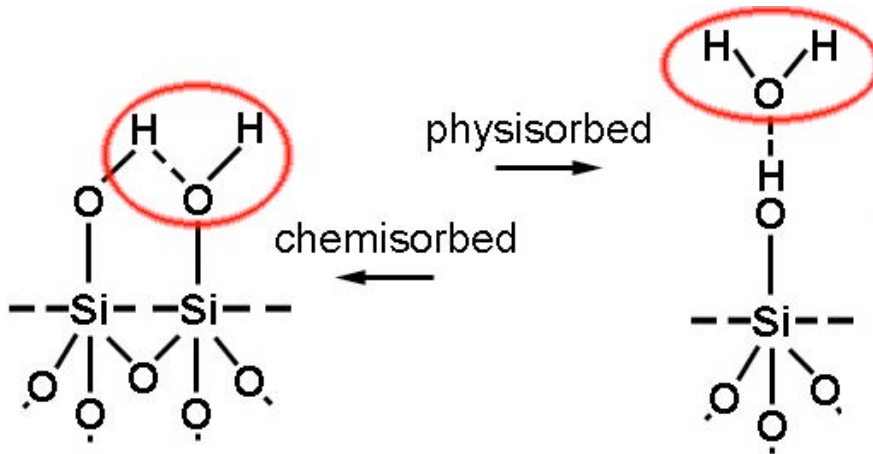


Figure 2.3.1.3. Models of chemisorbed water and physisorbed water (with the molecular water encircled) that may evolve in dehydroxylation and dehydration respectively.

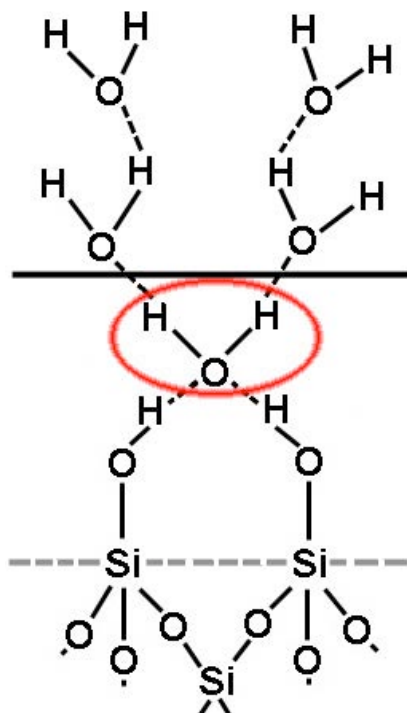


Figure 2.3.1.4. Lange's description of the two types of adsorbed water, hydrogen bonded (encircled) and physically bonded (everything above solid black line).⁸⁶

The temperature at which all physisorbed water has been removed from the surface was a subject of much debate in the 1960's and 1970's. According to de Boer and Vleeskens, all physisorbed water is removed at 115-120°C, but this was only for non-microporous silicas.⁸⁷ Lange suggested that a temperature of 180°C is required to remove physisorbed water from microporous silicas.⁸⁶ However, Young and Bursh found that some chemisorbed species are removed at this temperature and suggested that 170°C is sufficient to remove all physisorbed water.⁸⁸ Finally, Iler stated that a silica (formed in liquid) will lose its hydrogen-bonded water molecules at 150°C in atmosphere.²⁷ It is generally accepted as a rule that when starting with a fully hydroxylated silica surface, there are about 5 OH/nm² at 150°C and at 800°C, there are only 1 OH/nm². Silanol groups begin to condense water and rearrange to form siloxane bonds at 170°C. This reaction is shown in Figure 2.3.1.2. At 400°C, slightly less than half of the hydroxyl groups

have been removed and between 400 and 450°C, more hydroxyls are removed leaving siloxane areas. At 800°C, only free isolated silanol groups are evident at a concentration of 1 OH/nm².²⁷ Clearly dehydration is dependent on many factors including the origin of surface water, type of bonded surface water, location of bound water, atmospheric humidity and temperature. It is important to know for this study that silica (powdered especially) is covered with a monolayer of hydroxyl groups with a varying degree of physisorbed water depending on previous treatments.^{26,78,89,90}

The most recent discussions on the surface chemistry of amorphous silica have been put forth separately by Zhuravlev and Yaminsky.^{71,91-93} In 1987, Zhuravlev studied many types of amorphous silicas; gels, aerosils and porous glasses. He stated that the hydroxyl concentration can be varied by a number of methods and that this concentration controls many of the properties of such materials. He also concluded that the silanol number for a fully hydroxylated surface is a physicochemical constant that is independent of the type of silica examined.⁹¹ This constant is called the Kiselev-Zhuravlev constant and is 4.6 OH/nm².⁷¹ This value was actually used to determine the specific surface area of amorphous dispersed silica with a fully hydroxylated surface.⁹⁴ Then in 2000, Zhuravlev authored an extensive article reviewing the surface chemistry of amorphous silicas, as he, Kiselev and Davydov have studied it, and proposed his own model.^{71,81,90}

Here are listed the stages of Zhuravlev's model with increasing temperature in vacuo, as he stated them. Stage 1 (25°C): The SiO₂ surface is in a maximum state of hydroxylation at 4.6 OH/nm², all different types of silanols are present (isolated, geminal, and vicinal), the SiO₂ surface is covered with physically adsorbed water in multiple layers, the surface OH groups and adsorbed water are permeated with an H-bonded network, and OH groups are present on the internal skeleton of the silica. Between Stages 1 and 2: The first threshold temperature is 25°C, multiple layers of physisorbed water is removed completely, which is reversible upon

introduction of excess water. Stage 2 (25-190°C): The SiO₂ surface is still in a maximum state of hydroxylation at 4.6 OH/nm² and all silanols are still present, the surface is now covered with a single or less layer of adsorbed water that are predominantly bonded via H-bonds, and OH still exists internally. Between Stages 2 and 3: The second threshold temperature is 190°C, there is complete removal of the water monolayer, but the SiO₂ surface still remains fully hydroxylated, this process is readily reversible in excess of water. Stage 3 (190-400°C): The degree of surface hydroxylation decreases significantly while all types of silanols are still present, however the concentration of isolated silanols increases as vicinal silanols decreases and eventually disappears at 400°C, internal OH groups begin to disappear, dehydroxylation activation energy increases slightly, and the activation energy of dissociative adsorption is nearly zero. Between Stages 3 and 4: The third threshold temperature is 400°C, only free isolated and free geminal silanols exist on the surface, and the process is still reversible in excess of water. Stage 4 (400-900°C): Surface hydroxylation decreases still but less rapidly, isolated and geminal silanols decrease, at 800-900°C all geminal silanols are removed, internal OH groups disappear, the concentration of siloxane bridges increases dramatically on the surface, and the activation energy of dehydroxylation increases rapidly, sintering of the SiO₂ matrix begins. Between Stages 4 and 5: The third threshold temperature is ~900°C, there is complete removal of surface geminal silanols and internal OH groups, isolated silanols still exist on the surface, when brought to room temperature the process is hardly reversible in excess of water, but at elevated temperature (100°C) it is easily reversible. Stage 5 (900-1200°C): The concentration of surface isolated silanols continues to decrease until their disappearance, the degree of surface coverage of siloxane bridges continues to increase until the entire surface is either SiOSi or Si, the sintering and shrinkage of the matrix continues, and the activation energy of dehydroxylation continues to increase. Between Stages 5 and 6: The fifth

threshold temperature is 1200°C, there is complete removal of all surface OH groups and complete coverage of siloxane bonds. Stage 6 (above 1200°C): The silica surface consists of siloxane bridges only.⁷¹

This detailed model is of physico-chemical origin and through its use the concentration and distribution of the different types of silanols and siloxane groups can be determined. Strained bonds are more susceptible to chemical adsorption reactions.³⁹ There is a possibility of assessing the OH groups inside the silica skeleton as well. Also, the model allows the energetic heterogeneity of the silica surface as a function of heat treatment temperature to be characterized and to determine the kind of chemisorption of water.⁷¹ This model is currently the most advanced and detailed regarding silica surface chemistry.

2.3.2. Types of Surfaces

High surface area silicas, including fumed silicas, powders, colloidal silica and gels, such as aerogels are ideal for surface studies because they are comprised primarily of surface. These samples can have surface areas as high as $\sim 650\text{m}^2/\text{g}$.⁸⁰ The previous section discussed surface species, mainly hydroxyls, as they exist on a flat surface, but also within a powder. This combination is a contradiction because all colloids and gels have more curved surfaces than flat areas. Powders have very small diameters and gels are typically filled with pores. One could assume that the average of curvatures could equal zero in any given fumed silica. Many bulk silica forms are highly curved as well, either positively, as in fibers, or negatively, as inside capillaries or microchannels. Even “flat” bulk silica samples can have a fairly rough topography displaying areas of hills and valleys. Of course, these “flat” surfaces do not have a degree of surface curvature that will actually affect the interaction of surface species, or do they?

Consider colloidal silica, which is nearly spherical. The sizes of the particles can range from 1 μ m and below.⁹⁵ It is obvious that the degree of crowding of surface species decreases with positive radius of curvature and increases inversely with negative radius of curvature. A low negative radius of curvature, such as a tiny pore, will have the highest amount of crowding. A high negative radius of curvature, such as inside a capillary, will have moderate crowding. A high positive radius of curvature, such as a fiber surface will have a low degree of crowding. A low positive radius of curvature, such as a colloid, will have no crowding. A schematic of various radii of curvature is shown in Figure 2.3.2.1. Iler calculated the theoretical OH concentration based on the density of silica and also on Carman's statement that every Si on the hydrated surface must be tetrahedrally satisfied with an OH.^{26,66} Iler concluded with a value of 7.85 OH/nm².²⁶ This number will be less for crowded surfaces. Crowding is not necessarily an unwanted phenomenon. When silanols are close together they are more likely to form vicinal hydrogen bonded pairs.⁹⁶ Isolated silanols have no hydrogen bonds between them and thus are more readily removable at elevated temperatures.²⁷ As in negative radius of curvature surfaces, the silanols are so close together that dehydration is very difficult and requires even higher temperatures.

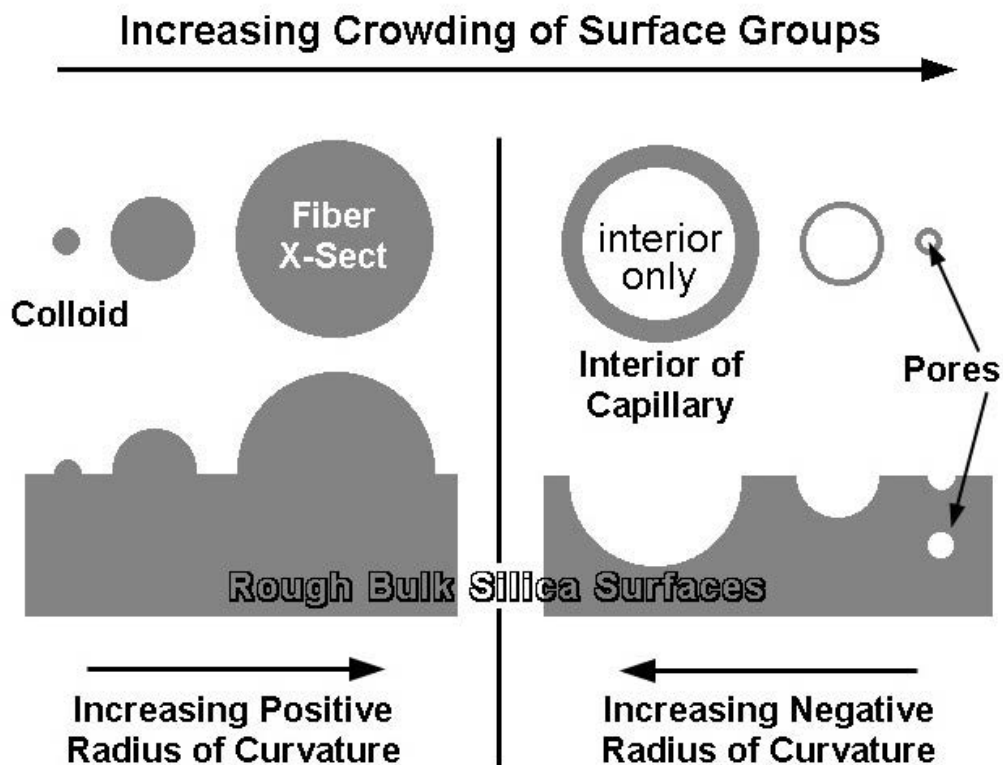


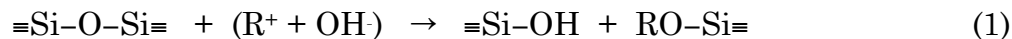
Figure 2.3.2.1. Various radii of curvature for silica surfaces. Typical examples of each extreme are noted and also the progression of crowding with changes in curvature. (After Iler²⁷)

2.3.3. Silica and Water

The discussion of silica surface hydroxyls leads directly into how silica behaves in water. A fully hydroxylated silica surface is hydrophilic and is able to absorb water in multiple layers.^{69,89,92} The Si-OH groups present on surfaces are the main source of hydrophilicity because they promote the adsorption of water.^{89,97} The removal of these Si-OH groups through heat treating above 850°C or by replacement of these Si-OH groups by hydrolytically stable Si-R (where R is CH₃) groups inhibits the adsorption of water and results in hydrophobic surfaces that will be unaffected by water.⁹⁷

Silica undergoes chemical reactions in water. Namely SiO₂ reacts with 2 H₂O to form Si(OH)₄ groups.⁹⁸ This reaction is considered the dissolution,

depolymerization or hydrolysis reaction.^{27,99} The solubility of silica is dependent on the particle size, temperature, and pH of the water.^{27,100} Further reaction will create physisorbed water in a multi-layer, as previously shown in Figure 2.3.1.3. Certain silica containing glasses, such as sodium silicate or soda-lime silicate have poor chemical durability compared to silica, worse so for sodium silicate. In addition to the reaction of silica with water forming monosilicic acid groups, sodium leaches out of the structure and molecular water is able to enter. This exchange creates what is known as the silica “gel layer” and is very similar to a gel created through wet chemical means. Pure silica forms however do not lend themselves to the creation of a gel layer due to the absence of an exchanging species. However, Yaminsky *et al.* have stated otherwise, that the surface of fused quartz swells under water to form these layers of silica gel.⁹² In the same article, Yaminsky *et al.* discuss many surface phenomena of silica including the history dependence of the state of the surface, effect of solution condition, and even evidence of “cold fusion”.⁹² At elevated temperatures water will etch pure silica through a dissolution reaction:



where R can be either H for water or any alkali ion for a basic solution.¹⁷ This reaction explains why silica is less durable in basic solutions of high pH. In any case, the rate of dissolution is a thermally activated process such that the natural log of the amount of material extracted has a linear relationship to the temperature with a slope of activation energy.¹⁷

Again, to study the interaction of silica surfaces with water, high surface area samples are practically required, although one study has suggested otherwise.¹⁰¹ Silica xerogels were studied in aqueous media as described by Okkerse.⁸⁰ He investigated the effect of various solutions at 80°C for a minimum of 14 hours on the texture of silica xerogel. The porous texture of xerogels is modified after treatment in water or electrolyte solutions. There is a decrease in specific surface area but the pore volume

remains constant. Water is essential for the changes to take place since immersion in both sulfuric acid and ethanol do not produce any effects.⁸⁰ Salt and acid solutions appeared to be more effective in increasing mean pore radius and the particle diameter than just pure water.⁸⁰ It was also found in the pore size distribution data that large pores grow in number while the small pores disappeared. This change was explained by the dissolution and reprecipitation of “silica”. Since the same volume of small particles and large particles will have more surface area in the small particles, and every system strives to minimize surface area/energy, the larger particles will grow at the expense of smaller ones.⁸⁰ The same is true for pores.

The influence of pH on this system was also studied by Okkerse. He found that the rate of the dissolution-reprecipitation reaction (and specific surface area change) is a minimum in buffered solutions at pH 2, the isoelectric point of silica. The change in specific surface area increases above and below a pH of 2.⁸⁰ A plot of dissolved silica versus time in buffered solutions with pHs of 2,4,6 and 8 kept at 60°C was put forth by Okkerse. It was deduced that the rate of dissolution is minimal at pH 2 and increases with increasing pH. Therefore, pH is a very important factor in the stability of silica in aqueous solutions. A compilation of data was done by Iler 10 years after Okkerse’s work and very different results were shown.²⁷ However, this data was obtained at much lower temperatures and the water was not said to be buffered at each pH. Iler presented a plot of solubility versus pH and the solubility appears to be constant (possibly decreasing slightly) from low pH to a pH of 8 and then increases drastically at pH 8 and above.²⁷ The effects of pH on silica systems is a difficult subject because of variations in the form of the silica and the type of solutions in which it is placed.

Okkerse and Iler also discussed the effect of electrolyte concentration of the solution on silica stability.^{27,80} A submicroporous silica was treated in a sodium chloride buffered solution of varying concentration of sodium chloride by Okkerse. It was observed that the change in salt concentration

changes the specific surface area of the silica to a small extent. This change was much smaller than the pH effect.⁸⁰ Iler also reported from the data he compiled that the electrolyte concentration essentially has no effect on the solubility of silica.²⁷

The diffusion of water into silica and its analysis by infrared spectrometry is a field in which Tomozawa excels. Although it was Doremus that first proposed that molecular water is the diffusing species through silica and that it will penetrate until it confronts an agreeable site with which to react; $\text{H}_2\text{O} + \text{Si-O-Si} \rightarrow 2 \text{Si-OH}$.¹⁰² Tomozawa *et al.* found that water accelerates structural changes in silica during isothermal hydration heat-treatments.^{103,104} There is an acceleration of structural relaxation. Also, when the rate of structural relaxation is slower than the rate of hydroxyl diffusion at a temperature less than 850°C, the hydroxyl surface concentration and the hydroxyl content in the glass is a maximum.¹⁰³ Tomozawa *et al.* proved that Doremus' proposal was indeed correct at high temperatures.¹⁰³

2.3.4. Surface Treatments

2.3.4.1. "Cleaning"

Since the surface of silica controls many of its properties, treating the surface is a method of engineering the material. Just by placing silica in water, chemical reactions occur which change the structure of the surface and therefore change active species on the surface. Something that seems as simple as grinding or polishing silica on a wheel encompasses mechanical, thermal and chemical processes.^{99,105} Even what one person considers cleaning a glass may actually be much more, or less. A freshly manufactured glass surface is considered to be pristine, but only for a short amount of time as water and organics in the environment will react with it.

The "cleaning" of a glass surface is a term that is used subjectively. A "clean" surface of a computer chip has a much more defined meaning than a

“clean” window. Basically however, cleaning is meant to remove surface contaminants and reveal the true surface of a material. These surface contaminants can range from fats and oils to adsorbed ions or oxide films. The American Society for Testing and Materials (ASTM) began to understand this broad topic of cleanliness in 1975 and started writing ASTM standards for measuring cleanliness. The first two ASTM standards were C812 and C813, a steam condensation method and a contact angle method respectively.¹⁰⁶ Since then there have been few methods approved by the ASTM for measuring cleanliness of a surface.¹⁰⁷

Cleaning a glass is typically a prerequisite to any further chemical treatments such as silanization.⁴⁷ It is also done prior to any attachment of organic films or biological molecules to remove contamination and create or reveal surface attachment sites such as hydroxyl groups.¹⁰⁸ Numerous cleaning methods exist for fused silica in preparation for biological attachment such as using gas plasmas, exposure to acids and bases, or rinsing with organic solvents all done at varying temperatures and possibly with the use of an ultrasonicator. Henke *et al.* evaluated a “well-established” cleaning method and its effect on the surface roughness of silica through the use of AFM.¹⁰⁸ Their cleaning method consisted of a combination of washing with peroxides, first basic then acidic. This method cleans and hydroxylates the surface.¹⁰⁸ They found that the surface roughness remained fairly abundant and gave 12% (30% prior to cleaning) more surface area than geometrical calculations of a flat surface.¹⁰⁸ The roughness of the surface came in three forms; surface nodules, pits/scratches and long range undulation. The roughness was dominated by the surface nodules.¹⁰⁸ However, the cleaning method reduced the RMS roughness and it was observed to reduce surface nodules, but increase the depth of pits and scratches.¹⁰⁸

An aluminoborosilicate glass (Corning code 1737) was cleaned using the “RCA clean” and the sample surfaces were measured using XPS and

AFM.⁴⁸ The “RCA clean” consists of 5 steps. 1- A solution soak of (1:1:5) $\text{NH}_4\text{OH}:\text{H}_2\text{O}_2:\text{H}_2\text{O}$ at 75°C for a fixed time. Then, 2- A cascade rinse in room temperature DI water until the resistivity of the water measured $8\text{ M}\Omega\text{-cm}$. Then, 3- A solution soak of (1:1:6) $\text{HCl}:\text{H}_2\text{O}_2:\text{H}_2\text{O}$ at 75°C for a fixed time. And, 4- A cascade rinse with ultrapure water ($>17\text{ M}\Omega\text{-cm}$ resistivity) until the resistivity reached $16\text{ M}\Omega\text{-cm}$. Finally, 5- A spin drying of the samples. Using this cleaning method, Couillard *et al.* found that the aluminoborosilicate glass leached, where SiO_2 samples were not affected. XPS analysis of the aluminoborosilicate showed that the surface was depleted in aluminum, calcium, boron, and barium, leaving a layer rich in silica.⁴⁸ AFM measurements did not show an increase in RMS roughness of the cleaned surface.⁴⁸

Glass microscope slides in preparation for silanization must be cleaned to remove organic residue and expose the silanol surface sites.⁴⁷ Cras *et al.* reported the evaluation of eight different chemical cleaning methods commonly used to clean glass microscope slides through contact angle measurements. The slides were soda-lime silicate in composition and the chemical treatments are shown in Table I. Each soaking treatment was followed by either a rinse in water and/or drying in nitrogen.⁴⁷ Of the methods mentioned, it was determined by the workers that only the first four were capable of removing organic contaminants and leaving a hydrophilic surface. The post cleaning silanization of the glass slides cleaned with methods 1-4 resulted in high contact angles (indicating a hydrophobic surface) with low variability.⁴⁷

Table I. Eight Cleaning Methods Evaluated by Cras *et al.*⁴⁷

Method	Steps
1	30 min in (1:1) MeOH:HCl
2	Method 1 + 30 min in conc. H ₂ SO ₄
3	Method 2 + 30 min in 100°C H ₂ O
4	5 min in 1:1:5 NH ₄ OH:H ₂ O ₂ :H ₂ O at 80°C
5	Method 4 + 5 min in 1:1:5 HCl:H ₂ O ₂ :H ₂ O
6	30 min in 10% KOH in isopropanol
7	20 min in 1M NaOH
8	Method 7 + 30 min in piranha (1:2 H ₂ O ₂ :H ₂ SO ₄)

A unique study was performed by Bowen *et al.* where they used an AFM to measure adhesive interaction forces between a silica sphere and a planar silica surface.¹⁰⁹ The surfaces of the sphere and the plane were treated by ethanol washing or plasma treatment and the AFM measurements were taken in NaCl solutions at pH 3 and 8.¹⁰⁹ The pH did not have a significant effect on the adhesion forces for a given cleaning procedure. They found that the magnitude of the adhesion forces are considerably more for the ethanol cleaned surfaces than the plasma cleaned surfaces.¹⁰⁹ This high adhesion for ethanol is a very interesting phenomenon. Schicht *et al.* characterized flatglass surfaces with XRF, SIMS, SEM, AES, contact angle, emission photometry, UV/vis spectroscopy, and reflection measurements as a function of washing with three solutions; neutral water, acidic water, and alkaline water.¹¹⁰ Three types of glass were used. Glass 1 was lower in alumina and calcia content compared to Glass 2, but had more silica content. The identity of Glass 3 is not important in relation to the current study. Washing these glasses in neutral water resulted in a stronger leaching of sodium in Glass 1, but a stronger leaching of alkaline-earth oxides in Glass 2. SiO₂ and Al₂O₃ are both enriched in the surface. Acidic washing decreases the glass surface energy by reducing the sodium content even more than washing with water. Alkaline washing does not improve sodium leaching, but dissolves the silicate network for both glasses.¹¹⁰

A study on plasma cleaning processes was performed by Kruger *et al.*⁵⁶ Organic surface contaminants were removed by oxidizing plasmas such as O₂, H₂O, CO₂, NO₂, and H₂O₂.⁵⁶ They found that glass fibers are significantly roughened by Ar, NH₃, or O₂ plasma exposure. Plasmas were created in a microwave or by radio-frequency power. They also stated that it is possible to remove contaminants by noble gas plasma sputtering, by oxidation of the organic contaminants, or reduction of oxides or sulfides by hydrogen plasma.⁵⁶

2.3.4.2. Treatments on Multi-Component Glasses

Surface technological treatments come in many flavors. They can be done during forming or immediately afterward to induce structural or stress changes. These changes can be mechanical, chemical, or thermal in nature and be done on glasses of any composition or age. Filatova and Shulakov studied mechanical polishing, chemical polishing, and laser annealing on the atomic short range order of silicon atoms in SiO₂-based glasses.^{58,111} They used ultrasoft X-ray reflectometry to monitor the changes in the surface. The treatments result in a thin surface layer of SiO₄ tetrahedron distortions, more so for polishing and less obvious after laser annealing.^{58,111}

Cook published a very extensive study on the chemical processes in glass polishing.⁹⁹ Her mechanochemical model for glass/slurry interactions and the rate of material removal from the glass surface is a combination of the following processes: molecular water diffusion into the glass surface, glass dissolution, adsorption rate of dissolution products onto the polishing agent, silica redeposition onto the glass surface, and the aqueous corrosion rate of the polishing particles. The main factors influencing these processes are the load and velocity of the polishing particles, the elastic properties of the polishing particles and the glass, the chemical durability of the glass, the surface charges of the glass and the particles, and the ion-exchange capacity of the polishing particles.⁹⁹

A study conducted at The Pennsylvania State University investigated the effects of polishing, fiber-drawing, melt-casting, and chemical etching on alkali and alkaline-earth aluminosilicate glasses using XPS and AFM.⁴⁶ XPS was used to determine the surface composition changes and AFM was used to characterize the effects on RMS roughness. The chemical etchants included NaOH, NH₄OH and HF. All glasses were melted, polished and ultrasonicated in acetone prior to chemical etching. They found that all polished glasses were left with a silica-rich surface layer.⁴⁶ This layer can be eliminated in the sodium aluminosilicate glasses following an etch in HF or NaOH, but not in NH₄OH.⁴⁶ The most effective etchant for the calcium aluminosilicate glasses was NH₄OH. An “effective” etchant was one in which the surface composition matches the bulk composition as closely as possible after polishing and etching. The calcium aluminosilicate glasses that were remelted, poured into a mold and not annealed had a surface composition enriched in Al, but depleted in Ca. After annealing, the composition at the surface was only slightly depleted in Al and Ca and was very close to the bulk composition. The fibers drawn from this glass had a surface slightly depleted in Al, but moderately enriched in Ca.⁴⁶ Overall, the treatment that resulted in a surface composition most closely matching the bulk was a melted/annealed surface.⁴⁶

Soda-lime silicate glass was treated with urea solutions and evaluated by Gorokhovskiy *et al.* using IR spectroscopy.¹¹² In an attempt to increase the strength while increasing the polymer adhesion properties of float glass, urea solutions at various temperatures were used as a surface treatment. It was found that the optimal treatment conditions with an aqueous solution of urea is between 140-160°C. This treatment increases adhesion and also the mechanical strength while keeping the surface clean.¹¹² Cho *et al.* showed that bioactivity can be induced in a glass-ceramic containing MgO, CaO, SiO₂, P₂O₅, and Al₂O₃ by treatment in HCl, but not NaOH solutions.¹¹³ Apatite formation on the surface in simulated body fluid after the HCl

treatments is due to a hydrated silicon layer.¹¹³ This glass-ceramic is believed to be able to bond directly to bone after such a treatment.

One of the most popular methods of surface modification comes with the use of ion beam sputtering. Brow studied simple binary oxide glasses with XPS as the glasses were bombarded with argon ions.¹¹⁴ The sodium silicate glass surface was found to lose alkali ions followed by the repolymerization of the surface structure. The sodium phosphate glass surface was determined to enrich in sodium with argon sputtering and then depolymerize.¹¹⁴ Krishnamurthy and Kamel studied argon plasma treatment of glass surfaces using FTIR and SEM.⁵⁷ They began with a cleaned (with NaOH solution and DI water rinse) E-glass surface and exposed the samples to an inductively coupled plasma source of argon. This treatment resulted in an increased surface area due to etching and a rearrangement of the silicate network.⁵⁷ In addition, the argon was observed to increase the hydrophilicity of the E-glass surface.⁵⁷

Various plasma gases (argon, ammonia, and nitrogen) were used to treat an alkali-lead-silicate glass containing rubidium and cesium.⁵⁹ The glass was pretreated with hydrogen to create electrical conductivity, which led to an enrichment of Cs and Rb in the surface. The compositional effects on the surface were monitored using SIMS and XPS. The use of nitrogen or ammonia in the plasma gas results in the implantation of nitrogen ions into the glass surface to a depth of $\sim 100\text{\AA}$.⁵⁹ It was found that any plasma treatment results in the depletion of cesium and rubidium and this effect is caused by many factors. Some of the factors include sputtering, ionic diffusion and vaporization by the plasma. The argon plasma aided in improving the short-term water adsorption properties of the glass.⁵⁹ It was evident that upon plasma treatment, alkali ions from the surface migrate into the bulk leaving the surface depleted in alkali. Also, the silicate network rearranges and repolymerizes after dealcalization and reduction of non-bridging oxygens upon treatment in argon plasma. This was shown by Zhou

et al. using a soda-lime silicate glass and IR band shifting.¹¹⁵ A high-frequency plasma pencil has been developed by Janca *et al.*¹¹⁶ This tool can be hand operated and used in atmospheric, reduced or increased pressure. Gas, liquid or a mixture of dispersed particles in liquid can also be sent down the plasma pencil.¹¹⁶ This tool offers wide diversity and has been used in many applications.¹¹⁶

The above discussion involved mainly flat glasses, but it is also important to review processing effects and surface treatment studies on glass fiber. Since most glass fibers are coated, either with polymer for telecommunications fiber, binder for wool fiber, or embedding in epoxy for composites, the reaction of the fiber surface to certain conditions has been studied. In 1997, Bledzki *et al.* used four different methods of investigation to characterize surfaces of treated glass fibers.¹¹⁷ The four techniques involved were capillary rise measurements, zeta potential measurements, inverse gas chromatography (IGC), and field emission scanning electron microscopy (FE-SEM). The glass fibers investigated were all coated with either a polymer or an aminosilane, an organic-inorganic coupling agent. The four different surface coatings utilized were: polyethylene, polyurethane/aminosilane, epoxy-resin/aminosilane, and cationic silane sizing. The results from IGC, FE-SEM, and zeta potential measurements showed that the polyurethane/aminosilane coating led to an amphoteric surface (capable of displaying basic and acidic qualities).¹¹⁷ The polyethylene treatment resulted in a complete coverage of PE on the fiber. The epoxy-resin/aminosilane and the cationic aminosilane treatments rendered a glass fiber with basic surface character.¹¹⁷

Fiber surface treatments were performed on fibers to be embedded into vinyl ester to examine changes in impact properties of the composite.¹¹⁸ The fibers were treated with polybutadiene, an aminosilane, and a combination of the two. It was found that polybutadiene treated fiber composites exhibited a higher impact energy absorption than aminosilane treated fiber composites.

However, the combination treated fiber composites showed the highest impact energy absorption.¹¹⁸ Benzarti *et al.* carried out a similar study of increased mechanical properties of fiber/epoxy composites with fiber surface treatment.¹¹⁹ They found that the most reactive sizings (coatings, treatments) promoted the highest interfacial strength, which increases the ultimate mechanical properties such as stress resistance, strain, and energy at failure.¹¹⁹ The two most reactive sizing additives were trifunctional epoxy and pentaglycidyl ether of cyclosilicone.¹¹⁹ Increasing the interfacial bonding increases strength since interfacial failure is the source of most composite failure.¹¹⁹

Tomao *et al.* examined the influence of time and temperature on hydrothermal treatments on borosilicate glass fiber surfaces.⁵¹ After the hydrothermal treatment, fibers were reacted with trimethylchlorosilane (TMCS) for quantitative silanol analysis in conjunction with FT-IR analysis. The hydroxyl band occurs between 3700 and 3200 cm^{-1} .⁵¹ The hydroxylation of the surface becomes more efficient in the solution with increasing temperature, but above 100°C the surfaces become altered as seen with the SEM. Between 40 and 100°C, the hydrothermal treatment generates reactive silanol sites with increasing temperature as seen using TMCS and FT-IR.⁵¹

Two processing effects on commercial glass fibers were examined by Palmisiano *et al.* using SIMS and XPS.¹²⁰ The techniques were flame attenuation and continuous filament drawing. The fiber compositions consisted of approximately 65mol%SiO₂, 11%B₂O₃, 11%Na₂O, 4%Al₂O₃, 2%K₂O, 3%ZnO, 2%BaO, 2%CaO and 1%F₂.¹²⁰ The flame attenuated fibers exhibited a surface layer depleted in boron compared to the continuously drawn fiber. This B depletion created a surface that limits out-diffusion of other species.¹²⁰

Alkali disilicate fibers were produced under various temperatures by Murach *et al.*¹²¹ Optical birefringence, the apparent stress optical constant, density changes, and expansion were measured relative to the bulk glass in

an attempt to determine structural changes. The apparent stress optical constant increases with increasing temperature of fiber formation. The thermal expansion behavior showed an anomaly, which was expected of the disilicate glasses. The density and diameter data were compared and it was deduced that thin fibers exhibit radial expansion and high drawing stresses, where thick fibers show radial shrinkage and small drawing stresses.¹²¹ Another study by Murach and Brukner on silica glass fibers showed very different results.¹²² Silica glass fibers exhibit axial shrinkage and radial expansion over the temperature range. It was also found that there was a large degree of anisotropy in the open structure of the three-dimensional network, which confirms the existence of asymmetric hollows in the fibers. These hollows are oriented by the fiber drawing process and thus these fibers have much higher stresses than their bulk counterparts.¹²² More treatment analyses on silica glasses are described in the following section.

2.3.4.3. Treatments on Silica Glass

There have been numerous studies regarding structural changes as a function of formation or surface treatment for silica glasses.¹²³ It is apparent that drawing conditions have an effect on the interior structure and consequently the surface structure of silica fibers.¹²² The drawing process is known to produce paramagnetic defects, such as E' centers and nonbridging oxygen hole centers (NBOHC), and peroxy radicals, which give rise to induced optical absorption bands in optical fibers.^{124,125} Li *et al.* reported for the first time the existence of two drawing-enhanced defects in low OH content oxygen deficient silica optical fibers using EPR.¹²⁵

It has already been mentioned that thermal treatments are capable of dehydroxylating the surface of silica and, depending on the maximum temperature reached, the process may be reversible.^{26,27,53,55,67,71,81,86-88,90-94} Lygin stated that there are two stages of thermal dehydroxylation.^{53,126} The first step is between 500-600°C and consists of the condensation of hydrogen-

bonded surface silanol groups and the formation of slightly strained siloxane bonds. A relaxation of the structure of silica near these strained bonds reduces the stress. The second stage is between 600-1200°C that incorporates reconstruction of separate surface sites upon removal of free silanol groups. The properties of the remaining surface hydroxyl groups change, such as the appearance of stable sites that oppose rehydroxylation in the formation of new electron-acceptor and reactive centers.⁵³ Kuzuu *et al.* performed a study on the structural change in the near-surface region of a silica glass block with heat treatment.⁵⁵ They also used infrared spectra to follow the changes and found that certain absorption bands were induced following a heat treatment, which they called annealing, at 1160°C for 120 hours. The appearance of certain absorption bands only occurred on certain surfaces of the glass block, either the side surfaces or the top surface.⁵⁵ It was found that the OH reduction on the top surface was approximately 45 ppm with the heat treatment and that of the side surfaces was 60 ppm.⁵⁵

Modifying the silica surface with stress in a wet or dry atmosphere results in different relaxation states in the surface.¹²⁷ This was determined by Webb III *et al.* through molecular dynamics simulations of a glass surface creating an interface with a crystal surface. It was determined that some of the stresses created in this interface were retained after separation and consisted mainly of strained siloxane bonds. These strained bonds may react more readily with water. It was observed in their simulations that a surface in the presence of water before and after interface creation had an increase in the number of Si-O bond ruptures and siloxane bond formations.¹²⁷ In addition, there were a higher occurrence of Si-O bonds reacting to form Si-OH sites.¹²⁷

One very interesting investigation recently carried out by Nazabal *et al.* concentrated on the structural modification of silica surfaces induced by thermal poling.¹²⁸ Thermal poling is accomplished by placing a glass in an electric field at an elevated temperature and inducing a permanent second-

order nonlinear susceptibility.¹²⁹⁻¹³¹ The second harmonic (SH) signal generation is measured since the SH can be induced only in isotropic materials such as glass.¹³² The charge transport of mobile ions driven by the poling field from the anode to the cathode creates a negatively charged depletion layer at the anode surface.^{129,130} After or during poling, ions begin to deposit and create a large frozen-in electrostatic field in the anodic surface layer.¹²⁸ Bridging Si-O-Si bonds are broken during poling and are only partly restored after thermal treatment. There is also a decrease of hydroxyls associated with an increase of non-bridging oxygen species.¹²⁸

Silanol levels on synthetic quartz crystals were examined by Wood *et al.* as a function of surface treatment.⁷⁵ Their surface treatments included; water plasma, heating in a vacuum to 500°C, heating in a vacuum to >1000°C, and an inert gas ion bombardment in vacuum.⁷⁵ Secondary ion mass spectroscopy (SIMS) was utilized to follow the ion ratios (SiOH⁺:SiO⁺, SiOH⁺:Si⁺, and OH:O) as a function of temperature.⁷⁵ The water plasma treatment resulted in a maximum of surface hydroxylation and the >1000°C heat treatment resulted in a minimum of surface hydroxylation.⁷⁵ They found a linear relationship between ion ratio and temperature.⁷⁵ Ion beam sputtering has also been used as a method for inducing changes in a silica surface. Flamm *et al.* studied the topographical effects of low-energy argon ion beam sputtering with an AFM.¹³³ As ion beam sputtering is a common technique for depth profiling it is important to understand how this technique alters the surface of a silica glass. It was determined that the sputtering caused a ripple feature to appear on the surface and that the wavelength of this feature was dependent on the energy of the incident ion beam.¹³³

Point defects on the silica surface were created by Radtsig through chemical modification and analyzed using ESR, IR and optical spectroscopy.¹³⁴ Point defects are highly reactive and implies that either a silicon or oxygen atom on the surface has a different number of nearest

neighbors than chemically appropriate. Radtsig applied mechanical treatments such as cleaving under vacuum and also a thermochemical treatment consisting of the creation of Si-OCH₃ from Si-OH followed by a high temperature pyrolysis.¹³⁴ Silanone groups, ($\equiv\text{Si-O}$)₂Si=O, were detected on the surface of mechanically activated silica and thermochemically activated silica. Various other sites were stabilized through these treatments such as paramagnetic sites and diamagnetic sites. Paramagnetic sites include; silyl radicals (tri-coordinated silicon atoms ($\equiv\text{Si-O-}$)₃Si*), oxy radicals (non-bridging oxygen atoms ($\equiv\text{Si-O-}$)₃Si-O*), and peroxide radicals ($\equiv\text{Si-O-}$)₃Si-O-O*). Diamagnetic point defects include; silylene or bicoordinated silicon atoms (Si atom is linked to two lattice oxygen atoms) and silanone groups (($\equiv\text{Si-O}$)₂Si=O).¹³⁴

Other chemical modifications on silica surfaces have included adsorption of acetaldehyde, methyl acetate, ethyl acetate, and methyl trifluoroacetate.¹³⁵ Through the use of microcalorimetric analysis, IR spectroscopy and temperature-programmed-desorption studies it was determined that the chemistries adsorb to silica primarily through two hydrogen bonds per adsorbate. This involves the donation of electrons from the lone-pair orbital on the adsorbate's carbonyl oxygen to hydrogen atoms in the surface silanol groups.¹³⁵ This was detected through IR due to the shifts in the C=O and O-H bond stretching bands.¹³⁵ Oleic acid, polymethyl methacrylate, and polyacrylic acid were coated on soda-lime-silicate and silica glasses and measured using IR spectroscopy by Lee and Condrate Sr..¹³⁶ They posed three possible reactions of the organics with the glass surfaces. The first two being that the organic compounds with an alcohol (-OH) or a carboxylate (-COOX, where X is H or CH₃) group bonds with the glass through hydrogen bonding or chelate bonding (forming several bonds to a metal ion). The third possibility is that a condensation or esterification reaction occurs between the functional groups of organics and the silanol groups on the glass surface.¹³⁶ They found that metal-chelate species are

formed when organic compounds with carboxylate groups are placed on soda-lime silicate surfaces.¹³⁶ The soda-lime silicates contained numerous metal ions with which to form bonds such as sodium, calcium, magnesium, aluminum and potassium. The bonding species was not identified for the silica coated glasses. Other chemical modifications of the silica surface include a wide range of organosilane, alkoxy silane or aminosilane treatments. Organosilanes create a bridge between the inorganic glass surface and any organic molecule. Treating a surface with a silane is a common method to enhance bonding and, therefore, the silanes are typically referred to as coupling agents.^{123,137}

2.3.4.4. Silanization of Silica Surfaces

Silanizing a silica surface is a method by which the surface can be modified and functionalized. There are many types of silanes and the one to use is highly dependent on the application and/or further chemical processes through which the surface must undergo. Aminopropyltriethoxysilane or APTS is one of the most commonly used and, because of its electron-rich amine center, it can hydrogen bond with hydroxyls or other amines.¹²³ Once an aminosilane is exposed to a silica, the amine bonds to a surface hydroxyl group through hydrogen bonding. Then, the amine group can catalyze the condensation of the silicon portion of the molecule with a surface silanol. Siloxane bonds with the surface are formed.^{49,123} The coating is then cured by a thermal treatment. For a complete description of the many silane treatments for silica, among other surface treatments, see the book by Vansant *et al.* or the article by van der Voort and Vansant.^{49,123}

The influence of the silane coupling agents on surface properties of silica precipitates was discussed by Jesionowski and Krysztafkiewicz.¹³⁷ They modified the silica with three different silanes, one of which was APTS, the others being a mercaptosilane and a vinylsilane. The degree of hydrophobization was determined as well as the concentration of surface

silanol groups after treatment. The highest degree of hydrophobicity induced on the silica particles was accomplished with mercaptosilane and vinylsilane.¹³⁷ The highest degree of silanol group condensation, and thus the lowest concentration of surface silanols, was obtained after treatment with mercaptosilane.¹³⁷ Another study involving the silica surface change from hydrophilic to hydrophobic was conducted by Fuji *et al.*¹³⁸ They concentrated on the change of the geometric structure of the modifying surface treatment and how it affected the wettability.¹³⁸ AFM was used to follow the structure of the surface modifications. The chemistry applied to the surface was not a silane but a dodecoxy alcohol. At 50% of surface modification the chains on the modifier arranged into a hexagonal packed structure.¹³⁸

One very important surface preparation method (the creation of self-assembled monolayers) involves the use of aminosilanes.⁴⁹ In this technique, highly ordered films, much like Langmuir-Blodgett films, of polar molecules are deposited onto flat surfaces using a dip coating approach. The result is a very dense layer with full surface coverage. These types of surfaces are used for boundary lubricants, orienting films for liquid crystals, functionalized surfaces for DNA adsorption, and surfaces for micro-lithography.¹³⁹⁻¹⁴⁶ Imura *et al.* observed the chlorosilane monolayer formation as a function of temperature and discussed the characteristic temperature, T_c .¹⁴⁷ When the monolayers are prepared below T_c , the hydrocarbon chains are ordered and closely packed. However, above T_c , there is disorder and low density in the monolayer.¹⁴⁷ The adsorption processes were followed using FTIR and AFM analysis.

Surface functionalized silica particles have also found applications in catalysts and sensors in addition to the above mentioned applications.¹⁴⁸ Deng *et al.* examined how to control the surface expression of functional groups on silica particles by varying the time of the silane addition to a solution of forming silica particles.¹⁴⁹ The particles are formed similarly to

the Stöber process and the silanes were added at various times during the silica particle formation.³¹ It was found that for amine functionalized particles, the highest number of surface groups are created if the organosilane is added to the solution 30 min after the addition of TEOS.¹⁴⁹ The most advantageous time to add the modifier is highly dependent on the type of silane.¹⁴⁹

Many silica surfaces treated with silanes are created with the intent to adhere biological molecules to the functional groups. For example, human macrophage cells, foreign body giant cells, streptavidin protein, and nucleic acids have been analyzed on silanized surfaces.¹⁵⁰⁻¹⁵² Alkylsilane was utilized to modify glass surfaces in order to examine the influence of the alkyl surface chemistry on human macrophage adhesion and foreign body giant cell (FBGC) formation.¹⁵² Jenney and Anderson found that the small alkyl chain length modified surfaces maintained a high cell density and supported macrophage development as well as FBGC formation. Whereas the long alkyl chain lengths on the glass prevented long-term macrophage density and thus did not support FBGC formation.¹⁵² Streptavidin on glass surfaces was analyzed by Birkert *et al.* as a means to determine sensor formation quality.¹⁵¹ Beginning with a SiO₂ surface, diaminopolyethylene glycol was covalently attached to the surface. Biotin was then attached covalently to the amino groups of the polyethylene glycol followed by a monolayer of streptavidin being immobilized onto the biotin surface with high affinity. Finally, biotinylated estrone derivatives were assayed on this layered surface.¹⁵¹ Estrone is a very important hormone that controls endocrine action in the body making its detection useful. It was found that this type of layered sensor surface is very stable and regenerable.¹⁵¹

Benters *et al.* developed a similar surface activation procedure, but intended it for the production of micrarrays for DNA, protein and low-molecular weight component containment.¹⁵⁰ Their procedure was carried out as follows; a glass substrate was subjected to a homogeneous and high

yield aminosilylation, then the surface amino groups were activated with a homobifunctional linker, and allowed to react with a dendrimer containing 64 primary amino groups on its surface, which is again covered with a homobifunctional spacer.¹⁵⁰ These surfaces proved to be twice as sensitive to oligomers with a decreased steric hindrance. In addition, the reactive film was found to be highly resistant to alkaline regeneration procedures, and thus had high stability. This film can be used for the covalent attachment of amino-modified molecules such as oligonucleotides.¹⁵⁰

2.4. Characterization

2.4.1. Common Surface Techniques for Powders

Silica surface studies are almost always carried out on silica powders since they have a high surface area to mass ratio. Barby described many techniques useful for analyzing powder surfaces.²⁵ The most common of which are BET nitrogen adsorption and infrared spectroscopy.^{25,79} Calorimetric studies in which heat of the sample and/or power supplied to the heating elements around the sample are measured results in data that relies heavily on the type of silica powder examined.^{25,88} These types of studies have all but been abandoned for analyzing silica surfaces. An exhaustive, yet slightly dated, collection of descriptions for surface analytical tools is found in a book edited by Kane and Larrabee.⁶⁴ This book does not include any of surface probe microscopies such as atomic force microscopy, nanoindentation, or surface tunneling microscopy. In this text, they separate the techniques into physical and chemical characterization capabilities. The physical characterization techniques used in 1974 were; light microscopy, multiple-beam interferometry, various stylus techniques, electron microscopies (transmission, scanning, auger), field ion microscopies, and X-ray diffraction methods.¹⁵³⁻¹⁵⁹ Among the chemical characterization techniques were; electrochemical techniques, emission spectroscopy, internal reflection

spectroscopy, radioisotope techniques, X-ray fluorescence analysis, X-ray photoelectron spectroscopy (XPS), electron spectroscopy for chemical analysis (ESCA), resonance methods (nuclear magnetic, electron paramagnetic), Mössbauer spectroscopy, Rutherford scattering, accelerator microbeam techniques, electron probe microanalysis, examining X-ray emission fine features, analytical auger electron spectroscopy, mass spectrometry, particle bombardment (ion, electron, neutral atom), and ion impact radiation analysis.^{84,160-176} There were also a number of surface characterization techniques for bulk silica sample surfaces.

2.4.2 Surface Characterization on Bulk Samples

Evaluating the topography of a glass surface is commonly accomplished using atomic force microscopy (AFM),^{48,52,138,177-186} scanning electron microscopy (SEM),¹⁸⁷ glancing incidence X-ray analysis (GIXA)¹⁸⁸⁻¹⁹⁸ or optical interferometry,¹⁹⁹⁻²⁰¹ with the latter two methods mainly producing roughness data. GIXA is also capable of giving the thickness and density of any number of surface films. In regards to determining any surface species present, Fourier transform infrared spectroscopy (FTIR) in partnership with different techniques such as diffuse reflectance or attenuated total reflectance can be a useful tool.^{54,72,90,136,147,202-204} FTIR has been used to examine surface hydroxyls and identify their states.^{72,81,83,138} Hoffmann and Knozinger were the first to assign IR absorption bands to free terminal groups at 3749.3cm^{-1} , geminal groups at 3747.5cm^{-1} , and vicinal silanol groups at 3743.5cm^{-1} .¹²⁶ Glancing incidence X-ray fluorescence is yet another variation on GIXA that yields elemental depth profiling information and therefore can determine surface layer chemical compositions.^{191,198,205-209} SEM in conjunction with energy dispersive spectroscopy (EDS) or wavelength dispersive spectroscopy (WDS) can yield information on the presence of

certain elements in an interaction volume of the sample.¹⁸⁷ X-ray photoelectron spectroscopy (XPS) is a powerful tool in characterizing specific features of the chemical structure and surface chemistry of a glass.^{39,48,74,120,191,210-212} XPS is known for its surface analysis capabilities because the electrons that are ejected originate from the outermost atomic layers of a surface. Secondary ion mass spectroscopy (SIMS) is also used for structural and chemical analysis of surfaces.^{74,75,120,133,211} In SIMS, ions or ionized clusters are ejected from a surface following ion bombardment and are detected by a mass spectrometer. Nuclear magnetic resonance (NMR) performed on high surface area samples provides information on the chemical state and nuclear environment of the magnetically active nuclei at the surface.^{123,213-215} There are many other techniques capable of analyzing the surfaces of glasses such as NEXAFS, LEED, SEELFS, and ARXPS. For a complete review and reference list of most of the surface analysis techniques available, please see the article by Bach²¹⁶ or the appendix in the book by Vansant *et al.*¹²³ The techniques mentioned in the previous two sections are applicable for flat surfaces, high surface area powders and many apply to bulk interior characterization as well. There is a need however for a reliable surface characterization technique that probes unique surfaces, such as inside capillary tubes or fiber surfaces. A few of the surface techniques that were used in the present study are described in more detail in the following sections.

2.4.3. Atomic Force Microscopy

Atomic force microscopy is a very powerful tool for analyzing the surfaces of materials. AFM is used extensively on glasses instead of SEM because a conducting surface is not required for AFM. The AFM works by scanning a fine ceramic (Si_3N_4) or semiconductor (Si) tip over a surface much

the same way as a phonograph needle scans a record. The tip is positioned at the end of a flexible cantilever beam, having a specific spring constant. As the tip is repelled by or attracted to the surface, the cantilever beam deflects in the z-direction. The magnitude of the deflection is captured by a laser that reflects at an oblique angle from the mirrored end of the cantilever. Figure 2.4.3.1 shows the principle configuration for an AFM. A position sensitive photodiode detects the deflection of the laser beam. A plot of the laser deflection versus tip position on the sample surface provides the resolution of the hills and valleys that constitute the topography of the surface. The AFM can work with the tip touching the sample (contact mode), or the tip can tap across the surface (tapping mode). The main forces contributing to the deflection of the cantilever are electrostatic repulsive forces and van der Waals attractive forces between the atoms of the sample surface and those of the tip.^{177,217} AFM tips have a radii of between 4 and 60 nm, which leads to the ultra-sharp resolution of the images obtained.

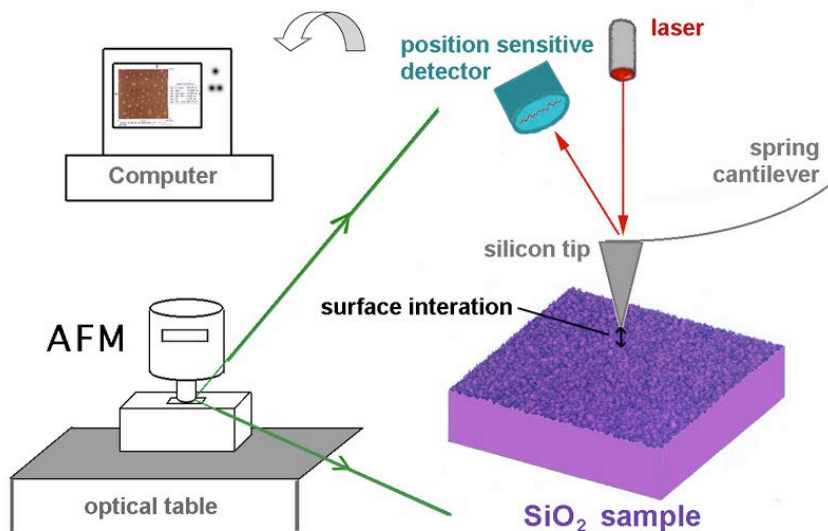


Figure 2.4.3.1. Schematic representation of an AFM. The right side of the schematic is an enlarged version of what occurs under the AFM head.

The AFM can operate in various modes; contact, tapping, phase imaging, force modulation and non-contact mode. All five modes are shown

in Figure 2.4.3.2. In contact mode, or constant force mode, an electronic feedback loop keeps the force between tip and sample constant. In this mode the tip is kept in physical contact with the surface. This mode is designed for surface topography imaging and is best suited for hard samples.¹⁸⁶ The image is obtained by monitoring the force signals required to keep the tip in contact with the sample. Some very interesting variations on contact mode can be performed with special tips. If the tip is modified with functional groups, such as $-\text{COOH}$ or $-\text{CH}_3$, hydrophilic or hydrophobic areas on a sample can be imaged, respectively. Stronger interactions between a functionalized tip and the sample leads to higher friction and, therefore, more deflection of the cantilever.²¹⁸ This type of imaging is called chemical force microscopy (CFM).²¹⁹

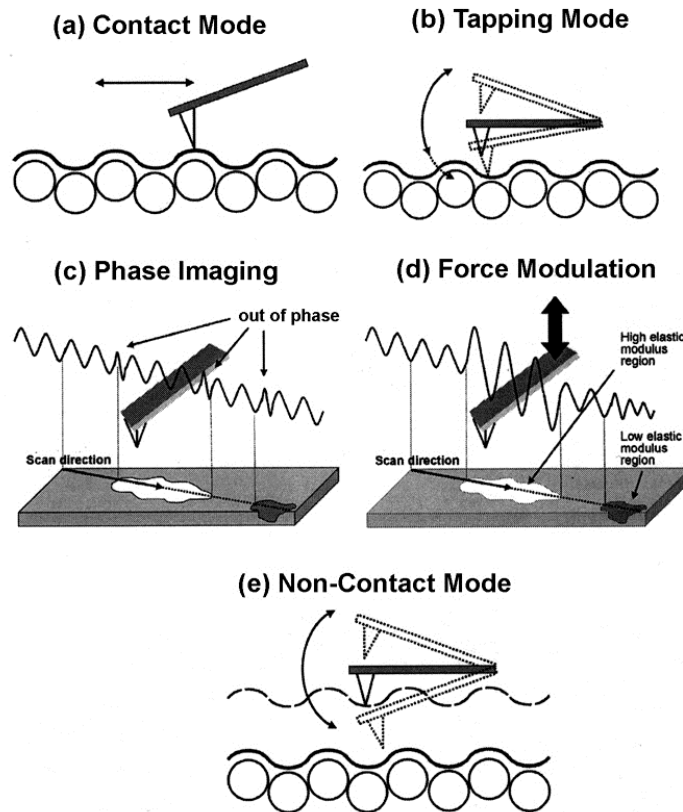


Figure 2.4.3.2. The five modes of the AFM.²¹⁷

Tapping mode (Figure 2.4.3.2.b) utilizes the oscillation of the tip at a certain amplitude and frequency. When the tip comes into contact with the

surface, the energy loss translates into a reduction in tip amplitude, and this variation in signal is used to image the surface.¹⁷⁹ This mode can be used not only in air but in fluids when combined with a specialized liquid cell. The frequency of the oscillating tip in fluids is much lower than in air. The third mode, phase imaging (Figure 2.4.3.2.c), takes advantage of tapping mode in that the tip-sample interactions depend on both topography and elastic modulus.²²⁰ Variations in sample hardness lead to cantilever oscillation phase lag in relation to the signal sent to the cantilever.¹⁸⁰ This difference is monitored and recorded as a phase image. The combination of topography and elasticity gives a very detailed image. Surface anomalies can be more easily identified with phase imaging than with other modes. The fourth mode (Figure 2.4.3.2.d) is called force modulation and is a combination of tapping and contact mode in that the contact force applied to the sample is modulated. Lastly, in non-contact mode (Figure 2.4.3.2.e), the tip is placed at a z-position of attractive force and as the tip moves over the surface, force gradients are detected. For a more complete explanation of AFM modes and uses of the AFM, see the recent article by Jandt.²¹⁷

AFM has been used extensively to examine ceramic and glass surfaces including biomaterials. Jandt explained that a “biomaterials scientist is especially interested in the structure, surface roughness, chemistry and mechanical properties of biomaterials, and in studying the interaction of biomaterials with biological matter.”²¹⁷ One major advantage of the AFM is that a material can be examined in its native state, which leads to more definitive information about the material’s surface. AFM on dental samples has proven very effective in studying the enamel fine structure, enamel demineralization, enamel development, and nanomechanical properties of tooth enamel.²²¹⁻²²⁵ AFM has also been used in fractographic analysis of biomaterials to determine the mechanisms of failure.²²⁶ There are so many uses for AFM in biomaterials that a complete description is better described by Grainger and Healy, Jandt, or Revenko.^{184,217,227} The reader is also

referred to Volume 491 of Surface Science which consists of selected papers covering a wide range of AFM uses in biomaterials analysis.²²⁸

As for AFM on glasses, surface topography of fracture surfaces,^{52,178} characterization of surface treatments,^{138,177,181,185} nanostructure to property relations,¹⁷⁷ and evaluation of roughness^{108,178,229} are a few of the many uses. One thing to keep in mind about imaging silicate surfaces is that the surface is unavoidably going to have a silica “gel layer” or hydroxylated layer just due to the interaction it will have with water vapor in the air.¹⁷⁷ Radlein and Frischat exclaimed that AFM can be used to examine surface defects and changes in overall surface topology caused by treatments such as cleaning, aging, polishing or corroding.¹⁷⁷ Nanometer-scale swellings were found on aged fracture surfaces of soda-lime silicate in air, but these features were not observed on fused silica.¹⁷⁷ A vertical resolution of less than 1nm and a lateral resolution of several nanometers were possible. Exposure of a fused silica fiber surface to water at neutral pH was observed to increase the roughness.¹⁷⁷ The isotropic nature of glass was also confirmed by their study as the AFM did not find any atomically flat areas on the glass.¹⁷⁷ Radlein and Frischat have defined the “glass pattern” observed by numerous scientists in many different studies. The “glass pattern” is basically a ripple pattern and is found in the smoothest areas of a glass surface. The pattern seems to be common to silicate and other glass surfaces regardless of their histories.¹⁷⁷

Eske *et al.* produced glass slides and single crystal quartz samples with about 20 different surface treatments ranging from acidic treatments to basic treatments to sputtering treatments. They show an AFM image of every surface treatment and the effects are very interesting. One of the most intriguing is the KOH treatment of quartz, which results in a surface with very regular and distinguished peaks and valleys.¹⁸¹ On single crystal quartz samples, the hydrochloric acid treatment resulted in a roughened surface with gradual peaks and valleys. The peaks and valleys became less

pronounced and much smaller (more granular-like) as the acid etchant went from hydrochloric, to sulfuric, nitric, chromic, acetic and finally to phosphoric. For the glass microscope slides, which was most likely a soda-lime silicate, most of the acid treatments gave very similar roughened surfaces except for the chromic acid, which resulted in a very smooth surface. Hydrochloric acid did give a slightly more gradual roughening like it did for the quartz surface.¹⁸¹

Bukaraev *et al.* developed an *in situ* observation technique for HF etching of SiO₂ in the AFM. They bombarded silica with Fe⁺ ions and then proceeded to HF etch the surface. Their findings include nanoscale enhanced etching by the Fe ions with HF by deconvoluting original AFM images while taking into account the AFM tip-surface area.¹⁸⁵ Gupta *et al.* compared a fracture surface of silica to a melt formed surface.²²⁹ They attribute the RMS roughness values obtained from the AFM to surface tension (for melt formed) and intrinsic inhomogeneities (for the fracture surface).

Reducing surface roughness is an important technique to master and can be accomplished by polishing or cleaning.¹⁰⁸ Henke *et al.* used a well established method of preparing a surface for good adhesion of biomolecules for biosensor development. It is important to determine the surface roughness in order to obtain a surface area value when binding biomolecules. This method consisted of washing the fused silica surface in basic peroxide, followed by acidic peroxide to clean and hydroxylate the surface.²³⁰ This cleaning method has not been accepted as an optimal method for cleaning glass.⁴⁷ However, this method is often used to prepare fused silica for immobilization of proteins and nucleic acid oligomers, and therefore was studied by Henke *et al.* Using the AFM, they found that the fused silica slides presented three surface features; nodules, pits/scratches, and some evidence of surface undulation (overall roughness). The cleaning method was determined to decrease the RMS roughness, decrease the number and size of surface nodules, but increase the depth of the surface pits and scratches.¹⁰⁸

One must question therefore whether the surface nodules (impurities) controlled the calculation of RMS roughness and whether the cleaning method actually increased the roughness of the fused silica itself.

Another cleaning study by Bowen *et al.* utilized the adhesion force sensitivity of the AFM to examine the interactions between a silica sphere and a planar silica surface after cleaning.¹⁰⁹ Their cleaning methods were either ethanol washing or an oxygen plasma treatment. Silica spheres were adhered to the tip of a cantilever for the force interaction measurements. The force curves were measured in an aqueous environment of pH 3 and 8. They observed a much lower adhesion of the silica beads to the silica surface for the oxygen plasma treatment at pH 3 than the ethanol treatment at the same pH. At pH 8, the repulsion forces for the oxygen plasma treated surfaces was much greater than that for the ethanol treated surfaces. This is in agreement with the view that the plasma treatment would increase the density of silicic acid groups, which would be negatively charged at pH 8.¹⁰⁹ In other words, there is an increased electrostatic double layer at this pH for such a treatment, which increases repulsion.

A ground-breaking study of silica fracture surfaces in ultra-high vacuum was performed by Poggemann *et al.*⁵² They imaged features as small as the interatomic separation distances (Si-O or O-O) with the AFM. They also imaged groups of atoms, such as the SiO₄ tetrahedron and rings of tetrahedra. The images they obtained supported Zachariassen's view of the network structure of silica glass. The preparation of fracture surfaces in vacuum prevents the reaction of water vapor with the highly active surface, which allows the direct imaging of the surface species without having to deal with the interfering water layer. Their images, shown in Figure 2.4.3.3, are incredible in resolution. This direct representation of the surface of silica will lead to great advances in understanding these surfaces for biomolecular adhesion and many other applications.

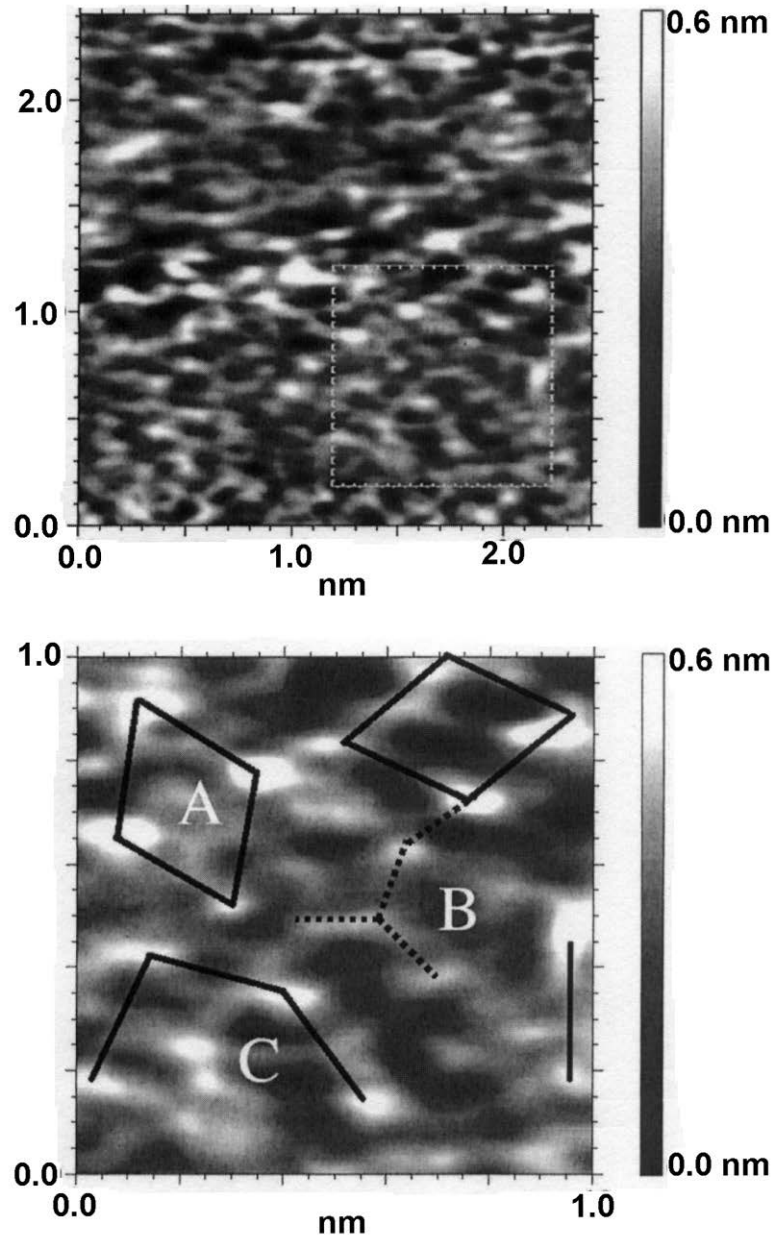


Figure 2.4.3.3. A non-contact AFM image of a silica glass fracture surface, fractured under ultra-high vacuum (top) and imaged in vacuum (bottom). The insert from the upper image with possible O-O (solid lines, A,C) and Si-O (dashed lines,B) bonds.⁵²

2.4.4. Fluorescence

Luminescence of a material can be separated into two sub-categories, fluorescence and phosphorescence. The difference between the two lies in the nature of the states between which the emission occurs. In order to understand this difference, one must consider the spin states of the electrons involved in the transitions. Multiplicity is given as $2S+1$, where S is the spin, either $+1/2$ or $-1/2$. Consider two electrons in a “ground” level with opposite spins. The multiplicity is therefore 1, and this is called a singlet state. Upon excitation, one electron will jump to an “excited” level. If this excited electron retains its original spin state, then the transition is considered to conserve multiplicity and the excited state is a singlet. The resulting emission will be fluorescence. If the excited electron changes its spin state so that it is no longer opposed to the electron remaining in the “ground” level, the total spin (S) is unity. Therefore, the multiplicity ($2S+1$) of this state is 3 and it is a triplet. The resulting emission will be phosphorescence.²³¹ For practicality, the difference between fluorescence and phosphorescence is in their lifetimes. Fluorescence has a short lifetime (10^{-7} to 10^{-10} sec), while phosphorescence has a longer lifetime (10^{-3} to 10 sec).

Fluorescence is a very interesting property of a material and is usually controlled by impurities. It occurs when a specific atom is hit with a certain energy and an electron in its orbitals is excited to a higher state. The electron then decays in multiple steps (usually), giving off light of a visible wavelength as long as the energy of the gaps, $h\nu$, is between 1.8 eV and 3.1 eV.²³² The incident energy can be high-energy electromagnetic radiation, such as ultraviolet light or X-rays, heat, mechanical or chemical energy. Figure 2.4.4.1 shows a general energy band diagram for fluorescence. Fluorescence can occur in gases (atoms), liquids (molecules) or in solids (atoms, ions, or molecules). Typically though, one thinks of fluorescence as a color emitted from a solid material when ultraviolet light is incident upon it. And this is a very useful tool for characterizing the structure of glass in

particular, but so is X-ray fluorescence, where the incident and emitted energy is in the X-ray region.

The most basic example of atomic fluorescence is that of sodium vapor. The sodium D-lines are emitted in fluorescence if Na vapor is illuminated by light of the same wavelength, which is then in resonance with the absorption.²³³ The vapor pressure of the sodium must be low in order to prevent atomic collisions that quench fluorescence. Liquids, or rather solutions, may exhibit fluorescence as well depending on the constituents. The more complex the chemical structure of the substance, the more likely it is to emit a strong fluorescence. This can be explained by the prevention of collisions with the fluorescing part of the molecule, as it is typically found on the inside of complex molecules. Nearly all simple organic compounds will fluoresce in solution, but inorganic salts do not generally show fluorescence due to their simple constitution.²³³ Benzene is the most common example of simple organic liquid fluorescence. Aromatic hydrocarbons possess pi electrons, which are less strongly bound than sigma electrons (found in aliphatic compounds, which do not fluoresce).²³⁴

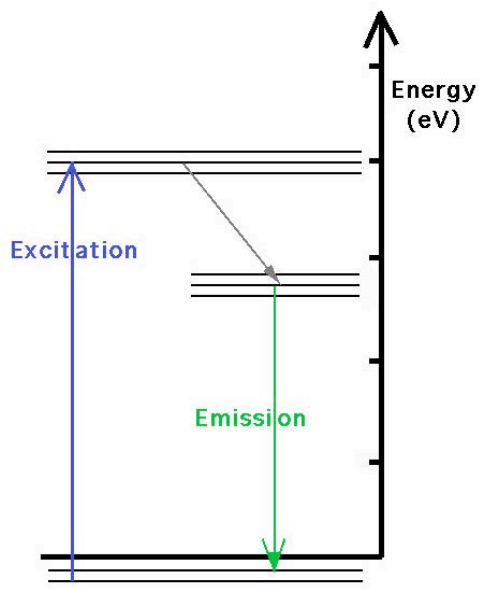


Figure 2.4.4.1. A general energy band diagram for fluorescence. The excitation energy is typically in the ultraviolet and the emission energy is typically in the visible region of the electromagnetic spectrum.

As the density of the material increases so does the complexity of its fluorescence. The increased number of bonds and the existence of many different types of fluorescent species results in a wide range of possibilities. Just about any element could be made to fluoresce depending on its ionic state. The energy levels of an ion, such as Cu^+ , in a glass will be sensitive to its surroundings and therefore it may be able to probe the local structure of that ion.²³⁵ 2002 2002 2002 2002 Glass is a common host material for fluorescent species due to the UV transparency of most glasses. Transition metal and rare earth ions are frequently studied in various types of glasses to probe for their local structures. Some examples of rare earth probes include, ytterbium in phosphate glass,²³⁶ erbium in silica,²³⁷⁻²³⁹ cerium in a sodium borate glass,²⁴⁰ praseodymium in zirconium fluoride glasses,²⁴¹ praseodymium in arsenic sulfide glass,²⁴² and neodymium in fluoroarsenate glass.²⁴³ Fluorescence spectroscopy can probe for the oxidation states of many

glasses.²⁴⁴ X-ray fluorescence is also useful for surface analysis of chemical composition, as for example, in the analysis of ancient glass.²⁴⁵

2.5. Proteins

2.5.1. Protein Background

Proteins are comprised of amino acids, of which there are commonly twenty types. The basic side chained amino acids are lysine, arginine, and histadine. The acidic side chained amino acids are aspartic acid and glutamic acid. The uncharged polar side chained amino acids are asparagine, glutamine, serine, threonine, and tyrosine. Finally, the non-polar side chained ones are; glycine, alanine, valine, leucine, isoleucine, proline, phenylalanine, methionine, tryptophan and cysteine. Of the 20 amino acids, 19 have the general structure:



They differ only in the chemical structure of the side chain **R**. Proline is the unique protein in that its side chain is bonded to the nitrogen atom as well as the α -carbon. The entire set of amino acid structures can be found in Figure 2.5.1.²⁴⁶

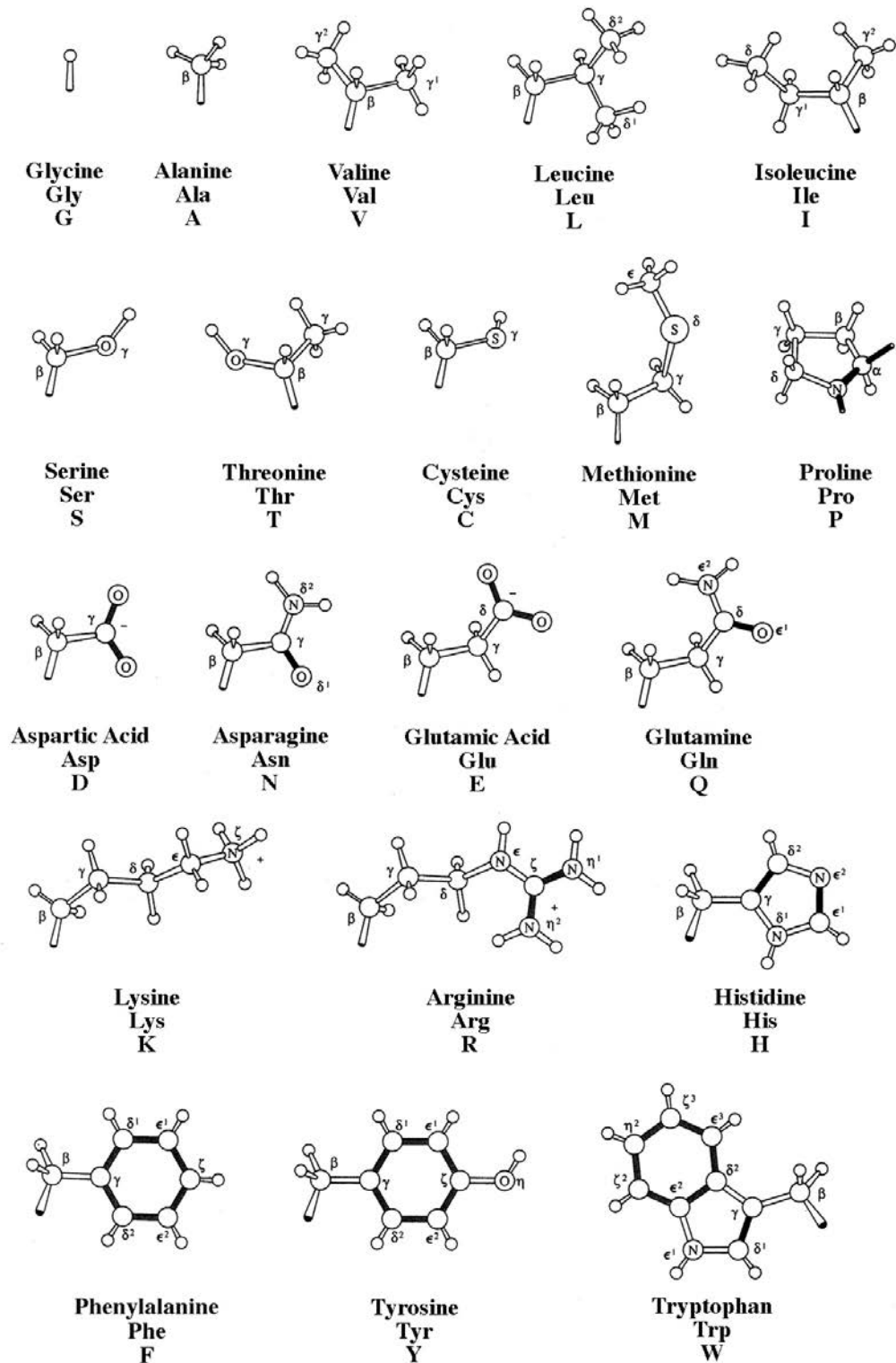
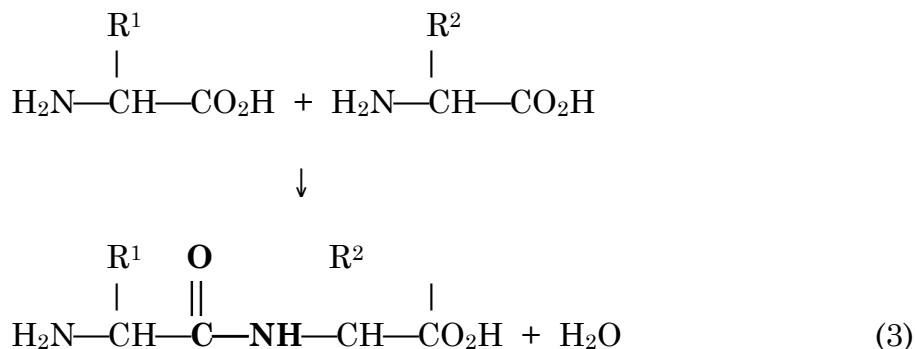


Figure 2.5.1.

All 20 amino acid structures (and names) that are the building blocks for proteins.²⁴⁶

Proteins are very flexible and can adopt many shapes or conformations, but for any given protein under physiological conditions one particular shape is preferred. The amino acids form weak non-covalent bonds with each other and water. The formation of the peptide bond is shown in bold in equation 3:



The peptide bond appears to have partial double bonded character due to resonance and this resonance tends to redistribute its electrons.²⁴⁶ The polypeptide backbone is correspondingly polar. The H and C atoms are positively charged while the N and O atoms are negatively charged. This leads to a substantial permanent dipole moment for the peptide bond that is crucial for the three-dimensional structure of proteins.

There are four levels of protein structure; primary, secondary, tertiary and quaternary. The primary structure consists of the amino acid sequence or the polypeptide chain. The secondary structure is caused by regular hydrogen bond interactions within contiguous stretches of polypeptides. This can result in either β -sheets (folding back and forth upon itself) or α -helices (turning about itself to form a rigid cylinder). Combinations of α -helices and β -sheets can pack together to form compactly folded globular units called protein domains. These domains can be in the form of motifs such as the “hairpin beta motif” or the “beta-alpha-beta motif”. Figure 2.5.2 shows these two aforementioned motifs. The part of the motif of most interest is in the connection between the secondary structures. These connections are called

loop regions and often form the binding sites for other molecules. In certain proteins, the loop linking the carboxy-terminal end of the first beta-strand to the amino terminal end of the helix is involved in the binding of ligands or substrates. Since the loop regions are frequently exposed to water, the amino acids in the loops are often hydrophilic (polar) in nature. These loop positions can frequently be predicted from careful examination of the amino acid sequence. Tertiary structures are domains and monomers and quaternary structures are dimers.



Figure 2.5.2. Two examples of protein motifs with loop regions indicated by arrows. (a) The hairpin beta motif and (b) the beta-alpha-beta motif.

An unfolded protein is termed denatured. Introducing heat or a solvent to a protein solution causes denaturing. Removing the solvent can cause certain proteins to fold back into their native conformation. The non-polar side chains are hydrophobic and will tend to pack into the interior of a protein away from the water rich environment. Polar amino acids are usually found on the outside of a protein so it can react with water and other polar molecules. The polar sites and the location and identity of loop regions are key in understanding a protein's interaction with a glass surface.

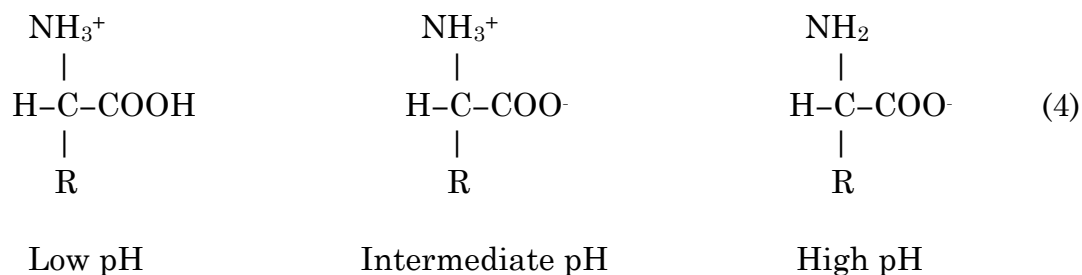
Proteins also fluoresce. Many proteins contain the aromatic amino acids; tryptophan, tyrosine and phenylalanine, giving them intrinsic fluorescence. Proteins can also be complexed with fluorophores, such as fluorescein, and this fluorescence is referred to as extrinsic. Fluorescence is a cyclical process, meaning it can continue to occur, unless the fluorochrome is

destroyed during the excited state. Destruction of the fluorochrome leads to photobleaching.²⁴⁷ Both types of fluorescence can be utilized to characterize the structure of a protein. The intrinsic type serving to give information about internal structure and the extrinsic helping to characterize binding sites on proteins.²⁴⁸ The fluorescence of amino acids varies with the pH. Tryptophan's fluorescence is a maximum between pH 10 and 11 where tyrosine's is between pH 4 and 9.²³¹ Tryptophan also displays a constant fluorescence at low pH until pH 3 where the intensity drops off dramatically.²³¹ Table II shows the spectroscopic properties of the three aromatic amino acids.

Table II. Spectroscopic Properties of the Aromatic Amino Acids at Neutral pH²⁴⁶

	Wavelength at Maximum Intensity (nm)	
	Absorbance	Emission
Phenylalanine	257.4	282
Tyrosine	274.6	303
Tryptophan	279.8	348

At neutral pH (~7), amino acids are neutrally charged, but they act as zwitterions (dipoles). The positive charge is formed by the amino group becoming -NH_3^+ , while the dissociated carboxyl group becomes -COO^- and is negatively charged.²¹² At high pH values the amino group is neutral and the carboxyl group stays negative, while at low pH values, the amino group is positive and the carboxyl group is neutral. Schematically this is shown as:



Due to the amino and carboxyl group behavior with pH, and in addition, the ionizable groups of some of the side chains ($-\text{SH}$ and $-\text{OH}$), the pKa values range from ~ 2 to ~ 12 .²¹² The value, pKa, is derived from the equilibrium acid ionization constant:

$$pK_a = -\log(K_a) \quad (5)$$

$$K_a = \frac{[H_3O^+][A^-]}{HA} \quad (6)$$



The pKa value for the amino group is ~ 7.4 and that of the carboxyl group is ~ 3.9 .²⁴⁶

2.5.2. Proteins Used in this Study

All of the proteins used in this study were selected based on five criteria. The first is that they are used frequently in literature and thus can be compared to other studies. Secondly, their structures have been solved and published. Third, their binding is orientationally sensitive owing to their structural asymmetry. The fourth is that they bind with a very high affinity to their complex and the fifth is that they are inexpensive.

2.5.2.1. Albumins

Human serum albumin (HSA) and bovine serum albumin (BSA) fall under the first, second and fifth categories. There have been an extensive number of studies done using these two serum albumin proteins.^{7,9,249-254} Albumins are simple proteins found in the body fluids and tissues of animals and in some plant seeds. Albumins have low molecular weights (~66,000Da for HSA), are soluble in water, and contain an excess of acidic amino acids. Due to their high charge to mass ratios, albumins will bind Ca^{2+} , Na^+ , K^+ , water, hormones and drugs. Their main biological function is to regulate the colloidal osmotic pressure of blood. Since HSA and BSA contain a high percentage of nitrogen (16%), they are often used as standards in calibrations of protein assays. The amino acid sequences of HSA and BSA have been determined and the proteins are single polypeptide chains with disulfide bonds.

2.5.2.2. Streptavidin

Streptavidin is a tetrameric protein of molecular weight $4 \times 15,000\text{Da}$. It is isolated from the actinobacterium *Streptomyces avidinii* and can bind up to four molecules of biotin.²⁵⁵ The sequence and secondary structure of streptavidin is given in Figure 2.5.2.2.1. Streptavidin has D₂ (222) symmetry and each monomer folds into an eight-stranded anti-parallel β -barrel. This cyclically hydrogen bonded barrel has several hairpin loops that extend out, one of which is near the carboxyl terminus that binds to another streptavidin monomer creating a dimer. A tetramer is formed by two stable dimers that are associated relatively weakly by van der Waals interactions across a small intersubunit contact area.^{256,257} These complex structures are shown schematically as stereograms in Figure 2.5.2.2.2.²⁵⁸

```

1  DPSKDSKAQV SAAERGITGT MYNQLGSTFI UTAGADGALT GTYESAUGNA
   HHHH EE EEETTS EEE EEE TTSEEE EEEE SSSS

51  ESRVULTGRY DSAPATDGS G TALGUTVAHK NHYRNAHSAT TMSGQYUGGA
   S EEEEEEE SS STT EEEEEEEESB SS D SEEE EEEEEEE SS

101 EARINTQULL TSGTTEANA KSTLUGHDTF TKVKP
   S EEEEEEE EE GGGGG G EEEEEEE EE

```

Figure 2.5.2.2.1. Streptavidin amino acid sequence from Protein Data Bank file 1SLF.pdb. The Trp-Lys sequences at positions 79-80 and 120-121 are underlined.

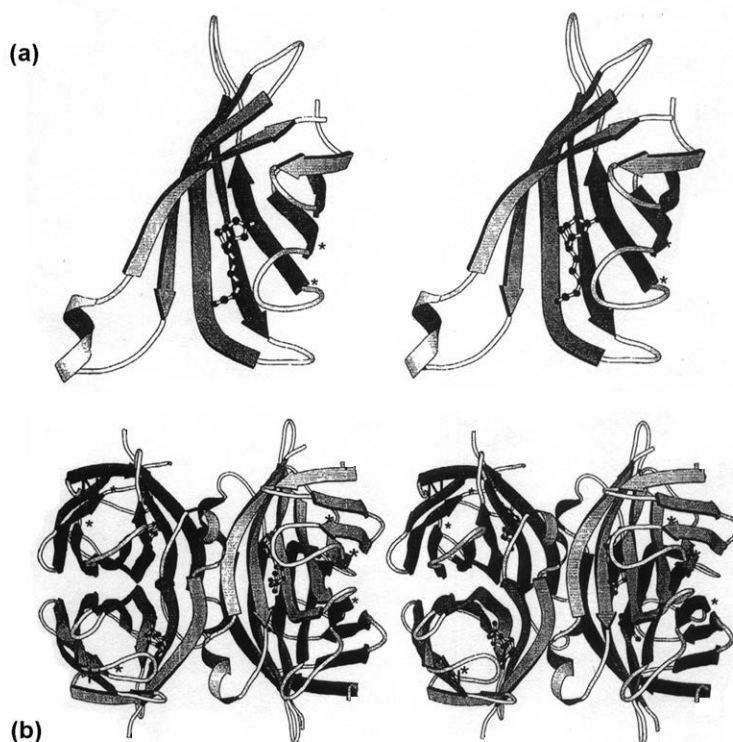


Figure 2.5.2.2.2. Stereograms of (a) one monomer of streptavidin forms a β -barrel with extended hairpin loops and biotin (ball and stick molecule) is bound at the open end of the barrel. The asterisks denote the termini of the loop that folds over biotin. (b) A streptavidin tetramer. (After Freitag *et al.*²⁵⁸)

Biotin is bound in the open end of the twisted barrel and one surface loop folds over the binding site when biotin is bound.^{257,258} Streptavidin is a

very expensive protein, but it is used quite extensively in literature due to its known structure^{259,260} and orientation sensitive binding.^{151,258,261-263} It also has the strongest known non-covalent binding affinity for its complex, biotin.^{257,258,264-266} It is thought that biotin may bind to the site where the Trp-Lys (W-K) sequence exists, at positions 79-80 and 120-121 (underlined in Figure 2.5.2.2.1.).²⁶⁴ The biotin binding site in streptavidin has been proven to be much deeper than in its counterpart avidin.²⁶⁴ This extremely high-affinity essentially irreversible protein-ligand interaction has led to their widespread use in diagnostic assays.²⁶⁷ The streptavidin-biotin system is used extensively in immunosensor/biosensor applications for biomolecular recognition in ordered arrays, affinity chromatography and many other applications.^{151,261,262,268-278} For a complete review of “all” of the applications of the (strept)avidin-biotin system, see the Pierce handbook or the article by Wilchek and Bayer.^{264,279} One study concluded that the high affinity is due to multiple hydrogen bonds and van der Waals interactions, together with the ordering of surface polypeptide loops that bury biotin in the streptavidin interior.²⁵⁷ It is evident that streptavidin changes its conformation upon binding to its ligand.^{260,280,281}

Streptavidin shows a wide range of pH stability and is highly resistant to denaturation by acids.^{282,283} Streptavidin immobilized on 6% crosslinked, beaded agarose is stable over a pH range of 2-13 as an affinity support.²⁶⁴ Cohen *et al.* suggests that streptavidin is stable in terms of enzymatic activity between a pH of 3 and 12.²⁸³ The isoelectric point or pI of streptavidin is 5-6 according to Savage *et al.*²⁶⁴ and 6-6.5 according to Leckband *et al.*²⁷⁸ Streptavidin being “stable” in this wide pH range does not imply that the protein remains unchanged. In fact, a decrease in the pH from 7.2 to 6.0 results in a complete charge reversal on the biotin binding surface from net negative to net positive.²⁷⁸ Changing the pH of a streptavidin solution will alter the interaction forces between streptavidin and other charged species in the solution.

According to Yang and Honig, a large net charge accumulates on a protein surface when the pH of its solution is far from its isoelectric point.²⁸⁴ They base this statement on the Linderstrom-Lang model which treats a protein as a simple charged sphere whose electrostatic value is the square of the net surface charge and is therefore repulsive at all pHs except at its isoelectric point. This model assumes that the distribution of charge on the sphere surface is continuous, which is incorrect because of the existence of specific charged groups on the surface. Therefore, Yang and Honig attempted to develop a method to calculate the pH stability dependence (free energy of protein unfolding) of a protein.²⁸⁴

2.5.2.3. Immunoglobulin G

Immunoglobulins have a basic four-chain monomeric structure consisting of two identical heavy (H) chains and two identical light (L) chains with interchain disulfide bonds. Each chain has a constant (C) region and a variable (V) region as shown in Figure 2.5.2.3.1. There are five heavy chain classes; M, D, G, E, and A. Each class is distinguished by certain effector functions and of course each unique heavy chain. Immunoglobulins are antibody molecules that have biological functions, such as transport across the maternal-fetal membranes, but they are also used in immunological tests such as enzyme-linked immuno-sorbent assay (ELISA). IgG proteins have a molecular weight of 150,000Da, almost 2.5 times the weight, and therefore size, of streptavidin. Immunoglobulins are complex heterogeneous mixtures of proteins that exhibit two fundamental types of structural variation. Subtle structural differences in their antigen combining sites (shown in Figure 2.5.2.3.1 left), or variable (V) regions, account for their unique antigen binding specificities. Structural differences outside their antigen combining sites, in the so-called constant (C) regions, correlate with the different effector functions mediated by antibodies, such as complement activation or binding to one or more of the antibody Fc receptors. The variable (V) and

constant (C) regions of antibodies arise from distinct structural domains and are shown in Figure 2.5.2.3.1 on the right.

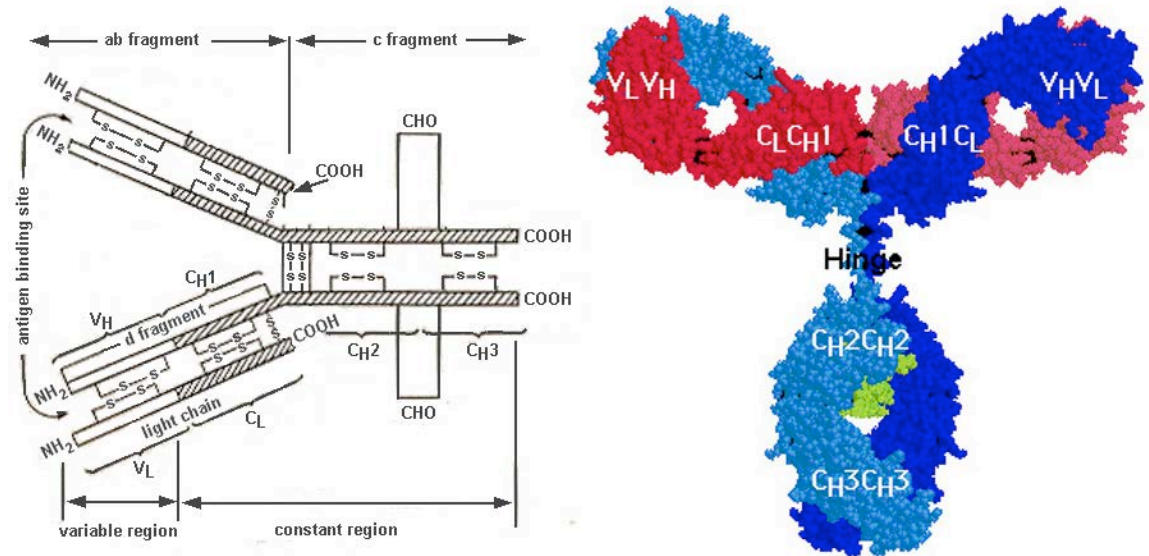


Figure 2.5.2.3.1. A schematic diagram of the structural features of an IgG molecule (left). The constant region is identified by the crosshatches. A spacefill model of IgG (right) shows how the molecule structures twist around each other.

It can be seen from Figure 2.5.2.3.1 that IgG is highly asymmetric and has a hinge section that separates the two “fragments” of the molecule. The largely variable section is denoted the Fab fragment and the other half is called the Fc fragment. Due to its structure, IgG is orientation sensitive during binding. It is possible to obtain proteins that will react with only the Fab sections or the Fc sections. There have been a number of studies that take advantage of this orientation sensitive binding of fragment specific anti-immunoglobulin antibodies.²⁸⁵⁻²⁹¹ Dubrovsky *et al.* and Buijs *et al.* found that the IgG molecules bind to a surface with their Fc fragments leaving their Fab fragments oriented outside towards the surface.^{286,290} They both used the anti-IgG Fab or Fc specific antibodies to see how well they bound to the IgG layer to determine its orientation. Dubrovsky *et al.* used mouse-IgG and a

silanized quartz surface for their study while Buijs *et al.* used mouse-IgG, oxidized silicon wafers and chemically treated silica slides.

2.6. Characterizing Proteins

2.6.1. Common Assays and Detection Methods

The characterization of proteins can be accomplished in any of a number of ways. There are far too many methods to characterize, detect or identify proteins, all of which can be called an assay, to describe here. For an extensive list of protein assays, see the book entitled “Proteins Labfax”.²⁹² The various areas of protein detection include: photometric assays (absorption, fluorescence, and turbidity), radiometric assays, HPLC-based assays, electrochemical assays, gel electrophoresis-based assays, and immunological assays. The determination of protein concentration can be effectively done eight ways; gravimetrically, using the Biuret method, using UV absorbance, through amino acid analysis (recommended above all), using the Lowry method, using bicinchoninic acid (BCA), using coomassie blue binding, or through reaction with *o*-phthalaldehyde.²⁹³ Separating proteins in a mixture can be done by salting out (preparatively), chromatography (preparatively) or electrophoresis (analytically). Silica particles play a large role in the success of chromatography, but this is another issue entirely.³²⁻³⁶ Protein crystallization studies are extremely difficult and involved and are done either by X-ray diffraction or by nuclear magnetic resonance.²⁹⁴ The size of a protein can be determined by ultracentrifugation, light scattering, precision densimetry, viscosimetric analysis, X-ray scattering, neutron scattering, or mass spectrometry (ESI – electrospray ionization or MALDI – matrix assisted laser desorption ionization).^{283,295-297} Structural studies without crystallization can be done using infrared and Raman spectroscopy, circular dichroism, spectroscopic ellipsometry, NMR, or electron

paramagnetic resonance (EPR) spectroscopy.²⁹⁸⁻³⁰⁷ Most of these same techniques can be used for studying adsorbed protein orientation on surfaces, as well as XPS, ToF-SIMS, X-ray reflectivity and surface plasmon resonance (SPR).^{250,251,297,308,309} Likewise, protein stability is measured by fluorescence, UV absorbance, circular dichroism, or differential scanning calorimetry (DSC).^{248,310-318} Protein imaging by optical microscopy, electron microscopy, or atomic force microscopy (AFM) is another beneficial method of analysis.^{183,319-322}

2.6.2. Gel-Electrophoresis

Gel electrophoresis is a simple concept, but can be difficult to perform and obtain reliable results since there are many factors that affect the outcome. In principle, a mixture of proteins are separated in an acrylamide (or similar) gel according to their molecular weights via an electrical potential difference across this gel. The proteins travel through the gel because they are given charges proportional to their molecular weight by the sample buffer. The Laemmli system is the most widely used electrophoretic system.³²³ A subsequent staining procedure with the stain of choice allows one to observe the existence of a wide range of proteins that were in the original mixture.

Polyacrylamide gel-electrophoreses (PAGE) can be divided into three main types; SDS-denaturing, nondenaturing (native), or isoelectric focusing. Sodium dodecyl sulfate (SDS) is an anionic detergent that bestows a negative charge to the proteins. The migration of these proteins is therefore dependent on their electrical charge and their mobility is inversely proportional to their molecular mass.³²⁴ The system developed by Laemmli is an SDS-based system.³²³ Native gel electrophoresis is capable of maintaining the structure and enzymatic activity of proteins. This type is commonly used

in binding studies when the desorbing energy is to be found by increasing the temperature at which the electrophoresis is performed. Isoelectric focusing separates enzymes in a pH gradient gel, such that they are separated according to their isoelectric points.³²⁴ Two-dimensional gel electrophoresis was developed by O'Farrell.³²⁵ In this technique, it is possible to separate the proteins into more components. Typically, one combines isoelectric focusing and SDS electrophoresis, each in their own dimension in the gel.³²⁵

To give some background into how gel-electrophoresis is accomplished, a brief explanation of the procedure follows. Protein mixtures, single protein solutions, or proteins bound to small samples (that can fit in a well) are loaded into the gel wells with a sample loading buffer containing the appropriate constituents (such as SDS or β -mercaptoethanol). Sample loading buffer typically is dyed so that the progress can be monitored visually. A potential difference is then applied to the gel by a voltage source. Protein standard markers, a combination of proteins with known molecular weight, are loaded into one of the wells in order to correlate unknown proteins to their molecular masses. Fixing and staining of the gel is then performed. Stain selection is a very important step because some proteins will not stain with certain types. Coomassie blue is a popular choice, but silver staining is more sensitive and gives various colors depending on the brand. Staining is sensitive to the amount of protein found in the bands for any given protein and therefore it is possible, although very difficult, to do quantitative analysis.

2.6.3. Fluorimetry of Proteins

Fluorescence-labeling is becoming one of the most important techniques in biological studies.³²⁶ A fluorescence probe is a fluorophore designed to localize within a specific region of a biological specimen and

sometimes is meant to respond to a specific stimulus. Fluorophores are generally dyes and have a distinct and intense fluorescence emission. The emission efficiency is measured by two quantities, the molar extinction coefficient and the quantum yield. Fluorescence intensity is a product of these two quantities. The molar extinction coefficient is specified at the maximum of absorption. Quantum yield is a measure of the total photon emission across the entire fluorescence profile and ranges from 0 to 1. A list of most of the common fluorophores and their absorption and emission ranges are shown in Figure 2.6.3.1.

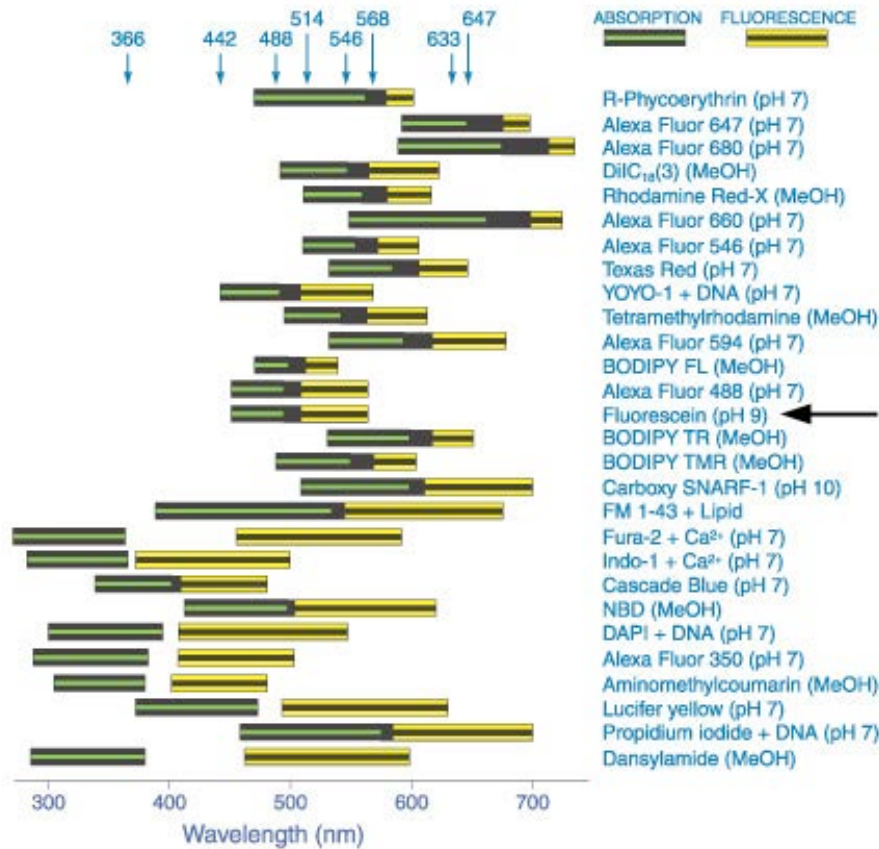


Figure 2.6.3.1. Common fluorophores used to label proteins, their absorption range and emission range. The arrow is pointing to fluorescein, a label used in the current study.³²⁷

Most streptavidin detection by fluorescence is done using a fluorescently labeled biotin complex.^{311-313,315,328-330} Biotin-fluorescein and

biotin-PEG-pyrene were used by Gruber *et al.* for reliable quantitation of streptavidin^{311,330} The biotin-fluorescein conjugate is quite popular because it equally mimics the binding of D-biotin since the fluorescein chain is small. Synthesis of smaller fluorophore probes is essential, and biotin-4-fluorescein and biotin-4-FITC have been produced for this reason.³¹² Haas and Mohwald created an ordered streptavidin (fluorescently labeled) array and analyzed it through fluorescence microscopy and X-ray reflectivity.³⁰⁸

Streptavidin also has intrinsic fluorescence due to its high content in aromatic amino acids, especially tryptophan. Tyrosine and tryptophan have similar quantum yields, 0.21 and 0.20, respectively, while phenylalanine has a very low quantum yield at 0.04.²⁴⁶ Although the natural fluorescence of proteins has been known for about 35 years, not many studies have analyzed streptavidin through its natural fluorescence.²⁴⁸ One study did incorporate a non-natural amino acid, which is site specific, into streptavidin as a sensitive fluorescent probe to monitor structural changes at that site.³¹⁷

Mouse IgG and goat anti-mouse IgG-FITC conjugated have been used to successfully develop a heterogeneous fluoroimmunoassay.³¹⁴ Kakabakos *et al.* measured the fluorescence signal directly from the proteins adsorbed to a solid surface (microtiter plate).³¹⁴ They used a microtiter plate fluorescence reader at an excitation of 485nm with an emission detection at 538nm. They examined the type of plastic used for the well material based on fluorescence signal intensity, precision, and sensitivity for mouse IgG. The white-opaque wells are the most promising and should be used in fluoroimmunoassays.³¹⁴

There are primarily four fluorescence instruments that give very different information. Spectrofluorimeters and microplate readers give the average properties of a bulk sample (liquid or solid). Fluorescence microscopes are able to analyze microscopic samples and report their fluorescence as a function of spatial coordinates. Fluorescence scanners analyze the spatial fluorescence of larger samples. Flow cytometers measure the fluorescence in a cell. New and upcoming methods of observing

fluorescence include video fluorescence, 3D electron microscopy, and confocal microscopy.^{316,331} Mironov *et al.* have proposed a conceptual microscopy combining in vivo fluorescence video microscopy and taking advantage of the resolution afforded by electron microscopy. They have termed it correlative video-light electron microscopy.³¹⁶ Confocal microscopy requires that the focus of the illumination and detection systems are in the same plane. This way only the light from the illuminated portion of the sample is detected.²⁴⁷ The latest form of confocal microscopy uses a scanning laser, can provide intense, deeply penetrating excitation energy and can image in four dimensions (X,Y,Z, and time).³³² Another modern spin-off of confocal microscopy is fiber optic monitoring of fluorescence signals in the brain, which is used to monitor gene expression.³³³

2.6.4. Circular Dichroism

Circular dichroism (CD) spectroscopy is sensitive to the structure of proteins and can therefore be used to characterize protein conformation. Circular dichroism arises from optically active matter that absorbs right and left handed circularly polarized light differently. The CD bands of proteins that occur in the near-ultraviolet range are caused by tryptophan, tyrosine, phenylalanine, and cystinyl groups. The information is representative of the tertiary and quaternary structure of the proteins.²⁹⁹ The CD bands that occur in the far-ultraviolet range originate from amide chromophores and is representative of the secondary structure of the proteins.²⁹⁹ The near-UV range is considered to be 340nm to 250nm and the far-UV range is between 260nm and 178 nm. Linear polarized light can be considered as being a superposition of opposite (left and right) circular polarized light of equal phase and amplitude. When this light passes through an optically active sample that has a different absorbance for one of the circular components,

then the amplitude of the absorbed component will be less upon exciting the sample. The resulting projection will no longer be a line but will appear as an ellipse, which is called circular dichroism.

CD spectroscopy is utilized in a number of different types of studies. The analysis of protein denaturation as a function of temperature or addition of chemical denaturants can be accomplished. The effects of pH, solvents and salts on the conformation of proteins can be analyzed. The secondary structure content of proteins can be determined.³³⁴ Studying the interactions between various biomolecules can also be done with circular dichroism. The conformation changes in proteins upon adsorption to other materials can be studied. Typically, the CD spectra of a given protein is taken before and after adsorption and the change in the spectra is indicative of the binding interaction. One can correlate this change to a specific structural component of the protein and can surmise whether this component is active in binding.

The adsorption of proteins to ultrafine silica particles has been extensively studied by Kondo *et al.* using CD spectroscopy.^{303,335-337} Various proteins were adsorbed to silica particles in suspension and the changes in their conformation were observed. They discovered many phenomena in their studies. The CD spectra of soft proteins change much more than the CD spectra of rigid proteins after binding.³³⁷ The CD spectra of BSA binding change more dramatically with decreasing pH. They concluded that the amount of change in the spectra depends on both the flexibility of the protein and the adhesion forces between protein and particle.³³⁶ They also found that the CD spectra of BSA returns to the original state upon desorption from the particles, suggesting that the protein refolds to its natural conformation. This behavior of BSA was also observed by Giacomelli and Norde, who studied it in slightly more detail.³³⁸ The amount of protein adsorbed to the silica particles is a maximum at the proteins isoelectric point.^{303,336} The kinetics of adsorbed proteins were also studied by Kondo *et al.* who found

that the rate of conformational change is generally affected by pH, ionic strength, and temperature.³³⁵

Another group, led by Billsten *et al.*, observed changes in T4 lysosyme (and mutants) upon binding to silica nanoparticles.³⁰² They were able to attribute spectral changes to loss of the α -helix secondary structure, mostly observed in the tryptophan mutant.³⁰² They concluded that the less stable nature (structurally and thermally) of the tryptophan mutant is responsible for the drastic CD spectra change observed. CD spectra is not confined to nanoparticles or ultrafine particles, it can also be used on flat surfaces. The only problem is that flat surface adsorption offers much lower intensity of the spectra signal and, therefore, multiple plates must be used to increase the sensitivity.³³⁹ Vermeer and Norde did just that.³³⁹ They created a multiple quartz cell setup and performed initial studies on IgG protein. At pH 6, the adsorbed IgG did not display a conformation change as measured by CD, but at pH 8.1, the adsorbed protein did alter its structure. Vermeer and Norde attributed this to the fact that at pH 6 (close to the i.e.p. of IgG) the two surfaces are slightly charged and the interactions (electrostatic and hydrophobic) are weak, inducing no structural change. However, at high pH, the electrostatic interaction is greater and induces a structural change in IgG.³³⁹ McMillin and Walton examined two blood proteins with transmission CD spectroscopy as they bound to a quartz substrate in multi-plate formation.³⁰⁴ Again, their findings suggested that the rigidity of a protein greatly affects its susceptibility to conformational changes.³⁰⁴ In their study, Vermeer and Norde also mention that FTIR attenuated total reflection is also a useful tool in analyzing protein conformation through secondary structure.

2.6.5. FTIR Spectroscopy of Proteins

Fourier transform infrared attenuated total reflectance (FTIR-ATR) is a sensitive technique for studying low levels of protein. Quantities as low as a monolayer of protein adsorbed on a surface are detectable. However, it does have serious limitations that cause the data analysis to be viewed with skepticism.³³⁹ The basics of IR spectroscopy lies in the dipole moment changes of vibrating molecular bonds. If there is a change in polarizability of a system, then it is Raman active.²⁹⁸ Typically changes in dipole moment occur for asymmetric systems of atoms, such as $\text{C}=\text{O}$. The FT in FTIR stands for Fourier transform, which is basically a mathematical process that is applied to the collected data to deconvolute it. FTIR systems generally employ a Michelson interferometer, which allows the whole frequency range to be collected simultaneously and significantly decreases data collection times versus monochromatic based systems.

Dried protein films can be analyzed in FTIR systems, however, dried proteins have a set conformation. Studying a protein in solution is much more difficult since most aqueous solutions have strong IR absorptions. Attenuated total reflectance is helpful since a portion of the protein solution can be placed on a crystal and the total internal reflection IR is measured. The evanescent wave travels about a wavelength of distance into the protein solution and interacts with it.²⁹⁸ CaF_2 is a common crystal window material with limited application due to its spectral cut-off at 1100cm^{-1} . Most protein vibrations occur well above this cut-off, so the limit of CaF_2 is usually not a problem.

The most widely observed IR band is that of amide I ($\text{C}=\text{O}$), which occurs between 1600 and 1680cm^{-1} . Changes in intensity and location of this band indicate conformation changes in the $\text{C}=\text{O}$ bonds of the protein. Since proteins have many of these bonds, it is sometimes desirable to probe single groups in macromolecules, but this signal is very weak compared to the

background. Table III is a list of IR bands and the corresponding molecule vibrations that are of primary importance in analyzing IR spectra of proteins. There are methods available that aid in deconvoluting spectra that result in secondary structure information.^{298,306}

Table III. Important IR Bands in the Study of Biological Molecules²⁹⁸

Frequency (cm ⁻¹)	Group vibration	Biological molecule
3700–3100	O–H stretch	Very strong in IR; only usable with nonaqueous samples
3700–3100	N–H stretch	Not generally visible in aqueous solution
3200–2800	C–H stretch	Lipids, protein, DNA
2250	C≡N stretch	Ligand binding model, e.g. for O ₂
1750–1700	C=O stretch	COOH, esters, lipids
1680–1600	C=O stretch	Amide 1, proteins
1640	O–H bend	Can obscure C=O in H ₂ O; D ₂ O often used to avoid this
1610–1540	C–O asym. stretch	COO ⁻ , proteins, fatty acids
1580–1500	C–N stretch, N–H bend	Amide 2, proteins
1460–1400	C–O sym. stretch	COO ⁻ , proteins, fatty acids
1400–1350	CH ₂ wagging	Lipids
1250–1200	P=O asym. stretch	DNA, phospholipids
1150–1000	P=O sym. stretch	DNA, phospholipids

The early work on FTIR spectroscopy of proteins dealt with proteins of the blood in order to investigate the use of implants in the cardio-vascular system of animals and humans. It is imperative to understand how proteins react to a foreign surface in the blood for an implant to be successful. A pioneering study using IR by Morrissey and Stromberg examined the conformation changes of three proteins bound to silica as a function of adsorbed amount, time of adsorption, pH, and the ionic strength of the solution.³⁰⁷ The three proteins were BSA, prothromin and fibrinogen. The conformation of all three proteins was found to be independent of time of adsorption. However, the bound fraction of fibrinogen was found to increase

with increasing time suggesting the formation of aggregates.³⁰⁴ The effects of pH and ionic strength were not clearly identified.

The effects of the environment on the structure of various adsorbed proteins using FTIR was observed by Jakobsen and Wasacz.³⁰⁶ They assigned new values to the infrared vibrations of molecules in the protein backbone that were specific to aqueous environments. These assignments are related to the secondary structure with the changes in structure being determined as the environment of the proteins changed.³⁰⁶ The values that they assigned to the amide I, II, and III bands for each protein they studied were much more specific than those previously reported. For example, IgG, which they determined to be a “ β ” protein based on the amount of β -sheets present, was given an amide I value of 1637cm^{-1} , an amide II value of 1546cm^{-1} and an amide III value of 1235cm^{-1} (with $\pm 2\text{cm}^{-1}$ for error). For albumin, which was an “ α ” protein, the amide I value was 1656cm^{-1} , amide II was 1548cm^{-1} and amide III was 1298cm^{-1} .³⁰⁶ These values are surprisingly specific. As for their results, IgG and albumin behaved similarly in that neither protein exhibited a change in conformation with time adsorbed on a germanium surface. The environmental changes of IgG led to these conclusions. Varying the pH does not produce an α -helix structure, but does alter the β -sheet structure. Exposure to ethylene glycol produces a helical structure and also alters the β -sheet structure.³⁰⁶

The reaction of a globular protein to hydrophobic versus hydrophilic surfaces was observed using FTIR-ATR by Marsh *et al.*³⁴⁰ The fraction of the protein adsorbed to the surfaces is generally higher for hydrophobic surface than for hydrophilic surfaces. This proved that the lactoglobulin protein binds more quickly and with more affinity to hydrophobic surfaces.³⁴⁰

It was mentioned previously that FTIR spectroscopy of proteins in aqueous solutions poses some difficulties. More specifically, the amide I band is overlapped strongly by the water bending vibration. In replacing H_2O by D_2O , which resolves the overlap problem, the protein will alter conformation

due to the solution change. The spectral bands for the β -turns and random coil structures are difficult to find because of their low intensity.³³⁹ Regardless of these problems in FTIR-ATR of protein solutions, the information obtained can be valuable and unique. As is usually the case however, utilizing more than one method of characterization is the best solution to obtaining good information.

2.7. Chemical Force Microscopy

A specialized form of atomic force microscopy called chemical force microscopy (CFM) where the AFM tips are functionalized can be used to probe surfaces and biological molecules.²¹⁹ The most simple method of CFM is using a single molecule on the tip and interacting it with a plain surface. Then adding elements like surface treatments and sensing forces on a liquid covered surface increases the complexity.^{109,184,186,217,218,341-346} It has also been used to study receptor-ligand interactions, protein-protein interactions, molecule-cell interactions, cell-cell interactions, DNA interactions and to create force maps of surfaces.^{223,265,278,319,321,322,345,347-365} The chemical force microscopy setup is shown in Figure 2.7.1.

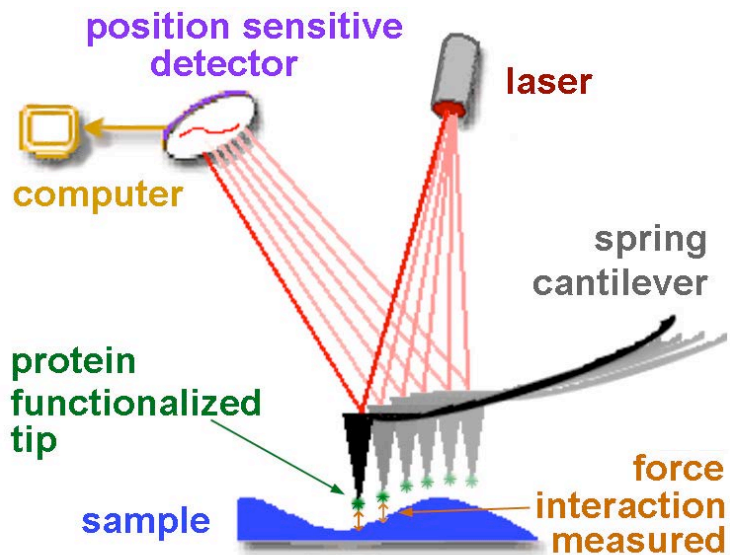


Figure 2.7.1. Basic function of a CFM setup.

One actually does not need a molecule on the end of a tip to measure a force-distance curve. The tip itself will have a force relationship with any surface. Figure 2.7.2 shows an example of a force-distance curve.²¹⁷ It is possible to image the surface and then examine the interaction forces in the exact same area. As the AFM tip approaches to the surface (section one in Figure 2.7.2), the cantilever will deflect from its equilibrium position. Attractive forces will bend the cantilever toward the sample.^{343,364} At distances greater than about 10nm, hydrophobic and electrostatic forces are dominant. Closer than 10nm, attractive van der Waals forces dominate. Once the tip becomes close enough to the surface (attractive forces overcome cantilever spring constant), the cantilever will jump to the surface and an immediate contact is formed. This distance is called the jump-to-contact point and is denoted as section two in Figure 2.7.2. The cantilever then begins to deflect further under an increasing force and this results in a linear response of the force-distance curve (section three in Figure 2.7.2). Once the tip begins to be retracted from the surface, the force on the cantilever decreases linearly. The cantilever will bend beyond the initial jump-to-contact point as the tip is adhered to the surface. This bending is shown as

section four in Figure 2.7.2. The tip eventually releases from the surface once the adhesion and capillary forces are overcome (section five of Figure 2.7.2). This regime is the pull-off point and is indicative of rupture forces in bonds. There will almost always be a hysteresis in the diagram due to the difference between the jump-to-contact and the pull-off force.³⁶⁴

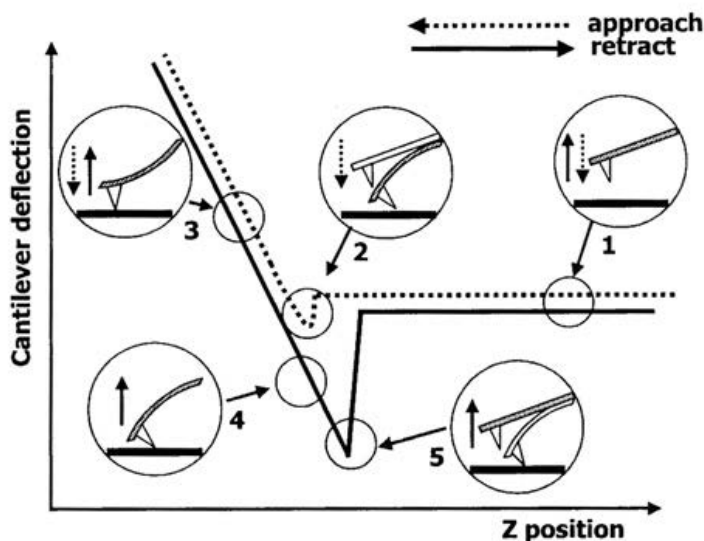


Figure 2.7.2. Example of a force-distance curve. (1) Approach of tip to surface. (2) Jump-to-contact point. (3) Linear cantilever deflection under increasing force. (4) Retraction leads to a negative deflection of the cantilever. (5) Pull-off point.²¹⁷

Force-distance curves should be obtained under a fluid environment whenever possible since capillary forces in air can be overwhelming.^{182,217,342} The analysis of a force-distance curve is accomplished by knowing the spring constant of the cantilever used. The simple relationship used to analyze the force on the cantilever is $F=-kz$, where k is the spring constant and z is the deflection of the cantilever. Therefore, by measuring the cantilever deflection (y-axis in Figure 2.7.2) one can calculate the force. The measurement of an array of force-distance curves is called force volume mapping and this requires a large time investment.^{365,366} Force mapping will produce a two-

dimensional map of specific molecular interaction sites. An actual map or image can then be produced displaying an adhesion force, for example, at each pixel point.³⁶⁵ So, one can imagine using a protein or even a simple functional group such as $-\text{COOH}$, to characterize an unknown surface. This would presume that the interaction forces are known by using the same functional tip on a surface of known interaction sites, such as a crystal.

There are many other types of force curves that can be obtained using various functionalities on the CFM tip. Eight examples are shown in Figure 2.7.3 along with the basic tip interactions and the equation used to analyze them.³⁴⁵ Any combination of these interactions can be present in a CFM experiment and deconvolution of these forces is imperative in order to understand the surface-tip relationship fully.

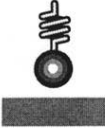
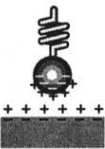
Approach		Retraction			
a van der Waals  $F(D) = \frac{AR}{12D^2}$	e Adhesion  $F = -3\pi R\gamma$				
b Electrostatic  $F(D) = \frac{4\pi R\lambda\sigma_R\sigma_S}{\epsilon} e^{-D/\lambda}$	f Capillary force  $F = 4\pi R\gamma_L \cos\theta$				
c Brush  $F(D) \approx \frac{50kT}{s^3} e^{-2\pi D/L}$ <p style="text-align: center;">$0.2 \leq D/2L \leq 0.9$</p>	g Polymer extension  $F(x) = \frac{kT}{a} L^* \left(\frac{x}{Na} \right)$				
d Elastic  $F(\delta) = \frac{4E\sqrt{R}}{3(1-\nu^2)} \delta^{3/2}$	h Binding  $F = \frac{U - kT \ln(\tau/\tau_0)}{\Lambda}$				
Definitions					
A	Hamaker constant	T	Absolute temperature	Λ	Characteristic length of bond
a	Monomer length	U	Bond energy	λ	Debye length of the medium
D	Probe-sample separation distance	x	Elongation of polymer	θ	Angle related to the geometry of the tip-sample contact
E	Elastic modulus	δ	Indentation depth	σ_R	Surface-charge density of sphere
k	Boltzmann's constant	ϵ	Dielectric of the medium	σ_S	Surface-charge density of sample
L	Brush thickness in a good solvent	γ	Surface energy between tip and sample	τ	Period over which the bond will rupture
L*	Inverse Langevin function	γ_L	Surface energy of the liquid	τ_0	Reciprocal of the natural bond frequency
N	Number of units in polymer	v	Poisson ratio		
R	Radius of probe sphere				
s	Mean distance between polymers				

Figure 2.7.3. Examples of CFM interactions and the force laws needed to interpret the corresponding curves.³⁴⁵

The strength of a covalent bond was measured using CFM by Grandbois *et al.*³⁶⁷ They anchored a polysaccharide molecule between a surface (with varying chemistries) and an AFM tip and then ruptured this bond. In doing so they found that the silicon-carbon bond ruptures at ~ 2.0 nN and the sulfur-gold bond ruptures at ~ 1.4 nN.³⁶⁷ Very weak interactions can also be studied by CFM. Forces as small as 1×10^{-11} N have been measured by

Hoh *et al.*³⁴⁶ This small interaction force was observed between a tip made of silicon nitride and a glass surface in water. Hoh *et al.* attribute this force to either hydrogen binding or ordering of water layers.³⁴⁶ A silanated silica surface was studied by Aston and Berg and they found that long-range attraction forces could be measured.³⁴¹ Electrostatic and hydrophobic forces were studied between a silica plate and sphere in aqueous fluid.³⁴¹

Single molecule force spectroscopy (SMFS), a part of CFM, utilizes individual molecules and includes studies of the conformation of proteins, polymers, DNA, and receptor-ligand systems.²¹⁷ The measurement of force-distance curves allows nanomechanical and nanoconformational properties of a molecule to be discovered. A single molecule called *Bombyx mori* Silk Fibroin was analyzed using CFM to determine its nanomechanics.³⁶² In an article by Bustamante *et al.* they describe the uses of the AFM/CFM in manipulating and studying these single molecule interactions in aqueous environments.³⁴⁴ IgG was successfully imaged and the biotin-avidin interaction using force-distance measurements were analyzed by Fritz *et al.*³⁵⁰ The interaction was performed using a biotin-functionalized tip and an avidin-functionalized glass surface in phosphate buffer solution. They observed an adhesion force for this system of 120pN. They also examined the interaction between a gold-coated AFM tip and a silanated glass surface in water. A considerable adhesion force of 2.5nN was measured for this system, which they attributed to the bond between gold and -SH groups on the surface, a hydrophobic (non-specific) interaction.³⁵⁰ Two relatively short review articles on CFM single molecule microscopy were written by Engel *et al.* and Radmacher.^{348,356} Three very involved articles outlining various intermolecular and intramolecular interactions as well as surface selection for imaging bio-molecules and force map generation were put forth by Yang and Shao, Zlatanova *et al.* and Willemsen *et al.*^{359,361,363}

In the article by Zlatanova *et al.* there is a very useful table of articles giving information on ligand-receptor pair interactions, specifically

streptavidin-biotin interactions.³⁶³ Some of the information in these articles is presented here. But first, a unique study of SEM on streptavidin functionalized CFM tips shows that there is a limit to the useful time of a tip such as this, but also that optimization of these tips is possible and necessary.³⁶⁸ Florin *et al.* utilized biotinylated bovine serum albumin (BSA) adsorbed on a tip, which was then incubated with avidin and interacted with biotinylated agarose beads. Only a limited number of pairs could interact and the force required to separate tip and bead was found to be ~ 160 pN.³⁴⁹ Lee *et al.* utilized biotinylated BSA adsorbed onto glass microspheres, which were then glued to cantilevers, and a mica surface incubated with streptavidin. The average interaction force observed for this system was ~ 340 pN.³⁵⁴ Moy *et al.*³⁵⁴ again used biotinylated BSA adsorbed onto a tip with a subsequent avidin and also streptavidin adsorption, and a biotin coated surface. The unbinding force for avidin-biotin was measured to be ~ 160 pN and the force for the streptavidin-biotin system was ~ 257 pN.³⁶⁹ Work by Wong *et al.* dealt with covalently functionalized carbon nanotubes to image patterned samples based on molecular interaction to measure the binding force between biotin and streptavidin. A rupture force of 200 pN was observed for this system.³⁷⁰ It is interesting to note that the forces mentioned are for a single interaction and oftentimes multiples of these forces were measured indicating multiple interactions.^{349,354,369,370} The work of Allen *et al.* on a biotinylated AFM probe and a streptavidin coated immunoassay well gave binding forces of ~ 300 pN.²⁶⁹ It is evident that the binding force for (strept)avidin-biotin is highly reproducible among various workers. Interaction between other systems such as *Escherichia coli*/anti-*E. coli* antibody and ICAM-1/LFA-1 have also been measured.^{358,360} The interaction of simple functional groups such as CH_3/CH_3 , CH_3/COOH and COOH/COOH has also been studied and may be the most informative of the studies since the molecules are simple and the interactions are limited.²¹⁹

2.8. Related Research

In 1966, Boehm published work concerning the functional groups on the surfaces of solids.⁷⁸ In it, he discusses surface compounds on carbon, silica, titania and alumina. He also briefly discusses crystalline surfaces and the meaning of a “clean” surface. He states that the surface of a crystalline material can be regarded as an extreme lattice defect and that the only forces acting on the surface are those holding the molecules together. The van der Waals forces on the surface can only form loose bonds with foreign atoms and thus only physisorption can occur.⁷⁸ He also says that the surface adsorption in amorphous solids is similar since the short-range order is similar to that in a crystal. “Clean” surfaces are rare since oxygen and water are constantly present in the atmosphere. Therefore, many surfaces are covered with surface oxides and hydroxides.⁷⁸ Boehm states that under “normal” conditions only two types of end groups are possible on the silica surface; siloxanes and silanols. The silanol groups are chemically reactive, weakly acidic, and can be titrated in NaCl with NaOH. All silanol groups are neutralized at pH 9, and further addition of NaOH will break siloxane bonds.⁷⁸ This titration can lead to determining the concentration of silanol groups on the surface as does reaction with thionyl chloride (SOCl_2). With the detection of the surface silanol groups came the conclusion that siloxane bonds must also be present on the surface because the values for silanol content were not sufficient to cover the entire surface. The heat treatment of silica, as already described, results in reversible hydroxylation (below 450°C) or complete irreversible rehydroxylation (between 800 and 1000°C) in water vapor. The 1000°C treated silica can regenerate silanol groups in an aqueous solution over several months. This difference is due to the siloxane groups formed. At low temperatures the siloxane group that is formed upon dehydroxylation is highly strained and so reintroducing water from the atmosphere will create a reaction forming silanols. However, for siloxanes

formed at high temperature, thermal energy allows siloxane rearrangement that reduces strain and promotes stability.⁷⁸

In 1986, Horbett and Brash compiled a review of proteins at interfaces including surface activity of proteins, states of adsorbed proteins, and competitive adsorption behavior of proteins.⁷ The molecular properties of proteins influence their surface activity and are summarized in Table IV. All of the items mentioned in Table IV are fundamentally linked to the protein's amino acid sequence.⁷ Therefore, differences in surface activity among proteins is due to the variation in their primary structure. Since proteins are thought to form multiple contact points upon adsorption, larger proteins may have an advantage over smaller ones for successful adsorption. Protein carbonyl groups contact silica surfaces upon adsorption.³⁰⁷ The bound fraction of peptide carbonyl groups, as determined from infrared frequency shifts, was found to be between 0.05 and 0.20.³⁰⁷ This corresponds to 77 contacts for an adsorbed albumin protein and 703 contacts for a bound fibrinogen protein.³⁰⁷ However, size is sometimes not the overriding factor since hemoglobin (65 kDa) is far more surface active than fibrinogen (330 kDa). Charged amino acids are present on the surface of proteins and so pH has a strong effect on activity. At interfaces with fixed ionic charges, the adsorption is strongly affected by the degree of opposite charge between protein and material and also by the amount of charged ions in the solution.⁷ Adsorption to charged materials is the basis for separation of proteins by ion exchange chromatography.

Table IV. Molecular Properties of Proteins that May Influence Surface Activity⁷

1. Size: Larger molecules may have more contact points.
2. Charge: Molecules nearer to their isoelectric pH may adsorb more easily.
3. Structure:
 - a. *Stability*: Less stable proteins may be more surface active.
 - b. *Unfolding rates*: More rapid unfolding may favor surface activity.
 - c. *Cross-linking*: Disulfide (-S-S-) bonds may reduce surface activity.
 - d. *Subunits*: More subunits may increase surface activity.
4. Other Chemical Properties:
 - a. *Amphipathicity*: Some proteins may have more of the types of side chains favored for bonding.
 - b. *Oiliness*: More hydrophobic proteins may be more surface active.
 - c. *Solubility*: Less soluble proteins may be more surface active.

It is thought that proteins may adsorb in multiple states and in various orientations.⁷ If the substrate sites are spread further than the molecular size of the protein, the proteins will not cover the surface completely. On the other hand, if the substrate sites are closer together than the size of the protein, the proteins may be forced to change their orientation, with some “lying down” and others “standing up”. Electrostatic repulsion may also play a role in the distribution of proteins on a surface. Highly charged proteins will have a tendency to spread out more than lightly charged proteins. A very important cause of orientation variability in regard to this work is the presence of multiple types of binding sites for the protein. Figure 2.8.1 shows various possibilities of protein binding orientations as caused by multiple binding sites. Certain sites may favor different amino acid residues located around the surface of the protein yielding various orientations of binding. Evidence supporting multiple states of protein

adsorption include results indicating weakly and tightly bound proteins.⁷ Some, but not all of the proteins can be removed by various treatments suggesting various binding strengths of different bonds.

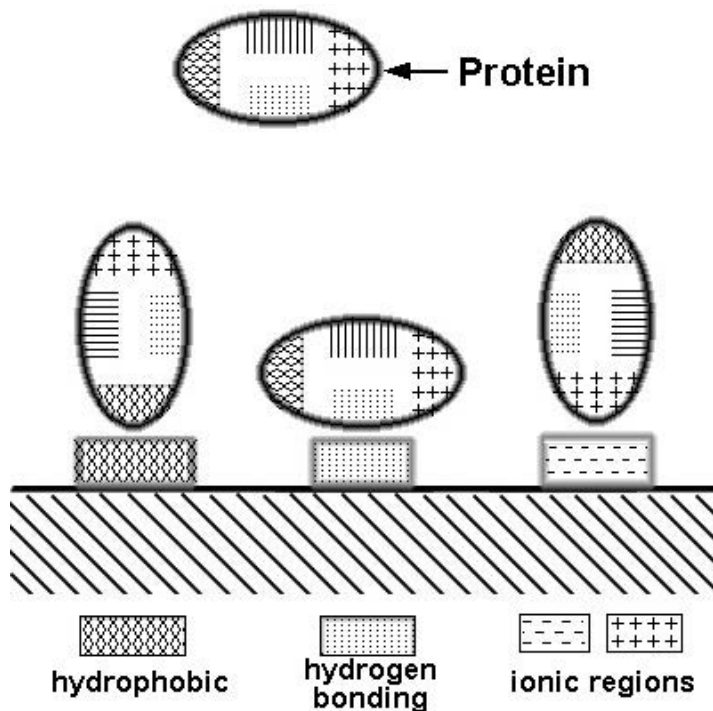


Figure 2.8.1. Multiple adsorbed orientations of a protein due to multiple binding sites.

Specific evidence for various states of adsorption was not mentioned in the review by Horbett and Brash but indirect evidence was suggested. The fraction of the peptide bound carbonyl groups involved in serum albumin binding to colloidal silica was measured by Morrissey and Stromberg.³⁰⁷ The IR band of bound carbonyl is different from unbound carbonyl and so can be measured directly. It was found that more carbonyl groups were bound when adsorption occurred from lower concentrations of protein in solution than higher concentrations. This observation implies that the fraction of protein that would interact with the silica depends on the area available to do so and that the proteins may adsorb in more than one way.⁷ Work on IgG on silica and silanized silica provided more evidence of multiple adsorbed states.³⁷¹

The desorption of IgG from silica, when it is allowed to dwell on the surface for less than 100 minutes, is linear with the square root of time. This suggests that a single state exists. However, after longer residence times (>1000 min), the desorption curves show two distinct regions. IgG desorption on silanized silica displays two regions as well at any protein residence times. This biphasic behavior suggests that the protein exists on the surface in two different states.³⁷¹ It was evident that allowing more time for the protein to bind or creating a hydrophobic surface converts the protein binding from one state to two.

Morrissey and Stromberg, in 1974, published a paper on the conformation of adsorbed blood proteins to Cab-o-Sil® fumed silica.³⁰⁷ They measured the carbonyl groups of adsorbed proteins, this fraction being referred to as the bound fraction. Serum albumin, prothrombin and fibrinogen were the proteins studied. For serum albumin and prothrombin, it was found that the internal bonding is sufficient to retain the native conformation of the proteins after adsorption to silica even when surface sites are highly available. The bound fraction for these two proteins was found to be 0.11 for the carbonyl groups at all values of surface population.³⁰⁷ The conformation of all three proteins was determined to be independent of the time allowed for adsorption.³⁰⁷

Proteins have been known to adsorb to surfaces in groups or islands with interspersed empty patches of surface.³⁷²⁻³⁷⁴ This island formation is direct evidence that proteins interact differently with different surfaces. Furthermore, the exterior proteins of the island most likely bind differently than the interior island proteins due to lack of nearest neighbor influences. It may also be that certain proteins adsorb to a surface individually while others prefer to adsorb in agglomerates.⁷

The mechanism by which proteins adsorb to porous glass membrane surfaces was evaluated in a study by Messing.³⁷⁵ The original intent of his work was to evaluate the possibility of using glass membranes with

controlled pore sizes to separate macromolecules according to their molecular size by dialysis. The glass studied was Corning code 7930 and he quickly found that a considerable amount of protein was taken out of solution by the glass membrane. Protein was removed from solution at a very high rate during the first 20 minutes of exposure to the membrane. After the first 20 minutes it was observed that the protein uptake was dependent on the size of the molecules and thus is diffusion controlled. The initial reaction was found to be related to the isoelectric pH of the protein and is quicker for proteins with high isoelectric points. These high i.e.p. proteins contain more reactive basic groups, such as NH_3^+ that suggests that the initial uptake of protein is accomplished through an ionic bond between the amine groups of the protein and the dissociated silanol (SiO^-) groups of the glass.³⁷⁵ However, strong acids or urea do not remove the protein alone. Urea in conjunction with acids must be used in the solution to successfully remove the tightly bound proteins, which suggests that hydrogen bonding is also active in the adherence of protein to glass as well as the ionic amine silicate bond. The acid in the solution most likely protonated the silanol group, releasing the protein amine, while the urea broke the hydrogen bonds between the protein and glass.³⁷⁵ Therefore, he concluded that the porous glass is not a good dialysis membrane for protein separation.

The two rates of protein uptake observed by Messing were dependent on the relative number of amines on the protein surface for the rapid initial reaction while the slow secondary reaction is dependent on the molecular weight of the protein. The initial reaction was found to be a function of the isoelectric pH of the protein, with the rate increasing with increasing i.e.p.. The second process was thus related to the permeability of the protein through the porous glass.³⁷⁶

Some of the most in-depth work on silica surfaces and biological reactions comes from research on silicosis and the possible carcinogenicity of vitreous silica and its crystalline counterparts.^{2,12,377} The generation of

reactive oxygen species by crystalline silica particles is well known.³⁷⁸ Reactive oxygen species (ROS) are; molecules like hydrogen peroxide (H_2O_2), ions like the hypochlorite ion (OCl^-), radicals like the hydroxyl radical ($^*\text{OH}$, it is the most reactive of them all and it differs from the hydroxyl ion), and the superoxide anion ($^*\text{O}_2^-$) which is both ion and radical. A radical (also called a "free radical") is a cluster of atoms, one of which contains an unpaired electron in its outermost shell of electrons. This is an extremely unstable configuration and radicals quickly react with other molecules or radicals to achieve the stable configuration of 4 pairs of electrons in their outermost shell (one pair for hydrogen). In biology, one of the insidious things about free radicals is that in interacting with other molecules to gain a stable configuration of electrons, they convert that target molecule into a radical. So a chain reaction begins that will propagate until two radicals meet each other and each contributes its unpaired electron to form a covalent bond linking the two.

The ability of quartz dusts to release ROS was examined in conjunction with its cytotoxicity and transforming potency on Syrian hamster embryo (SHE) cells.^{12,377} For one of the studies, Fubini *et al.* examined a single quartz dust that was treated with heat, iron and HF acid. The heat treatment transformed the quartz dust into cristobalite dust. The cristobalite dust was fully inert, meaning no cytotoxic effects, no transforming effects, and no free radical generation. Once this cristobalite is ground however, radicals are weakly generated and the dust has mild transforming potency.³⁷⁷ HF treatment of the quartz dust also decreases the transforming potency from the original quartz dust, while cytotoxicity is unaffected. When the surface iron content is reduced, the $^*\text{OH}$ yield and the cytotoxicity are both decreased, but the transforming potency is greatly decreased.³⁷⁷ It was concluded that silicon-based surface radicals and iron ions at the surface are both responsible for reactions that generate $^*\text{OH}$ upon contact with a cell. Cytotoxicity is dependent on the hydrophilicity and thus

the distribution of silanols on the surface. The variability of the cellular response is related to the state of the surface (number and type of active sites) rather than the structure of the bulk material.³⁷⁷ In a similar study, the pyrogenic amorphous silicas were found to have no cytotoxic or morphological transformation effects.¹²

Protein adsorption is interesting for a number of scientific and technical reasons and in particular any conformational changes undergone by the protein upon binding. These changes will determine the structure and behavior of the adsorbed layer and the new surface. Consider surfaces of hydrophobic and hydrophilic nature and a globular protein. It has been thought that proteins alter their conformations more on hydrophobic surfaces than hydrophilic ones in order for the protein's hydrophobic residues to be in contact with the surface's and thus satisfy both so that they need not be in contact with water.^{340,379-381} Interestingly, circular dichroism studies of protein conformation on hydrophobic and hydrophilic surfaces reveal that the ordered secondary structure of proteins are reduced once bound to hydrophilic surfaces, but increase once bound to hydrophobic surfaces.^{334,382} Evidence has also been found of a globular protein adopting a "squashed" state after adsorption to a hydrophobic surface and that the binding is stronger with a hydrophobic surface than a hydrophilic one.^{340,383} Also, protein layers are more strongly adsorbed to hydrophobic surfaces at longer times than at shorter times.³⁴⁰ The conformation of the adsorbed protein changes relatively slowly once adsorbed, which leads to a more tightly bound protein for both types of surfaces. However, the resulting conformation is very different between the two surfaces. It should be noted that the hydrophilic surface in the aforementioned study was an oxidized silicon wafer presenting a silanol surface and the hydrophobic surface was a silicon wafer coated with octadecyltrichlorosilane.³⁴⁰

An immunoassay is where a ligand is immobilized on a surface and the protein (or the molecule to assay for) binds to its ligand and is detected.

When using reflectometric interference spectroscopy (RifS) for detection, all proteins binding on a surface are measured, so it is important to eliminate non-specific binding of proteins. In a study by Piehler *et al.* glass surfaces were modified with an amino-functionalized silane followed by various hydrophilic polymers being coupled to the surface.³⁸⁴ The functional groups of the polymers bound to the ligand a-hapten through carbodiimide-activated coupling. The polymer layers allowed for specific binding of antibodies to the surface.³⁸⁴ Thus, the non-specific adsorption of proteins was reduced significantly. It was determined that the polymer aminodextran (AMD) gave the best results in terms of reduced non-specific binding and increased specific adsorption over a silanized surface.³⁸⁴

Engineered proteins were used in a study to demonstrate that protein adsorption to functional surfaces involves multiple interactions between a single protein and specific binding “sites” distributed on the surface.³⁸⁵⁻³⁸⁷ This multi-point interaction will govern the protein binding affinity since it is sensitive to the arrangement of surface binding sites. This type of binding will result in heterogeneous coverage because a protein will show the highest affinity for surface arrangements that best match its own distribution of functional groups.³⁸⁵⁻³⁸⁷ The heterogeneous coverage results because these functional groups are usually randomly dispersed on an amorphous surface, but can also be regularly dispersed on a crystalline surface, which causes homogeneous protein binding. Lateral interactions between the adsorbed protein molecules must also be taken into consideration, as they will affect the protein distribution as well.³⁸⁸

Porous silicas with large surface areas and controllable pore diameters are inviting candidates to host large molecules such as proteins.³⁸⁹ The encapsulation of proteins in sol-gels has a possible use in biosensor applications. It is feasible to design the characteristics such as pore size and charge of silica foams to match specific proteins. The charge is altered by derivatizing the surface silanol groups with functional organic silanes.³⁸⁹

Patterning of functional antibodies on substrates is also beneficial for sensors. Mooney *et al.* created a highly layered two dimensional pattern of proteins on a glass substrate.³⁹⁰ They coated silica with an alkyl silane, which can be selectively removed with UV photolithography. The silane adsorbs a monolayer of bovine serum albumin (BSA) while the silica adsorbs less than 2% of BSA. Biotin is then bound to the BSA pattern and streptavidin is further adsorbed to the biotin layer. Streptavidin will then bind any other biotinylated species. In their study, fluorescently labeled biotinylated mouse IgG was selectively bound to the pattern.³⁹⁰ A study on patterned glass surfaces having an effect on the direction of cell adhesion and outgrowth was conducted by Saneinejad and Shoichet.³⁹¹ They created glass surfaces with areas of peptide functionality and areas of polyethylene glycol (PEG). Hippocampal neurons adhered preferentially to the peptide-functionalized surfaces over the PEG areas. Neurite outgrowth was then limited to the peptide region demonstrating that cell growth can be directed. This research is very important for the regeneration of the nervous system.³⁹¹

DNA biosensors also utilize immobilized oligonucleotides on glass surfaces. Lu *et al.* have created an oligonucleotide hybridized probe on an optical fiber surface.²⁶⁸ Streptavidin was covalently linked to the core surface of the optical fiber and a thin layer of biotinylated oligonucleotide probes was then adsorbed to the streptavidin.²⁶⁸ Next, fluorescein labeled oligonucleotides were introduced to the fiber for hybridization. The fluorescence of the molecules was excited with a specific wavelength and the evanescent wave of the emission enters into the fiber, which then propagates down the fiber for detection.²⁶⁸ Since the evanescent wave detection method will only take into account bound proteins, it achieves a high signal to noise ratio.

A Ukrainian research group has done many studies on the adsorption of proteins to silicas, mostly fumed silica.^{249,254} Fumed silica synthesized at high temperatures form aggregates by siloxane bonds and agglomerations are

formed through hydrogen bonding. These agglomerates can be partially broken up in an aqueous solution due to interactions of water molecules with the hydrophilic silica surface. Fumed silica in solution has a high affinity for proteins and their interaction can change both the electrical double layer around the particles and the protein conformation. The interaction between silica and proteins occurs through hydrogen bonds using $\equiv\text{SiOH}$ groups and interfacial water. So at certain pHs, the H^+ transfer between the silica and the protein is key.²⁷ Protein bonding to oxide surfaces occurs by flocculation with formation of bridges between protein and silica and possible H^+ transfers between them. Protein adsorption can occur on both hydrophilic and hydrophobic surfaces. The adsorption to a hydrophilic surface is highly reversible, but requires the cleavage of all adsorption bonds simultaneously, since there are most likely more than one interaction between protein and silica. Binding to a hydrophobic material is slightly more complicated and proteins typically change their conformation on these surfaces. The interaction of hydrophobic groups on the protein with hydrophobic groups on the modified silica surface is thermodynamically preferred.²⁴⁹ Therefore, the rearrangement of the protein conformation sometimes occurs in order to expose the hydrophobic sites to the silica surface.

Since the silica surface is negatively charged at pHs greater than 2.2, there are strong electrostatic interactions between the silica and the positively charged groups of proteins (RNH^+).²⁴⁹ NMR data has shown that the interaction of proteins with the silica particles leads to a decrease in the average thickness of the hydrate layers of silica and protein molecules. The flocculation of the silica particles in aqueous solution, as well as the flocculation of the protein molecules, is caused by the strong interaction of the RNH^+ amino groups and the SiO^- . Multicentered adsorption complexes are formed, which become more stable in water with increasing size of the proteins.²⁴⁹

Gun'ko *et al.* found that protein molecules adsorbed on fumed silica aggregates form hydrogen bonds with $\equiv\text{Si-OH}$ or $\equiv\text{SiO}^-$ groups by amino groups of the protein.^{249,254} This binding occurs via hydrogen bonds. Since hydrogen bonding is responsible for the adsorption with the participation of $\equiv\text{Si-OH}$ groups and interfacial water, varying the pH will greatly effect the binding capability as H^+ transfer between surfaces and molecules play an important role.²⁴⁹ In addition, the formation of a few adsorption (hydrogen) bonds causes irreversible adsorption due to the small probability of breaking all bonds simultaneously. The interaction cross-section area of protein molecules with a surface upon adsorption have been known to reach several nm^2 for BSA or HSA.²⁵⁴ A maximum adsorption of BSA and HSA to an oxide surface was observed at a pH close to their isoelectric points (~ 6), when the molecules have the smallest cross-sectional area.^{27,254} There is a change in the protein conformation with a change in pH. If the protein becomes unfolded, there may be more protein-protein interactions, which will affect the protein-surface interactions.^{7,254} It is clear that pH plays a significant role in protein adsorption phenomena. The exact interaction of a protein with a silica surface is most likely due to hydrogen bonding between surface amines and silanols, but there is a possibility of other reactions as well.

2.9 References

1. A. Jedlicka, "Compositional Dependence of in Vitro Response to Commercial Silicate Glasses"; Ph.D. Thesis, Alfred University, Alfred, NY, 1998.
2. M. Ding, F. Chen, X. Shi, B. Yucesoy, B. Mossman, and V. Vallyathan, "Diseases Caused by Silica: Mechanisms of Injury and Disease Development," *Int. Immunopharmacol.*, **2** [2-3] 173-82 (2002).
3. J. C. Barrett, "Cellular and Molecular Mechanisms of Asbestos Carcinogenicity: Implications for Biopersistence," *Environ. Health Perspect.*, **102** [Suppl. 5] 19-23 (1994).
4. "How Safe is Fiber Glass?" *Glass Ind.*, **69** [6] 17-8 (1988).
5. M. F. Ottaviani, M. Tomatis, and B. Fubini, "Surface Properties of Vitreous Fibers," *J. Colloid Interface Sci.*, **224** [1] 169-78 (2000).
6. R. E. Baier and R. C. Dutton, "Initial Events in Interactions of Blood with a Foreign Surface," *J. Biomed. Mater. Res.*, **3** [1] 191-206 (1969).
7. T. A. Horbett and J. L. Brash, *Proteins at Interfaces: Current Issues and Future Prospects*, Vol. 343; pp. 1-33. Edited by J. L. Brash and T. A. Horbett. American Chemical Society, Washington, DC, 1987.
8. W. Norde, "Driving Forces for Protein Adsorption at Solid Surfaces," *Macromol. Symp.*, **103** [1] 5-18 (1996).
9. Y. Takami, S. Yamane, K. Makinouchi, G. Otsuka, J. Glueck, R. Benkowski, and Y. Nose, "Protein Adsorption onto Ceramic Surfaces," *J. Biomed. Mater. Res.*, **40** [1] 24-30 (1998).
10. J. Mei, R. L. Sammons, R. M. Shelton, and P. M. Marquis, *The Influence of Proteins on the Surface Modification of Calcium Phosphate Compounds During Immersion in Simulated Body Fluids*, Vol. 6; pp. 67-72. Edited by P. Ducheyne and D. Christiansen. Butterworth-Heinemann, Philadelphia, 1993.

11. T. A. Horbett, B. D. Ratner, J. M. Schakenraad, and F. J. Schoen, "Some Background Concepts," Ch. 3 in *Biomaterials Science - An Introduction to Materials in Medicine*. Edited by B. D. Ratner, A. S. Hoffman, F. J. Schoen, and J. E. Lemons. Academic Press, San Diego, CA, 1996.
12. Z. Elias, O. Poirot, M. C. Daniere, F. Terzetti, A. M. Marande, S. Dawigaj, H. Pezerat, I. Fenoglio, and B. Fubini, "Cytotoxic and Transforming Effects of Silica Particles with Different Surface Properties in Syrian Hamster Embryo (SHE) Cells," *Toxicol. Vitro*, **14** [5] 409-22 (2000).
13. R. S. Pandurangi, M. S. Seehra, B. L. Razzaboni, and P. Bolsaitis, "Surface and Bulk Infrared Modes of Crystalline and Amorphous Silica particles: A Study of the Relation of Surface Structure to Cytotoxicity of Respirable Silica," *Environ. Health Perspect.*, **86** 327-36 (1990).
14. R. P. Nolan, A. M. Langer, and K. W. Foster, "Particle Size and Chemically-Induced Variability in the Memolytic Activity of Quartz: Preliminary Observations," pp. 39-50 in *In Vitro Effects of Mineral Dusts*. Edited by E. G. Beck and J. Bignon. Springer-Verlag, Berlin, Germany, 1985.
15. D. R. Hemenway, M. Absher, M. Landesman, L. Trombley, and R. J. Emerson, "Differential Lung Response Following Silicon Dioxide Polymorph Aerosol Exposure," pp. 106-15 in *Silica, Silicosis and Cancer*. Edited by D. F. Goldsmith, D. M. Win, and C. M. Shy. Praeger, New York, 1986.
16. X. Shi, N. S. Dalal, X. N. Hu, and V. Vallyathan, "The Chemical Properties of Silica Particle Surface in Relation to Silica-Cell Interactions," *J. Toxicol. Environ. Health*, **27** [4] 435-54 (1989).
17. A. K. Varshneya, *Fundamentals of Inorganic Glasses*. Academic Press, San Diego, CA, 1994.
18. F. Machatschki, "Kristallstruktur von Tiefquarz," *Fortschr. Mineral.*, **20** 45-57 (1936).
19. R. W. G. Wyckoff, "Kriterien fuer Hexagonale Raumgruppen und die Kristallstruktur von beta Quarz," *Z. Kristallogr.*, **26** 507-37 (1926).
20. R. Jenkins and R. L. Snyder, *Introduction to X-ray Powder Diffraction*; pp. 23-6. John Wiley & Sons, New York, 1996.

21. A. C. Wright, G. A. N. Connell, and J. W. Allen, "Amorphography and the Modelling of Amorphous Solid Structures by Geometric Transformations," *J. Non-Cryst. Solids*, **42** 69-86 (1980).
22. R. L. Mozzi and B. E. Warren, "The Structure of Vitreous Silica," *J. Appl. Crystallogr.*, **2** [4] 164-72 (1969).
23. A. C. Wright, A. G. Clare, D. I. Grimley, and R. N. Sinclair, "Neutron Scattering Studies of Network Glasses," *J. Non-Cryst. Solids*, **112** [1-3] 33-47 (1989).
24. W. C. Bauer and J. E. Bailey, "Raw Materials/Batching," pp. 378-85 in Engineered Materials Handbook, Vol. 4, *Ceramics and Glasses*. Edited by S. J. Schneider, Jr., J. R. Davis, G. M. Davidson, S. R. Lampman, M. S. Woods, and T. B. Zorc. ASM International, Materials Park, OH, 2000.
25. D. Barby, "Silicas," Ch. 8 in *Characterization of Powder Surfaces*. Edited by G. D. Parfitt and K. S. W. Sing. Academic Press, London, England, 1976.
26. R. K. Iler, *The Colloidal Chemistry of Silica and Silicates*. Cornell University Press, Ithaca, NY, 1955.
27. R. K. Iler, *The Chemistry of Silica*. John Wiley & Sons, New York, 1979.
28. C. J. Brinker and G. W. Scherer, *Sol-Gel Science*. Academic Press, New York, 1990.
29. R. D. Shoup, "Sol-Gel Processes," pp. 446-52 in Engineered Materials Handbook, Vol. 4, *Ceramics and Glasses*. Edited by S. J. Schneider, Jr., J. R. Davis, G. M. Davidson, S. R. Lampman, M. S. Woods, and T. B. Zorc. ASM International, Materials Park, OH, 2000.
30. S. S. Kistler, "Coherent Expanded Aerogels," *J. Phys. Chem.*, **36** [1] 52-64 (1932).
31. W. Stober, A. Fink, and E. Bohn, "Controlled Growth of Monodisperse Silica Spheres in the Micron Size Range," *J. Colloid Interface Sci.*, **26** [1] 62-9 (1968).

32. R. Janzen, K. K. Unger, H. Giesche, J. N. Kinkel, and M. T. W. Hearn, "Evaluation of Advanced Silica Packings for the Separation of Biopolymers by High-Performance Liquid Chromatography V. Performance of Non-Porous Monodisperse 1.5 micron Bonded Silicas in the Separation of Proteins by Hydrophobic-inter-action Chromatography," *J. Chromatogr.*, **397** 91-7 (1987).
33. K. K. Unger, B. Anspach, and H. Giesche, "Optimum Support Properties for Protein Separations by High-Performance Size Exclusion Chromatography," *J. Pharm. Biomed. Anal.*, **2** [2] 139-51 (1984).
34. K. K. Unger, G. Jilge, R. Janzen, H. Giesche, and J. N. Kinkel, "Non-Porous Microparticulate Supports in High-Performance Liquid Chromatography (HPLC) of Biopolymers - Concepts, Realization and Prospects," *Chromatographia*, **22** [7-12] 379-80 (1986).
35. K. K. Unger, J. N. Kinkel, B. Anspach, and H. Giesche, "Evaluation of Advanced Silica Packings for the Separation of Biopolymers by High-Performance Liquid Chromatography I. Design and Properties of Parent Silicas," *J. Chromatogr.*, **296** 3-14 (1984).
36. G. Jilge, R. Janzen, H. Giesche, K. K. Unger, J. N. Kinkel, and M. T. W. Hearn, "Evaluation of Advanced Silica Packings for the Separation of Biopolymers by High-Performance Liquid Chromatography III. Retention and Selectivity of Proteins and Peptides in Gradient Elution on Non-Porous Monodisperse 1.5-micron Reversed-Phase Silicas," *J. Chromatogr.*, **397** 71-80 (1987).
37. H. Giesche, "Synthesis of Monodispersed Silica Powders I. Particle Properties and Reaction Kinetics," *J. Eur. Ceram. Soc.*, **14** [3] 189-204 (1994).
38. H. Giesche, "Synthesis of Monodispersed Silica Powders II. Controlled Growth Reaction and Continuous Production Process," *J. Eur. Ceram. Soc.*, **14** [3] 205-14 (1994).
39. C. G. Pantano, "What Do We Know about Glass Surfaces?" *Ceram. Eng. Sci. Proc.*, **22** [1] 137-48 (2001).
40. F. E. Woolley, "Melting/Fining," pp. 386-93 6 in Engineered Materials Handbook, Vol. 4, *Ceramics and Glasses*. Edited by S. J. Schneider, Jr., J. R. Davis, G. M. Davidson, S. R. Lampman, M. S. Woods, and T. B. Zorc. ASM International, Materials Park, OH, 2000.

41. M. E. Schlesinger, "Melting Points, Crystallographic Transformation, and Thermodynamic Values," pp. 883-91 in *Engineered Materials Handbook, Vol. 4, Ceramics and Glasses*. Edited by S. J. Schneider, Jr., J. R. Davis, G. M. Davidson, S. R. Lampman, M. S. Woods, and T. B. Zorc. ASM International, Materials Park, OH, 2000.
42. H. J. Stevens, "Forming," pp. 394-401 in *Engineered Materials Handbook, Vol. 4, Ceramics and Glasses*. Edited by S. J. Schneider, Jr., J. R. Davis, G. M. Davidson, S. R. Lampman, M. S. Woods, and T. B. Zorc. ASM International, Materials Park, OH, 2000.
43. R. Mace, "Surface Quality - Fused Quartz," PowerPoint presentation, GE Quartz, Willoughby, OH, 2003, (unpublished).
44. F. V. Tooley, "Fiberglass," pp. 402-8 in *Engineered Materials Handbook, Vol. 4, Ceramics and Glasses*. Edited by S. J. Schneider, Jr., J. R. Davis, G. M. Davidson, S. R. Lampman, M. S. Woods, and T. B. Zorc. ASM International, Materials Park, OH, 2000.
45. J. F. Stroman, "Optical Fibers," pp. 409-17 in *Engineered Materials Handbook, Vol. 4, Ceramics and Glasses*. Edited by S. J. Schneider, Jr., J. R. Davis, G. M. Davidson, S. R. Lampman, M. S. Woods, and T. B. Zorc. ASM International, Materials Park, OH, 2000.
46. N. P. Mellott, S. L. Brantley, J. P. Hamilton, and C. G. Pantano, "Evaluation of Surface Preparation Methods for Glass," *Surf. Interface Anal.*, **31** [5] 362-268 (2001).
47. J. J. Cras, C. A. Rowe-Taitt, D. A. Nivens, and F. S. Ligler, "Comparison of Chemical Cleaning Methods of Glass in Preparation for Silanization," *Biosens. Bioelectron.*, **14** [8-9] 683-8 (1999).
48. J. G. Couillard, D. G. Ast, C. Umbach, J. M. Blakely, C. B. Moore, and F. P. Fehlner, "Chemical Treatment of Glass Substrates," *J. Non-Cryst. Solids*, **222** 429-34 (1997).
49. P. Van Der Voort and E. F. Vansant, "Silylation of the Silica Surface. A Review," *J. Liq. Chromatogr. Relat. Technol.*, **19** [17&18] 2723-52 (1996).
50. L. Zeng, V. L. Lou, M. Tomozawa, and J. Hong, "Removal of Hydroxyl and Hydride in Silica Glass at High Temperature," *Fall Meeting of the Glass and Optical Materials Division*, poster, 2002 (unpublished).

51. V. Tomao, A. M. Siouffi, and R. Denoyel, "Influence of Time and Temperature of Hydrothermal Treatment on Glass Fibers Surface," *J. Chromatogr., A*, **829** [1-2] 367-76 (1998).
52. J.-F. Poggemann, A. Goss, G. Heide, E. Radlein, and G. H. Frischat, "Direct View of the Structure of a Silica Glass Fracture Surface," *J. Non-Cryst. Solids*, **281** [1-3] 221-6 (2001).
53. V. I. Lygin, "The Structure of the Silica Surface and Its Modification by Thermal Treatment," *Kinet. Catal.*, **35** [4] 480-6 (1994).
54. D. H. Lee and R. A. Condrate, Sr., "FTIR Spectral Characterization of Thin Film Coatings of Oleic Acid on Glasses: I. Coatings on Glasses from Ethyl Alcohol," *J. Mater. Sci.*, **34** [1] 139-46 (1999).
55. N. Kuzuu, J. W. Foley, and N. Kamisugi, "Structural Change in the Near-Surface of a Silica Glass Block by Heat Treatment," *J. Ceram. Soc. Jpn.*, **106** [5] 525-7 (1998).
56. P. Kruger, R. Knes, and J. Friedrich, "Surface Cleaning by Plasma-Enhanced Desorption of Contaminants (PEDC)," *Surf. Coat. Technol.*, **112** [1-3] 240-4 (1999).
57. V. Krishnamurthy and I. L. Kamel, "Argon Plasma Treatment of Glass Surfaces," *J. Mater. Sci.*, **24** [9] 2245-3352 (1989).
58. E. O. Filatova and A. S. Shulakov, "Glass Surface Atomic Structure after Technological Treatments," *J. Colloid Interface Sci.*, **169** [2] 361-4 (1995).
59. A. S. D'Souza, S. Liephart, and C. G. Pantano, "RF-Plasma Treatments of Surface-Conductive Alkali-Lead Silicate Glass and Microchannel Plate Devices," *Appl. Surf. Sci.*, **148** [1-2] 126-32 (1999).
60. A. S. D'Souza and C. G. Pantano, "Mechanisms for Silanol Formation on Amorphous Silica Fracture Surfaces," *J. Am. Ceram. Soc.*, **82** [5] 1289-93 (1999).
61. H. D. Bijsterbosch, M. A. Cohen Stuart, G. J. Fleer, P. van Caeter, and E. J. Goethals, "Nonselective Adsorption of Block Copolymers and the Effect of Block Incompatibility," *Macromolecules*, **31** [21] 7436-44 (1998).

62. V. A. Bakaev, W. A. Steele, T. I. Bakaeva, and C. G. Pantano, "Adsorption of CO₂ and Ar on Glass Surfaces. Computer Simulation and Experimental Study," *J. Chem. Phys.*, **111** [21] 9813-21 (1999).
63. W. A. Weyl, *Some Practical Aspects of the Surface Chemistry of Glass*. 1947 (also published in *Glass Industry*, **28**).
64. P. F. Kane and G. B. Larrabee, *Characterization of Solid Surfaces*. Plenum Press, New York, 1974.
65. F. Haber and F. Kerschbaum, "The Measurement of Low Pressures with a Vibrating Quartz Fiber. (Determination of the Vapor Pressures of Mercury and Iodine.)," *Z. Elektrochem.*, **20** 296-305 (1914).
66. P. C. Carman, "Constitution of Colloidal Silica," *Trans. Faraday Soc.*, **36** 964-73 (1940).
67. A. V. Kiselev, "The Structure of Silicic Acid Gels," *Kolloidn. Zh.*, **2** 17-26 (1936).
68. J. Casanovas, G. Pacchioni, and F. Illas, "²⁹Si Solid State NMR of Hydroxyl Groups in Silica from First Principle Calculations," *Mater. Sci. Eng.*, **B68** [1] 16-21 (1999).
69. M. L. Hair, "Hydroxyl Groups on Silica Surface," *J. Non-Cryst. Solids*, **19** 299-309 (1975).
70. M. M. Branda, R. A. Montani, and N. J. Castellani, "The Distribution of Silanols on the Amorphous Silica Surface: A Monte Carlo Simulation," *Surf. Sci.*, **446** [1-2] L89-L94 (2000).
71. L. T. Zhuravlev, "The Surface Chemistry of Amorphous Silica. Zhuravlev Model," *Colloids Surf., A*, **173** [1-3] 1-38 (2000).
72. T. Takei, K. Kato, A. Meguro, and M. Chikazawa, "Infrared Spectra of Geminal and Novel Triple Hydroxyl Groups on Silica Surface," *Colloids Surf., A*, **150** [1-3] 77-84 (1999).
73. L. D. Belyakova, O. M. Dzhigit, A. V. Kiselev, G. G. Muttk, and K. D. Shcherbakova, "Reply to the Article by V.F. Kiselev and K.G. Krasil'nikov: 'The Absolute Adsorptive Properties of Silica and Silicate Surfaces'," *Russ. J. Phys. Chem.*, **33** 551-4 (1959).

74. A. S. D'Souza, C. G. Pantano, and K. M. R. Kallury, "Determination of the Surface Silanol Concentration of Amorphous Silica Surface Using Static Secondary Ion Mass Spectroscopy," *J. Vac. Sci. Technol., A*, **15** [3] 526-31 (1997).
75. B. J. Wood, R. N. Lamb, and C. L. Raston, "Static SIMS Study of Hydroxylation of Low-Surface-Area Silica," *Surf. Interface Anal.*, **23** [9] 680-8 (1995).
76. Y. Hayashi and K. Matsumoto, "Determination of Surface Silanol Group on Silicate Glasses Using Static SIMS," *J. Ceram. Soc. Jpn.*, **100** [8] 1038-41 (1992).
77. T. A. Dang and R. Gnanasekaran, "Determination of Amino and Silanol Functional Groups on Glass via Chemical Derivatization and ESCA," *Surf. Interface Anal.*, **18** [2] 113-8 (1990).
78. H.-P. Boehm, "Functional Groups on the Surfaces of Solids," *Angew. Chem., Int. Ed.*, **5** [6] 533-44 (1966).
79. M. L. Hair, *Infrared Spectroscopy in Surface Chemistry*. Marcel Dekker, New York, 1967.
80. C. Okkerse, "Porous Silica," Ch. 5 in *Physical and Chemical Aspects of Adsorbents and Catalysts*. Edited by B. G. Linsen. Academic Press, London, England, 1970.
81. V. Y. Davydov, A. V. Kiselev, and L. T. Zhuravlev, "Study of the Surface and Bulk Hydroxyl Groups of Silica by Infra-red Spectra and D₂O Exchange," *Trans. Faraday Soc.*, **60** [12] 2254-64 (1964).
82. B. A. Morrow and A. J. McFarlan, "Chemical Reactions at Silica Surfaces," *J. Non-Cryst. Solids*, **120** 61-71 (1990).
83. K. Yoshinaga, M. Rikitake, T. Kito, Y. Yamamoto, H. Eguchi, and M. Komatsu, "A Convenient Determination of Surface Hydroxyl Group on Silica Gel by FT-IR Spectroscopy," *Chem. Lett.*, **5** [11] 1129-32 (1991).
84. Y. Duval, J. A. Mielczarski, O. S. Pokrovsky, E. Mielczarski, and J. J. Ehrhardt, "Evidence of the Existence of Three Types of Species at the Quartz-Aqueous Solution Interface at pH 0-10: XPS Surface Group Quantification and Surface Complexation Modeling," *J. Phys. Chem. B*, **106** [11] 2937-45 (2002).

85. S. Takeda, K. Yamamoto, Y. Hayasaka, and K. Matsumoto, "Surface OH Group Governing Wettability of Commercial Glasses," *J. Non-Cryst. Solids*, **249** [1] 41-6 (1999).
86. K. R. Lange, "The Characterization of Molecular Water on Silica Surfaces," *J. Colloid Sci.*, **20** [3] 231-40 (1965).
87. J. H. de Boer and J. M. Vleeskens "Surface Hydroxyls on Amorphous Silica," *Proc. K. Ned. Wet., Ser. B: Phys. Sci.*, **B60** [23] 45-54 (1957).
88. G. J. Young and T. P. Bursh, "Immersion Calorimetry Studies of the Interaction of Water with Silica Surfaces," *J. Colloid Sci.*, **15** [4] 361-9 (1960).
89. V. V. Turov and I. F. Mironyuk, "Adsorption Layers of Water on the Surface of Hydrophilic, Hydrophobic and Mixed Silicas," *Colloids Surf., A*, **134** [3] 257-63 (1998).
90. A. V. Kiselev and V. I. Lygin, "Supplement to Chapter 10. Surface Hydroxyl Groups and Their Perturbance by Adsorbed Molecules," pp. 274-95 in *Infrared Spectra of Adsorbed Species*. Edited by L. H. Little. Academic Press, New York, 1966.
91. L. T. Zhuravlev, "Concentration of Hydroxyl Groups on the Surface of Amorphous Silicas," *Langmuir*, **3** [3] 316-8 (1987).
92. V. V. Yaminsky, B. W. Ninham, and R. M. Pashley, "Interaction Between Surfaces of Fused Silica in Water. Evidence of Cold Fusion and Effects of Cold Plasma Treatment," *Langmuir*, **14** [12] 3223-35 (1998).
93. V. V. Yaminsky and E. A. Vogler, "Hydrophobic Hydration," *Curr. Opin. Colloid Interface Sci.*, **61** [4] 342-9 (2001).
94. L. T. Zhuravlev and A. V. Kiselev, "Surface Concentration of Hydroxyl Groups on Amorphous Silicas Having Different Specific Surface Areas," pp. 155-60 in *Surface Area Determination*. Edited by D. H. Everett and R. H. Ottewill. Butterworth & Co., London, England, 1970.
95. J. S. Reed, *Principles of Ceramic Processing*, 2nd ed.; p. 70. John Wiley & Sons, New York, 1995.

96. M.-A. Einarsrud, L. Rormark, S. Haereid, and T. Grande, "Effect of Microstructure on Thermal Dehydroxylation of Silica Gels," *J. Non-Cryst. Solids*, **211** [1-2] 49-55 (1997).
97. P. B. Wagh and S. V. Ingale, "Comparison of Some Physico-Chemical Properties of Hydrophilic and Hydrophobic Silica Aerogels," *Ceram. Int.*, **28** [1] 43-50 (2002).
98. J. E. Shelby, W. C. LaCourse, and A. G. Clare, "Engineering Properties of Oxide Glasses and Other Inorganic Glasses," pp. 845-57 in *Engineered Materials Handbook, Vol. 4, Ceramics and Glasses*. Edited by S. J. Schneider, Jr., J. R. Davis, G. M. Davidson, S. R. Lampman, M. S. Woods, and T. B. Zorc. ASM International, Materials Park, OH, 2000.
99. L. M. Cook, "Chemical Processes in Glass Polishing," *J. Non-Cryst. Solids*, **120** [1-3] 152-71 (1990).
100. D. B. Shukla, P. M. Oza, and V. P. Pandya, "Studies of Surface Chemistry - Physico-Chemical Aspects of Porous Silicate Surfaces," *Powder Technol.*, **47** [3] 233-8 (1986).
101. G. M. Nishioka and J. A. Schramke, "Thermodesorption of Water from Silicate Surfaces," *J. Colloid Interface Sci.*, **105** [1] 102-11 (1985).
102. R. H. Doremus, "The Diffusion of Water in Fused Silica," pp. 667-71 in *Reactivity in Solids*. Edited by J. W. Mitchell, R. C. DeVries, R. W. Roberts, and P. Cannon. Wiley-Interscience, New York, 1969.
103. K. M. Davis and M. Tomozawa, "Water Diffusion into Silica Glass: Structural Changes in Silica Glass and Their Effect on Water Solubility and Diffusivity," *J. Non-Cryst. Solids*, **185** [3] 203-20 (1995).
104. M. Tomozawa, D. Kim, A. Agarwal, and K. M. Davis, "Water Diffusion and Surface Structural Relaxation of Silica Glasses," *J. Non-Cryst. Solids*, **288** [1-3] 73-80 (2001).
105. B. H. Reader and H. G. Scafer, Jr., "Grind/Polish," pp. 464-70 in *Engineered Materials Handbook, Vol. 4, Ceramics and Glasses*. Edited by S. J. Schneider, Jr., J. R. Davis, G. M. Davidson, S. R. Lampman, M. S. Woods, and T. B. Zorc. ASM International, Materials Park, OH, 2000.

106. P. B. Adams, "Clean Glass: ASTM Standard Methods," *J. Non-Cryst. Solids*, **19** 275-6 (1975).
107. "Standard Practice for Designing a Process for Cleaning Technical Glasses" (1993) ASTM International. Accessed on: December 10, 2002. Available at <<http://www.astm.org/cgi-bin/SoftCart.exe/STORE/filtrexx40.cgi?U+mystore+jcgf3275+-L+CLEAN:GLASS+/usr6/htdocs/astm.org/DATABASE.CART/PAGES/C912.htm>>
108. L. Henke, N. Nagy, and U. J. Krull, "An AFM Determination of the Effects on Surface Roughness Caused by Cleaning of Fused Silica and Glass Substrates in the Process of Optical Biosensor Preparation," *Biosens. Bioelectron.*, **17** [6-7] 547-55 (2002).
109. W. R. Bowen, N. Hilal, R. W. Lovitt, and C. J. Wright, "An Atomic Force Microscopy Study of the Adhesion of a Silica Sphere to a Silica Surface - Effects of Surface Cleaning," *Colloids Surf., A*, **157** [1-3] 117-25 (1999).
110. H. Schicht, M. Emonds, and J. Esser, "Pin-Pointed Modification of Glass Surfaces by Using Specific Washing Compounds," *J. Non-Cryst. Solids*, **218** [1] 210-7 (1997).
111. E. O. Filatova and A. S. Shulakov, "Glass Surface Atomic Structure after Technological Treatments," *Proc. SPIE-Int. Soc. Opt. Eng.*, **2453** [1] 122-9 (1995).
112. A. Gorokhovskiy, K. Matzov, and J. I. Escalante-Garcia, "Modification of the Float-Glass Surface by Treatment with Urea Aqueous Solution," *J. Non-Cryst. Solids*, **291** [1-2] 43-9 (2001).
113. S. Cho, F. Miyaji, T. Kokubo, and T. Nakamura, "Induction of Bioactivity of a Non-Bioactive Glass-Ceramic by a Chemical Treatment," *Biomaterials*, **18** [22] 1479-85 (1997).
114. R. K. Brow, "Glass Surface Modifications During Ion Beam Sputtering," *J. Non-Cryst. Solids*, **107** [1] 1-10 (1988).
115. X. Zhou, P. F. Johnson, R. A. Condrate, Sr., and Y. M. Guo, "Structural Investigation of Plasma-Enhanced Glass Surface Modification Using FTIR Spectroscopy," *Mater. Lett.*, **9** [5,6] 207-10 (1990).

116. J. Janca, M. Klima, P. Slavicek, and L. Zajickova, "HF Plasma Pencil - New Source for Plasma Surface Processing," *Surf. Coat. Technol.*, **116-119** 547-51 (1999).
117. A. K. Bledzki, J. Lieser, G. Wacker, and H. Frenzel, "Characterization of the Surfaces of Treated Glass Fibres Using Different Methods of Investigation," *Compos. Interfaces*, **5** [1] 41-53 (1997).
118. R. Park and J. Jang, "A Study of the Impact Properties of Composites Consisting of Surface-Modified Glass Fibers in Vinyl Ester Resin," *Compos. Sci. Technol.*, **58** [6] 979-85 (1997).
119. K. Benzarti, L. Cangemi, and F. D. Maso, "Transverse Properties of Unidirectional Glass/Epoxy Composites: Influence of Fibre Surface Treatments," *Compos. Pt. A, Appl. Sci. Manuf.*, **32** [2] 197-206 (2001).
120. M. N. Palmisiano, A. L. Boehman, and C. G. Pantano, "Processing Effects on the Surface Composition of Glass Fiber," *J. Am. Ceram. Soc.*, **83** [10] 2423-328 (2000).
121. J. Murach, S. Jander, and R. Bruckner, "Structure-Sensitive Investigations on Alkali Disilicate Glass Fibers with Reference to Metasilicate and Silica Glass Fibers," *J. Non-Cryst. Solids*, **217** [1] 92-8 (1997).
122. J. Murach and R. Bruckner, "Preparation and Structure-Sensitive Investigations on Silica Glass Fibers," *J. Non-Cryst. Solids*, **211** [3] 250-61 (1997).
123. E. F. Vansant, P. Van Der Voort, and K. C. Vrancken, *Characterization and Chemical Modification of the Silica Surface*, Vol. 93. Elsevier Science B.V., Amsterdam, The Netherlands, 1995.
124. E. J. Friebele, G. H. Siegel, Jr., and D. L. Griscom, "Drawing-Induced Defect Centers in a Fused Silica Core Fiber," *Appl. Phys. Lett.*, **28** [9] 516-8 (1976).
125. J. Li, S. Kannan, R. L. Lehman, and G. H. Siegel, Jr., "Drawing-Enhanced Defect Precursors in Low-OH Content, Oxygen-Deficient Synthetic Silica Optical Fibers," *Appl. Phys. Lett.*, **64** [16] 2090-2 (1994).

126. P. Hoffmann and H. Knozinger, "Novel Aspects of Mid and Far IR Fourier Spectroscopy Applied to Surface and Adsorption Studies on SiO₂," *Surf. Sci.*, **188** [1] 181-98 (1987).
127. E. B. Webb III and S. H. Garofalini, "Relaxation of Silica Glass Surfaces Before and After Stress Modification in a Wet and Dry Atmosphere: Molecular Dynamics Simulations," *J. Non-Cryst. Solids*, **226** [1-2] 47-57 (1998).
128. V. Nazabal, E. Fargin, G. LeFlem, V. Briois, C. CartierDitMoulin, T. Buffeteau, and B. Desbat, "Structural Modification on Silica Glass Surface Induced by Thermal Poling for Second Harmonic Generation," *J. Synchrotron Radiat.*, **8** [2] 788-90 (2001).
129. T. Fujiwara, M. Takahashi, and A. J. Ikushima, "Second-Harmonic Generation in Germanosilicate Glass Poled with ArF Laser Irradiation," *Appl. Phys. Lett.*, **71** [8] 1032-4 (1997).
130. T. G. Alley, S. R. J. Brueck, and R. A. Myers, "Space Charge Dynamics in Thermally Poled Fused Silica," *J. Non-Cryst. Solids*, **242** [2-3] 165-76 (1998).
131. N. Wada and K. Morinaga, "Mechanism of Second-Harmonic Generation for Thermal Poled Silica Glasses," *J. Jpn. Inst. Met.*, **62** [10] 932-8 (1998).
132. V. Nazabal, E. Fargin, C. Labrugère, and G. LeFlem, "Second Harmonic Generation Optimization in Thermally Poled Borophosphate Glasses and Characterization by XANES and XPS," *J. Non-Cryst. Solids*, **270** [1-3] 223-33 (2000).
133. D. Flamm, F. Frost, and D. Hirsch, "Evolution of Surface Topography of Fused Silica by Ion Beam Sputtering," *Appl. Surf. Sci.*, **179** [1-4] 95-101 (2001).
134. V. A. Radtsig, "Point Defects on Silica Surface: Structure and Reactivity," *Kinet. Catal.*, **40** [5] 693-715 (1999).
135. M. A. Natal-Santiago, J. M. Hill, and J. A. Dumesic, "Studies of the Adsorption of Acetaldehyde, Methyl Acetate, Ethyl Acetate, and Methyl Trifluoroacetate on Silica," *J. Mol. Catal. A: Chem.*, **140** [2] 199-214 (1999).

136. D. Lee and R. A. Condrate, Sr., "Infrared Reflectance Spectral Characterization of Various Organic Coatings on Glasses," *J. Non-Cryst. Solids*, **222** [1] 435-41 (1997).
137. T. Jesionowski and A. Krysztafkiewicz, "Influence of Silane Coupling Agents on Surface Properties of Precipitated Silicas," *Appl. Surf. Sci.*, **172** [1-2] 18-32 (2001).
138. M. Fuji, K. Machida, T. Takei, T. Watanabe, and M. Chikazawa, "Surface Geometric Structure of Chemically Modified Silica Studied by Direct Atomic Force Microscopy (AFM) Imaging and Adsorption Method," *Langmuir*, **16** [7] 3281-7 (2000).
139. P. C. Rieke, B. J. Tarasevich, L. L. Wood, M. H. Engelhard, D. R. Baer, G. E. Fryxell, C. M. John, D. A. Laken, and M. C. Jaehnig, "Spatially Resolved Mineral Deposition on Patterned Self-Assembled Monolayers," *Langmuir*, **10** [3] 619-22 (1994).
140. J. Ruehe, V. J. Novotny, K. K. Kanazawa, T. Clarke, and G. B. Street, "Structure and Tribological Properties of Ultrathin Alkylsilane Films Chemisorbed to Solid Surfaces," *Langmuir*, **9** [9] 2383-8 (1993).
141. N. Mino, K. Nakajima, and K. Ogawa, "Control of Molecular Tilt Angles in Oriented Monolayers Deposited by a Chemical Adsorption Technique and Application of the Monolayers as an Alignment Film," *Langmuir*, **7** [7] 1468-72 (1991).
142. V. DePalma and N. Tillman, "Friction and Wear of Self-Assembled Trichlorosilane Monolayer Films on Silicon," *Langmuir*, **5** [3] 868-72 (1989).
143. B. Bhushan, A. V. Kulkarni, V. N. Koinkar, M. Boehm, L. Odoni, C. Martelet, and M. Belin, "Microtribological Characterization of Self-Assembled and Langmuir-Blodgett Monolayers by Atomic and Friction Force Microscopy," *Langmuir*, **11** [8] 3189-98 (1995).
144. C. S. Dulcey, J. H. Georger, Jr., M.-S. Chen, S. W. McElvany, C. E. O'Ferrall, V. I. Benezra, and J. M. Calvert, "Photochemistry and Patterning of Self-Assembled Monolayer Films Containing Aromatic Hydrocarbon Functional Groups," *Langmuir*, **12** [6] 1638-50 (1996).
145. N. L. Jeon, P. G. Clem, D. A. Payne, and R. G. Nuzzo, "A Monolayer-Based Lift-Off Process for Patterning Chemical Vapor Deposition Copper Thin Films," *Langmuir*, **12** [22] 5350-5 (1996).

146. A. L. Weisenhorn, M. Egger, F. Ohnesorge, S. A. C. Gould, S. P. Heyn, H. G. Hansma, R. L. Sinsheimer, H. E. Gaub, and P. K. Hansma, "Molecular-Resolution Images of Langmuir-Blodgett Films and DNA by Atomic Force Microscopy," *Langmuir*, **7** [1] 8-12 (1991).
147. K.-i. Iimura, Y. Nakajima, and T. Kato, "A Study on Structures and Formation Mechanism of Self-Assembled Monolayers of n-alkyltrichlorosilanes Using Infrared Spectroscopy and Atomic Force Microscopy," *Thin Solid Films*, **379** [1-2] 230-9 (2000).
148. U. Schubert, N. Huesing, and A. Lorenz, "Hybrid Inorganic-Organic Materials by Sol-Gel Processing of Organofunctional Metal Alkoxides," *Chem. Mater.*, **7** [11] 2010-27 (1995).
149. G. Deng, M. A. Markowitz, P. R. Kust, and B. P. Gaber, "Control of Surface Expression of Functional Groups on Silica Particles," *Mater. Sci. Eng.*, **C11** [2] 165-72 (2000).
150. R. Benters, C. M. Niemeyer, and D. Wöhrle, "Dendrimer-Activated Solid Supports for Nucleic Acid and Protein Microarrays," *ChemBioChem*, **2** 686-94 (2001).
151. O. Birkert, H.-M. Haake, A. Schutz, J. Mack, A. Brecht, G. Jung, and G. Gauglitz, "A Streptavidin Surface on Planar Glass Substrates for the Detection of Biomolecular Interaction," *Anal. Biochem.*, **282** [2] 200-8 (2000).
152. C. R. Jenney and J. M. Anderson, "Alkylsilane-Modified Surfaces: Inhibition of Human Macrophage Adhesion and Foreign Body Giant Cell Formation," *J. Biomed. Mater. Res.*, **46** [1] 11-21 (1999).
153. W. C. McCrone, "Light Microscopy," Ch. 1 in *Characterization of Solid Surfaces*. Edited by P. F. Kane and G. B. Larrabee. Plenum Press, New York, 1974.
154. A. C. Hall, "Multiple-Beam Interferometry," Ch. 2 in *Characterization of Solid Surfaces*. Edited by P. F. Kane and G. B. Larrabee. Plenum Press, New York, 1974.
155. C. Laird, "Electron Microscopy," Ch. 4 in *Characterization of Solid Surfaces*. Edited by P. F. Kane and G. B. Larrabee. Plenum Press, New York, 1974.

156. O. Johari and A. V. Samudra, "Scanning Electron Microscopy," Ch. 5 in *Characterization of Solid Surfaces*. Edited by P. F. Kane and G. B. Larrabee. Plenum Press, New York, 1974.
157. D. J. Whitehouse, "Stylus Techniques," Ch. 3 in *Characterization of Solid Surfaces*. Edited by P. F. Kane and G. B. Larrabee. Plenum Press, New York, 1974.
158. P. F. Kane, "Field Ion Microscopy," Ch. 6 in *Characterization of Solid Surfaces*. Edited by P. F. Kane and G. B. Larrabee. Plenum Press, New York, 1974.
159. R. D. Dobrott, "X-Ray Diffraction Methods," Ch. 7 in *Characterization of Solid Surfaces*. Edited by P. F. Kane and G. B. Larrabee. Plenum Press, New York, 1974.
160. G. N. Greaves, "EXAFS for Studying Corrosion of Glass Surfaces," *J. Non-Cryst. Solids*, **120** 108-16 (1990).
161. W. L. Baun, "X-Ray Emission Fine Features," Ch. 19 in *Characterization of Solid Surfaces*. Edited by P. F. Kane and G. B. Larrabee. Plenum Press, New York, 1974.
162. C. C. Chang, "Analytical Auger Electron Spectroscopy," Ch. 20 in *Characterization of Solid Surfaces*. Edited by P. F. Kane and G. B. Larrabee. Plenum Press, New York, 1974.
163. J. V. Gilfrich, "X-Ray Fluorescence Analysis," Ch. 12 in *Characterization of Solid Surfaces*. Edited by P. F. Kane and G. B. Larrabee. Plenum Press, New York, 1974.
164. D. Haneman, "Resonance Methods," Ch. 14 in *Characterization of Solid Surfaces*. Edited by P. F. Kane and G. B. Larrabee. Plenum Press, New York, 1974.
165. N. J. Harrick and K. H. Beckmann, "Internal Reflection Spectroscopy," Ch. 10 in *Characterization of Solid Surfaces*. Edited by P. F. Kane and G. B. Larrabee. Plenum Press, New York, 1974.
166. S. H. Hercules and D. M. Hercules, "Surface Characterization by Electron Spectroscopy for Chemical Analysis (ESCA)," Ch. 13 in *Characterization of Solid Surfaces*. Edited by P. F. Kane and G. B. Larrabee. Plenum Press, New York, 1974.

167. M. C. Hobson, Jr., "Mossbauer Spectroscopy," Ch. 15 in *Characterization of Solid Surfaces*. Edited by P. F. Kane and G. B. Larrabee. Plenum Press, New York, 1974.
168. G. A. Hutchins, "Electron Probe Microanalysis," Ch. 18 in *Characterization of Solid Surfaces*. Edited by P. F. Kane and G. B. Larrabee. Plenum Press, New York, 1974.
169. J. A. Keenan and G. B. Larrabee, "Radioisotope Techniques," Ch. 11 in *Characterization of Solid Surfaces*. Edited by P. F. Kane and G. B. Larrabee. Plenum Press, New York, 1974.
170. D. M. MacArthur, "Electrochemical Techniques," Ch. 8 in *Characterization of Solid Surfaces*. Edited by P. F. Kane and G. B. Larrabee. Plenum Press, New York, 1974.
171. W. D. Mackintosh, "Rutherford Scattering," Ch. 16 in *Characterization of Solid Surfaces*. Edited by P. F. Kane and G. B. Larrabee. Plenum Press, New York, 1974.
172. D. V. McCaughan and R. A. Kushner, "Impurity-Movement Problems in Analysis Methods Using Particle Bombardment," Ch. 22 in *Characterization of Solid Surfaces*. Edited by P. F. Kane and G. B. Larrabee. Plenum Press, New York, 1974.
173. J. M. McCrea, "Mass Spectrometry," Ch. 21 in *Characterization of Solid Surfaces*. Edited by P. F. Kane and G. B. Larrabee. Plenum Press, New York, 1974.
174. T. B. Pierce, "Accelerator Microbeam Techniques," Ch. 17 in *Characterization of Solid Surfaces*. Edited by P. F. Kane and G. B. Larrabee. Plenum Press, New York, 1974.
175. J. L. Seeley and R. K. Skogerboe, "Emission Spectrometry," Ch. 9 in *Characterization of Solid Surfaces*. Edited by P. F. Kane and G. B. Larrabee. Plenum Press, New York, 1974.
176. C. W. White, D. L. Simms, and N. H. Tolk, "Surface Composition by Analysis of Neutral and Ion Impact Radiation," Ch. 23 in *Characterization of Solid Surfaces*. Edited by P. F. Kane and G. B. Larrabee. Plenum Press, New York, 1974.

177. E. Radlein and G. H. Frischat, "Atomic Force Microscopy as a Tool to Correlate Nanostructure to Properties of Glasses," *J. Non-Cryst. Solids*, **222** 69-82 (1997).
178. E. D. Larson, L. D. Pye, D. Radlein, G. H. Frischat, and R. A. Weeks, "Atomic Force Microscopy Investigations on Libyan Desert Glass and Other Silica Glasses of Different Origins," *Chem. Erde*, **56** 423-30 (1996).
179. N. A. Burnham, O. P. Behrend, F. Oulevey, G. Gremaud, P.-J. Gallo, D. Gourdon, E. Dupas, A. J. Kulik, H. M. Pollock, and G. A. D. Briggs, "How Does a Tip Tap?" *Nanotechnology*, **8** [2] 67-75 (1997).
180. K. L. Babcock and C. B. Prater, "Phase Imaging: Beyond Topography," Digital Instruments, Philadelphia, PA, (1995).
181. L. D. Eske and D. W. Galipeau, "Characterization of SiO₂ Surface Treatments Using AFM, Contact Angles and a Novel Dewpoint Technique," *Colloids Surf., A*, **154** [1-2] 33-51 (1999).
182. O. Marti, B. Drake, and P. K. Hansma, "Atomic Force Microscopy of Liquid-Covered Surfaces: Atomic Resolution Images," *Appl. Phys. Lett.*, **51** [7] 484-6 (1987).
183. M. Raghavachari, H.-M. Tsai, K. Kottke-Marchant, and R. E. Marchant, "Surface Dependent Structures of von Willebrand Factor Observed by AFM under Aqueous Conditions," *Colloids Surf., B*, **19** [4] 315-24 (2000).
184. I. Revenko, "Use of Atomic Force Microscopy for the Study of Biomaterials," *Am. Lab.*, **32** [8] 40-6 (2000).
185. A. A. Bukharaev, N. I. Nurgazizov, A. A. Mozhanova, and D. V. Ovchinnikov, "AFM Investigation of Selective Etching Mechanism of Nanostructured Silica," *Surf. Sci.*, **482-485** [2] 1319-24 (2001).
186. W. R. Bowen, T. Doneva, N. Hilal, and C. J. Wright, "Atomic Force Microscopy: Images and Interactions," *Microsc. Anal.*, **81** 5-8 (2001).
187. B. L. Gabriel, *SEM: A User's Manual for Materials Science*. American Society for Metals, Metals Park, OH, 1985.
188. O. Anderson and K. Bange, "Characterization of Glass Surfaces by X-Ray Reflectivity," *Glastech. Ber.*, **70** [10] 316-21 (1997).

189. D. K. Bowen and M. Wormington, "Grazing Incidence X-Ray Characterization of Materials," *Adv. X-Ray Anal.*, **36** 171-84 (1993).
190. J. M. Grimal, P. Chartier, and P. Lehuede, "X-ray Reflectivity: A New Tool for the Study of Glass Surfaces," *J. Non-Cryst. Solids*, **196** [1-3] 128-33 (1996).
191. M. Huppaufl and B. Lengeler, "Surface Analysis of Floatglass by Means of X-Ray Absorption, Reflection, and Fluorescence Analysis," *J. Appl. Phys.*, **75** [2] 785-91 (1994).
192. P. J. LaPuma, R. L. Snyder, S. Zdzieszynski, and R. Bruckner, "Characterization of the Tin Diffusion into Float Glass Using Glancing Angle X-Ray Characterization," *Adv. X-Ray Anal.*, **38** 705-9 (1995).
193. A. J. G. Leenaers, J. J. A. M. Vrakking, and D. K. G. de Boer, "Glancing Incidence X-Ray Analysis: More than Just Reflectivity!" *Spectrochim. Acta, Part B*, **52** [7] 805-12 (1997).
194. B. Lengeler, "X-Ray Reflection, A New Tool for Investigating Layered Structures and Interfaces," *Adv. X-Ray Anal.*, **35** 127-35 (1992).
195. I. Pape, B. K. Tanner, and M. Wormington, "Grazing Incidence X-ray Scattering Measurement of Silicate Glass Surfaces," *J. Non-Cryst. Solids*, **248** [1] 75-83 (1999).
196. L. G. Parratt, "Surface Studies of Solids by Total Reflection of X-Rays," *Phys. Rev.*, **95** [2] 359-69 (1954).
197. C. C. Umbach and J. M. Blakely, "Specular and Diffuse Scattering of X-rays from a Fusion-Drawn Glass Surface," *Nucl. Instrum. Methods Phys. Res., Sect. B*, **133** [1-4] 50-6 (1997).
198. G. Wiener, R. Gunther, C. Michaelsen, J. Knoth, H. Schwenke, and R. Bormann, "Ion Beam Sputtering Techniques for High-Resolution Concentration Depth Profiling with Glancing Incidence X-Ray Fluorescence Spectrometry," *Spectrochim. Acta, Part B*, **52** [7] 813-21 (1997).
199. O. Citterio, F. Mazzoleni, E. Monticone, and G. B. Picotto, "Surface Characterization of Electroformed Mirrors for an X-ray Telescope," *Surf. Sci.*, **377-379** 98-102 (1997).

200. M. Kopecky, A. Inneman, F. Franc, and L. Pina, "Surface Finishing by Lacquer-Coating Technique," *Nucl. Instrum. Methods Phys. Res., Sect. A*, **395** [2] 281-6 (1997).
201. R. Larsson and J. Lundbert, "Study of Lubricated Impact Using Optical Interferometry," *Wear*, **190** [2] 184-9 (1995).
202. H. Zhu, Y. Ma, Y. Fan, and J. Shen, "Fourier Transform Infrared Spectroscopy and Oxygen Luminescence Probing Combined Study of Modified Sol-Gel Derived Film," *Thin Solid Films*, **397** [1-2] 95-101 (2001).
203. D. H. Lee, K. D. Vuong, R. A. Condrate, Sr., and X. W. Wang, "FTIR Investigation of RF Plasma Deposited Indium-Tin Oxide Films on Glasses," *Mater. Lett.*, **28** [1-3] 179-82 (1996).
204. U. Senturk, D. H. Lee, R. A. Condrate, Sr., and J. R. Varner, "ATR-FTIR Spectral Investigation of SO₂-Treated Soda-Lime-Silicate Float Glass," *Mater. Res. Soc. Symp. Proc.*, **407** 337-42 (1996).
205. P. K. d. Bokx, C. Kok, A. Bailleul, G. Wiener, and H. P. Urbach, "Grazing-Emission X-Ray Fluorescence Spectrometry; Principles and Applications," *Spectrochim. Acta*, **52** [7] 829-40 (1997).
206. D. K. G. de Boer, "Glancing-Incidence X-Ray Fluorescence of Layered Materials," *Phys. Rev. B: Condens. Matter Mater. Phys.*, **44** [2] 498-510 (1991).
207. K. Tsuji and K. Hirokawa, "Takeoff Angle-Dependent X-Ray Fluorescence of Layered Materials Using a Glancing Incident X-Ray Beam," *J. Appl. Phys.*, **75** [11] 7189-94 (1994).
208. K. Tsuji and K. Wagatsuma, "Solid Surface Density Determination Using the Glancing-Takeoff X-Ray Fluorescence Method," *Jpn. J. Appl. Phys.*, **35** [11B] L1535-8 (1996).
209. J. E. C. S. K. Tsuji, K. Wagatsuma, K. Hirokawa, T. Yamada, and T. Utaka, "Development of Glancing-Incidence and Glancing-Take-Off X-Ray Fluorescence Apparatus for Surface and Thin-Film Analyses," *Spectrochim. Acta, Part B*, **52** [7] 841-6 (1997).

210. C. G. Pantano, "X-ray Photoelectron Spectroscopy of Glass," Ch. 5 in *Experimental Techniques of Glass Science*. Edited by C. J. Simmons and O. H. El-Bayoumi. American Ceramic Society, Westerville, OH, 1993.
211. G. W. Arnold, G. D. Mea, J. C. Dran, H. Kawahara, P. Lehuede, H. J. Matzke, P. Mazzoldi, M. Noshiro, and C. Pantano, "Surface Analysis of Coated Flat Glasses: A Comparison of Various Techniques," *Glass Technol.*, **31** [2] 68-3 (1990).
212. W. Olthuis and P. Bergveld, "The Acid-Base Behavior of Proteins Determined by ISFETs," pp. 374-6 in *Surface Characterization Methods: Principles, Techniques and Applications*. Edited by A. J. Milling. Marcel Dekker, New York, 1999.
213. F. Bauer, A. Freyer, H. Ernst, H.-J. Glasel, and R. Mehnert, "Application of Temperature-Programmed Oxidation, Multinuclear MAS NMR and DRIFT Spectroscopy to the Surface Characterization of Modified Silica Nanoparticles," *Appl. Surf. Sci.*, **179** [1-4] 118-21 (2001).
214. S. Leonardelli, L. Facchini, C. Fretigny, P. Tougne, and A. P. Legrand, "Silicon-29 Nuclear Magnetic Resonance Study of Silica," *J. Am. Chem. Soc.*, **114** [16] 6412-8 (1992).
215. O. A. Zaporozhets, O. V. Shulga, O. Y. Nadzhafova, V. V. Turov, and V. V. Sukhan, "The Nature of the Binding of High-Molecular Weight Aminoammonium and Quaternary Ammonium Salts with the Amorphous Silica Surface," *Colloids Surf., A*, **168** [2] 103-8 (2000).
216. H. Bach, "Advanced Surface Analysis of Silicate Glasses, Oxides and Other Insulating Materials: A Review," *J. Non-Cryst. Solids*, **209** [1-2] 1-18 (1997).
217. K. D. Jandt, "Atomic Force Microscopy of Biomaterials Surfaces and Interfaces," *Surf. Sci.*, **491** [3] 303-32 (2001).
218. T. Nakagawa, K. Ogawa, and T. Kurumizawa, "Atomic Force Microscope for Chemical Sensing," *J. Vac. Sci. Technol., B*, **12** [3] 2215-8 (1994).
219. C. D. Frisbie, L. F. Rozsnyai, A. Noy, M. S. Wrighton, and C. M. Lieber, "Functional Group Imaging by Chemical Force Microscopy," *Science*, **265** [5228] 2071-4 (1994).

220. I. Schmitz, M. Schreiner, G. Friedbacher, and M. Grasserbauer, "Phase Imaging as an Extension to Tapping Mode AFM for the Identification of Material Properties on Humidity-Sensitive Surfaces," *Appl. Surf. Sci.*, **115** [2] 190-8 (1997).
221. M. Finke, K. D. Jandt, and D. M. Parker, "The Early Stages of Native Enamel Dissolution Studied with Atomic Force Microscopy," *J. Colloid Interface Sci.*, **232** [1] 156-64 (2000).
222. M. Farina, A. Schemmel, G. Weissmüller, R. Cruz, B. Kachar, and P. M. Bisch, "Atomic Force Microscopy Study of Tooth Surfaces," *J. Struct. Biol.*, **125** [1] 39-49 (1999).
223. K. D. Jandt, M. Finke, and P. Cacciafesta, "Aspects of the Physical Chemistry of Polymers, Biomaterials and Mineralised Tissues Investigated with Atomic Force Microscopy (AFM)," *Colloids Surf., B*, **19** [4] 301-14 (2000).
224. O. Sollböhmer, K.-P. May, and M. Anders, "Force Microscopical Investigation of Human Teeth in Liquids," *Thin Solid Films*, **264** [2] 176-83 (1995).
225. Y. Yoshida, B. V. Meerbeek, J. Snauwaert, L. Hellemans, P. Lambrechts, G. Vanherle, K. Wakasa, and D. H. Pashley, "A Novel Approach to AFM Characterization of Adhesive Tooth-Biomaterial Interfaces," *J. Biomed. Mater. Res.*, **47** [1] 85-90 (1999).
226. R. A. Latour, Jr., *Handbook of Biomaterials Evaluation*. 2nd ed.; Ch. 3. Edited by A. F. vonRecum. Taylor & Francis, Philadelphia, 1999.
227. D. W. Grainger and K. E. Healy, *Handbook of Biomaterials Evaluation*. Ch. 7. Edited by A. F. vonRecum. Taylor & Francis, Philadelphia, 1999.
228. "Scanning Probe Microscopy of Biomaterials Surfaces," *Surf. Sci.*, **491** [3] 303-497 (2001).
229. P. K. Gupta, D. Inniss, C. R. Kurkjian, and Q. Zhong, "Nanoscale Roughness of Oxide Glass Surfaces," *J. Non-Cryst. Solids*, **262** [1-3] 200-6 (2000).
230. J.G. Couillard, D.G. Ast, C. Umbach, J.M. Blakely, C.B. Moore, F.P. Fehlner, "Chemical Treatment of Glass Substrates," *J. Non-Cryst. Solids*, **222** 429-434 (1997).

231. R. S. Becker, *Theory and Interpretation of Fluorescence and Phosphorescence*. John Wiley & Sons, New York, 1969.
232. W. D. Callister, Jr., *Materials Science and Engineering - An Introduction*, 3rd ed. John Wiley & Sons, New York, 1994.
233. E. Hirschlaff, *Fluorescence and Phosphorescence*. Chemical Publishing Company, New York, 1939.
234. E. L. Wehry, "Structural and Environmental Factors in Fluorescence," Ch. 2 in *Fluorescence - Theory, Instrumentation, and Practice*. Edited by G. G. Guilbault. Marcel Dekker, New York, 1967.
235. D. L. Edson, Alfred University, Alfred, NY, November 23, 2002, Private Communication.
236. Y. Mao, P. Deng, F. Gan, H. Yang, and W. Shen, "Spectroscopic Properties of Ytterbium in Phosphate Glass," *Mater. Lett.*, **57** [2] 439-43 (2002).
237. F. Rocca, M. Ferrari, A. Kuzmin, N. Daldosso, C. Duverger, and F. Monti, "EXAFS Studies of the Local Structure of Er³⁺ Ions in Silica Xerogels Co-Doped with Aluminium," *J. Non-Cryst. Solids*, **293-295** [November] 112-7 (2001).
238. A. Kozanecki, D. Kuritsyn, H. Przybylinska, and W. Jantsch, "Site-Selective Excitation of Er³⁺ Ions in Oxygen-Rich Silicon," *Phys. B (Amsterdam, Neth.)*, **308-310** [December] 354-6 (2001).
239. A. M. Jurdyc, B. Jacquier, J. C. Gâcon, J. F. Bayon, and E. Delevaque, "Fluorescence Line Narrowing in Erbium-Doped Silica Fibers," *J. Lumin.*, **60-61** [April] 89-92 (1994).
240. M. Cha, J. J. Ju, T. Y. Kwon, S. I. Yun, S. I. Kim, and J. H. Kim, "Spectroscopic Properties of Ce³⁺ Ions in a Barium-Sodium Borate Glass," *Mater. Lett.*, **28** [1-3] 149-53 (1996).
241. M. Eyal, E. Greenberg, R. Reisfeld, and N. Spector, "Spectroscopy of Praseodymium(III) in Zirconium Fluoride Glass," *Chem. Phys. Lett.*, **117** [2] 108-14 (1985).

242. J. Kobelke, J. Kirchhof, K. Schuster, and A. Schwuchow, "Effects of Carbon, Hydrocarbon and Hydroxide Impurities on Praseodymium Doped Arsenic Sulfide Based Glasses," *J. Non-Cryst. Solids*, **284** [1-3] 123-7 (2001).
243. J.-L. Adam, R. Balda, I. Melscoët, F. Smektala, L. M. Lacha, and J. Fernández, "Spectroscopy of Nd³⁺ Ions in New Rare-Earth-Rich Fluoroarsenate Glasses," *J. Non-Cryst. Solids*, **256-257** [October] 390-5 (1999).
244. D. J. Ames, "Fluorescence Spectroscopy as a Probe for Oxidation States in Glasses and Glass Melts"; M.S. Thesis, Alfred University, Alfred, NY, 1995.
245. S. Kossionides, M. Kokkoris, A. G. Karydas, T. Paradellis, G. Kordas, and G. Moraitou, "Analysis of Ancient Glass Using Ion Beams and Related Techniques," *Nucl. Instrum. Methods Phys. Res., Sect. B*, **195** [3-4] 408-13 (2002).
246. T. E. Creighton, *Proteins - Structures and Molecular Properties*, 2nd ed. W.H. Freeman and Company, New York, 1999.
247. N. J. Emptage, "Fluorescent Imaging in Living Systems," *Curr. Opin. Pharmacol.*, **1** [5] 521-5 (2001).
248. R. F. Chen, "Extrinsic and Intrinsic Fluorescence in the Study of Protein Structure: A Review," Ch. 11 in *Fluorescence - Theory, Instrumentation, and Practice*. Edited by G. G. Guilbault. Marcel Dekker, New York, 1967.
249. V. M. Gun'ko, V. V. Turov, V. I. Zarko, V. V. Dudnik, V. A. Tischenko, O. A. Kazakova, E. F. Voronin, S. S. Slitchenko, V. N. Barvinchenko, and A. A. Chuiko, "Aqueous Suspensions of Fumed Silica and Adsorption of Proteins," *J. Colloid Interface Sci.*, **192** [1] 166-78 (1997).
250. C. Werner, K.-J. Eichhorn, K. Grundke, F. Simon, W. Grahlert, and H.-J. Jacobasch, "Insights on Structural Variations of Protein Adsorption Layers on Hydrophobic Fluorohydrocarbon Polymers Gained by Spectroscopic Ellipsometry (Part I)," *Colloids Surf., A*, **156** [1-3] 3-17 (1999).

251. R. J. Green, J. Davies, M. C. Davies, C. J. Roberts, and S. J. B. Trendler, "Surface Plasmon Resonance for Real Time in situ Analysis of Protein Adsorption to Polymer Surfaces," *Biomaterials*, **18** [5] 405-13 (1997).
252. T. A. Horbett, *Adsorption to Biomaterials from Protein Mixtures*, Vol. 343; Ch. 16. Edited by J. L. Brash and T. A. Horbett. American Chemical Society, Washington, DC, 1987.
253. G. P. Lopez, B. D. Ratner, C. D. Tidwell, C. L. Haycox, R. J. Rapoza, and T. A. Horbett, "Glow Discharge Plasma Deposition of Tetraethylene Glycol Dimethyl Ether for Fouling-Resistant Biomaterial Surfaces," *J. Biomed. Mater. Res.*, **26** [4] 415-39 (1992).
254. V. M. Gun'ko, N. N. Vlasova, L. P. Golovkova, N. G. Stukalina, I. I. Gerashchenko, V. I. Zarko, V. A. Tischenko, E. V. Goncharuk, and A. A. Chuiko, "Interaction of Proteins and Substituted Aromatic Drugs with Highly Disperse Oxides in Aqueous Suspension," *Colloids Surf., A*, **167** [3] 229-43 (2000).
255. L. Chaiet and F. J. Wolf, "The Properties of Streptavidin, a Biotin Binding Protein Produced by Streptomyces," *Arch. Biochem. Biophys.*, **105** [1] 1-5 (1964).
256. G. O. Reznik, S. Vajda, C. L. Smith, C. R. Cantor, and T. Sano, "Streptavidins with Intersubunit Crosslinks Have Enhanced Stability," *Nat. Biotechnol.*, **14** [8] 1007-11 (1996).
257. P. C. Weber, D. H. Ohlendorf, J. J. Wendoloski, and F. R. Salemme, "Structural Origins of High-Affinity Biotin Binding to Streptavidin," *Science*, **243** [4887] 85-8 (1989).
258. S. Freitag, I. LeTrong, L. Klumb, P. S. Stayton, and R. E. Stenkamp, "Structural Studies of the Streptavidin Binding Loop," *Protein Sci.*, **6** [6] 1157-66 (1997).
259. W. A. Hendrickson, A. Pahler, J. L. Smith, Y. Satow, E. A. Merritt, and R. P. Phizackerley, "Crystal Structure of Core Streptavidin Determined from Multiwavelength Anomalous Diffraction of Synchrotron Radiation," *Proc. Natl. Acad. Sci. U. S. A.*, **86** [7] 2190-4 (1989).

260. A. Pahler, W. A. Hendrickson, M. A. G. Kolks, C. E. Argarana, and C. R. Cantor, "Characterization and Crystallization of Core Streptavidin," *J. Biol. Chem.*, **262** [29] 13933-7 (1987).
261. W. Knoll, M. Zizlsperger, T. Liebermann, S. Arnold, A. Badia, M. Liiley, D. Piscevic, F. Schmitt, and J. Spinke, "Streptavidin Arrays as Supramolecular Architectures in Surface-Plasmon Optical Sensor Formats," *Colloids Surf., A*, **161** [1] 115-37 (2000).
262. S. Kossek, C. Padeste, and L. Tiefenauer, "Immobilization of Streptavidin for Immunosensors on Nanostructured Surfaces," *J. Mol. Recognit.*, **9** [5-6] 485-7 (1996).
263. P. Weber, "Site-Specific Strategies Stylize Streptavidin," *Nat. Biotechnol.*, **13** [11] 1158 (1995).
264. M. D. Savage, G. Mattson, S. Desai, G. W. Nielander, S. Morgensen, and E. J. Conklin, *Avidin-Biotin Chemistry: A Handbook*. Pierce Chemical Company, Rockford, IL, 1994.
265. H. Grubmuller, B. Heymann, and P. Tavan, "Ligand Binding: Molecular Mechanics Calculation of the Streptavidin-Biotin Rupture Force," *Science*, **271** [5251] 997-9 (1996).
266. S. Miyamoto and P. A. Kollman, "Absolute and Relative Binding Free Energy Calculations of the Interaction of Biotin and Its Analogs with Streptavidin Using Molecular Dynamics/Free Energy Perturbation Approaches," *Proteins: Struct., Funct., Genet.*, **16** [3] 226-45 (1993).
267. P. R. Langer, A. A. Waldrop, and D. C. Ward, "Enzymatic Synthesis of Biotin-Labeled Polynucleotides: Novel Nucleic Acid Affinity Probes," *Proc. Natl. Acad. Sci. U. S. A.*, **78** [11] 6633-7 (1981).
268. H. Lu, Y. Zhao, J. Ma, W. Li, and Z. Lu, "Characterization of DNA Hybridization on the Optical Fiber Surface," *Colloids Surf., A*, **175** [1-2] 147-52 (2000).
269. S. Allen, J. Davies, A. C. Dawkes, M. C. Davies, J. C. Edwards, M. C. Parker, C. J. Roberts, J. Sefton, S. J. B. Tendler, and P. M. Williams, "In Situ Observation of Streptavidin-Biotin Binding on an Immunoassay Well Surface Using an Atomic Force Microscope," *FEBS Lett.*, **390** [2] 161-4 (1996).

270. K. Fujita, S. Kimura, Y. Imanishi, E. Rump, and H. Ringsdorf, "Molecular Recognition of Biotinyl Hydrophobic Helical Peptides with Streptavidin at the Air/Water Interface," *J. Am. Chem. Soc.*, **116** [5] 2185-6 (1994).
271. M. Li, K. K. W. Wong, and S. Mann, "Organization of Inorganic Nanoparticles Using Biotin-Streptavidin Connectors," *Chem. Mater.*, **11** [1] 23-6 (1999).
272. V. H. Perez-Luna, M. J. O'Brien, K. A. Opperman, P. D. Hampton, G. P. Lopez, L. A. Klumb, and P. S. Stayton, "Molecular Recognition between Genetically Engineered Streptavidin and Surface-Bound Biotin," *J. Am. Chem. Soc.*, **121** [27] 6469-78 (1999).
273. Z. Ding, R. B. Fong, C. J. Long, P. S. Stayton, and A. S. Hoffman, "Size-Dependent Control of the Binding of Biotinylated Proteins to Streptavidin Using a Polymer Shield," *Nature*, **411** [1] 59-62 (2001).
274. J. Zempleni and D. M. Mock, "Chemical Synthesis of Biotinylated Histones and Analysis by Sodium Dodecyl Sulfate-Polyacrylamide Gel Electrophoresis/Streptavidin-Peroxidase," *Arch. Biochem. Biophys.*, **371** [1] 83-8 (1999).
275. V. Bulmus, Z. Ding, C. J. Long, P. S. Stayton, and A. S. Hoffman, "Site-Specific Polymer-Streptavidin Bioconjugate for pH-Controlled Binding and Triggered Release of Biotin," *Bioconjugate Chem.*, **11** [1] 78-83 (2000).
276. C. A. Rowe-Tait, J. W. Hazzard, K. E. Hoffman, J. J. Cras, J. P. Golden, and F. S. Ligler, "Simultaneous Detection of Six Biohazardous Agents Using a Planar Waveguide Array Biosensor," *Biosens. Bioelectron.*, **15** [11-12] 579-89 (2000).
277. M. S. Barbarakis, W. G. Qaisi, S. Daunert, and L. G. Bachas, "Observation of 'Hook Effects' in the Inhibition and Dose-Response Curve of Biotin Assays Based on the Interaction of Biotinylated Glucose Oxidase with (Strept)Avidin," *Anal. Chem.*, **65** [4] 457-60 (1993).
278. D. E. Leckband, F.-J. Schmitt, J. N. Israelachvili, and W. Knoll, "Direct Force Measurements of Specific and Nonspecific Protein Interactions," *Biochemistry*, **33** [15] 4611-24 (1994).

279. M. Wilchek and E. A. Bayer, "The Avidin-Biotin Complex in Bioanalytical Applications," *Anal. Biochem.*, **171** [1] 1-32 (1988).
280. M. Gonzalez, L. A. Bagatolli, I. Echabe, J. L. R. Arrondo, C. E. Argarana, C. R. Cantor, and G. D. Fidelio, "Interaction of Biotin with Streptavidin," *J. Biol. Chem.*, **272** [17] 11288-94 (1997).
281. B. A. Katz, "Binding of Biotin to Streptavidin Stabilizes Intersubunit Salt Bridges Between Asp61 and His87 at Low pH," *J. Mol. Biol.*, **274** [5] 776-800 (1997).
282. L. Chaiet, T. W. Miller, F. Tausig, and F. J. Wolf, "Antibiotic MSD-235. II. Separation and Purification of Synergistic Components," *Antimicrob. Agents Chemother.*, **3** [1] 28-32 (1963).
283. L. R. H. Cohen, K. Strupat, and F. Hillenkamp, "Analysis of Quaternary Protein Ensembles by Matrix Assisted Laser Desorption/Ionization Mass Spectrometry," *J. Am. Soc. Mass Spectrom.*, **8** [10] 1046-52 (1997).
284. A. Yang and B. Honig, "On the pH Dependence of Protein Stability," *J. Mol. Biol.*, **231** [2] 459-74 (1993).
285. L. Bin, M. R. Smyth, and R. O'Kennedy, "Immunological Activities of IgG Antibody on Pre-Coated Fc Receptor Surfaces," *Anal. Chim. Acta*, **331** [1-2] 97-102 (1996).
286. T. Dubrovsky, A. Tronin, and C. Nicolini, "Determination of Orientation of the IgG Molecules in Immobilized Langmuir Monolayers by Means of Binding with Fragment Specific Anti-Immunoglobulin Antibodies," *Thin Solid Films*, **257** [1] 130-3 (1995).
287. A. Tronin, T. Dubrovsky, G. Radicchi, and C. Nicolini, "Optimisation of IgG Langmuir Film Deposition for Application as Sensing Elements," *Sens. Actuators, B*, **34** [1-3] 276-82 (1996).
288. T. Dubrovsky, S. Dubrovskaya, C. Nicolini, O. Guryev, and A. Tronin, "Langmuir Films of Fc Binding Receptors Engineered from Protein A and Protein G as a Sublayer for Immunoglobulin Orientation," *Thin Solid Films*, **284-285** [15] 698-702 (1996).
289. I. Mazsaroff, S. Cook, and F. E. Regnier, "Molecular Orientation of Immunoglobulin G at High Concentration on an Ion-Exchange Sorbent," *J. Chromatogr., A*, **443** 119-31 (1988).

290. J. Buijs, D. D. White, and W. Norde, "The Effect of Adsorption on the Antigen Binding by IgG and Its F(ab)₂ Fragments," *Colloids Surf., B*, **8** [4-5] 239-49 (1997).
291. N. J. Geddes, A. S. Marin, F. Caruso, R. S. Urquhart, D. N. Furlong, J. R. Sambles, K. A. Than, and J. A. Edgar, "Immobilisation of IgG onto Gold Surfaces and its Interaction with Anti-IgG Studied by Surface Plasmon Resonance," *J. Immunol. Methods*, **175** [2] 149-60 (1994).
292. N. C. Price, *Proteins*. Edited by N. C. Price. Academic Press, San Diego, CA, 1996.
293. N. C. Price, "Determination of Protein Concentration," pp. 27-30 in *Proteins*. Edited by N. C. Price. Academic Press, San Diego, CA, 1996.
294. L. Sawyer, "Crystallization Procedures," pp. 155-60 in *Proteins*. Edited by N. C. Price. Academic Press, San Diego, CA, 1996.
295. A. R. Pitt, "Size Determination of Proteins. B. Mass Spectrometric Methods," pp. 174-86 in *Proteins*. Edited by N. C. Price. Academic Press, San Diego, CA, 1996.
296. O. Byron, "Size Determination of Proteins. A. Hydrodynamic Methods," pp. 161-74 in *Proteins*. Edited by N. C. Price. Academic Press, San Diego, CA, 1996.
297. J.-B. Lhoest and D. G. Castner, "Identification and Quantification of Adsorbed Proteins with Static Secondary Ion Mass Spectrometry," *Trans. Annu. Meet. Soc. Biomater.*, **22** 356 (1999).
298. C. W. Wharton, *FTIR and Raman Spectroscopies in the Study of Proteins and Other Biological Molecules*. pp. 187-94. Edited by N. C. Price. Academic Press, San Diego, CA, 1996.
299. S. R. Martin, "Circular Dichroism," pp. 195-203 in *Proteins*. Edited by N. C. Price. Academic Press, San Diego, CA, 1996.
300. R. Cammack and J. K. Shergill, "EPR Spectroscopy of Proteins," pp. 217-31 in *Proteins*. Edited by N. C. Price. Academic Press, San Diego, CA, 1996.
301. B. Whitehead and J. P. Waltho, "NMR Structure Determination of Proteins," pp. 205-16 in *Proteins*. Edited by N. C. Price. Academic Press, San Diego, CA, 1996.

302. P. Billsten, M. Wahlgren, T. Arnebrant, J. McGuire, and H. Elwing, "Structural Changes of T4 Lysozyme upon Adsorption to Silica Nanoparticles Measured by Circular Dichroism," *J. Colloid Interface Sci.*, **175** [1] 77-82 (1995).
303. A. Kondo, F. Murakami, M. Kawagoe, and K. Higashitani, "Kinetic and Circular Dichroism Studies of Enzymes Adsorbed on Ultrafine Silica Particles," *Appl. Microbiol.*, **39** [6] 726-31 (1993).
304. C. R. McMillin and A. G. Walton, "A Circular Dichroism Technique for the Study of Adsorbed Protein Structure," *J. Colloid Interface Sci.*, **48** [2] 345-9 (1974).
305. A. M. Micetich, "Protocol Development for Study of Biological Molecule Adsorption to Glass Surfaces"; B.S. Thesis, Alfred University, Alfred, NY, 1999.
306. R. J. Jakobsen and F. M. Wasacz, *Effects of the Environment on the Structure of Adsorbed Proteins: Fourier Transform Infrared Spectroscopic Studies*, Vol. 343; Ch. 22. Edited by J. L. Brash and T. A. Horbett. American Chemical Society, Washington, DC, 1987.
307. B. W. Morrissey and R. R. Stromberg, "The Conformation of Adsorbed Blood Proteins by Infrared Bound Fraction Measurements," *J. Colloid Interface Sci.*, **46** [1] 152-64 (1974).
308. H. Haas and H. Mohwald, "Ordered Protein Arrays as Mesophases," *Mater. Sci. Eng., C*, **1** [2] 75-8 (1994).
309. J.-B. Lhoest, E. Detrait, P. van den Bosch de Aguilar, and P. Bertrand, "Fibronectin Adsorption, Conformation, and Orientation on Polystyrene Substrates Studied by Radiolabeling, XPS, and ToF SIMS," *J. Biomed. Mater. Res.*, **41** [1] 95-103 (1998).
310. M. F. Garcia-Parajo, J.-A. Veerman, G. M. J. Segers-Nolten, B. G. deGroot, J. Greve, and N. F. vanHulst, "Visualising Individual Green Fluorescent Proteins with a Near Field Optical Microscope," *Cytometry*, **36** [3] 239-46 (1999).
311. H. J. Gruber, M. Marek, H. Schindler, and K. Kaiser, "Biotin-Fluorophore Conjugates with Poly(ethylene glycol) Spacers Retain Intense Fluorescence after Binding to Avidin and Streptavidin," *Bioconjugate Chem.*, **8** [4] 552-9 (1997).

312. G. Kada, H. Falk, and H. J. Gruber, "Accurate Measurement of Avidin and Streptavidin in Crude Biofluids with a New, Optimized Biotin-Fluorescein Conjugate," *Biochim. Biophys. Acta*, **1427** [1] 33-43 (1999).
313. G. Kada, K. Kaiser, H. Falk, and H. J. Gruber, "Rapid Estimation of Avidin and Streptavidin by Fluorescence Quenching or Fluorescence Polarization," *Biochim. Biophys. Acta*, **1427** [1] 44-8 (1999).
314. S. E. Kakabakos, K. Georgiou, P. S. Petrou, and I. Chrisofidis, "Heterogeneous Fluoroimmunoassays Using Fluorescein as Label with Measurement of the Fluorescence Signal Directly onto the Solid-Phase," *J. Immunol. Methods*, **222** [1-2] 183-7 (1999).
315. M. Marek, K. Kaiser, and H. J. Gruber, "Biotin-Pyrene Conjugates with Poly(ethylene glycol) Spacers are Convenient Fluorescent Probes for Avidin and Streptavidin," *Bioconjugate Chem.*, **8** [4] 560-6 (1997).
316. A. A. Mironov, R. S. Polishchuk, and A. Luini, "Visualizing Membrane Traffic *in vivo* by Combined Video Fluorescence and 3D Electron Microscopy," *Trends Cell Biol.*, **10** [8] 349-53 (2000).
317. M. Taki, T. Hohsaka, H. Murakami, K. Taira, and M. Sisido, "A Non-natural Amino Acid for Efficient Incorporation into Proteins as a Sensitive Fluorescent Probe," *FEBS Lett.*, **507** [1] 35-8 (2001).
318. L. Zheng, W. R. Reid, and J. D. Brennan, "Measurement of Fluorescence from Tryptophan to Probe the Environment of Reaction Kinetics within Protein-Doped Sol-Gel Derived Glass Monoliths," *Anal. Chem.*, **69** [19] 3940-9 (1997).
319. R. Lal and S. A. John, "Biological Applications of Atomic Force Microscopy," *Am. J. Physiol.*, **266** [1] C1-C21 (1996).
320. G. Griffiths, "Bringing Electron Microscopy Back into Focus for Cell Biology," *Trends Cell Biol.*, **11** [4] 153-4 (2001).
321. B. L. Blackford, M. H. Jericho, and P. J. Mulhern, "A Review of Scanning Tunneling Microscope and Atomic Force Microscope Imaging of Large Biological Structures: Problems and Prospects," *Scanning Microsc.*, **5** [4] 907-18 (1991).
322. M. Radmacher, R. W. Tillmann, M. Fritz, and H. E. Gaub, "From Molecules to Cells: Imaging Soft Samples with the Atomic Force Microscope," *Science*, **257** [5078] 1900-5 (1992).

323. U. K. Laemmli, "Cleavage of Structural Proteins During the Assembly of the Head of Bacteriophage T4," *Nature*, **227** 680-5 (1970).
324. D. Patel and D. Rickwood, "Electrophoresis Methods," pp. 85-99 in *Proteins*. Edited by N. C. Price. Academic Press, San Diego, CA, 1996.
325. P. H. O'Farrell, "High Resolution Two-Dimensional Electrophoresis of Proteins," *J. Biol. Chem.*, **250** [10] 4007-21 (1975).
326. M. Katoh and M. Sodeoka, "Polymer-Bound N-Hydroxysuccinimide Esters: A Column-Free Fluorescent-Labeling Method," *Bioorg. Med. Chem. Lett.*, **9** [6] 881-4 (1999).
327. "Introduction to Fluorescence Techniques" (1999) [Probes]. Accessed on: November 13, 2002. Available at <www.probes.com>
328. K. Shahdeo and H. T. Karnes, "Post-column Reaction Detection Based on Fluorescence Energy Transfer in the Far Red Spectral Region," *J. Pharm. Biomed. Anal.*, **21** [2] 361-70 (1999).
329. A. Feltus, N. G. Hentz, and S. Daunert, "Post-Capillary Reaction Detection in Capillary Electrophoresis Based on the Streptavidin-Biotin Interaction Optimization and Application to Single Cell Analysis," *J. Chromatogr., A*, **918** [2] 381-92 (2001).
330. H. J. Gruber, G. Kada, M. Marek, and K. Kaiser, "Accurate Titration of Avidin and Streptavidin with Biotin-Fluorophore Conjugates in Complex, Colored Biofluids," *Biochim. Biophys. Acta*, **1381** [2] 203-12 (1998).
331. D. V. Nicolau and R. Cross, "Protein Profiled Features Patterned via Confocal Microscopy," *Biosens. Bioelectron.*, **15** [1-2] 85-91 (2000).
332. R. J. Palmer, Jr. and C. Sternberg, "Modern Microscopy in Biofilm Research: Confocal Microscopy and Other Approaches," *Curr. Opin. Biotechnol.*, **10** [3] 263-8 (1999).
333. S. E. Ilyin, M. C. Flynn, and C. R. Plata-Salaman, "Fiber-Optic Monitoring Coupled with Confocal Microscopy for Imaging Gene Expression in vitro and in vivo," *J. Neurosci. Methods*, **108** [1] 91-6 (2001).

334. W. C. Johnson, "Protein Secondary Structure and Circular Dichroism: A Practical Guide," *Proteins: Struct., Funct., Genet.*, **7** [3] 205-14 (1990).
335. A. Kondo and H. Fukuda, "Effects of Adsorption Conditions on Kinetics of Protein Adsorption and Conformational Changes at Ultrafine Silica Particles," *J. Colloid Interface Sci.*, **198** [1] 34-41 (1998).
336. A. Kondo, S. Oku, and K. Higashitani, "Structural Changes in Protein Molecules Adsorbed on Ultrafine Silica Particles," *J. Colloid Interface Sci.*, **143** [1] 214-21 (1991).
337. A. Kondo, S. Oku, F. Murakami, and K. Higashitani, "Conformational Changes in Protein Molecules upon Adsorption on Ultrafine Particles," *Colloids Surf., B*, **1** [3] 197-201 (1993).
338. C. E. Giacomelli and W. Norde, "The Adsorption-Desorption Cycle. Reversibility of the BSA-Silica System," *J. Colloid Interface Sci.*, **233** [2] 234-40 (2001).
339. A. W. P. Vermeer and W. Norde, "CD Spectroscopy of Proteins Adsorbed at Flat Hydrophilic Quartz and Hydrophobic Teflon Surfaces," *J. Colloid Interface Sci.*, **225** [2] 394-7 (2000).
340. R. J. Marsh, R. A. L. Jones, and M. Sferrazza, "Adsorption and Displacement of a Globular Protein on Hydrophilic and Hydrophobic Surfaces," *Colloids Surf., B*, **23** [1] 31-42 (2002).
341. D. E. Aston and J. C. Berg, "Long-Range Attraction Between Silanated Silica Materials Studied by an Electrolyte Titration with Atomic Force Microscopy," *Colloids Surf.*, **163** [2] 247-63 (2000).
342. G. Binnig, "Force Microscopy," *Ultramicroscopy*, **42-44** [Part 1] 7-15 (1992).
343. N. A. Burnham and R. J. Colton, "Measuring the Nanomechanical Properties and Surface Forces of Materials Using an Atomic Force Microscope," *J. Vac. Sci. Technol., A*, **7** [4] 2906-13 (1989).
344. C. Bustamante, C. Rivetti, and D. Keller, "Scanning Force Microscopy Under Aqueous Solutions," *Curr. Opin. Struct. Biol.*, **7** [5] 709-16 (1997).

345. W. F. Heinz and J. H. Hoh, "Spatially Resolved Force Spectroscopy of Biological Surfaces Using the Atomic Force Microscope," *Trends Biotechnol.*, **17** [4] 143-50 (1999).
346. J. H. Hoh, J. P. Cleveland, C. B. Prater, J. Revel, and P. K. Hansma, "Quantized Adhesion Detected with the Atomic Force Microscope," *J. Am. Chem. Soc.*, **114** [12] 4917-8 (1992).
347. M. D. Garrison and B. D. Ratner, "Scanning Probe Microscopy for the Characterization of Biomaterials and Biological Interactions," *Ann. N. Y. Acad. Sci.*, **831** [1] 101-13 (1997).
348. A. Engel, H. E. Gaub, and D. J. Muller, "Atomic Force Microscopy: A Forceful Way with Single Molecules," *Curr. Biol.*, **9** [4] R133-R6 (1999).
349. E.-L. Florin, V. T. Moy, and H. E. Gaub, "Adhesion Forces Between Individual Ligand-Receptor Pairs," *Science*, **264** [5175] 415-7 (1994).
350. J. Fritz, D. Anselmetti, J. Jarchow, and X. Fernandez-Busquets, "Probing Single Biomolecules with Atomic Force Microscopy," *J. Struct. Biol.*, **119** [2] 165-71 (1997).
351. T. Furuno, "Embedding and Immobilizing Protein Molecules into Two-Dimensional Protein Arrays for Single-Molecule Imaging by Tapping Mode Atomic Force Microscopy," *Jpn. J. Appl. Phys., Part 1*, **39** [11] 6435-40 (2000).
352. E. Hendersen, P. G. Haydon, and D. S. Sakaguchi, "Actin Filament Dynamics in Living Glial Cells Imaged by Atomic Force Microscopy," *Science*, **257** [5078] 1944-6 (1992).
353. G. U. Lee, L. A. Chrisey, and R. J. Colton, "Direct Measurement of the Forces Between Complementary Strands of DNA," *Science*, **266** [5186] 771-3 (1994).
354. G. U. Lee, D. A. Kidwell, and R. J. Colton, "Sensing Discrete Streptavidin-Biotin Interactions with Atomic Force Microscopy," *Langmuir*, **10** [2] 354-7 (1994).
355. M. Ludwig, W. Dettmann, and H. E. Gaub, "Atomic Force Microscope Imaging Contrast Based on Molecular Recognition," *Biophys. J.*, **72** [1] 445-8 (1997).

356. M. Radmacher, "Single Molecules Feel the Force," *Phys. World*, **Sept.** 33-7 (1999).
357. N. B. Sheller, S. Petrash, M. D. Foster, and V. V. Tsukruk, "Atomic Force Microscopy and X-ray Reflectivity Studies of Albumin Adsorbed onto Self-Assembled Monolayers of Hexadecyltrichlorosilane," *Langmuir*, **14** [16] 4535-44 (1998).
358. T. Tanaka, N. Nakamura, and T. Matsunaga, "Atomic Force Microscope Imaging of *Escherichia coli* Cell Using anti-*E. coli* Antibody-Conjugated Probe (In Aqueous) Solutions," *Electrochim. Acta*, **44** [21-22] 3827-32 (1999).
359. O. H. Willemsen, M. M. E. Snel, A. Cambi, J. Greve, B. G. De Groot, and C. G. Figdor, "Biomolecular Interactions Measured by Atomic Force Microscopy," *Biophys. J.*, **79** [6] 3267-81 (2000).
360. O. H. Willemsen, M. M. E. Snel, K. O. van der Werf, B. G. de Groot, J. Greve, P. Hinterdorfer, H. J. Gruber, H. Schindler, Y. van Kooyk, and C. G. Figdor, "Simultaneous Height and Adhesion Imaging of Antibody-Antigen Interactions by Atomic Force Microscopy," *Biophys. J.*, **75** [5] 2220-8 (1998).
361. J. Yang and Z. Shao, "Recent Advances in Biological Atomic Force Microscopy," *Micron*, **26** [1] 35-49 (1995).
362. W. Zhang, Q. Xu, S. Zou, H. Li, W. Xu, and X. Zhang, "Single-Molecule Force Spectroscopy on *Bombyx mori* Silk Fibroin by Atomic Force Microscopy," *Langmuir*, **16** [9] 4305-8 (2000).
363. J. Zlatanova, S. M. Lindsay, and S. H. Leuba, "Single Molecule Force Spectroscopy in Biology Using the Atomic Force Microscope," *Prog. Biophys. Mol. Biol.*, **74** [1-2] 37-61 (2000).
364. N. A. Burnham, R. J. Colton, and H. M. Pollock, "Interpretation of Force Curves in Force Microscopy," *Nanotechnology*, **4** [2] 64-80 (1993).
365. N. H. Green, S. Allen, M. C. Davies, C. J. Roberts, S. J. B. Tendler, and P. M. Williams, "Force Sensing and Mapping by Atomic Force Microscopy," *TrAC, Trends Anal. Chem.*, **21** [1] 64-73 (2002).
366. W. F. Heinz, E. A-Hassan, and J. H. Hoh, "Applications of Force Volume Imaging with the Nanoscope Atomic Force Microscope," Digital Instruments, Philadelphia, PA (1999).

367. M. Grandbois, M. Beyer, M. Rief, H. Clausen-Schaumann, and H. E. Gaub, "How Strong is a Covalent Bond?" *Science*, **283** [5408] 1727-30 (1999).
368. M. Micic, A. Chen, R. M. Leblanc, and V. T. Moy, "Scanning Electron Microscopy Studies of Protein-Functionalized Atomic Force Microscopy Cantilever Tips," *Scanning*, **21** [6] 394-7 (1999).
369. V. T. Moy, E.-L. Florin, and H. E. Gaub, "Intermolecular Forces and Energies between Ligands and Receptors," *Science*, **266** 257-9 (1994).
370. S. S. Wong, E. Joselevich, A. T. Woolley, C. L. Cheung, and C. M. Lieber, "Covalently Functionalized Nanotubes as Nanometre-Sized Probes in Chemistry and Biology," *Nature*, **394** [2] 52-5 (1998).
371. V. Hlady, R. A. VanWagenen, and J. D. Andrade, "Surface and Interfacial Aspects of Biomedical Polymers," p. 81 in Vol. 2, *Protein Adsorption*. Edited by J. D. Andrade. Plenum Press, New York, 1985.
372. B. D. Ratner, T. A. Horbett, D. Shuttleworth, and H. R. Thomas, "Analysis of the Organization of Protein Films on Solid Surfaces by ESCA," *J. Colloid Interface Sci.*, **83** [2] 630-42 (1981).
373. M. L. Rudee and T. M. Price, "The Initial Stages of Adsorption of Plasma Derived Proteins on Artificial Surfaces in a Controlled Flow Environment," *J. Biomed. Mater. Res.*, **19** [1] 57-66 (1985).
374. R. W. Paynter, B. D. Ratner, T. A. Horbett, and H. R. Thomas, "XPS Studies on the Organization of Adsorbed Protein Films on Fluoropolymers," *J. Colloid Interface Sci.*, **101** [1] 233-45 (1984).
375. R. A. Messing, "Molecular Inclusions. Adsorption of Macromolecules on Porous Glass Membranes," *J. Am. Chem. Soc.*, **91** [9] 2370-1 (1969).
376. R. A. Messing, "Adsorption of Proteins on Glass Surfaces and Pertinent Parameters for the Immobilization of Enzymes in the Pores of Inorganic Carriers," *J. Non-Cryst. Solids*, **19** 277-83 (1975).
377. B. Fubini, I. Fenoglio, Z. Elias, and O. Poirot, "Variability of Biological Responses to Silicas: Effect of Origin, Crystallinity, and State of Surface on Generation of Reactive Oxygen Species and Morphological Transformation of Mammalian Cells," *J. Environ. Pathol., Toxicol. Oncol.*, **20** [1] 95-108 (2001).

378. V. Vallyathan, X. Shi, N. S. Dalal, W. Irr, and V. Castranova, "Generation of Free Radicals from Freshly Fractured Silica Dust: Potential Role in Acute Silica-Induced Lung Injury," *Am. Rev. Respir. Dis.*, **138** [5] 1213-9 (1988).
379. F. MacRitchie, "The Adsorption of Proteins at the Solid/Liquid Interface," *J. Colloid Interface Sci.*, **38** [2] 484-8 (1972).
380. U. Jonsson, B. Ivarsson, I. Lundstrom, and L. Berghem, "Adsorption Behavior of Fibronectin on Well-Characterized Silica Surfaces," *J. Colloid Interface Sci.*, **90** [1] 148-63 (1982).
381. W. J. Dillman, Jr. and I. F. Miller, "On the Adsorption of Serum Proteins on Polymer Membrane Surfaces," *J. Colloid Interface Sci.*, **44** [2] 221-41 (1973).
382. W. Norde, "Proteins at Solid Interfaces," in *Physical Chemistry of Biological Interfaces*. Edited by A. Baszkin and W. Norde. Marcel Dekker, New York, 2000.
383. R. J. Marsh, R. A. L. Jones, M. Sferrazza, and J. Penfold, "Neutron Reflectivity Study of the Adsorption of beta-Lactoglobulin at a Hydrophilic Solid/Liquid Interface," *J. Colloid Interface Sci.*, **218** [1] 347-9 (1999).
384. J. Piehler, A. Brecht, K. E. Geckeler, and G. Gauglitz, "Surface Modification for Direct Immunoprobes," *Biosens. Bioelectron.*, **11** [6-7] 579-90 (1996).
385. R. J. Todd, R. D. Johnson, and F. H. Arnold, "Multiple-Site Binding Interactions in Metal-Affinity Chromatography : I. Equilibrium Binding of Engineered Histidine-Containing Cytochromes c," *J. Chromatogr., A*, **662** [1] 13-26 (1994).
386. D. S. Gill, D. J. Roush, and R. C. Willson, "Adsorption Heterogeneity and Thermodynamic Driving Forces in Anion Exchange Equilibria of Cytochrome b5," *J. Colloid Interface Sci.*, **167** [1] 1-7 (1994).
387. V. Dowd and R. J. Yon, " Heterogeneous Binding of Aldolase to Phosphocellulose : Interpretation in Terms of a "Concerted Cluster" Model of Multivalent Affinity," *J. Chromatogr., A*, **627** [1-2] 145-51 (1992).

388. R. D. Johnson, Z.-G. Wang, and F. H. Arnold, "Surface Site Heterogeneity and Lateral Interactions in Multipoint Protein Adsorption," *J. Phys. Chem.*, **100** [12] 5134-9 (1996).
389. Y.-J. Han, G. D. Stucky, and A. Butler, "Mesoporous Silicate Sequestration and Release of Proteins," *J. Am. Chem. Soc.*, **121** [42] 9897-8 (1999).
390. J. F. Mooney, A. J. Hunt, J. R. McIntosh, C. A. Liberko, D. M. Walba, and C. T. Rogers, "Patterning of Functional Antibodies and Other Proteins by Photolithography of Silane Monolayers," *Proc. Natl. Acad. Sci. U. S. A.*, **93** [22] 12287-91 (1996).
391. S. Saneinejad and M. S. Shoichet, "Patterned Glass Surfaces Direct Cell Adhesion and Process Outgrowth of Primary Neurons of the Central Nervous System," *J. Biomed. Mater. Res.*, **42** [1] 13-9 (1998).

3. Experimental Procedure

“Life shrinks or expands in proportion to ones’ courage” - Anais Nin

“Procrastination is the art of keeping up with yesterday” - Don Marquis

3.1. Sample Preparation

This work deals with the variation in protein binding as a function of sample forming or treatment. Thus, in order to reduce the variables, this work concentrates on one simple glass composition, silica. Initially, soda-lime silicate forms and borosilicate forms were studied using a few characterization techniques to evaluate these techniques. For completeness, these studies will be mentioned. Six product forms of silica were examined; flat (slides), cane, fiber, precipitated microspheres, fumed silica, and natural quartz single crystals. To increase the difference between surfaces, modification treatments were applied to the silica forms where appropriate. These surface treatments include cleaning with ethyl alcohol, autoclaving, etching with HF acid, exposure to water plasma and heat treatments at 1000°C.

Silica slides were obtained from Quartz Scientific Inc., catalog number QMS3 and part number 212000. The slides are originally manufactured by GE Quartz Inc. via the electric melting of high purity sand to produce GE 214 glass. The 214 glass is then cut in sheets, ground, and mechanically polished. These sheets are then sectioned to produce the silica slides. Soda-lime silicate slides were obtained in two forms; coated and uncoated. Fisher’s Finest soda-lime silicate slides (Fisher, 12-544-1) are made with a “non-stick” polymer coating so that biological materials will not adhere to the slides. Upon contacting Erie Scientific, which is the supplier for Fisher, and speaking with their senior research scientist, non-coated soda-lime silicate

slides were also obtained.¹ It is assumed that the non-coated silicate slides are made via the float glass process.

Cane was obtained in three compositions; silica, borosilicate, and soda lime silicate. The silica cane, or “quartz rod” as it is labeled, was ordered from the Sutter Instrument Co., catalog number QR-100-7.5. The rod is 1 mm in diameter and 7.5 cm in length. The borosilicate glass rod, also from Sutter (BR-100-15) is 1 mm in diameter and 15 cm in length. Soda-lime silicate cane was pulled from 3 mm diameter rod (Glass Warehouse, cat # W29001) using the Heathway draw tower. An image of the draw tower is shown in Figure 3.1.1.



Figure 3.1.1. Photograph of the Heathway fiber redraw tower in Room 106 of the Hall of Glass Science and Engineering.

Soda-lime silicate fiber was also pulled from rod form using the draw tower. During drawing, the diameter is constantly monitored using a LaserMike™ laser micrometer. The final diameter of soda-lime silicate fiber was approximately 230 micrometers. Silica fiber (Alcatel) was prepared from telecommunications fiber by stripping off its polymeric coating. Stripping of the fiber was accomplished by first submerging sections of fiber in methylene chloride until the inner polymer was dissolved and the outer polymer sloughed off. Then, two fuming sulphuric acid baths were used to remove any

remaining polymer by submerging the fiber in each bath for 20 seconds. A final exposure of only a few seconds to an almost boiling DI water bath was used to remove any residue and leave a pristine surface.

Soda-lime spheres, 100-120 micrometers in diameter, were made by introducing particulate glass (sieved to 100-120 microns) into an oxy-fuel flame. This high temperature flame melts the irregularly shaped particles, which allows surface tension to form them into spheres. The cooled spheres are then collected. Silica microspheres, 1 micrometer in diameter, were made via the Stöber process. This process is described in the literature review, section 2.2. First a seed solution was prepared consisting of 12.48 grams of tetraethylorthosilicate (TEOS), 68.45 grams of NH_3 , and 178 grams of ethanol. This mixture was allowed to coalesce overnight while being agitated at 40-50°C. Next, additions of a 1:2 TEOS:ethanol mixture to the seed solution began the precipitation reaction. These additions were in 2-5 mL quantities at half hour intervals. The total amount of TEOS added was 45 grams. Once the precipitates were formed, they were allowed to settle to the bottom of the container and the supernatant was drawn off. The wet powder mixture was then dried in a warm (50°C) oven for a few days. The particles were finally calcined at 600°C for 3 hours to form the Stöber spheres. The particles were examined in a transmission electron microscope (TEM) to confirm their size and shape. The last form of silica powder used in this study was Cab-o-Sil® (Cabot, grade HS-5) amorphous fumed silica.

Natural quartz single crystals were obtained from Ward's Scientific (49 H 3640). The crystals are about 3 inches in length and slightly over 1 inch in diameter. They are singly terminated, hexagonal, slightly cloudy, crystals from Arkansas. Some of the terminals were cut off the crystal using a diamond saw. These terminals were examined in a X-ray diffractometer (Siemens) to determine the plane. The crystallographic orientation of the terminals will be discussed in Section 4.4. The synthetic quartz crystal was a

special order from Ward's scientific. It was grown parallel to the c-axis and is 6 inches long by 1.5 inches in diameter. This crystal is very pure and clear.

3.2. Surface Treatments

The silica samples were further modified by surface treatments. Table V lists all of the modifications performed on the various forms of silica. Autoclaving was performed in a Harvey SterileMax (model ST75925) autoclave set on the wrapped packs cycle. This cycle brings the temperature to 121°C for 15 minutes and increases the pressure correspondingly. The pressure is then released in a controlled fashion as the unit cools. Once the pressure is near atmospheric, the unit was opened to facilitate cooling. The samples were then immediately sealed to prevent contamination of the sterile samples. Cleaning with ethanol was a simple process of wiping the samples with a lint-free laboratory tissue soaked in ethanol, followed by a rinse in ethanol and a drying wipe with a clean, dry, lint-free laboratory tissue. The samples were handled only with sterile tweezers or laboratory tissues and stored in clean glass vials. Slides, however, were stored in disposable cuvettes.

The etching of the samples in hydrofluoric acid (HF acid) was performed in a fume hood with all the required protective clothing. This clothing consisted of a knee-length lab coat, a knee-length nitrile apron, latex gloves worn beneath nitrile gloves and, of course, a face shield, safety glasses, pants and covered shoes. The HF acid etchant was 10% HF diluted from 50% HF with nanopure (>18M Ω resistance) water. Samples were placed in a teflon beaker and agitated in the etchant for various lengths of time. The optimal agitation time was determined to be 10 minutes. Samples were then removed and rinsed in nanopure water and dried on a laboratory tissue. They were stored in a clean glass vial until protein exposure. Slides were stored in disposable cuvettes.

Table V. Surface Treatments Applied to Various Silica Forms.

Silica Form (Supplier)	Dimensions or Amount	Surface Treatment				
		Original Form	Ethanol Clean	HF Acid Etch	Water Plasma	Heat @1000°C
Slides (Quartz Scientific)	1 of ~ 1.3 x 1.2 x 0.1 cm		X	X	X	X
Cane (Sutter Instruments)	2 of 2 cm (long) x 1 mm (dia)		X	X	X	X
Fiber (Alcatel)	10 of 4 cm (long) x 125 micron (dia)		X	X		X
Cab-o-sil (Cabot Corp.)	2 micrograms	X				X
Stober Spheres	20 micrograms	X				X

Both oxygen and water plasma treatments were initially applied to the silica samples. For simplicity, water plasma was chosen for all subsequent plasma treatments. The plasma was generated in a RF microwave unit (Mercator Control Systems LF-5 Plasma System). Samples were placed on a silica grid and the unit was evacuated to a pre-set pressure. The unit would then fill with water vapor and once a pressure of 0.6 Torr was achieved, the RF source would ignite the plasma. The power output was set to 400W. This state was maintained for 10 minutes after which the unit would release the vacuum and cool.

The heat treatments of the silica samples were done in air in an electric furnace at 1000°C for 4 hours. Samples were placed on a platinum grid for maximum exposure and carefully loaded into the furnace. Upon removal, the samples were cooled in air and then immediately placed in a dessicator to prevent exposure to water vapor. All samples were exposed to protein solutions within a week of their treatment.

3.3. Protein Solutions

All protein solutions were made with tris-buffed saline (TBS) at a pH of 7.40, except for the fluorescein biotin solutions. The recipe for the TBS is shown in Table VI. Human serum albumin (Sigma, A-8763) and bovine

serum albumin (Sigma, A-7511) were utilized initially to determine the binding capacity for various glasses because these proteins are relatively inexpensive. Dilutions of these proteins were 1.0 mg protein/ml TBS, 0.1 mg/ml, 0.01 mg/ml and 0.001 mg/ml. For example, protein may be ordered in a 1mg quantity and so addition of 1mL of TBS would create a 1.0 mg/ml dilution. Typically, aliquots of 1mL were prepared and frozen at -20°C in Nalgene cryogenic vials until use. All protein preparation was performed in a bio-guard hood to prevent both the contamination of the protein and human exposure. As an additional safety measure, latex gloves were worn at all times when dealing with protein solutions.

Streptavidin protein (Sigma, S-4762) from *Streptomyces avidinii* was affinity purified, lyophilized powder. Streptavidin dilutions were also 1.0 mg/ml, 0.1 mg/ml, 0.01 mg/ml and 0.001 mg/ml. Aliquots of 1 mL quantities were frozen until use. Biotin binds very strongly to streptavidin and can be fluorescently tagged. The biotin fluorescein obtained was called 5(6)-(Biotinamidocaproylamido)Pentylthioureidyl-Fluorescein (Sigma, B8889) or fluorescein biotin. This compound is not soluble in tris-buffered saline and so Dimethyl Sulfoxide (DMSO) was used as the solvent instead of TBS. The fluorescein biotin was obtained in vials of 1mg and to this quantity 0.5 mL of DMSO was added. The mixture was agitated until the solute (biotin) dissolved. The 2 mg/mL solution of biotin in DMSO was then diluted with TBS to the desired concentrations. The concentrations were the same as the Streptavidin solutions and 1 mL aliquots were frozen at -20°C.

Immunoglobulin G was also utilized in this study due to its asymmetrical nature and binding ability for other IgG molecules that can be fluorescently tagged. Technical grade mouse IgG (Sigma, I-8765) was diluted to the same concentrations as streptavidin, HSA and BSA with TBS. Aliquots of 1mL were frozen in Nalgene cryogenic vials until use. Goat anti-mouse IgG (F-5387) was Fc specific and conjugated with fluorescein

isothiocyanate (FITC). Again, dilutions were the same as before and aliquots were frozen at -20°C until use.

Table VI. Recipes for Common Chemicals Used in this Study.

Chemical	Amounts, Constituents, and Directions			
<i>Tris-Buffered Saline</i>	4.0 g NaCl	0.1 g KCl	1.5 g Tris Base	
	- dissolve in 400mL DI water, adjust pH to 7.4 with 5N HCl, bring to 500mL			
<i>Laemmli Sample Buffer, Reducing</i>	4.0 mL DI water	1.0 mL Tris *	0.8 mL Glycerol	1.6 mL 10% SDS **
	0.4 mL 2 β mercaptoethanol	0.2 mL BB ***		
<i>Laemmli Sample Buffer, Non-reducing</i>	4.0 mL DI water	1.0 mL Tris *	0.8 mL Glycerol	0.2 mL BB***
* 0.5 M Tris	6.0 g Tris Base	60 mL DI water	- bring to pH of 6.8 with 5N HCl	
** 10% Sodium Dodecyl Sulfate (SDS)	- dissolve 1.0 g of SDS in 10 mL of DI water with gentle stirring			
*** 0.05% Bromophenol Blue (BB)	- dissolve 5.0 mg of Bromophenol Blue in 10 mL of DI water			
<i>Laemmli Tank Buffer</i>	29.0 g Tris Base	144.0 g Glycine	10.0 g SDS	
	- dissolve in 1L DI water stirring gently, bring to 2L			

3.4. Binding Procedure

Once the protein solutions and silica samples are prepared to satisfaction, the binding of proteins to the silica can commence. Frozen protein solutions were placed in a 37°C water bath for at least 10 minutes to thaw and incubate the protein. The warmth incubates the protein so that it will bind efficiently to surfaces. The incubated primary protein solution was added to the vial containing the glass sample as quickly as possible under the bio-guard hood. The sealed vial was then placed in an incubation rocker set at 37°C and 75 rpm for 30 minutes. Tris-buffered saline was then warmed to 37°C and exchanged for the primary protein solution for 5 minutes in the incubation rocker. The purpose of this step was to remove any loosely bound primary proteins and to rinse the vial. The “diminished” primary protein solution was kept for analysis in the freezer. In a single protein binding procedure, at this point, the TBS would be removed from the vial and the glass sample frozen for future analysis. However, in the case of IgG (primary) and anti-mouse IgG (secondary) or streptavidin (primary) and

biotin (secondary) binding, once the glass sample was rinsed with TBS, the secondary protein was introduced. Again, this binding would take place in the incubated rocker at 37°C and 75 rpm for 5 minutes. After this step, another TBS 5 minute rinse in the rocker would take place. Both the second “depleted” protein solution and the “dry” glass sample were stored in the freezer.

3.5. Characterization Techniques

The final goal of this work is to develop a novel characterization technique using proteins to map the surfaces of glasses that cannot be characterized with conventional methods. In order to move toward this goal, many existing methods of surface analysis must be utilized in conjunction with proteins to establish the manner in which proteins and glass interact. Techniques common to glass analysis are put to the test on protein coated glasses and vice versa.

3.5.1. Electrophoresis

Poly-acrylamide gel electrophoresis (PAGE) is a very useful technique for determining the identity of proteins in a mixture and relative amounts. Electrophoresis works on the premise that charged molecules will travel through a medium according to their molecular weight and thus magnitude of charge. Lighter molecules will travel much farther in the same amount of time than heavier molecules, thus separating the molecules according to mass. In PAGE, the medium in which the proteins are separated is a poly-acrylamide gel. This gel can actually come in many types and the formula used in this study was 12% tris-glycine. The gels can be made in the

laboratory by pouring the liquid medium into a cast and gelling it, but a much more reliable route is to order the gels from a supplier. Tris-glycine gels of 12% solids content, 1mm thick, with 10 wells were ordered from Invitrogen (Novex, EC-6005).

All samples, standards and markers must be mixed with the Laemmli sample buffer (LSB-R), which contains the detergents that dissociates the proteins (2 β -mercaptoethanol) and adds the charge (sodium dodecyl sulfate). One half of a milliliter of LSB-R was added to each glass sample taken from the freezer. This vial was then sealed, locked and boiled for 5 minutes. After cooling, the sample was shaken to accumulate all moisture in the vial. Protein standards were made by pipetting the desired amount (typically 5 μ L) of protein solution into a microcentrifuge tube and adding a small amount of LSB-R (15 μ L). This vial was then sealed, locked and boiled for 5 minutes. After cooling, the tube was centrifuged to regain all moisture to preserve an accurate concentration. Samples were never opened to the atmosphere while warm to prevent evaporation, which would alter the concentration.

A gel was placed into the Novex XCell II Mini Cell (Invitrogen, EI9001) and the cell was filled with Laemmli tank buffer. The recipe for the reducing tank buffer is shown in Table VI and a schematic of the Mini Cell is shown in Figure 3.5.1. The wells of the gel were then filled with markers, standards and samples. Generally, 20 μ L was the amount of fluid added to each well. For the protein markers, 5-8 μ L of MultiMark (Invitrogen, LC5725) and Mark 12 (Invitrogen, LC5677) was added individually to two separate wells. Then 15 μ L of LSB-R was added and mixed with the markers in the well. The entire amounts of standards were next pipetted into their respective wells. Finally, 20 μ L of sample (from the 0.5mL of LSB-R added to the glass samples) was added to the proper wells. Any unused well was filled with 20 μ L of LSB-R. A schematic of a gel-loading set-up is shown in Figure 3.5.2. Once the lid of the Mini Cell, which holds the leads to the power source, was secure, the power source was turned on. The power source used was an EC

Apparatus Series 90 Programmable source (EC4000P). The voltage was set to 100V, the amperage was set to 80mA and the power was set to 55mW. The time for which the gel was placed under the applied voltage was dependent on the protein to be studied. Low molecular mass proteins require a much shorter run time than high molecular mass proteins. For streptavidin, a run time of 2 hours was deemed appropriate, while for IgG a run time of 3 hours was sufficient.

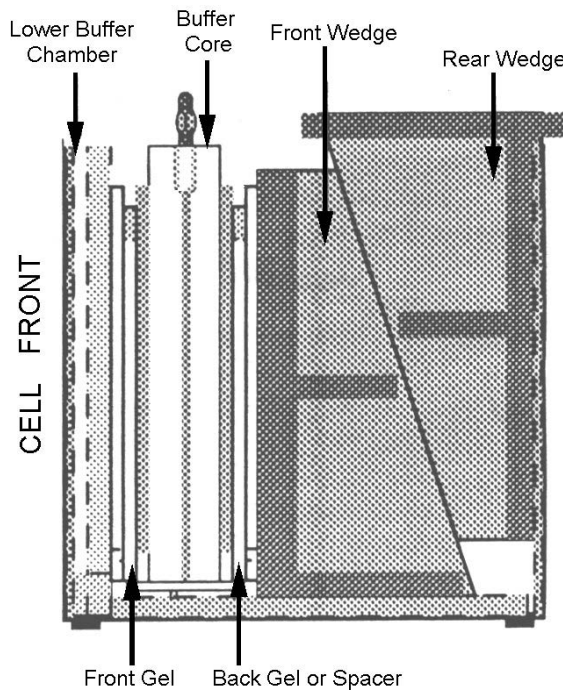


Figure 3.5.1. Side view schematic of the XCell II Mini Cell used for gel electrophoresis.

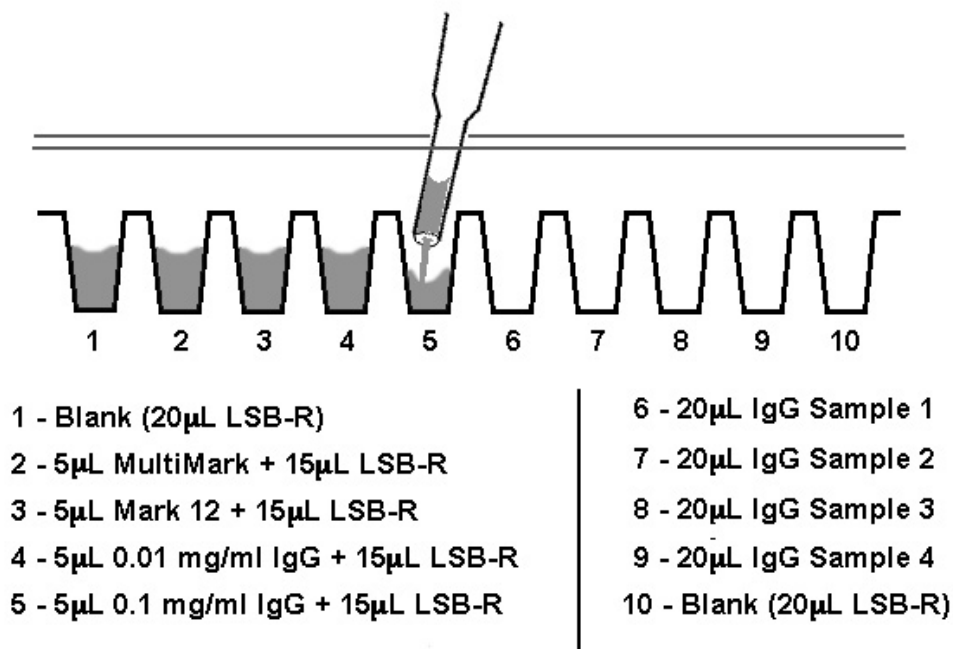


Figure 3.5.2. Schematic drawing of a gel loading set-up.

Once the proteins were satisfactorily separated in the gel, the gel was stained. Initially, the stain used was a silver stain by GelCode™ (Pierce, 18511xx series), but a more efficient silver stain called SilverQuest™ (Invitrogen, LC6070) was used in later experiments. Before staining, the gel must be fixed using a mixture of ethanol, water and glacial acetic acid (50:40:10) for approximately 20 minutes. The staining procedure was then applied as set forth in the SilverQuest™ package. After staining, the gel was sealed in a heat-sealing polymer jacket and stored in the refrigerator. A gel must be imaged for analysis. Since the Bio-Rad Fluor-S multi-imager gave spurious results, other imaging techniques were explored. With a back-light, the gels were photographed with a digital camera. This method resulted in better images than the Fluor-S imager, but were never reproducible because the high intensity of the back-light causes various background colors on the digital camera. Finally, a simple document scanner was determined to be the best option for imaging the gels and actually produced very good images. Since the gel analysis software only recognized TIFF files, the images of the

gels were saved as such. The Quantity One software (version 4.0) was then used to compare the lanes of proteins. The standards were used to determine the unknown sample quantities and the markers were used to verify the molecular weights of the proteins.

3.5.2. Fluorescence Spectroscopy

The procedure for fluorescence performed on protein solutions was exactly the same for each sample, except for the excitation and emission values. The natural fluorescence of streptavidin emanating from the aromatic amino acids was excited at 280 nm and the emission scan was from 285 to 500 nm. The fluorescein isothiocyanate (FITC) tag on the anti-mouse IgG proteins was excited at 485 nm with the emission scan from 490 to 620 nm. The fluorometer is a SPEX 1680 0.22m double grating spectrometer. A special fused quartz cuvette (Starna, 17F-Q-10) with a minimal required volume was used for all samples. A schematic diagram of the instrument including the path of the light is shown in Figure 3.5.3.1.

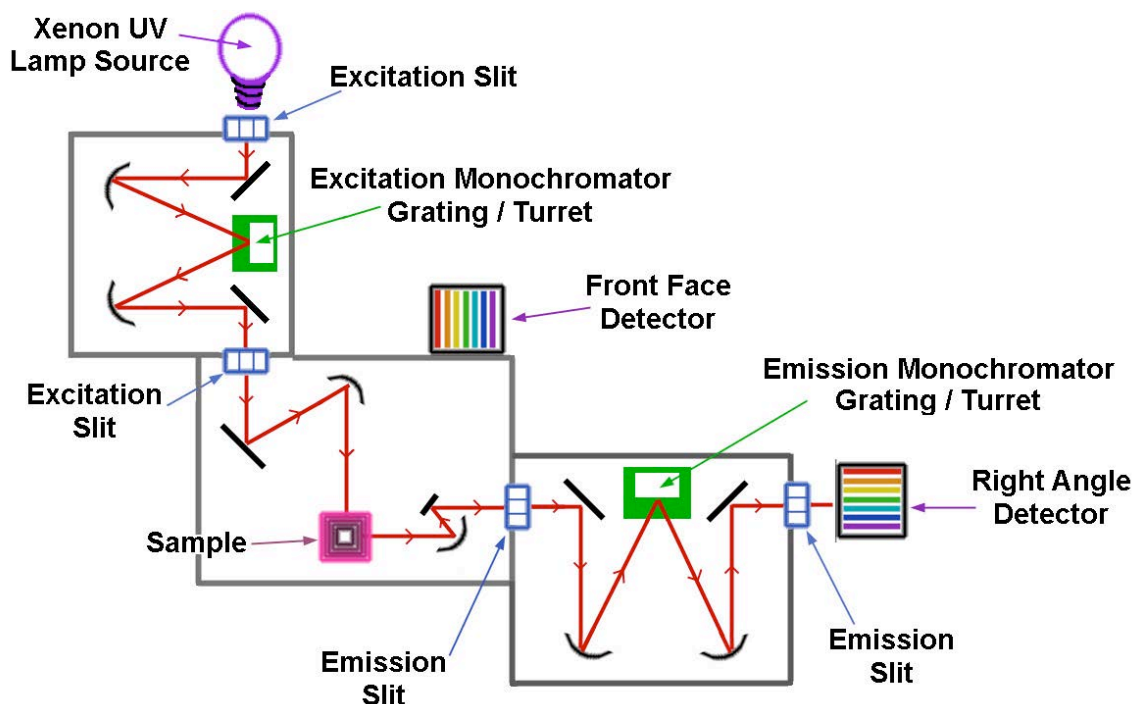


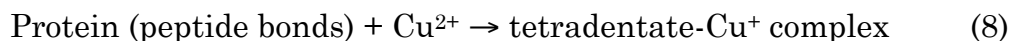
Fig. 3.5.3.1. Schematic diagram of SPEX 1680 fluorescence spectrometer.

400 μ L of sample was pipetted into the quartz cuvette for each analysis. For the first binding set, tris-buffered saline was vigorously forced in and out of the cuvette for cleaning between samples. This was determined to be sufficient to remove proteins adhered to the quartz after a short study. A “dummy” solution was placed in the cuvette prior to the first sample solution in order to create a similar environment for all samples. For the second binding set, ethanol was forced in and out of the cuvette and then the cuvette was dried with compressed air. This cleaning procedure was carried out between each sample. Most samples were run in triplicate for assessing reproducibility. The slits on the spectrometer were set to 2, 2, 1.5, and 1.5 mm respectively. The detector used was at the right angle position, the integration time was set to 1.0 second and the scan size was set to 1.0 nm. After the final sample, the quartz cuvette was cleaned with ethanol and dried in air.

Standard protein solutions were utilized to quantify the unknown protein solutions. The software used for data acquisition and analysis was Datamax (version 2.20). Integration of the emission peaks for the standards gave a relationship of area to mass of protein. Then, the unknown sample area was measured and related back to a mass of protein using the linear relationship obtained for the standards. Protein control samples were also prepared specifically for fluorescence measurements. These controls were prepared as described above for protein solutions, except they were not exposed to glass samples. The controls were also analyzed for their linear mass to fluorescence area relationship.

3.5.3. Bicinchoninic Acid (BCA) Assay

BCA protein assay is based on the reaction between copper ions, bicinchoninic acid and the protein to be analyzed. The reactions that take place are:



Reaction 8 takes place in an alkaline medium, which is known as the Biuret reaction and reaction 9 results in a purple colored complex. The complex exhibits a strong absorbance at 562nm, which is linear with protein concentration. The BCA protein assay reagent kit used was from Pierce (23225). This kit supplies 1L of reagent A, containing sodium carbonate, sodium bicarbonate, bicinchoninic acid and sodium tartrate in 0.2N sodium hydroxide and 25mL of reagent B, a 4% solution of cupric sulfate. Also in the kit are 10 ampules of 1mL of bovine serum albumin at a concentration of 2 mg/ml for use as the standards. By following the procedures outlined in the

reagent kit, a 96 well UV microtiter plate (Corning costar 3635) was filled with 10 μ L of standard or sample and 200 μ L of working reagent in each well. The plate was shaken for 30 seconds then covered and incubated for 30 minutes at 37°C. This heating step helps to develop the color. An image of a fully-loaded and developed plate is shown in Figure 3.5.3.1. The plate is then allowed to cool at room temperature and loaded into the plate reader. The plate reader utilized was a μ Quant (Bio-Tek Instruments) with model number 155336. This reader was programmed to recognize the identity of each well, whether it was a standard or an unknown sample. A print-out of each well identity and concentration in the well follows each reading. It was necessary to then back-calculate the actual concentration of the protein solution since it was diluted in each well with the working reagent.

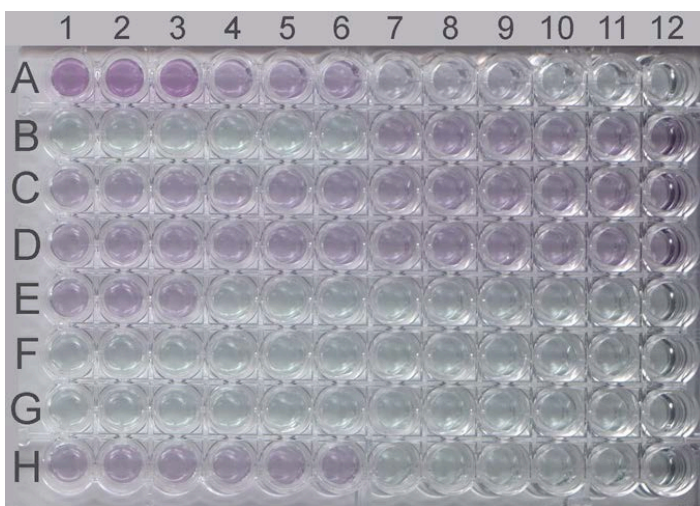


Fig. 3.5.3.1. A 96-well microtiter plate used for BCA assay. The more purple and deeper the color, the higher the protein concentration is in that well.

Protein solutions that were analyzed with this instrument were the aforementioned “diminished” solutions, which were obtained after exposure to a glass sample. The instrument uses an analysis similar to the one used in the fluorescence spectroscopy data analysis, whereby standard absorbance intensities are plotted against their concentration and the unknown sample

concentrations are then found using their absorbance and this linear relationship. At first the standards used were made from the BSA standards supplied with the kit. After some time, it was found that using standards with the same protein identity as the samples gave much better data. A series of streptavidin and mouse IgG standards were prepared with concentrations of: 5 $\mu\text{g/ml}$, 25, 50, 125, and 250 $\mu\text{g/ml}$. These standards were used for analyzing the corresponding unknown protein sample concentrations.

3.5.4. Glancing Incidence X-ray Analysis (GIXA)

Glancing incidence X-ray analysis provides data on surface roughness, film thickness, film density and film roughness. This data is obtained by matching a model to the sample data plot of intensity versus angle in arc seconds. The software used was called REFSIM Mercury (version 0.2) made by Siemens. A flat sample was placed in a X-ray diffractometer (Siemens, Kristalloflex), which sends X-rays at the sample at a grazing angle. A schematic of the experimental set-up is shown in Figure 3.5.4.1.

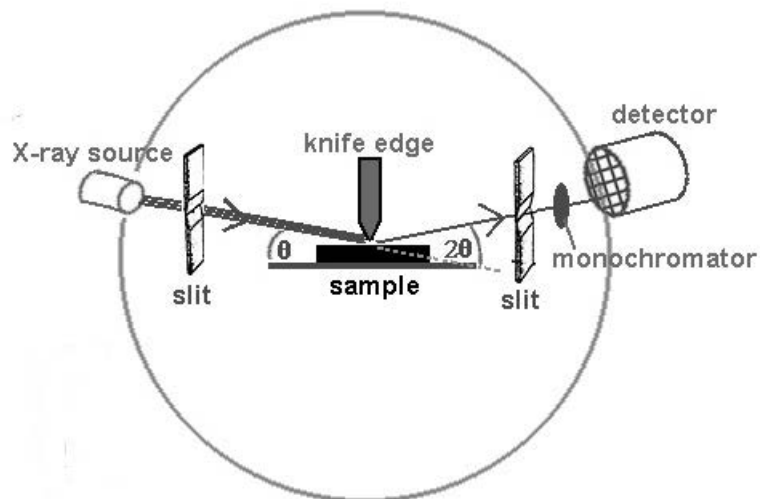


Figure 3.5.4.1. Schematic of the set-up for a glancing incidence X-ray analysis instrument.

3.5.5. Atomic Force Microscopy (AFM)

The atomic force microscope used for obtaining topographical images of silica samples was a Digital Instruments 3100 with a Nanoscope IIIa controller. Both tapping mode and contact mode were used for imaging depending on the circumstances. When purely topographical information was desired, tapping mode was used, which requires tapping mode tips. If further information was desired such as force-distance curves, contact mode was utilized, which requires contact mode tips. Tapping mode cantilever tips were obtained from NanoDevices (MPP-111000) and are comprised of silicon. Contact mode cantilever tips were obtained through Veeco (DNP-20) and are comprised of silicon nitride.

In tapping mode, after the normal protocol of placing the laser on the end of the tip and focussing of the surface and tip, the resonance frequency of the tip must be found and tuned. Only then can the tip be engaged with the

surface. Depending on the quality of the initial image, certain adjustments may be made to the parameters of the microscope such as changing the z-scale, the drive amplitude, the setpoint, the integral gain or the proportional gain. Switching the microscope to scope trace mode allows the user to make the optimal adjustments. Once the trace and retrace lines are falling on top of each other and the noise has been minimized, the height image obtained in image mode should be ideal. Typically, channel 1 is set to height information and, if desired, channel 2 can be set to phase. A phase image provides data on the interaction of the tip with the sample by measuring phase lag. Samples imaged using tapping mode were in their surface treated state unless the sample was prohibitively dirty. In the latter case, isopropyl alcohol was used to remove any excess dirt and dust.

Tapping mode can also be used in a fluid, which is essential for imaging native proteins interacting with a glass surface. Fluid tapping, as it is called, requires a special fluid cell cantilever tip holder. The resonance drive frequency is altered in fluid as well as the path of the laser and so both of these need to be modified again once fluid is introduced. Tris-buffered saline was the fluid of choice, since the proteins are readily dissolved in TBS at a pH of 7.40. The protocol outlined in the Digital Instruments/Veeco Dimension 3100 manual, which is available to purchase on their website, was followed during fluid tapping operations.²

In contact mode, once the laser is placed on the end of the tip, the signal is optimized, and the instrument has been focused on the surface and the tip independently, the tip can be engaged with the surface. Contact mode adjustments will be described in the chemical force microscopy section, since that is the mode used in CFM.

3.5.6. Chemical Force Microscopy (CFM) and Force Volume Imaging

Chemical force microscopy requires the microscope to be in contact mode. In order for the measurement to be considered chemical in nature, typically some form of chemical group is placed on the end of the cantilever tip. These tips are then called functionalized. For this project, a number of functionalized tips were utilized. Carboxyl (-COOH) tips, methyl (-CH₂), amine (R-NH₂) tips, and streptavidin tips were purchased from BioForce Nanosciences.

Once the tip was engaged with the surface, the microscope defaulted to image mode and a number of adjustments were made to optimize the contact of the tip with the surface. As in tapping mode, the deflection setpoint, the integral gain, and proportional gain were adjusted at first in scope mode. Reducing the gains reduced the noise up to a point where signal began to be lost, so it was important to find the right balance in gain. Good starting values prior to collecting force curves were: scan rate = 4-7 Hz, deflection setpoint = -2 (before engaging), integral gain = 3-5, and proportional gain = 3-5.

Collecting a force curve in contact mode was the next step towards obtaining force-volume images. Once the tip was in good contact with the surface by beginning the collection of a height image, the mode was changed to Mode/Force/Advanced. The setpoint was set to a negative value, if it wasn't initially, to put the force curve on scale. Adjusting of the Z scan rate (recommended 4 Hz) and Z scan size as well as other parameters in the "Z Scan Controls" box was done until a good force curve was obtained. The trigger parameters were set to "Relative" and a threshold of 25 nm. The sensitivity parameter was set by drawing a line on the force curve parallel to its slope in the contact region (V-portion of curve). The Z scan start, Z scan size and Z scan rate values were noted. Bringing the curve below the

setpoint by increasing the deflection setpoint was necessary to return to image mode.

To obtain a force volume image, the software was changed to View/Force/Volume and then Probe/Start. In the bottom three panels, the Height image was set to a samples per line value of 64, the Force plots was set to a number of samples of 64, and the Force Volume (FV) panel was set to 64 forces per line. The Z scan values were re-entered if they did not carry over and a force volume image was collected. The Digital Instruments / Veeco Metrology support notes by Hoh *et.al.* is valuable for a detailed force volume protocol.³ Force volume images were collected for all sample forms, including quartz terminals, and all surface treated samples. Force distance curves were obtained in air as well as in tris-buffered saline. All force volume images were obtained in air since the forces were much more distinguishable in air.

3.6. Experimental Procedure References

1. P. Sanford, Erie Scientific Company, Portsmouth, NH, March 15, 2000, Private Communication.
2. "Library - User's Manual" (2003) Veeco Instruments. Accessed on April 13, 2003. Available at <http://www.veeco.com/html/library_user_manual.asp>
3. J. H. Hoh, W. F. Heinz, and E. A-Hassan, "Force Volume," Digital Instruments, Philadelphia, PA, Support Note No. 240 Rev. A, 1997.

4. Results

“Sometimes if you want to see a change for the better, you have to take things into your own hands.” - Clint Eastwood

4.1 Gel Electrophoresis (SDS-PAGE)

In order to view the following gels intelligently, one must first understand what is being shown. A SDS-PAGE gel is a two-dimensional polyacrylamide gel with 10 wells (sometimes 12). Various protein solutions may be placed in these wells, as described in section 3.5.1. Typically, a protein standard marker is used to map the progress, and therefore the mass, of the unknown proteins. These molecular weight markers, either MultiMark™ or Mark 12™, usually both, were placed in the first two or leftmost wells. For quantification purposes, protein standards were also used in each gel. In wells three through five, for example, three protein solutions of known concentration were placed with the reducing sample buffer. The last five to seven wells were then filled with the unknown protein solutions and sample loading buffer. After the gel has been “run” or placed in a potential difference to create the separation of proteins, it is stained with a silver stain. The resulting gel will appear to have lanes, each lane of course corresponding to its original well. Sometimes a lane will be labeled “blank” and in this case only sample loading buffer was placed in the well. The molecular weight markers are very important for detecting the correct protein. Figure 4.1.1. is an image of the unstained “key” that is supplied with each marker upon purchase. This image is used to label the positions of the molecular weight in any given gel and therefore allows accurate detection of the proteins as they are separated, as long as the molecular weight of the protein is known. Once this marker is stained, the bands become darker and

many additional bands may be observed depending on the type and brand of stain used.

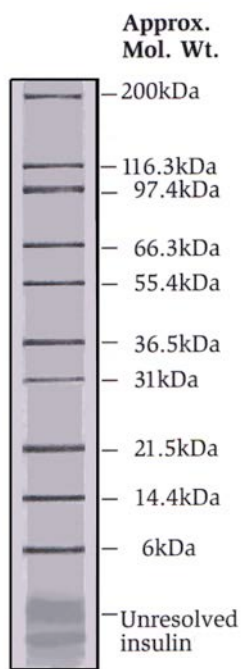


Figure 4.1.1. Mark 12™ molecular weight marker in the lane of a 4-20% gradient tris-glycine gel in the unstained state.

4.1.1. Human Serum Albumin (HSA)

The first piece of information needed was the protein binding capacities of the various forms of glass. The binding capacity was important to determine accurately because the streptavidin protein is fairly expensive and it is always prudent to be as economical as possible. To minimize costs, the relatively inexpensive protein human serum albumin (HSA) was selected due to its size similarity to streptavidin. Initially, soda-lime silicate and borosilicate glasses were considered in addition to silica glass. The samples chosen for these studies were silica (labeled S or Q), soda-lime (labeled SL or SLS), and borosilicate (labeled BS) glasses in the form of cane (or rod) 1 mm in diameter and approximately 2 cm in length. This cane form was chosen

because it is the easiest to work with in terms of handling and fitting into the microcentrifuge tubes.

Figure 4.1.1.1 is an image of a 12% tris-glycine protein stacking gel, hereafter referred to as a gel, with separated HSA proteins at four concentrations. It is important to note the position of the HSA protein in this type of gel for future comparison. Lane 5 in Figure 4.1.1.1 has 0.002 μg of HSA, Lane 6 has 0.02 μg , Lane 7 has 0.2 μg and Lane 8 has 2 μg of HSA protein in its band. Figure 4.1.1.2 is an image of a gel with separated HSA proteins after binding to silica cane. HSA has a molecular mass of 66.4 kDa and its position is labeled with an arrow in all images. The lanes labeled 0.001, 0.01, 0.1, 1.0 and 10.0 represent the concentration of the HSA protein solutions into which the silica cane samples were placed. One can clearly see that the density of the bands does not increase after 0.1 mg/ml exposure for 30 minutes. Therefore, it was concluded that a protein solution concentration of 0.1 mg/ml was sufficient to maximize the binding capacity of silica cane after 30 minutes of exposure. The same study was conducted for SLS cane and also BS cane. After 30 minutes of exposure to four concentrations of HSA solutions (0.001, 0.01, 0.1 and 1.0 mg/ml) the protein was then stripped off the cane using a denaturing sample loading buffer. Figure 4.1.1.3 and Figure 4.1.1.4 are images of the resulting gels for the SLS and BS cane, respectively. Again, it is visually clear that in a protein solution of concentration 0.1 mg/ml no additional protein binds to the glass samples after 30 minutes.

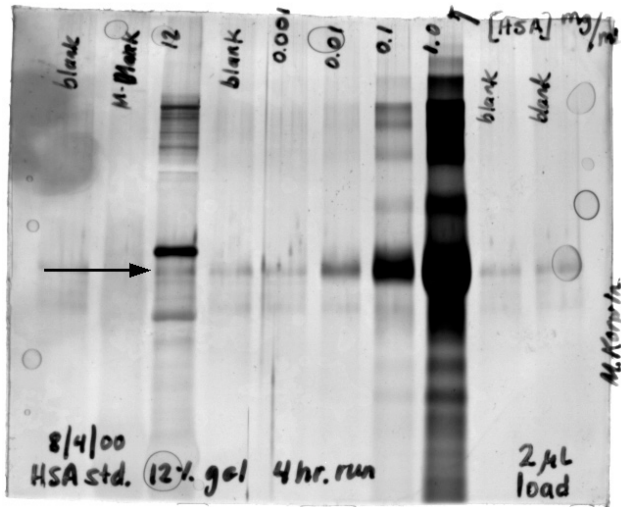


Figure 4.1.1.1. A gel image of four HSA standards (at the arrow) with order of magnitude increases in concentration.

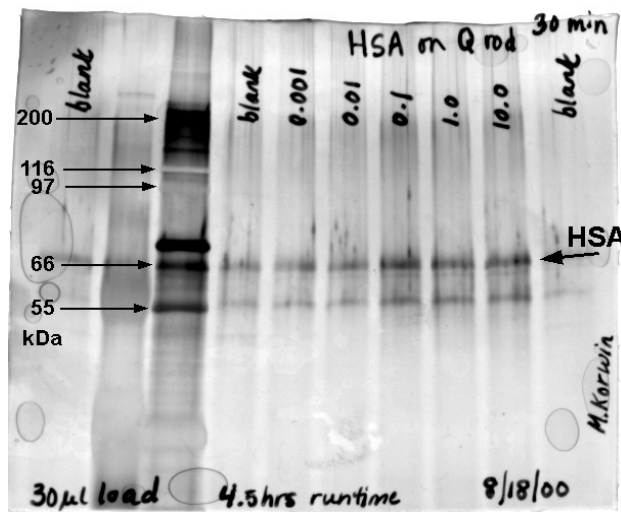


Figure 4.1.1.2. A gel image of five initial concentrations of HSA after being adsorbed for 30 minutes and then stripped from silica (Q) cane.

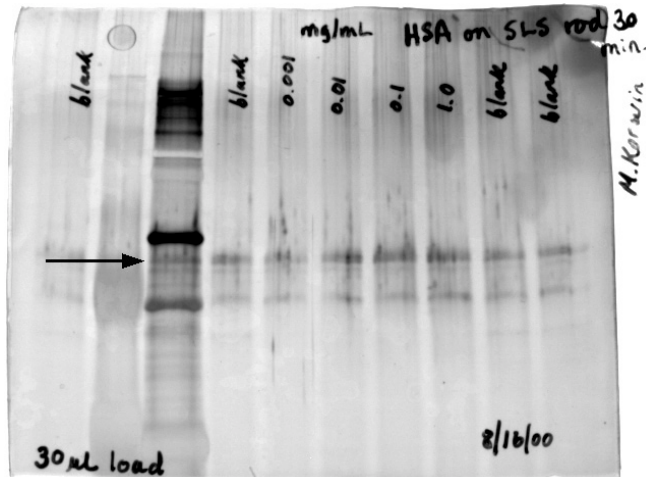


Figure 4.1.1.3. A gel image of four initial concentrations of HSA after being adsorbed for 30 minutes and then stripped from soda-lime silicate (SLS) cane.

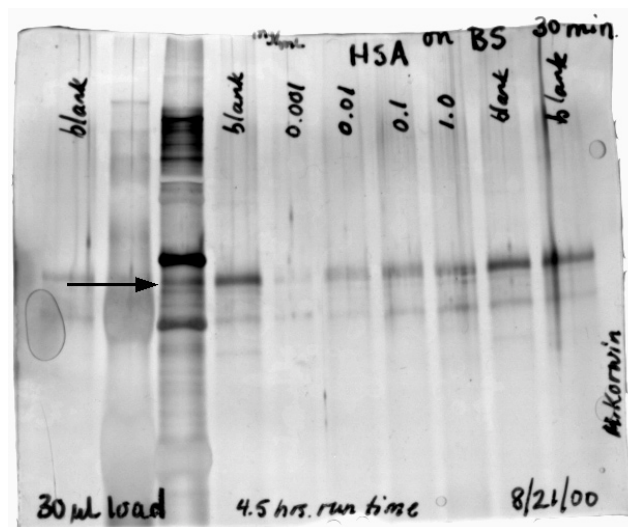


Figure 4.1.1.4. A gel image of four initial concentrations of HSA after being adsorbed for 30 minutes and then stripped from borosilicate (BS) cane.

It was then sensible to create a gel with all three compositions of glass cane using this optimal protein concentration for binding. Figure 4.1.1.5 is an image of such gel with internal standards for clear quantification of binding capacity. It was later discovered that HSA occurs at the same

position as the β -mercaptoethanol doublet because bands appeared consistently in all lanes. This chemical, β -mercaptoethanol, is the reducing agent in the loading buffer and is responsible for breaking disulfide bonds in the protein structure. The severing of these bonds is essential for the denaturing process to be complete after boiling. Without this, some proteins will refold after the boiling procedure. Nevertheless, it was still possible to obtain reliable results, by taking into account that the optical density is slightly higher than it should be. Figure 4.1.1.6 is a “compare lanes export”, done using the Quantity One software, of the gel with HSA after binding to Q, SLS and BS rods. The compare lanes export (CLE) allows the lanes to be plotted as optical density as a function of relative front (the position in the vertical direction of the gel image). It is clear from the CLE that silica (Q) and SLS glass binds a very similar amount of HSA per unit surface area, while BS adsorbs slightly more protein. Specifically, Q binds $2.14 \mu\text{g}/\text{cm}^2$, SLS binds $2.18 \mu\text{g}/\text{cm}^2$ and BS binds $2.89 \mu\text{g}/\text{cm}^2$.

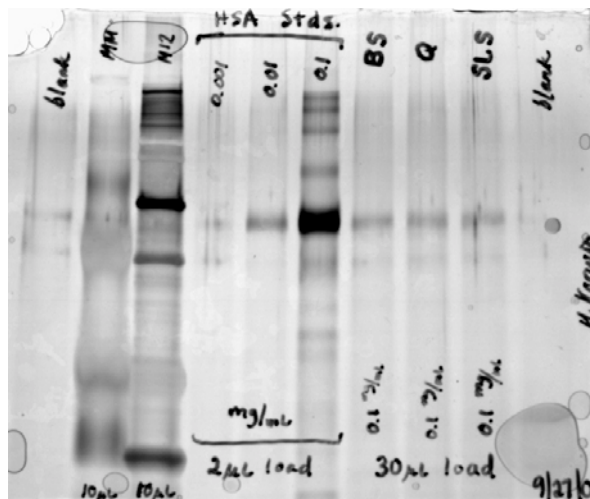


Figure 4.1.1.5. A gel image of the determined maximum required initial protein concentration for meeting binding capacity after being exposed to BS, Q, and SL cane with three internal standards.

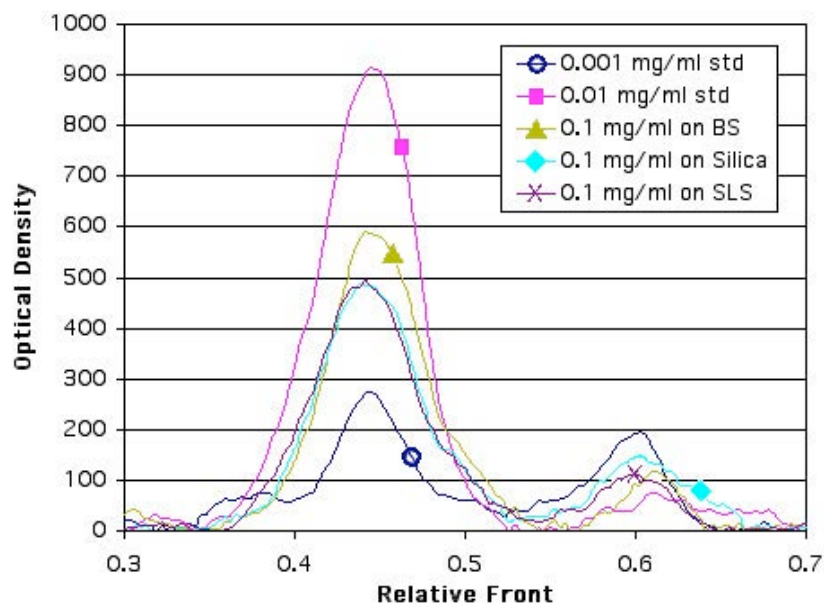


Figure 4.1.1.6. Compare lanes export of the gel in Figure 4.1.1.5 with HSA on Silica (Q), SLS and BS glass rods including two HSA standards.

4.1.2. Streptavidin

Streptavidin was the main protein of study for this research due to its orientation sensitivity with binding biotin. SDS-PAGE was conducted on numerous solutions containing streptavidin that was previously bound to a glass sample. One issue however that went unaddressed for some time was the fact that denatured streptavidin at 13 kDa happens to be of similar weight as the bromophenol blue dye in the sample buffer and so their bands slightly overlap. Once this was taken into account by removing the chemical, it was discovered that streptavidin is a very difficult protein to silver stain. At very low quantities it stains positive, very lightly. Then at higher quantities, streptavidin begins to stain negatively. This leads to much difficulty when trying to fit a linear curve to the optical density response. In an attempt to obtain positive staining of streptavidin, a few different stains were tried, but with little avail. In chronological order, the brand names of the stains attempted were GelCode™, SilverQuest™, and SilverXpress™ (Invitrogen, LC6100). Regardless of the staining problem, Figure 4.1.2.1 is a gel image of streptavidin after binding to silica and SLS slides with either no etch or a 10 minute etch in HF acid. Figure 4.1.2.2 is a plot of optical density versus relative front of the gel with streptavidin after being adsorbed to HF etched and unetched Q and SLS slides. Figure 4.1.2.3 is an image of a gel with streptavidin after having been adsorbed to silica and soda-lime silicate fibers. The silica fiber was a commercial telecommunications fiber of 125 μm in diameter and the soda-lime fiber was created from soda-lime rod on the draw tower and was 230 μm in diameter. Due to the negative staining effect, an inverse of the image data was created. This way, the negatively stained bands become positively stained bands and conventional data analysis is regained. Figure 4.1.2.4 is a CLE of the gel with streptavidin on Q and SLS fiber.

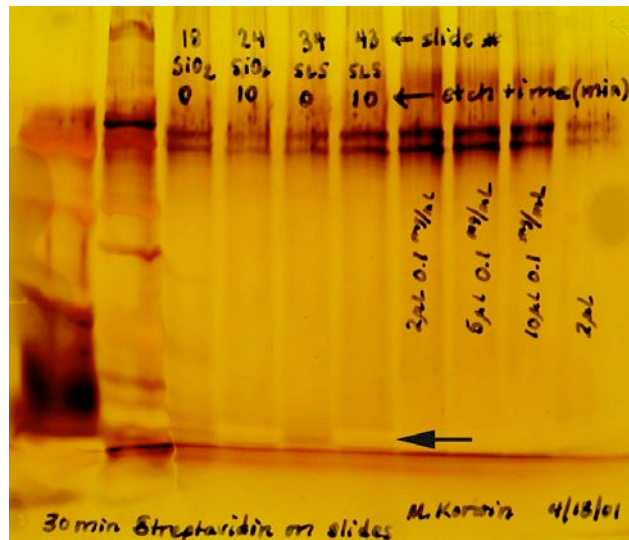


Figure 4.1.2.1. A gel image of streptavidin after binding to silica and SLS slides after no etch or 10 minutes of HF etching.

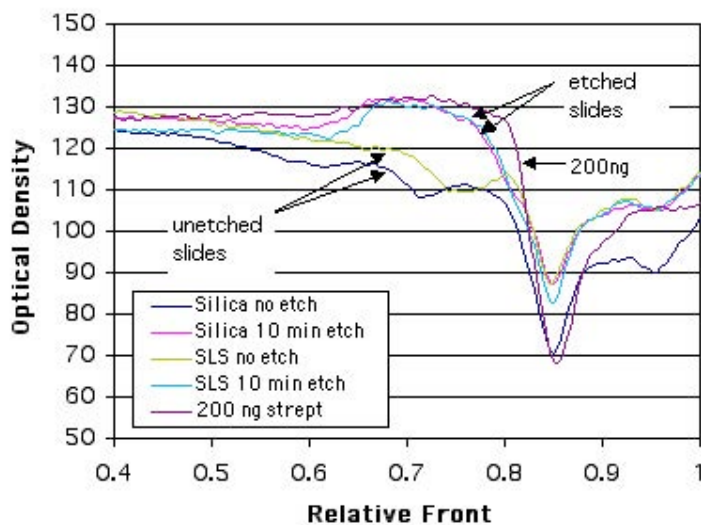


Figure 4.1.2.2. CLE of the gel in Figure 4.1.2.1 of streptavidin on HF etched or unetched Q and SLS slides.

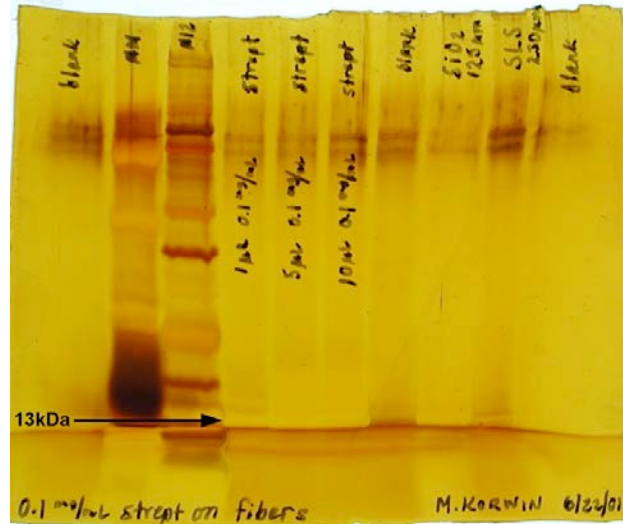


Figure 4.1.2.3. A gel image of streptavidin after binding to silica and soda-lime silicate fibers with internal standards.

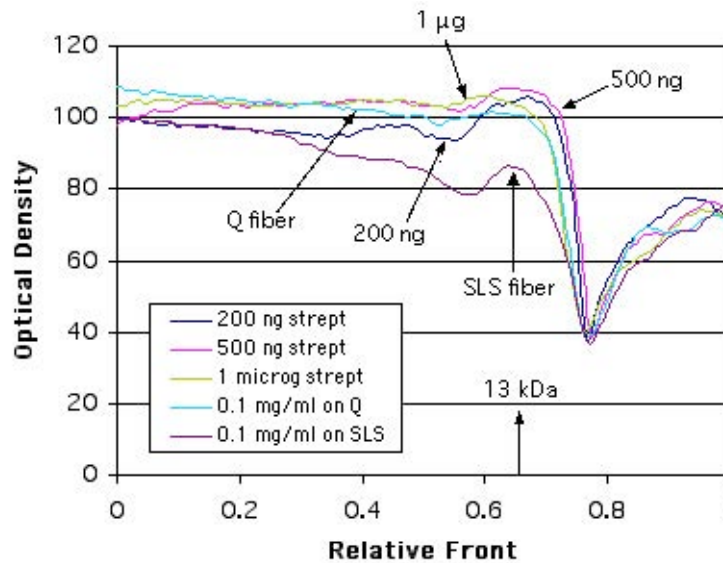


Figure 4.1.2.4. Compare lanes export of the gel in Figure 4.1.2.3 with streptavidin on Q and SLS fibers.

One way to determine the binding affinity of a given protein for a surface is to perform native gel electrophoresis as a function of temperature. This type of gel electrophoresis is called “native” because no denaturing agents are used to separate the proteins from the surface of interest or itself

other than temperature. A series of gels must be created, each at a different temperature, for a binding affinity to be determined. The amount of protein in the band will drastically increase at a given temperature, which corresponds to the energy of desorption for that protein. The image in Figure 4.1.2.5 is a gel resulting from native PAGE at 30°C. Three proteins were exposed to ~160 μm 25-10-65 SLS microspheres or beads. It is evident that at this temperature HSA readily releases from the SLS bead surface. Some BSA is also released while the streptavidin is not resolved at all (due to staining issues). Native gel electrophoresis can only be measured on samples that fit into the wells of the gel. Since the focus of this study changed to solely silica and silica beads can not be made only one native gel was created.

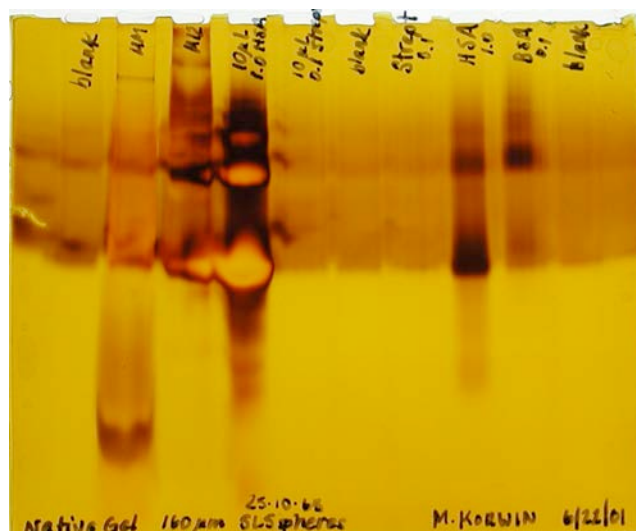


Figure 4.1.2.5. Image of a native gel created from HSA, BSA and streptavidin binding to SLS microspheres.

A binding series was created with 0.1 mg/ml streptavidin on silica cane, fiber, an untreated slide, a 10 minute HF etched slide, and Stöber micron-spheres. Figure 4.1.2.6 is an image of the gel made from this series. The streptavidin band occurs at the position of the arrow and with the GelCode™ staining kit, the bands did not appear. This binding set was then

run in another gel and stained with SilverQuest™. Figure 4.1.2.7 is the image of the resulting gel and the bands at the arrow are much more evident with this stain. Figure 4.1.2.8 is a comparison of the optical densities of the bands in Figure 4.1.2.7. The two bands of note are the 200 ng and 2 μg streptavidin standard bands. The optical density plots of these bands do not behave linearly and this effect must be avoided by decreasing the amount of protein. Due to the moderate success of the SilverQuest™ staining, the fiber binding of 0.1 mg/ml streptavidin to silica and SLS fiber was attempted again and stained with SilverQuest™. The gel image is shown in Figure 4.1.2.9. The resulting streptavidin bands are very light and it appears that the gel had expired due to the extreme spreading of the bands, which is greater than is typically observed.

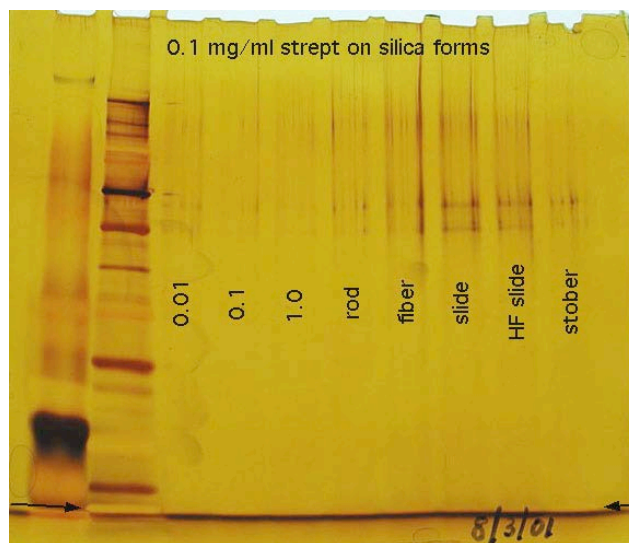


Figure 4.1.2.6. A gel image of 0.1 mg/ml streptavidin adsorbed to five silica forms. Stained with GelCode™.



Figure 4.1.2.7. A gel image of 0.1 mg/ml streptavidin adsorbed to five silica forms. Stained with SilverQuest™.

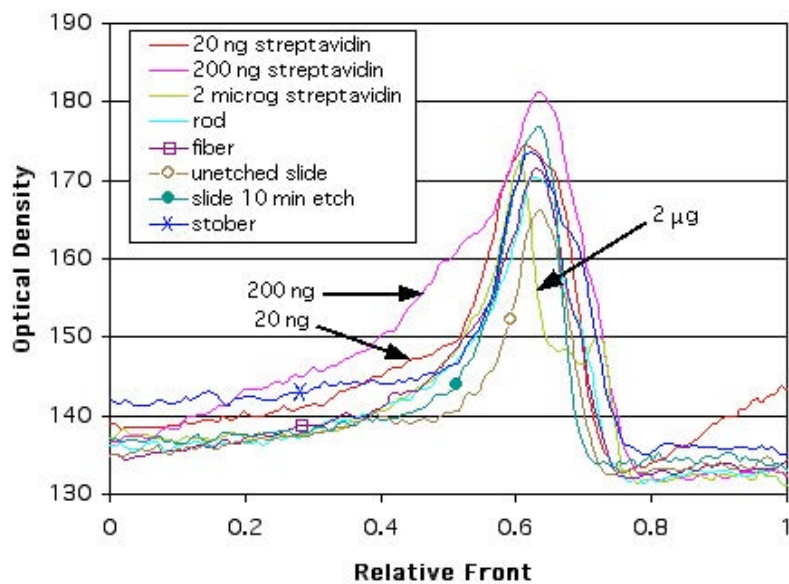


Figure 4.1.2.8. A CLE of the gel in Figure 4.1.2.7.

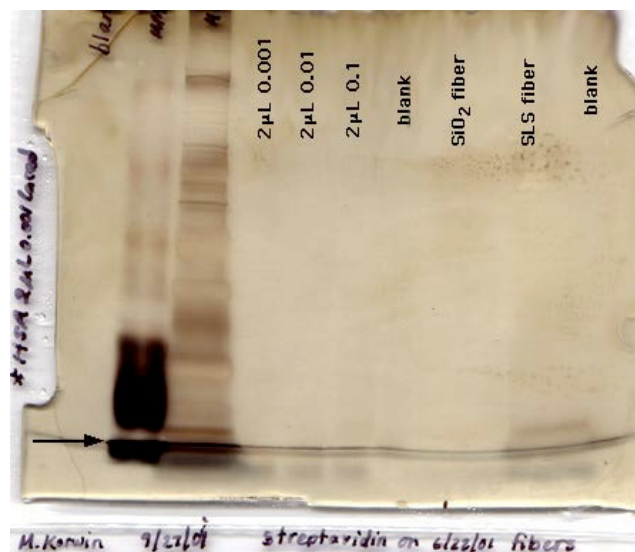


Figure 4.1.2.9. A gel image of 0.1 mg/ml streptavidin adsorbed to Q and SLS fibers. Binding was done on 6/22/01. Stained with SilverQuest™.

All of the samples that have already been discussed had been autoclaved prior to protein binding in order to sterilize and prepare the surface for the biological material. With the introduction of the ethanol cleaning and water plasma treatment as surface preparation methods, autoclaving was no longer an appropriate step. The next gel image, shown in Figure 4.1.2.10, contains duplicates of 0.1 mg/ml streptavidin adsorbed to ethanol cleaned (Lanes 6 & 7) and water plasma treated (Lanes 8 & 9) silica slides. There are also three streptavidin standards in Lanes 3, 4 and 5 in increasing orders of magnitude of concentration. It is evident that all of the sample lanes are outside of the linear region of the standards, meaning that the standards all have a higher concentration in the bands than all of the samples. This condition results in an inability to accurately quantify the amount of protein bound to the samples. Ideally, the sample bands are within the linear region of the standards in the same gel. Nevertheless, the gel in Figure 4.1.2.10 is stained beautifully and was clearly a fresh gel in good condition. Figure 4.1.2.11 is a compare lanes export of this gel and shows the intricacy of the overstained bands.

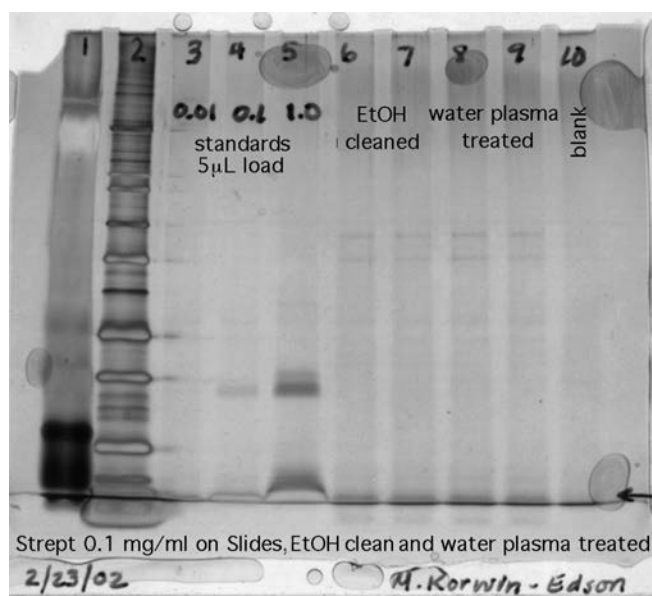


Figure 4.1.2.10. A gel image of 0.1 mg/ml streptavidin adsorbed to ethanol cleaned and H₂O plasma treated silica slides for 30 minutes. Stained with SilverQuest™.

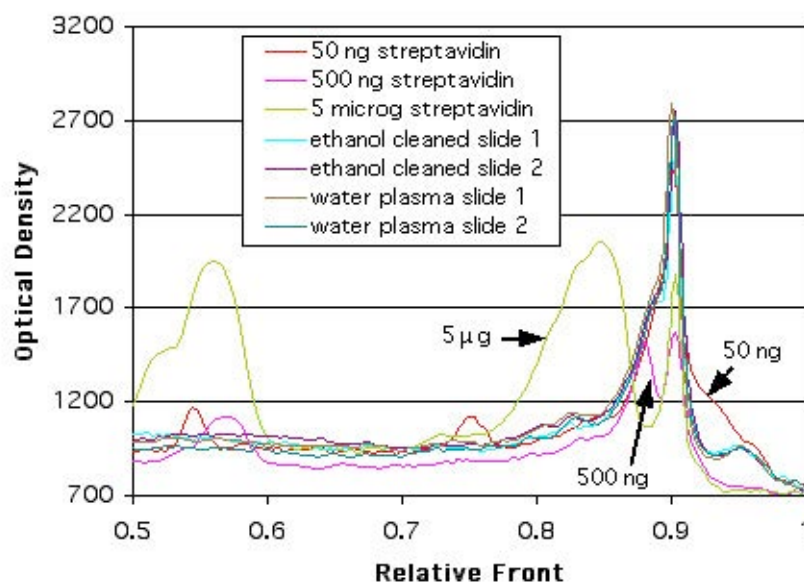


Figure 4.1.2.11. A CLE of the gel in Figure 4.1.2.10.

A hearty attempt was made at resolving the staining problems and many variables were changed amongst the following five gels. Silica (Q) and

borosilicate (BS) rods were chosen as the samples to bind three concentrations of streptavidin solutions (0.001, 0.01 and 0.1 mg/ml). Three standards were also used in each of the electrophoresis gels, namely 2 microliters of 0.1, 0.01 and 0.001 mg/ml, in that order. Figure 4.1.2.12 is the first attempt at determining the binding amounts on SiO₂ and BS rods. For this attempt, one rod was placed in each of the protein solutions for 30 minutes and then stripped off using the typical LSB-R, which includes bromophenol blue, 2β-mercaptoethanol, SDS, glycerine, and water. The resulting gel image shown in Figure 4.1.2.12 was stained with SilverQuest™.

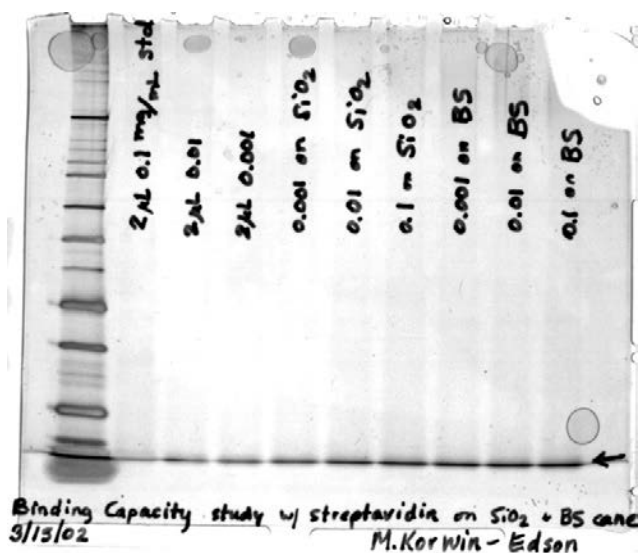


Figure 4.1.2.12. Strept #1. A gel image of three streptavidin solution concentrations exposed to one Q or BS cane for 30 minutes. Stained with SilverQuest™.

It is observed that between the lanes there is a continuous band and this was determined to be the bromophenol blue band that runs across the entire gel. The second gel image shown in Figure 4.1.2.13 is exactly the same as the gel shown in Figure 4.1.2.12, except that the binding procedure was recreated and this time the proteins were stripped off using an LSB-R that had no bromophenol blue. There is a strange broad gray band spanning the entire gel and what is not shown in the image is that the band actually

consists of many tiny bubbles. This gel was initially of poor quality, plus the staining with SilverQuest™ did not result in any visually detectable bands for streptavidin, except for the 200 ng band in Lane 2. Figure 4.1.2.14 shows the image of the third gel in the series and this gel is the same as the previous in that there was no bromophenol blue in the LSB-R. The only difference was an increase in the loading amounts. Instead of 2 microliters of standard, 5 microliters were used and 25 microliters of sample were loaded instead of 20 microliters.

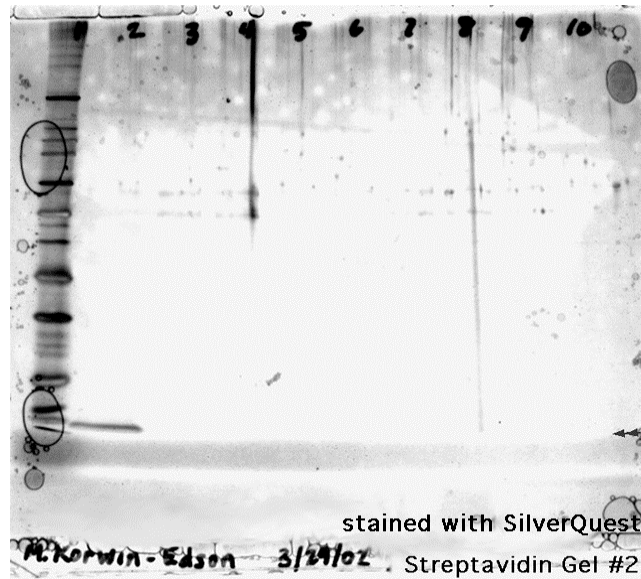


Figure 4.1.2.13. Strept #2. A gel image of three concentrations of streptavidin exposed to one Q or BS cane each. The LSB-R used had no bromophenol blue.

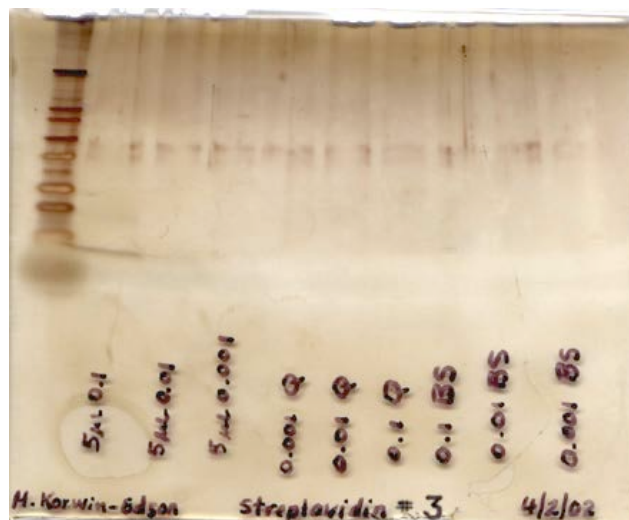


Figure 4.1.2.14. Strept #3. A gel image of three concentrations of streptavidin exposed to one Q or BS cane each. Loading quantities were higher than previous gel.

The doublet of 2 β -mercaptoethanol is clearly seen in Figure 4.1.2.14 between 66 and 55 kDa. Still, the only band visually detectable is the 500 ng quantity band in Lane 2. This is very poor, since SilverQuest™ is claimed to be able to resolve sub-nanogram levels of protein. The fourth gel in this series was an attempt to increase the level of protein in the sample lanes by exposing the various protein solutions to two pieces of cane instead of just one, plus the LSB-R was halved to 0.25 mL instead of 0.5 mL. The loading amounts for the standards were also doubled to ten microliters and the loading amount for the samples was 20 microliters. The picture in Figure 4.1.2.15 is of the resulting gel. Again, the only band able to be seen is the 1 microgram band in Lane 2. Even 100 ng of streptavidin is not detectable with SilverQuest™, as the band in Lane 3 is not evident. The limit of detection of the SilverQuest™ staining kit for streptavidin seems to be 200 ng. The fifth and last gel image in this series is shown in Figure 4.1.2.16. It is the same gel setup as the previous gel, except that the amount of protein in Lane 2 is only 200 ng. This gel was stained with a new silver staining kit called SilverXpress™ and the results are slightly better. All of the bands can

be seen but they are very faint, especially for the sample lanes. It is evident though that the sample bands are within the linear range of the standards in the same gel. This gel is finally deemed a success. SilverXpress™ is the best stain of the three examined in this study for silver staining streptavidin protein.

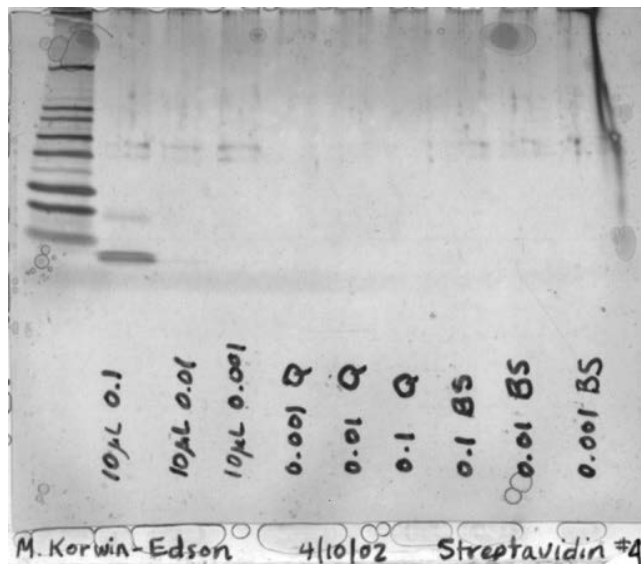


Figure 4.1.2.15. Strept #4. A gel image of three streptavidin solution concentrations exposed to two Q or BS rods each with half as much LSB-R (no dye) for boiling.

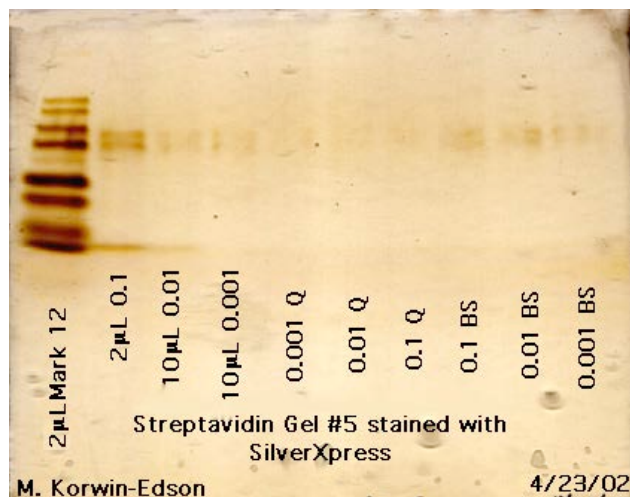


Figure 4.1.2.16. Strept #5. A gel image of three concentrations of streptavidin exposed to two Q or BS rods each. Stained with SilverXpress™.

Streptavidin solution at a concentration of 0.1 mg/ml was adsorbed to two quantities of Stöber microspheres. Amounts of 1.85 mg and 3.7 mg were chosen to see if there was a doubling in the amount of protein bound to the higher quantity of microspheres at the same concentration of protein. Figure 4.1.2.17 is an image of the resulting gel after staining with SilverXpress™. A clear increase of the band density by a factor of two for the higher amount of microspheres is not observed, which leads one to believe that with the higher surface area of the micron-sized silica spheres, the binding is no longer being quenched at this protein concentration. It is interesting to note that the doublet band, which was believed to be 2β-mercaptoethanol, only occurs in the four lanes designated for samples. It may be possible that these bands are not caused by the denaturing agent, but are a result of the binding and stripping of streptavidin off Stöber spheres.

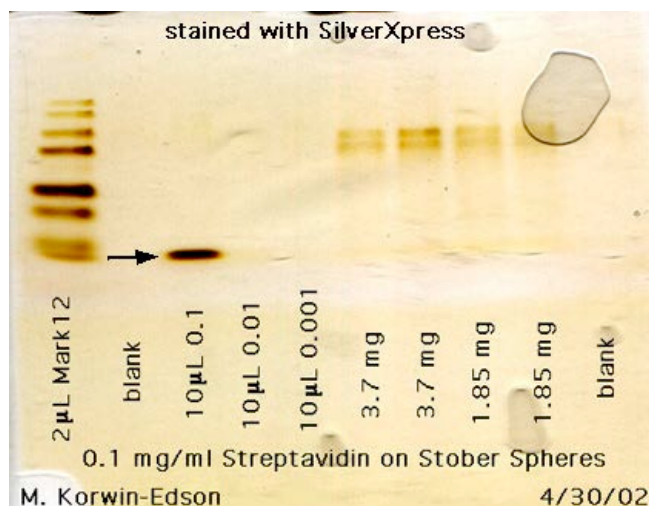


Figure 4.1.2.17. A gel image of 0.1 mg/ml streptavidin solutions exposed to either 3.7 mg of Stöber spheres or 1.85 mg of Stöber spheres. Stained with SilverXpress™.

For the purpose of brevity a sample naming system was created and will be used to refer to the samples from here on. The first two letters refer to the silica form; Sl for slides, Ca for cane, Fi for fibers, PC for Cab-o-Sil®, and SS for Stöber spheres. The second two letters refer to the surface

treatment; ethanol cleaned samples are labeled as Et, HF etched samples are labeled as HF, water plasma treated samples are labeled as WP, and the samples treated at 1000°C for 4 hours are labeled as Tt. For completeness, the third two letters of the sample naming system correspond to the protein to which the samples were exposed, either St for streptavidin or Ig for immunoglobulin G. The last number refers to the concentration of the protein solution, 01 stands for 0.01 mg/ml and 1 refers to 0.1 mg/ml. For example, SIHFSt01, is a silica slide that has been etched in HF for 10 minutes and is exposed to a 0.01 mg/ml streptavidin protein solution.

The streptavidin samples from binding set one were not put into gels, but those from binding set two were measured using SDS-PAGE. These gels were stained with SilverXpress™, as it was determined that of the silver stains examined, this stain works the best for streptavidin. Figure 4.1.2.18 is a gel image of 0.01 mg/ml streptavidin adsorbed to eight silica samples; an ethanol cleaned slide, a HF etched slide, a water plasma treated slide, a 1000°C heat treated slide, two ethanol cleaned cane, two HF etched cane, two water plasma treated cane, and two 1000°C heat treated cane. There are also three internal standards of quantities; 0.025 micrograms, 0.25 micrograms and 1.25 micrograms present in the gel. The bands at the arrow are only visible for the higher of the two standards and all other bands are not detectable. Figure 4.1.2.19 is the same gel setup, except that the protein concentration was 0.1 mg/ml streptavidin. Again, it is clear that at the arrow only the 1.25 microgram and 0.25 microgram standards are visible. It appears that the lower limit to staining sensitivity is therefore somewhere between 0.25 micrograms and 0.025 micrograms. For these two gels, the amount of LSB-R put in with the sample was 0.5 mL and the sample well loading amount was 20 µL.

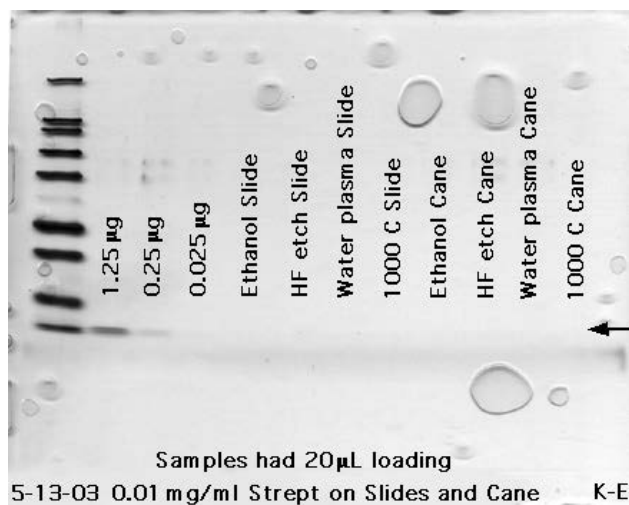


Figure 4.1.2.18. A gel image from Binding Set #2 with 0.01 mg/ml streptavidin adsorbed to silica slides and cane with various surface treatments and three internal standards. The streptavidin band occurs at the arrow.

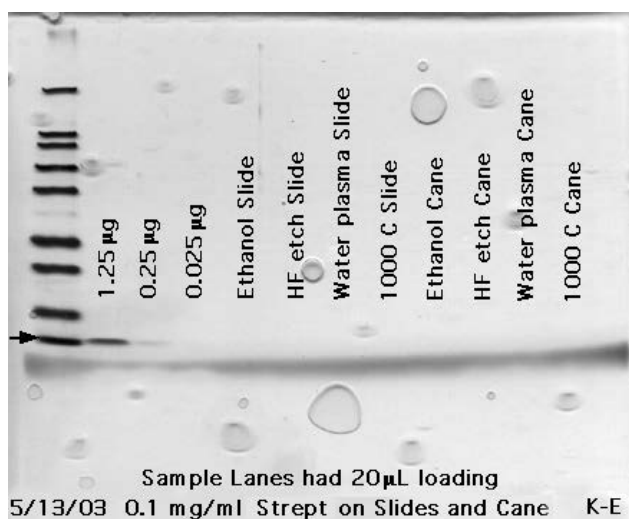


Figure 4.1.2.19. A gel image from Binding Set #2 with 0.1 mg/ml streptavidin adsorbed to silica slides and cane with various surface treatments and three internal standards. The streptavidin band occurs at the arrow.

From binding set two, the silica fiber, Cab-o-Sil® and Stöber spheres were then electrophoresed after exposure to 0.01 mg/ml and 0.1 mg/ml

streptavidin protein solutions separately. These two gels had only 0.25 mL of LSB-R for boiling instead of the previous 0.5 mL and again the sample well loading amount was 20 μ L. Figure 4.1.2.20 is a gel image of the 0.01 mg/ml on fiber and powders. Contrary to previous gels the 0.025 microgram band shows up in this gel as do most of the sample bands. The SilverXpress™ staining procedure was exactly the same as for the previous gels. Figure 4.1.2.21 is a gel image of the fiber and powder samples exposed to 0.1 mg/ml streptavidin for 30 minutes. In this gel, it is fairly evident that there are bands in all of the lanes at the 15 kDa arrow mark. The band is very strong for the standards as well as the fibers and as-made Stöber spheres. Table VII shows the values for the amount of protein in these bands and the corresponding binding based on surface area. The fit to the standards calibration plot of maximum intensity versus micrograms was an exponential of the form: Micrograms = 2.0939E-03 exp ((5.7104*10⁻⁰²)*MaxInt).

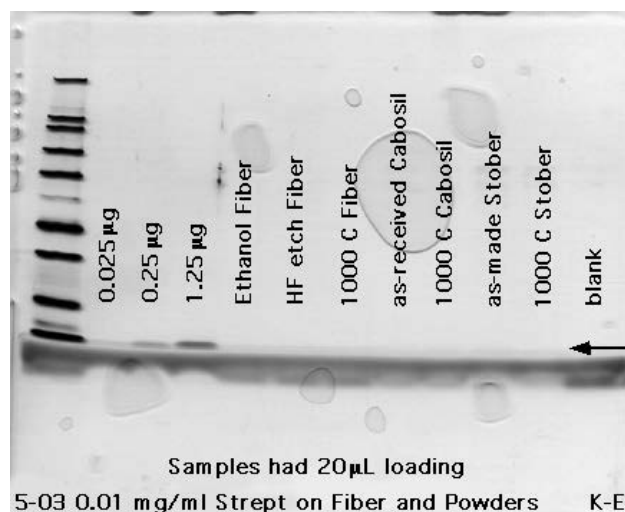


Figure 4.1.2.20. A gel image from Binding Set #2 with 0.01 mg/ml streptavidin adsorbed to silica fiber and powders with various surface treatments and three internal standards. The streptavidin band occurs at the arrow.

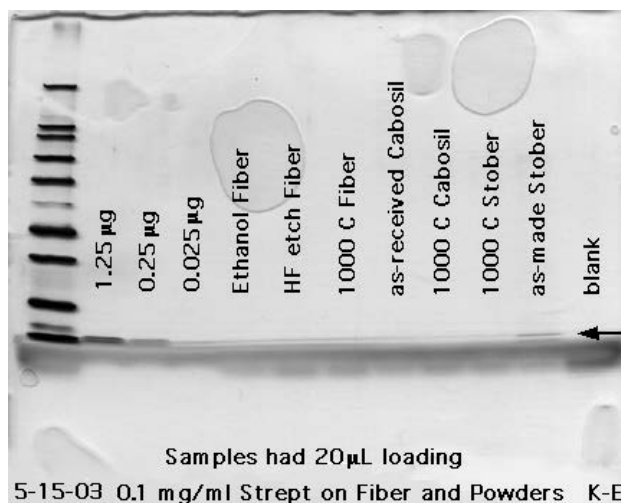


Figure 4.1.2.21. A gel image from Binding Set #2 with 0.1 mg/ml streptavidin adsorbed to silica fiber and powders with various surface treatments and three internal standards. The streptavidin band occurs at the arrow.

Table VII. Protein Band Quantification for the Gel in Figure 4.1.2.21 along with Calculated Binding Amounts

Lane	Maximum Intensity	Micrograms	Binding Amount ($\mu\text{g}/\text{cm}^2$)
1.25 microg	113.9	1.25	
0.25 microg	79.84	0.25	
0.025 microg	45.37	0.025	
FiEt	33.18	0.014	0.0088
FiHF	32.59	0.013	0.0085
FiTt	35.24	0.016	0.0099
PCar	28.98	0.011	1.808E-06
PCTt	19.31	0.006	1.041E-06
Ssar	59.28	0.062	7.925E-05
SSTt	21.22	0.007	9.018E-06

4.1.3. Immunoglobulin G (IgG)

The SDS-PAGE results for mouse IgG and anti-mouse IgG after being adsorbed to and then stripped off of several silica samples follows. Immunoglobulin is a protein of 150 kDa molecular weight that consists of two heavy chains with 50 kDa molecular weight and two light chains of 25 kDa molecular weight. Three distinct band regions for IgG are expected to be observed as it is denatured during the SDS-PAGE process. Two binding sets

were created, meaning that both 0.01 mg/ml and 0.1 mg/ml IgG protein solutions were exposed to the entire gamut of silica samples as a function of forming and surface treatments.

From the first binding set, Figure 4.1.3.1 is an image of a SDS-PAGE gel consisting of mouse IgG and anti-mouse IgG on HF etched fibers or ethanol cleaned fibers. Two internal standards were used for this gel, namely, 0.05 micrograms and 0.5 micrograms of anti-mouse IgG. All of the unknown samples are within the linear range of the standards. The blank lane shows that no extraneous protein is present. For the most part, three distinct bands can be seen for the 150kDa IgG band position, as well as three band regions for the high concentration lanes. For the 0.01 mg/ml samples, the amount of protein bound to the FiHF is 0.05 μg (0.032 $\mu\text{g}/\text{cm}^2$) and FiEt adsorbed 0.10 μg (0.064 $\mu\text{g}/\text{cm}^2$) of IgG. For the 0.1 mg/ml IgG solutions, the amount of protein adsorbed to FiHF is 0.27 μg (0.172 $\mu\text{g}/\text{cm}^2$) and to FiEt is 0.25 μg (0.159 $\mu\text{g}/\text{cm}^2$). These quantities were found using the calibration function in the Quantity One software, which integrates the area under the relative front versus optical density plot. It is also possible, as long as the bands are not overloaded, to use the maximum intensity of the optical density to determine the quantity of protein. This method can be done in Excel and the binding amounts found were quite different from those found using the Quantity One software. Sample FiHFIg01 bound 0.07 μg , the FiHFIg1 sample bound 0.26 μg , the FiEtIg01 sample bound 0.15 μg and the FiEtIg1 fiber bound 0.28 μg . On a per surface area basis this correlates to 0.04, 0.16, 0.10, and 0.18 $\mu\text{g}/\text{cm}^2$, respectively.

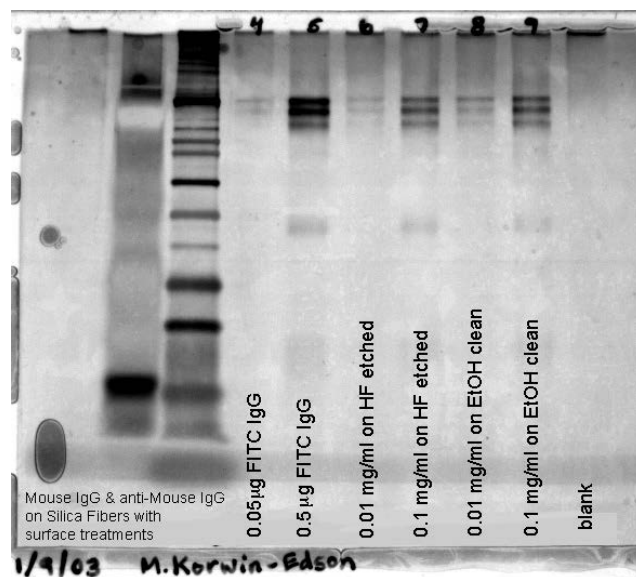


Figure 4.1.3.1. A gel image of two concentrations of mouse IgG and anti-mouse IgG on silica fibers with either an HF etch treatment or an ethanol clean treatment.

From the first binding set, silica slides were exposed to two concentrations of mouse IgG and anti-mouse IgG for 30 minutes. The surface treatment on these slides was either an ethanol clean, a HF etch for 10 minutes or a water plasma treatment for 10 minutes. Figure 4.1.3.2 is an image of a gel created from these slides. Again, internal standards were used in quantities of 0.05 µg and 0.5 µg. The densities of the sample bands fall between the standards, so it is safe to assume that quantification should be valid. The binding amounts from Quantity One (Q1) per square centimeter of slide surface are negligible for SIETIg01, negligible for SIHF Ig01, and negligible for SIWPIg01. The Q1 results for the 0.1 mg/ml IgG solutions are 0.011 µg/cm² for SIET, 0.032 µg/cm² for SIHF, and 0.029 µg/cm² for SIWP. By taking the maximum optical density values for the samples and comparing them to the standards, different results for binding amount are obtained. SIETIg01 bound 0.01 µg/cm², SIHF Ig01 bound 0.02 µg/cm², SIWPIg01 bound 0.02 µg/cm², SIETIg1 bound 0.06 µg/cm², SIHF Ig1 bound 0.09 µg/cm², and SIWPIg1 bound 0.04 µg/cm².

Figure 4.1.3.3 is an image of the SDS-PAGE gel from two concentrations of IgG adsorbed to silica cane. Q1 area results for CaEtIg01 are 0.016 $\mu\text{g}/\text{cm}^2$, for CaEtIg1 are 0.054 $\mu\text{g}/\text{cm}^2$, for CaHF Ig01 are negligible, for CaHF Ig1 are 0.07 $\mu\text{g}/\text{cm}^2$, for CaWPIg01 negligible, and for CaWPIg1 are 0.016 $\mu\text{g}/\text{cm}^2$. Excel maximum intensity results could not be compiled for the 0.01 mg/ml samples since these sample bands have optical densities below that of the lower standard and therefore is not within the linear region. The 0.1 mg/ml concentration was able to be calculated and CaEtIg1 bound 0.07 $\mu\text{g}/\text{cm}^2$, CaHF Ig1 adsorbed 0.08 $\mu\text{g}/\text{cm}^2$, and CaWPIg1 adsorbed 0.005 $\mu\text{g}/\text{cm}^2$.

Figure 4.1.3.4 is an SDS-PAGE gel of IgG on as-received Cab-o-Sil[®] and as-made Stöber spheres. It is clear from the image that both the fumed silica and the colloidal silica bind a very high amount of protein. Q1 found binding amounts of 6.3×10^{-5} (or 6.3E-5) $\mu\text{g}/\text{cm}^2$ for SSIg01 at 0.49 μg , 0.0012 $\mu\text{g}/\text{cm}^2$ for SSIg1 at 0.94 μg , 6.6E-5 $\mu\text{g}/\text{cm}^2$ for PCIg01 at 0.4 μg , and 1.7E-4 $\mu\text{g}/\text{cm}^2$ for PCIg1 at 1.05 μg . The maximum intensity calculation could only be done for 0.01 mg/ml samples. The Stöber spheres bound 0.44 micrograms of protein and the Cab-o-Sil[®] adsorbed 0.41 micrograms of protein. This correlates well with the Q1 data. On a surface area basis however, these large binding numbers dwindle to 0.0006 $\mu\text{g}/\text{cm}^2$ and 6.8E-5 $\mu\text{g}/\text{cm}^2$, respectively, due to the high specific surface area of the spheres. All protein quantities found in the gels and the binding amounts for each sample in binding set one are shown in Table VIII.

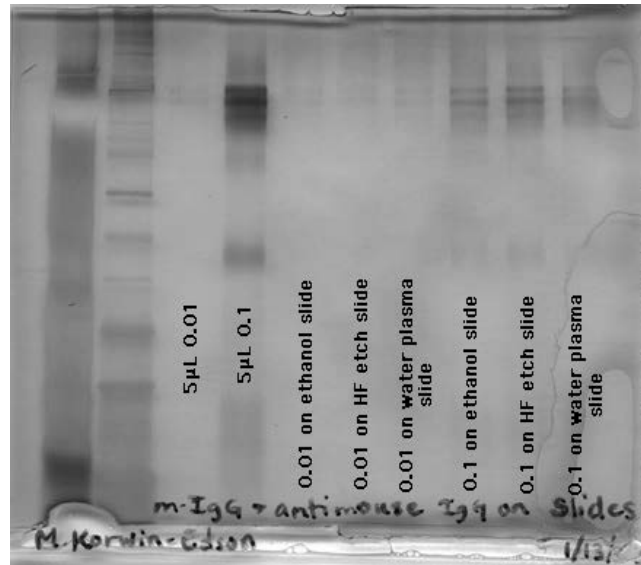


Figure 4.1.3.2. A gel image of two concentrations of mouse IgG and anti-mouse IgG on silica slides with one of three surface treatments.

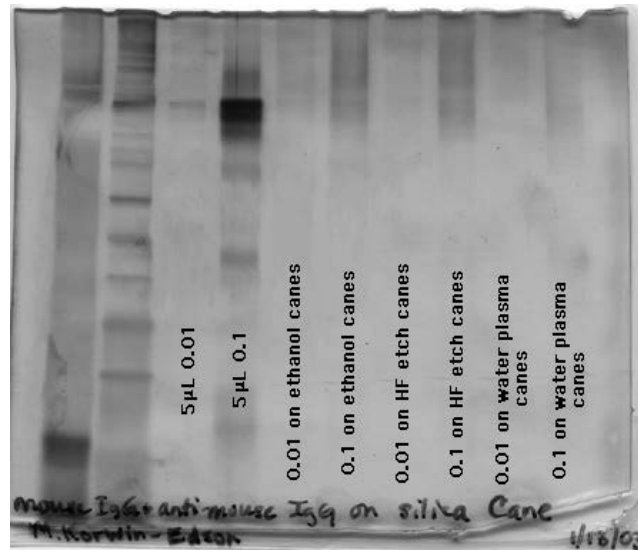


Figure 4.1.3.3. A gel image of two concentrations of mouse IgG and anti-mouse IgG on silica cane with one of three surface treatments.

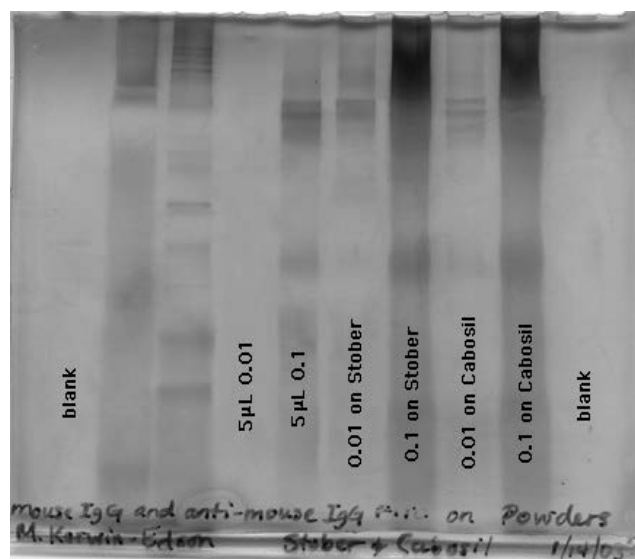


Figure 4.1.3.4. A gel image of two concentrations of mouse IgG and anti-mouse IgG on either silica Cab-o-Sil® or Stober spheres.

Table VIII. Primary and Secondary IgG Protein Binding Quantities Adsorbed to Surface Found Using Two Separate Methods for Binding Set One

Sample	Quantity One Area Values		Excel Maximum Intensity Values	
	Protein Adsorbed (micrograms)	Binding Coverage (microg/cm ²)	Protein Adsorbed (micrograms)	Binding Coverage (microg/cm ²)
SIETlg01	negligible	negligible	0.024	0.006
SIHFlg01	negligible	negligible	0.064	0.018
SIWPlg01	negligible	negligible	0.079	0.021
SIETlg1	0.040	0.011	0.240	0.064
SIHFlg1	0.110	0.032	0.298	0.085
SIWPlg1	0.100	0.029	0.154	0.045
CaETlg01	0.020	0.016	n/a	n/a
CaHFlg01	negligible	negligible	n/a	n/a
CaWPlg01	negligible	negligible	n/a	n/a
CaETlg1	0.070	0.054	0.094	0.073
CaHFlg1	0.090	0.070	0.108	0.084
CaWPlg1	0.020	0.016	0.006	0.005
FiETlg01	0.100	0.064	0.150	0.096
FiHFlg01	0.050	0.032	0.068	0.043
FiETlg1	0.250	0.159	0.283	0.180
FiHFlg1	0.270	0.172	0.259	0.165
PCarlg01	0.400	6.60E-05	0.410	6.80E-05
PCarlg1	1.050	1.70E-04	n/a	n/a
SSarlg01	0.490	6.30E-05	0.440	6.00E-04
SSarlg1	0.940	1.20E-03	n/a	n/a

The second binding set consists of all the samples in the first set plus an additional heat treatment of 1000°C for 4 hours that was applied to all forms of silica. This addition increased the sample number from 40 to 60 samples. Gels were again created from all samples, which were sorted mainly by protein type and concentration in an attempt to consistently achieve sample band optical densities within the standards. Gels for binding set two were of the 12 well variety, which allows higher efficiency. All of the IgG gels presented below were stained with SilverQuest™.

Figure 4.1.3.5 is an image of a gel with 0.01 mg/ml IgG on fibers and powders. Figure 4.1.3.6 is the corresponding compare lanes export plot of optical density versus relative front. Figure 4.1.3.7 is an image of a similar gel after exposure to a protein concentration of 0.1 mg/ml and Figure 4.1.3.8 shows the corresponding compare lanes export. Figures 4.1.3.9 and 4.1.3.10 are representations of the gel resulting from 0.01 mg/ml IgG protein adsorbed to silica slides and cane and the corresponding CLE. Figures 4.1.3.11 and 4.1.3.12 are a gel image of 0.1 mg/ml IgG adsorbed to silica slides and cane and its CLE, respectively. These four gels were quantified by the area method in Quantity and also by the maximum intensity method in Excel. The CLE results were used to calculate the binding quantities on a surface area basis. These quantities are combined and shown in table IX.

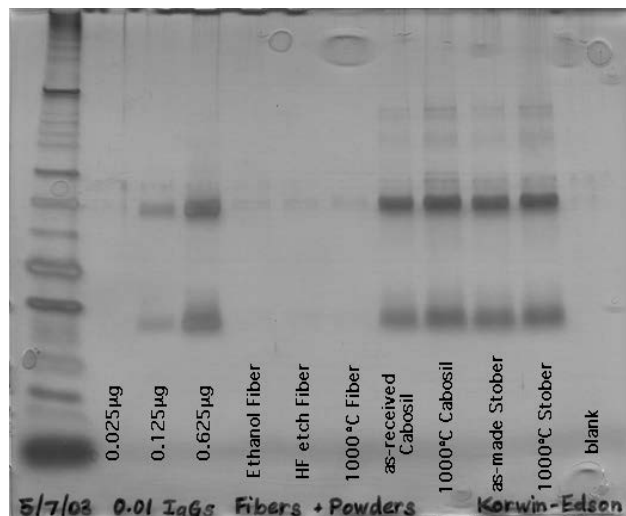


Figure 4.1.3.5. A gel image of 0.01 mg/ml mouse IgG and anti-mouse IgG adsorbed to silica fiber, Cab-o-Sil®, or Stöber spheres with various surface treatments.

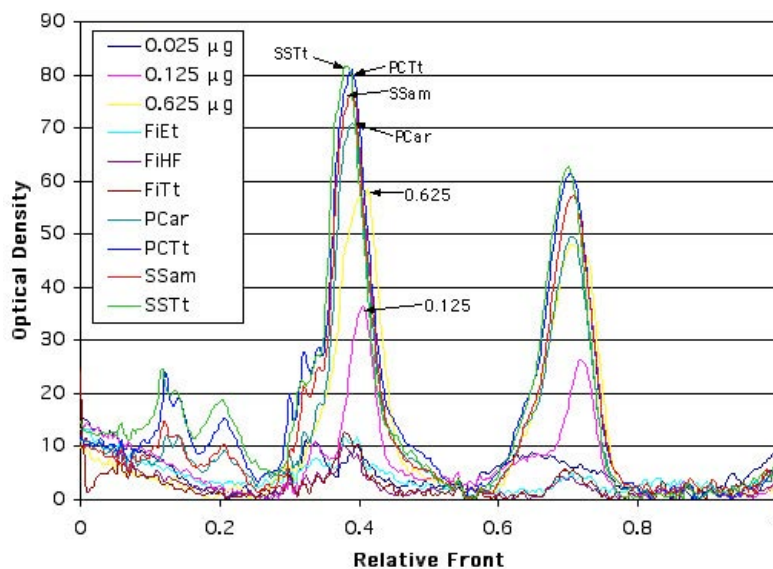


Figure 4.1.3.6. A CLE of 0.01 mg/ml mouse IgG and anti-mouse IgG adsorbed to silica fiber, Cab-o-Sil®, or Stöber spheres with various surface treatments.

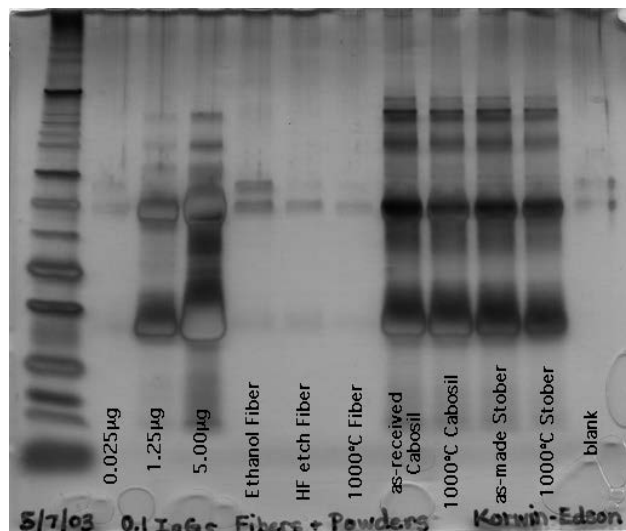


Figure 4.1.3.7. A gel image of 0.1 mg/ml mouse IgG and anti-mouse IgG adsorbed to silica fiber, Cab-o-Sil®, or Stöber spheres with various surface treatments.

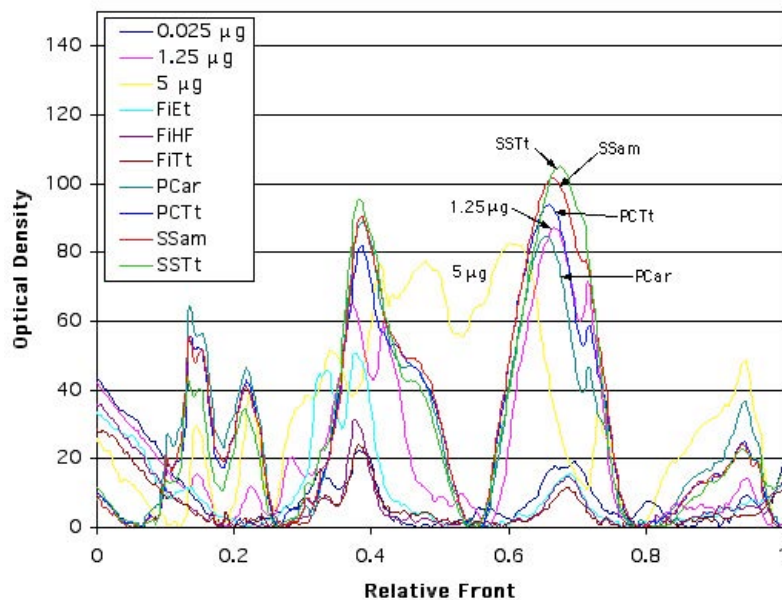


Figure 4.1.3.8. A CLE of 0.1 mg/ml mouse IgG and anti-mouse IgG adsorbed to silica fiber, Cab-o-Sil®, or Stöber spheres with various surface treatments.

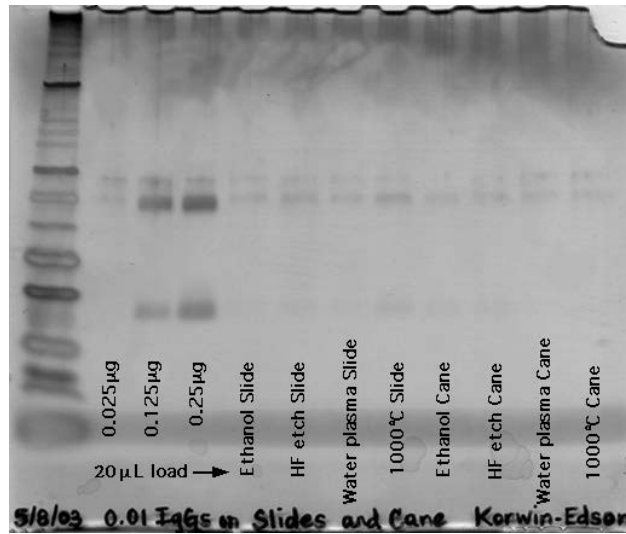


Figure 4.1.3.9. A gel image of 0.01 mg/ml mouse IgG and anti-mouse IgG adsorbed to silica slides and cane with various surface treatments. Sample wells had 20 μ L loading.

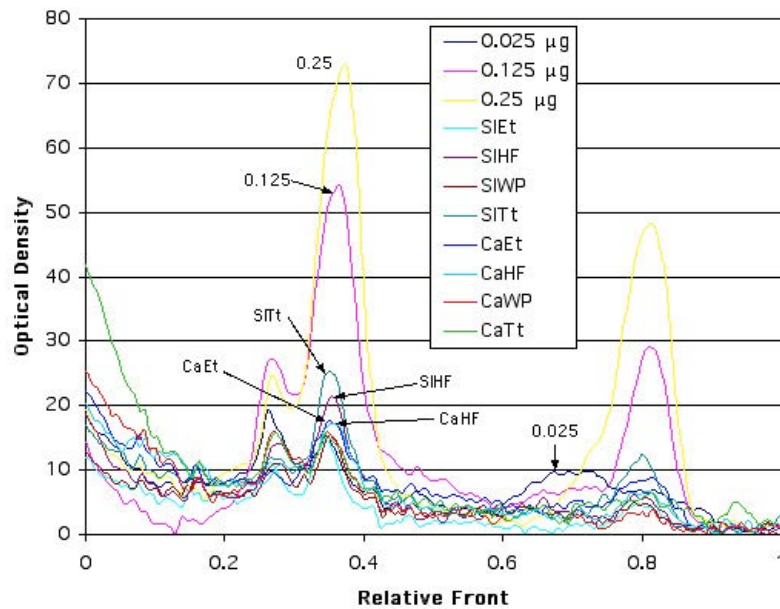


Figure 4.1.3.10. A CLE of 0.01 mg/ml mouse IgG and anti-mouse IgG adsorbed to silica slides and cane with various surface treatments.

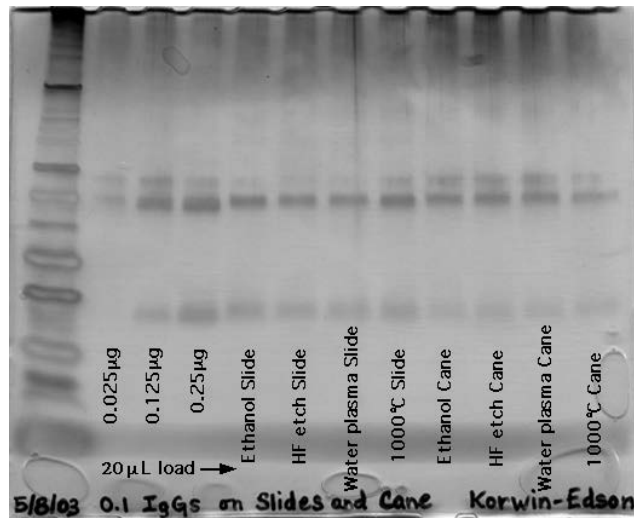


Figure 4.1.3.11. A gel image of 0.1 mg/ml mouse IgG and anti-mouse IgG adsorbed to silica slides and cane with various surface treatments. Samples wells had 20 μ L loading.

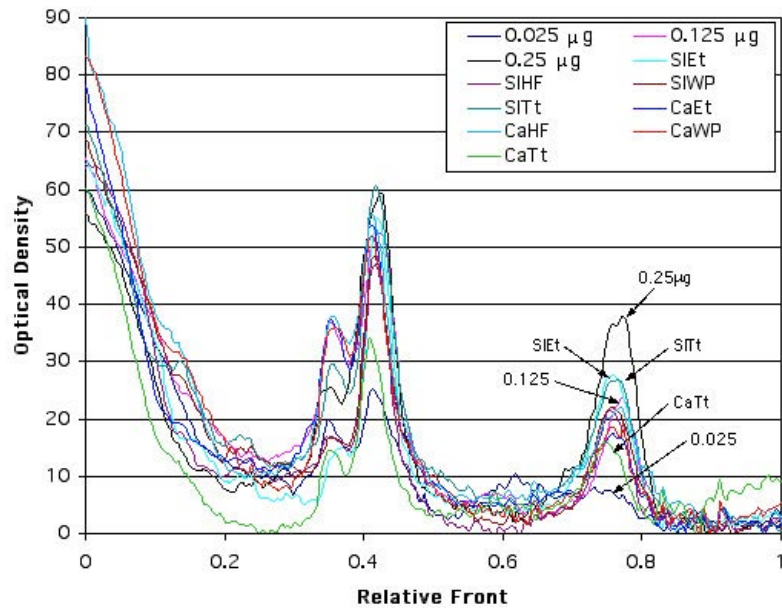


Figure 4.1.3.12. A CLE of 0.1 mg/ml mouse IgG and anti-mouse IgG adsorbed to silica slides and cane with various surface treatments.

Table IX. Primary and Secondary IgG Protein Binding Quantities Adsorbed to Surface Found Using Two Separate Methods for Binding Set Two

Sample	Quantity One Area Values		Excel Maximum Intensity Values	
	Protein Adsorbed (micrograms)	Binding Coverage (microg/cm ²)	Protein Adsorbed (micrograms)	Binding Coverage (microg/cm ²)
SIETlg01	0.020	0.005	0.031	0.008
SIHFlg01	0.030	0.007	0.053	0.013
SIWPlg01	0.020	0.005	0.034	0.009
SITtlg01	0.050	0.013	0.066	0.018
SIETlg1	0.090	0.022	0.167	0.041
SIHFlg1	0.070	0.020	0.122	0.036
SIWPlg1	0.090	0.023	0.126	0.032
SITtlg1	0.110	0.029	0.160	0.042
CaETlg01	0.030	0.023	0.041	0.032
CaHFlg01	0.030	0.023	0.040	0.031
CaWPlg01	0.020	0.016	0.036	0.028
CaTtlg01	0.020	0.016	0.034	0.027
CaETlg1	0.090	0.070	0.091	0.070
CaHFlg1	0.120	0.093	0.126	0.098
CaWPlg1	0.100	0.078	0.103	0.080
CaTtlg1	0.040	0.031	0.080	0.062
FiETlg01	0.010	0.006	0.101	0.064
FiHFlg01	negligible	negligible	0.089	0.057
FiTtlg01	0.020	0.013	0.108	0.069
FiETlg1	0.310	0.197	0.118	0.075
FiHFlg1	0.100	0.064	0.106	0.068
FiTtlg1	0.070	0.045	0.061	0.039
PCarlg01	0.690	1.139E-04	0.604	9.96E-05
PCTtlg01	0.870	1.436E-04	0.690	1.14E-04
PCarlg1	5.570	9.191E-04	1.178	1.94E-04
PCTtlg1	3.130	5.165E-04	1.319	2.18E-04
SSarlg01	0.810	1.038E-03	0.649	8.32E-04
SSTtlg01	0.850	1.090E-03	0.696	8.92E-04
SSarlg1	3.670	4.705E-03	1.436	1.84E-03
SSTtlg1	5.130	6.577E-03	1.491	1.91E-03

4.2. Fluorescence Spectrometry

“Nothing is particularly hard if you divide it into small jobs.” - Henry Ford

Fluorimetry was performed on “depleted” protein solutions, which means that the solution placed into the special quartz cuvette was the leftover protein solution after having removed the silica sample. Streptavidin is a naturally fluorescent protein due to the aromatic rings of some of its amino acids. Figures 4.2.1 and 4.2.2 are emission scans of three concentrations of streptavidin solutions at an excitation of 280 nm and 295 nm respectively. The figures have the same y-axis scale to allow a direct comparison of intensity resulting from the two excitation wavelengths. There is a clear difference in the intensities between the three concentrations while the TBS fluorescence is very close to that of the 0.001 mg/ml solution. Even though the increase in concentration is an order of magnitude between each sample, there is not an increase of an order of magnitude in the fluorescence intensities or band peak areas. For example, in Figure 4.2.1 the area under the 0.1 mg/ml band peak is 168,097,690 cps-nm, the area under the 0.01 mg/ml band is 29,065,666 cps-nm, and the area under the 0.001 mg/ml band is 6,853,373 cps-nm. The 280 nm scan clearly gives much higher intensities than the 295 nm scan, therefore, 280 nm was used as the excitation wavelength for all subsequent fluorimetry. Figure 4.2.3 is a combination scan, which shows both emission and excitation spectra for a 0.1 mg/ml streptavidin protein solution. One of the excitation scans for Figure 4.2.3 was held at an emission of 342 nm and the other was held at an emission of 350 nm. The excitation scan maximum intensity is slightly higher for the emission at 342 nm than that at 350 nm. The emission scan was held at an excitation wavelength of 280 nm.

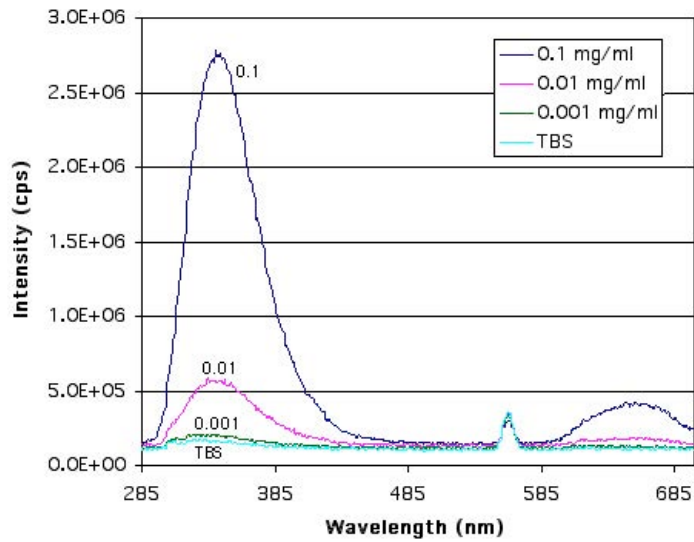


Figure 4.2.1. Fluorescence emission spectra of three concentrations of streptavidin protein solutions and TBS excited at 280 nm.

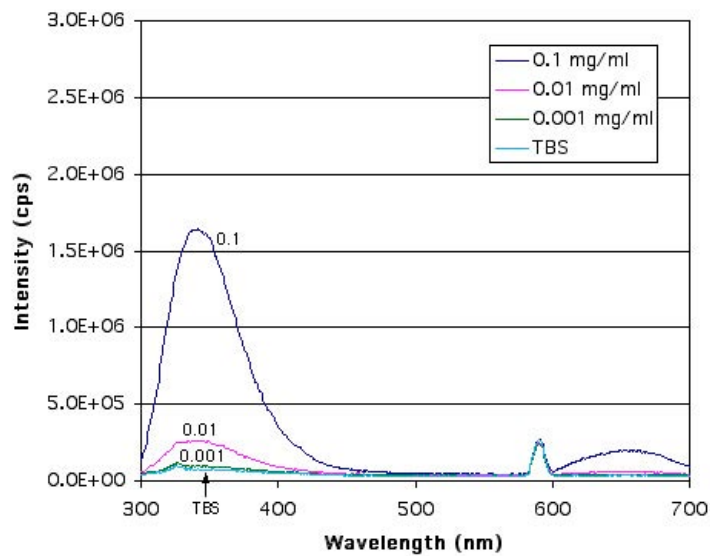


Figure 4.2.2. Fluorescence emission spectra of three concentrations of streptavidin protein solutions and TBS excited at 295 nm.

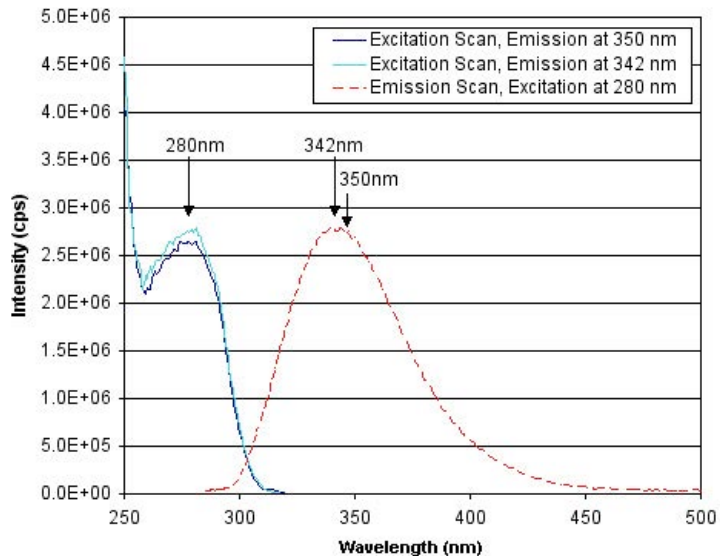


Figure 4.2.3. Dual excitation and emission spectra of a 0.1 mg/ml streptavidin solution.

Many of the issues of fluorimetry had to be addressed before the sample data could be understood. First of all, a limited amount of protein solution was available, so a diminished cuvette volume was required. A 400 μL quartz cuvette with a path length of 1cm was allocated. The fluorescence of the tris-buffered saline (TBS), the solvent for all protein solutions had to be determined. The correct excitation wavelength was found for the optimal emission intensity of streptavidin. Standards were analyzed to resolve whether the fluorescence technique would consistently work for quantification of protein in the cuvette. Various slit settings were attempted to determine the optimal peak intensity versus width ratios. For quite some time all samples were run in triplicate to decrease any variation in error. Figure 4.2.4 is an emission spectra with the excitation at 295 nm for three concentrations of streptavidin and TBS run in triplicate. The areas are listed next to the legend in the figure and roughly correspond to order of magnitude increases with the increases in concentration.

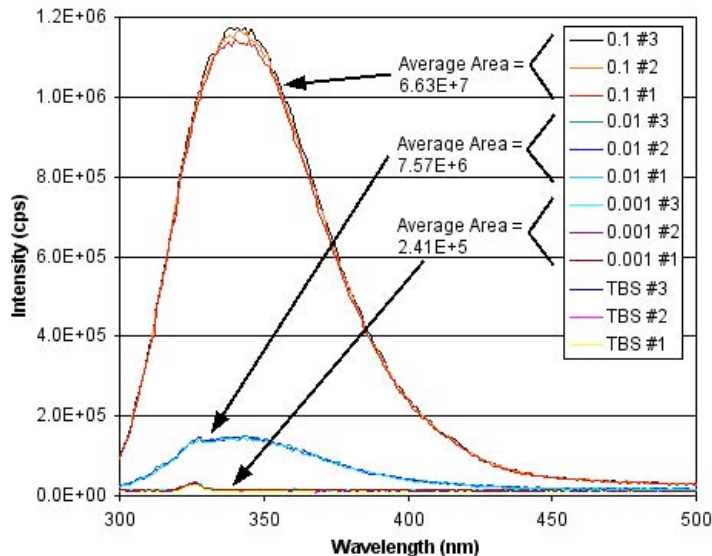


Figure 4.2.4. Fluorescence emission spectra of streptavidin protein solutions run in triplicate with the corresponding areas listed.

The next step was to begin analyzing the samples. Since it was first thought that fluorescent proteins adsorbed to a glass surface might not have enough intensity to be measured by the detector, protein solutions were investigated. However, in order for the protein bound to the glass to be determined, the protein solutions placed into the fluorimeter were those after the glass samples were removed. Since it is assumed that some quantity of protein is binding to the glass, once this glass is removed this quantity of protein is removed from the solution. These solutions are then termed as being “depleted”. The first such “depleted” sample solutions that were analyzed were originally 0.1 mg/ml streptavidin after having been incubated with autoclaved silica slides and 2 pieces of cane. Figure 4.2.5 is the emission scan of these samples at an excitation of 280 nm and Figure 4.2.6 is the emission scan of these samples at an excitation of 295 nm. The 280 nm plot shows spectra of the 0.1 mg/ml standard, the cane samples and one of the slide samples coinciding with each other, while the other slide sample has a slightly lower intensity. A slight variation in intensity between the samples is observed in the 295 nm spectra. Intensity increases in the order of 0.01

mg/ml standard, then one of the slides, the 0.1 mg/ml standard, one of the dual cane samples, followed by the other slide and cane samples. The lines shown are an average of three data collections. From the 295 nm data it was determined that 519 ng of protein per square centimeter adsorb to the cane and the silica slides bind 370 ng/cm².

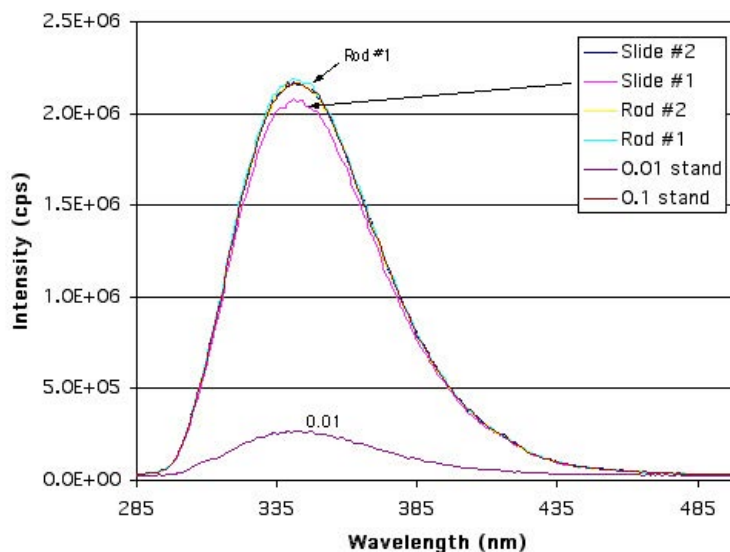


Figure 4.2.5. Fluorescence emission spectra of four depleted streptavidin solutions (originally 0.1mg/ml) after exposure to a section of silica slide or 2 pieces of silica cane each. Excited at 280 nm.

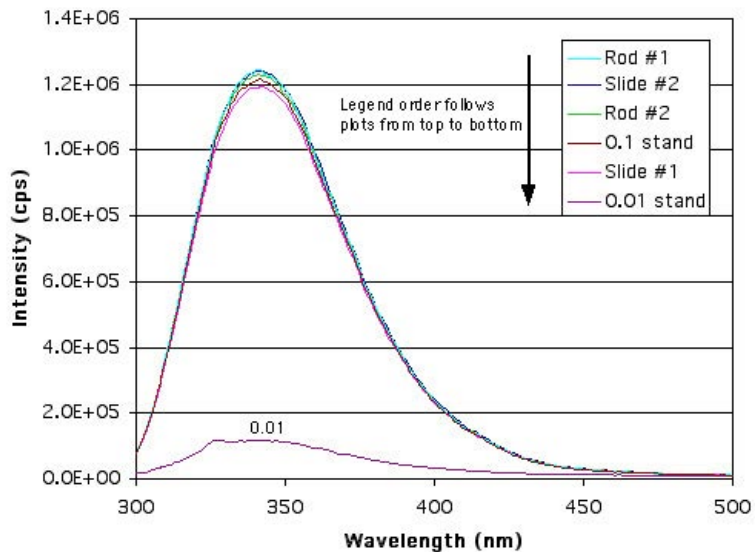


Figure 4.2.6. Fluorescence emission spectra of four depleted streptavidin solutions (originally 0.1mg/ml) after exposure to a section of silica slide or 2 pieces of cane each. Excited at 295 nm.

Next, the powders were exposed to 0.1 mg/ml streptavidin and again the depleted solutions were examined in the fluorimeter at both 280 nm and 295 nm excitations. Since the two spectra are very similar and the 280 nm spectrum has a higher intensity, only the 280 nm spectra are shown. Figure 4.2.7 shows the emission scan at an excitation of 280 nm for 20 mg Stöber spheres and 2 mg of Cab-o-Sil®. From this chart and the standards within it, a linear calibration plot can be made. Using the linear curve fit the amount of protein in the unknown depleted solutions in the cuvette can be determined. This amount is then divided by the volume of the cuvette (400 μ L) and a new concentration is found. Subtracting the new concentration from the original yields the amount of protein in mg that adsorbed to the sample since 1 mL is used. The Cab-o-Sil® adsorbs 68.2 micrograms and the Stöber spheres adsorb 70.1 micrograms, which gives a binding of 11.3 ng/cm² and 89.9 ng/cm², respectively.

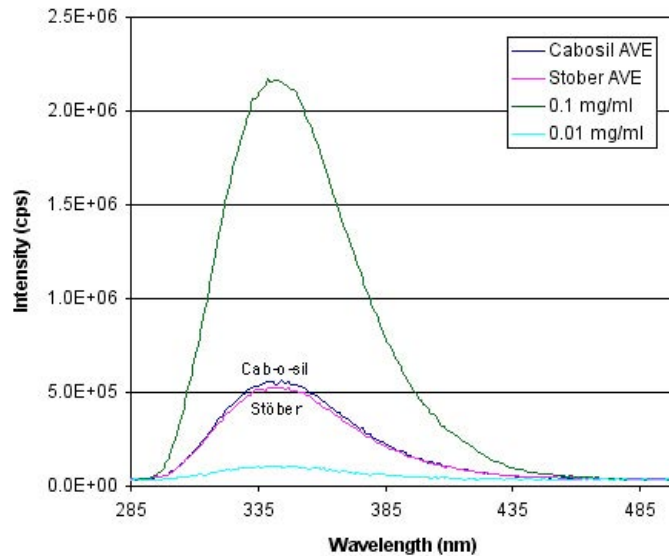


Figure 4.2.7. Fluorescence emission spectra of depleted streptavidin solutions (originally 0.1 mg/ml) after exposure to Cab-o-Sil® or Stöber spheres. Excited at 280 nm.

Slides, cane, Stöber spheres and Cab-o-Sil® were incubated with 0.01 mg/ml streptavidin and the depleted solutions were analyzed in the fluorimeter at both 280 nm and 295 nm excitations. Only the 280 nm excitation emission spectra will be shown to reduce redundancy. Using the standard and a point through zero, the equation method gives binding quantities. The silica slide binds 2.10 micrograms of protein for 626 ng/cm², the 2 pieces of cane bound 1.93 micrograms of protein for 1.50 µg/cm², the Cab-o-Sil® bound 3.78 micrograms of protein for 0.624 ng/cm², and the Stöber spheres bound 5.14 micrograms of protein for 6.59 ng/cm². Even though the peak intensity for the Cab-o-Sil® is lower than for the Stöber spheres, the overall area is larger due to the extra peak at a longer wavelength, so this quantity may not be accurate. All bulk samples up until this point were autoclaved prior to protein exposure to sterilize the surfaces.

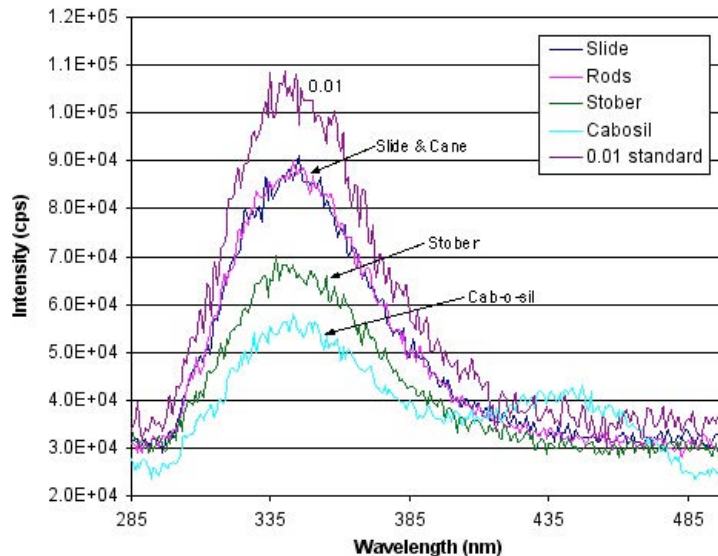


Figure 4.2.8. Fluorescence emission spectra of streptavidin solution (originally 0.01 mg/ml) after incubation with either a slide, cane, Stöber spheres or Cab-o-Sil®. Excited at 280 nm.

It was then logical to start applying surface treatments to the samples and then exposing them to the streptavidin solutions. The first treatment applied was a 10 minute HF etch in 10% acid solution for silica slides. Two slides were treated and then exposed to either a 0.1 mg/ml or 0.01 mg/ml streptavidin solution. Each sample was run in triplicate and then averaged. Figure 4.2.9 shows the resulting emission spectra including the spectra of three standards for accurate quantification. Figure 4.2.10 shows the calibration plot of the standards, the best-fit linear trendline and the resulting equation with r-squared value. The HF etched slide bound 3.71 micrograms of protein from the 0.1 mg/ml solution resulting in a binding of 1.49 micrograms/cm². The similar slide exposed to the 0.01 mg/ml concentration adsorbed 183.4 ng/cm² using a ratio technique to relate the actual quantity of the 0.01 mg/ml standard with the equation quantity of the standard.

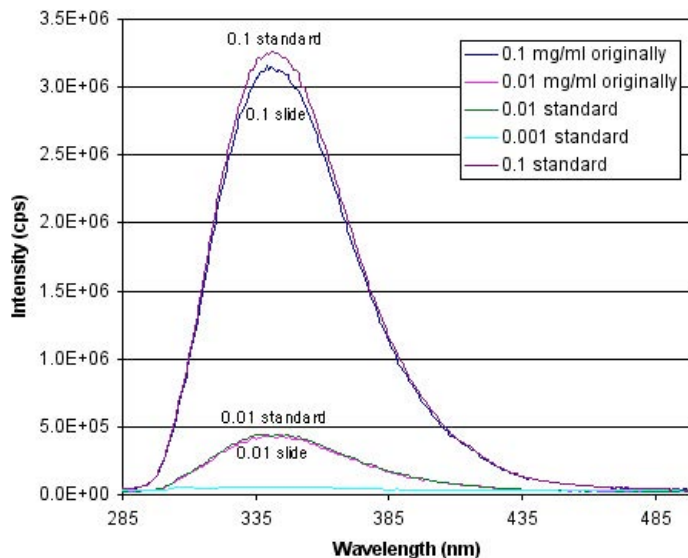


Figure 4.2.9. Fluorescence emission spectra of streptavidin solutions after a 30 min exposure to HF etched silica slides. Excited at 280 nm with three standards.

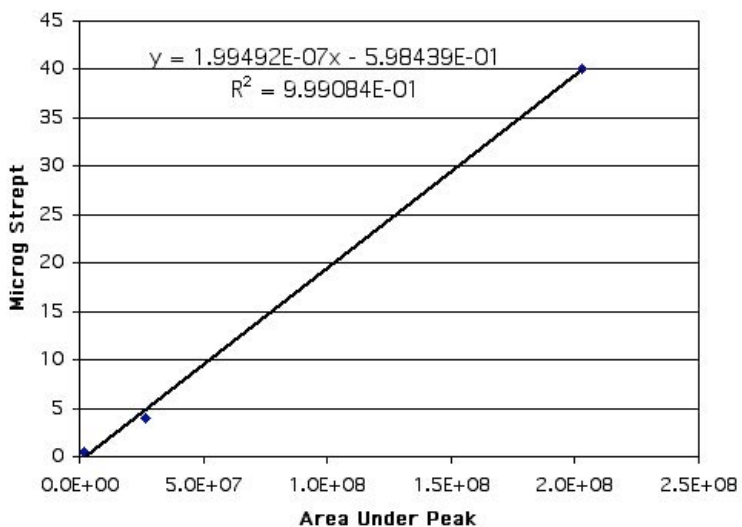


Figure 4.2.10. Plot of the known micrograms for the standards in Figure 4.2.9 as a function of their corresponding areas. The equation provides quantity of protein in unknown sample solutions by knowing the area under their emission peaks.

The next surface treatment that was explored was a 20 minute water plasma treatment done in a RF microwave at 400 Watts and roughly 0.65 to 0.75 torr of water vapor. Figure 4.2.11 shows the emission spectra of streptavidin solutions, both standards and depleted solutions, after having been incubated with a water plasma treated slide for 30 minutes. The same equation found from the linear fit to the standards given in Figure 4.2.10 applies for these samples. Using this equation and comparing the area for the 0.01 mg/ml standard in this experiment gives a quantity of 4.702 micrograms in the unexposed solution, where there should be only 4.00 micrograms. The ratio of the actual to measured quantity is 0.85, so any area found from the equation in this region should be multiplied by this value as a correction factor. The ratio technique had to be used for the 0.01 mg/ml sample and this water plasma treated slide adsorbed 311 ng/cm². The 0.1 mg/ml water plasma treated slide adsorbed 1.30 µg/cm².

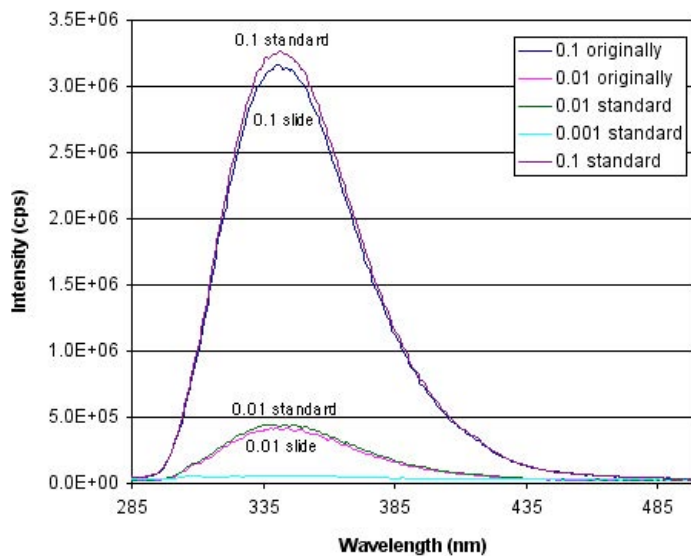


Figure 4.2.11. Fluorescence emission spectra of streptavidin solutions after having been exposed to a water plasma treated slide. Excited at 280 nm with three standards.

Due to the low intensity of the naturally occurring fluorescence of streptavidin, a fluorescently tagged protein was also investigated. Mouse Immunoglobulin G with its ligand anti-mouse IgG, which is Fc specific and is also FITC labeled, was chosen for various reasons. FITC is excited at 485 nm. The first set of fluorimetry experiments with this pair of IgG proteins, at an original concentration of 0.1 mg/ml, involved slides that were treated with an ethanol clean, an HF acid etch, or a water plasma exposure. Figure 4.2.12 shows the resulting emission spectra at an excitation wavelength of 485 nm. Only the FITC labeled IgG protein depleted solution was analyzed. Figure 4.2.13 shows the standards area versus quantity calibration plot, which provides the equation to determine unknown quantities from their fluorescence band areas. SIET adsorbed 1.43 $\mu\text{g}/\text{cm}^2$, SIHF adsorbed 2.363 $\mu\text{g}/\text{cm}^2$ and SIWP adsorbed 625 ng/cm^2 . Figure 4.2.14 is a similar experiment, but using a 0.01 mg/ml concentration of IgG proteins for binding to the slides. The resulting quantities for binding are; SIET at 863 ng/cm^2 , SIHF at 874 ng/cm^2 and SIWP at 1.13 $\mu\text{g}/\text{cm}^2$. These quantities are fairly accurate due to the high r-squared value for the linear fit to the three standards.

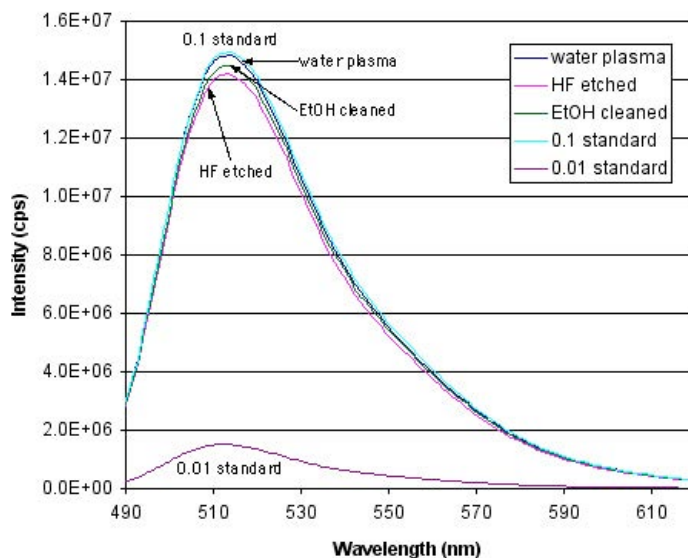


Figure 4.2.12. Fluorescence emission spectra of FITC IgG (originally 0.1 mg/ml) after exposure to a slide with the treatment indicated. Excited at 485 nm with two standards.

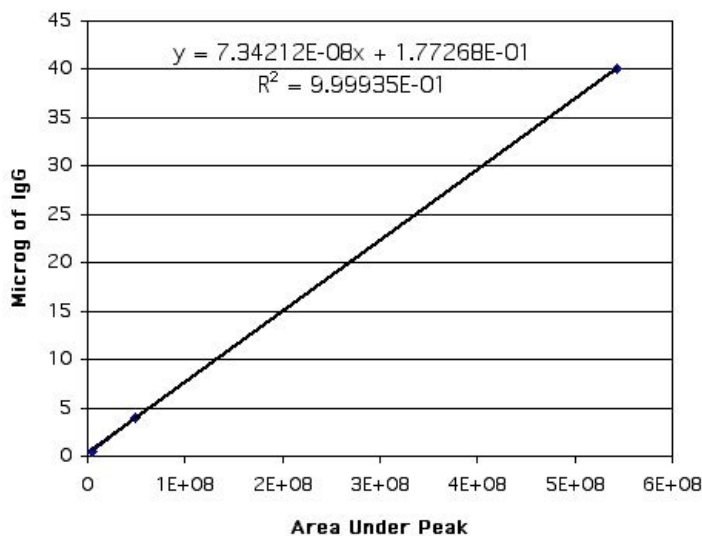


Figure 4.2.13. Standards plot for FITC labeled anti-mouse IgG for determining linear equation relating area under the emission peak to quantity of protein in cuvette.

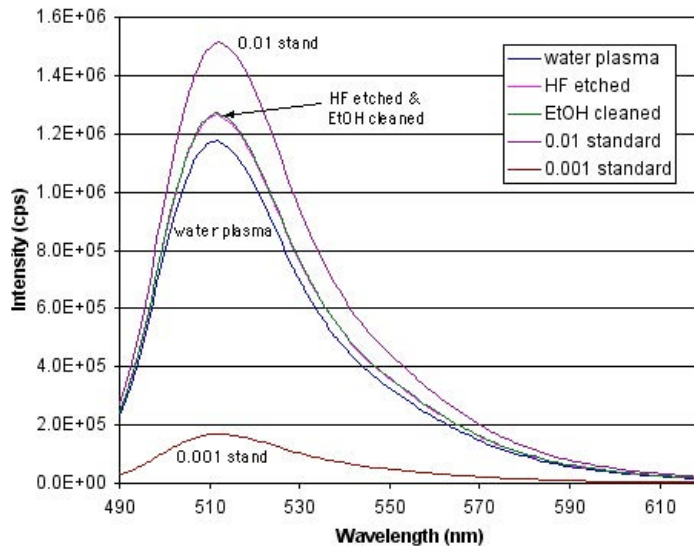


Figure 4.2.14. Fluorescence emission spectra of FITC IgG (originally 0.01 mg/ml) after exposure to a slide with the surface treatment indicated. Excited at 485 nm with two standards.

The water plasma and HF acid etch surface treatments were applied to the 1mm silica cane. These samples were exposed to both streptavidin and the pair of IgG proteins at concentrations of 0.01 mg/ml and 0.1 mg/ml. Figure 4.2.15 shows the fluorescence emission spectra of depleted 0.1 mg/ml streptavidin solutions after the two pairs of cane with 2 pieces for each vial. Figure 4.2.16 shows the 0.01 mg/ml streptavidin solution fluorescence emission spectra after exposure to similar cane samples. The total surface area for the two rods in each vial was 1.29 cm² and each quantity of protein was divided by this value to determine the binding for that surface. The CaHFSt1 sample bound 7.14 μg/cm² and the CaWPSt1 sample bound 1.45 μg/cm². The CaHFSt01 sample bound 2.09 μg/cm² and the CaWPSt01 sample adsorbed 811 ng/cm². Figure 4.2.17 is the fluorescence emission scan for 0.1 mg/ml FITC IgG after having been incubated with 2 rods with one of three surface treatments. Figure 4.2.18 is a similar plot as the previous except the FITC IgG protein concentration was 0.01 mg/ml initially. Figure 4.2.19 is a logarithmic plot of the three FITC IgG standards for this set of experiments.

It was found that an exponential fit to the standard data on a microgram versus area plot was the best. CaEtIg1 adsorbed $3.75 \mu\text{g}/\text{cm}^2$, CaHFIg1 adsorbed $12.95 \mu\text{g}/\text{cm}^2$, CaWPIg1 adsorbed $31.02 \mu\text{g}/\text{cm}^2$, CaEtIg01 could not be calculated since it outside the standard region, CaHFIg01 adsorbed $95.1 \text{ ng}/\text{cm}^2$, and CaWPIg01 adsorbed $246 \text{ ng}/\text{cm}^2$.

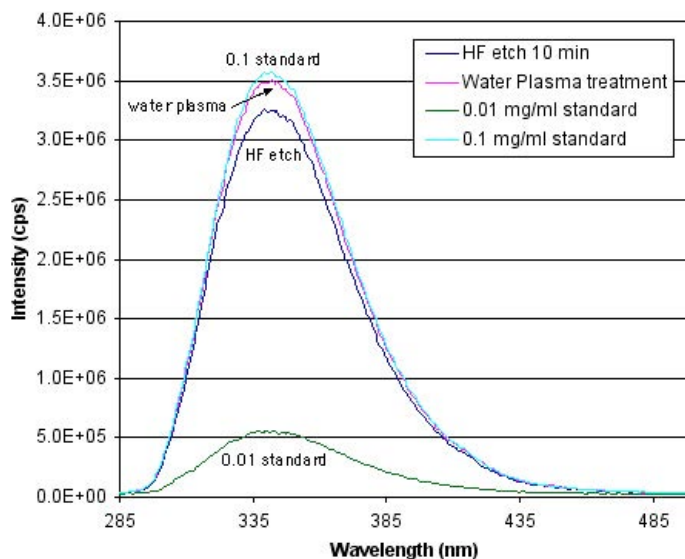


Figure 4.2.15. Fluorescence emission spectra for streptavidin solutions (originally $0.1 \text{ mg}/\text{ml}$) after exposure to either an HF etched slide or a water plasma treated slide. Excited at 280 nm with two standards.

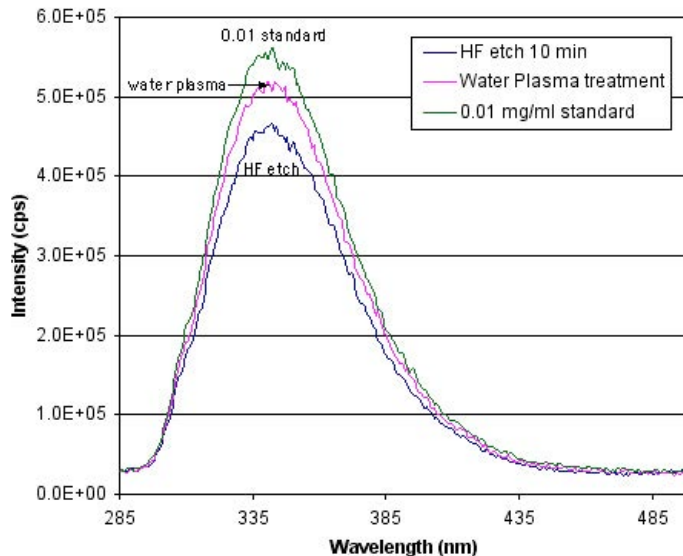


Figure 4.2.16. Fluorescence emission spectra of streptavidin solutions (originally 0.01 mg/ml) after exposure to either a HF etched slide or a water plasma treated slide. Excited at 280 nm with one standard.

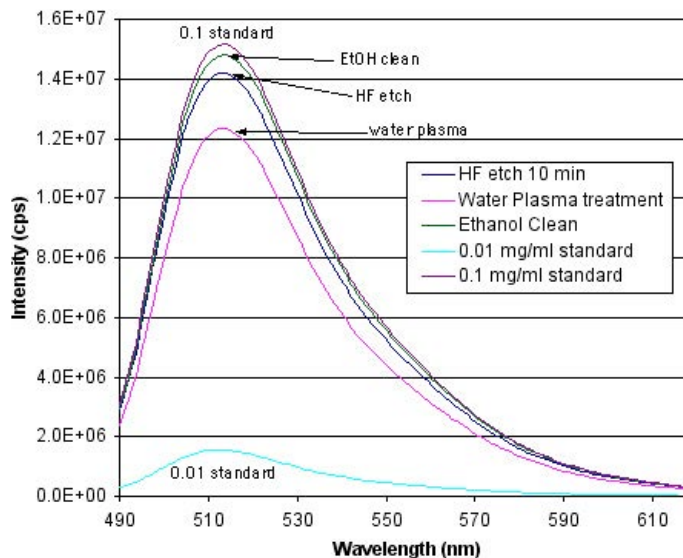


Figure 4.2.17. Fluorescence emission spectra of FITC IgG (originally 0.1 mg/ml) after incubation with cane having the surface treatment indicated. Excited at 485 nm with two standards.

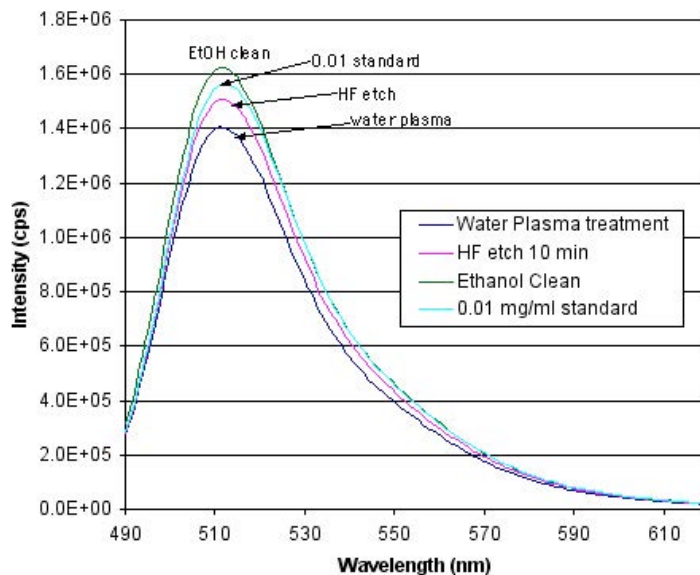


Figure 4.2.18. Fluorescence emission spectra of FITC IgG (originally 0.01 mg/ml) after incubation with cane having the surface treatment indicated. Excited at 485 nm with one standard.

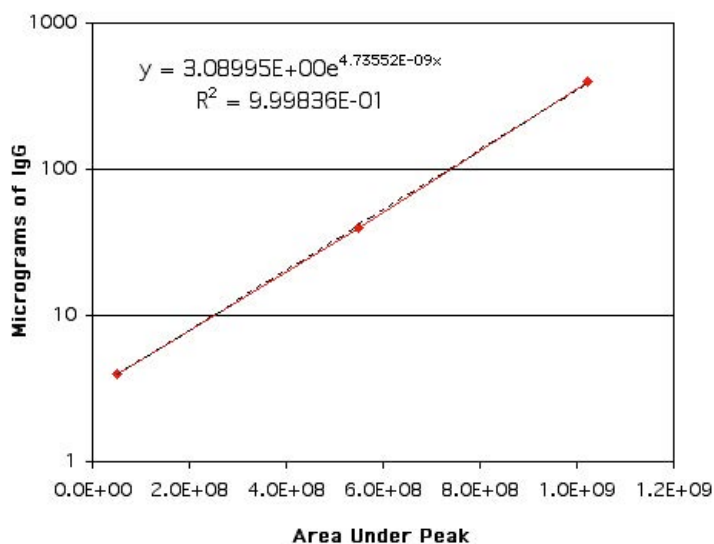


Figure 4.2.19. Logarithmic plot of the quantity versus fluorescence emission peak area for the FITC IgG standards. Equation is shown with r-squared best fit value.

The next samples to be analyzed were the silica fibers. Ten fibers were placed into their respective protein solutions and then the depleted solutions

were examined in the fluorimeter. Both streptavidin and the pair of IgG proteins were applied to the fibers after various surface treatments. Figure 4.2.20 shows the fluorescence emission spectra of two concentrations of streptavidin after incubation with either ten HF etched fibers or ten ethanol cleaned fibers. In this figure it is clear that for the 0.01 mg/ml exposed samples, the residual signal has a higher intensity than the standard at this concentration. This increase is a conundrum since the maximum amount of protein must be from the standard. Also the residual signal of the HF etched fiber at 0.1 mg/ml streptavidin has a higher intensity than its standard. Since there should not be an increase in protein after exposure to the sample, the difference may reflect the error inherent in the fluorescence measurement. There may be protein interaction with the vial wall, which interferes with the experimental results, or photobleaching may have occurred. These issues are addressed. Figure 4.2.21 is an emission scan of FITC IgG after exposure to twenty fibers with first either an ethanol clean or a HF etching then an incubation with mouse IgG. For this plot, all sample intensities are lower than their respective standards, as expected. FiEtIg1 adsorbed $3.42 \mu\text{g}/\text{cm}^2$, FiHFIg1 adsorbed $4.11 \mu\text{g}/\text{cm}^2$, FiEtIg01 adsorbed $4.06 \mu\text{g}/\text{cm}^2$ and FiHFIg01 adsorbed $3.20 \mu\text{g}/\text{cm}^2$.

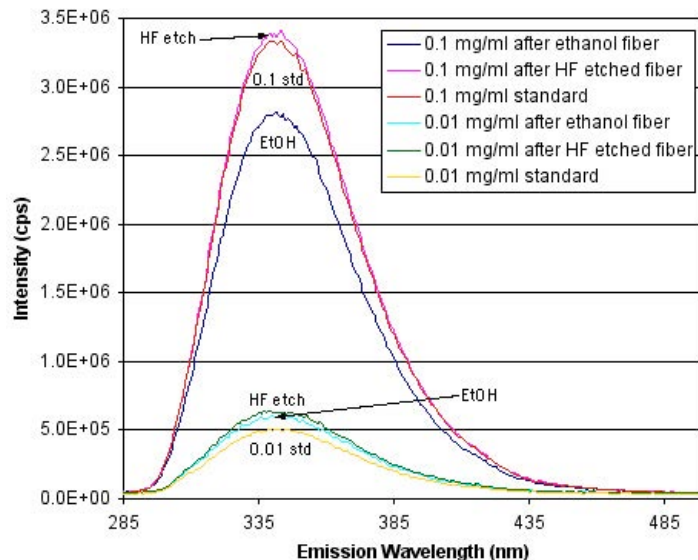


Figure 4.2.20. Fluorescence emission spectra of streptavidin protein solutions after incubation with ten fibers having the surface treatment indicated. Excited at 280 nm with two standards.

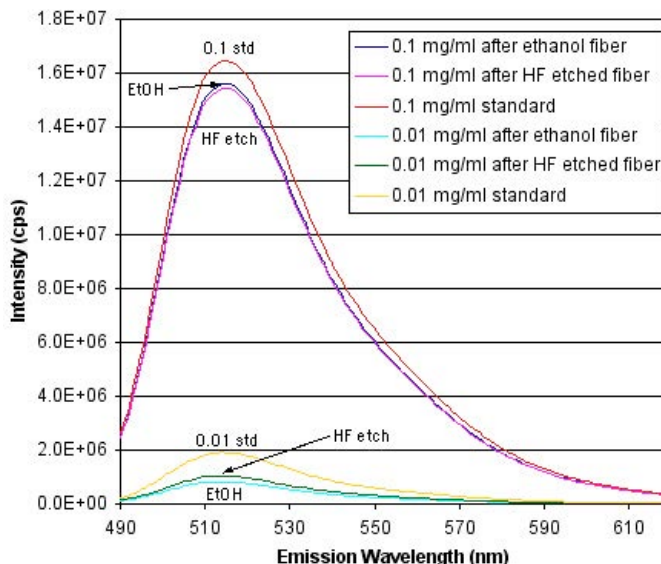


Figure 4.2.21. Fluorescence emission spectra of FITC IgG solutions after exposure to silica fibers with the treatment indicated and also an exposure to mouse IgG. Excited at 485 nm with two standards.

It was then observed that samples may have been experiencing light quenching or photobleaching. This phenomenon was therefore explored. A single streptavidin standard of 0.01 mg/ml concentration was chosen and analyzed in the fluorimeter after being exposed to various light conditions. Figure 4.2.22 shows the fluorescence emission spectra for the standard. The first five runs were successively performed, followed by removing and replacing the cuvette for the next five collections. The last five data collections were done successively after a one hour rest in a completely dark container. It may be difficult to see in the figure, but the important aspect is that the last five runs, i.e. those immediately after the dark period, exhibited a slightly greater intensity than any of the previous ten runs.

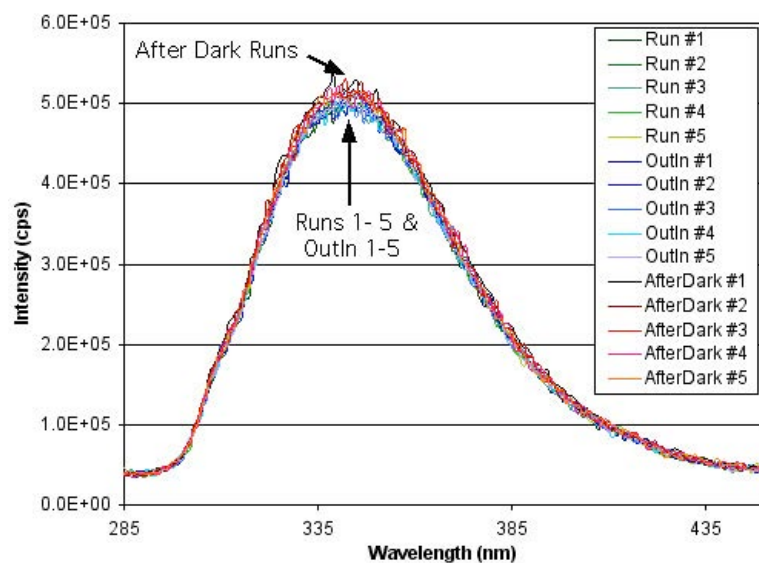


Figure 4.2.22. Fluorescence emission scan of a single 0.01 mg/ml streptavidin standard after three types of light exposure.

The photobleaching effects on FITC IgG were also investigated. Figure 4.1.23 shows the fluorescence emission spectra of a single 0.01 mg/ml FITC labeled anti-mouse IgG standard after the same light conditions of the previous streptavidin standard. It was found that the emission intensities of the spectra were entirely random and did not correlate at all with the light history of the sample. Photobleaching is not an issue with FITC IgG.

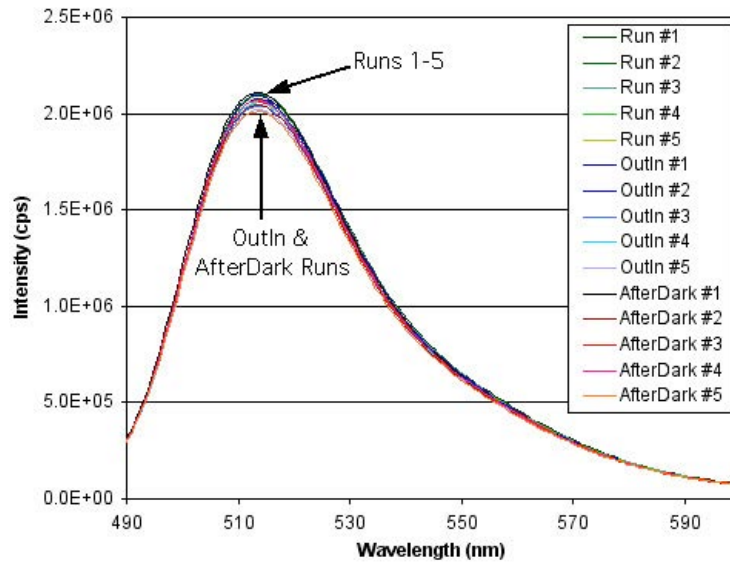


Figure 4.1.23. Fluorescence emission scan of a single 0.01 mg/ml FITC IgG standard after various light conditions.

Another issue that had to be addressed was the effectiveness of the cuvette cleaning process in between different samples since it was possible that binding of protein to the cuvette walls would cause anomalous binding capacities. A simple experiment was set up to determine the best cleaning method. A single standard solution was chosen (0.01 mg/ml), pipetted into a clean dry 400 μ L cuvette and the fluorescence emission spectrum was collected. The solution was then removed and the cuvette was filled with a fresh 400 μ L of the same standard. Its fluorescence emission spectrum was then collected. The same procedure was performed once more. Next, the solution was discarded and the cuvette was vigorously rinsed with TBS. The same fresh standard was then added to the cuvette and ran in the fluorimeter. This solution was then discarded and 400 μ L of LSB-R was used to rinse the cuvette followed by TBS. A fresh standard solution was again added to the cuvette and ran in the fluorimeter. Once more, the solution was discarded, the cuvette was rinsed vigorously with TBS, fresh solution was added and run the the fluorimeter. These six steps are called; initial, 2 – no clean, 3 – no clean, 4 – after TBS rinse, 5 – after LSB-R rinse, and 6 – after

TBS rinse. Figure 4.2.24 shows the six fluorescence emission spectra for streptavidin and Figure 4.2.25 shows the same for FITC IgG. The results were the same for both proteins. The initial intensity is the highest and the second data collection intensity is the lowest. The third collection intensity is below the first, but higher than the others. The last three step intensities are between the third and second collection intensities. It was determined that the TBS rinse is sufficient to remove any loosely bound protein that may be adhered to the quartz cuvette.

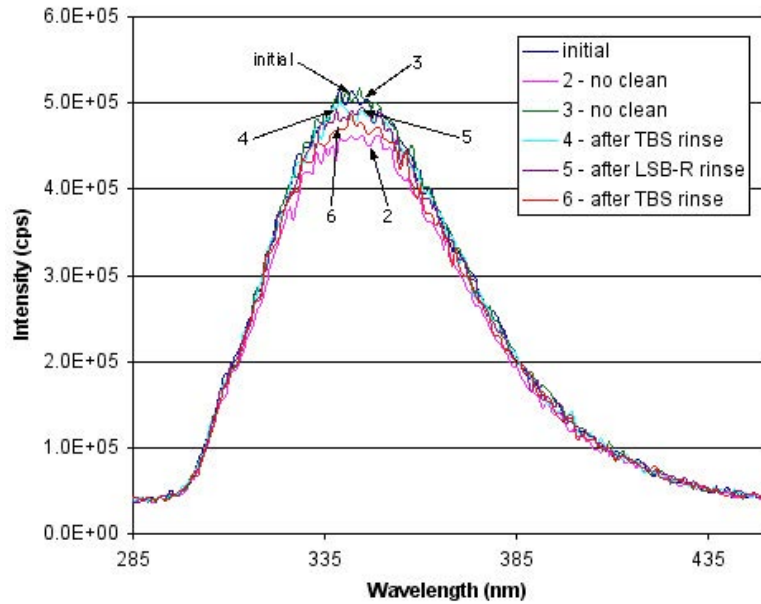


Figure 4.2.24. Fluorescence emission spectra of a 0.01 mg/ml streptavidin standard after six “rinsing” steps. Excited at 280 nm.

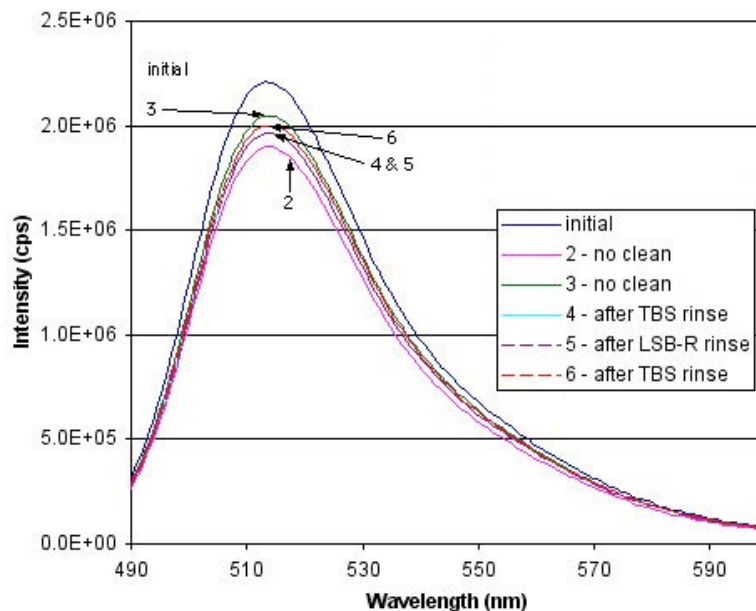


Figure 4.2.25. Fluorescence emission spectra of a 0.01 mg/ml FITC IgG standard after six “rinsing” steps. Excited at 485 nm.

It was the initial intention to place silica samples with adsorbed fluorescent protein into the fluorimeter for data collection. However, since the streptavidin protein had such a low emission intensity, it would not have been possible to detect the signal. But, with FITC IgG, the feasibility of detecting the fluorescent protein on the silica sample was determined. Figure 4.2.26 shows the fluorescence emission spectra of 1.0 mg/ml mouse IgG and FITC IgG adsorbed to an ethanol cleaned slide. The data collection was done one immediately after another, using the FF detector, except for the one hour of darkness in a sealed moist cuvette. The legend in Figure 4.2.26 from top to bottom is the order of the appearance of the data plots from top to bottom. Again, the initial collection has the highest intensity. There is a slight shift of the data to higher wavelengths with what is apparently drying. The drying may also denature the protein and cause a permanent decrease in fluorescence intensity, because the fluorescence does not recover after the slide was sealed in a moist cuvette.

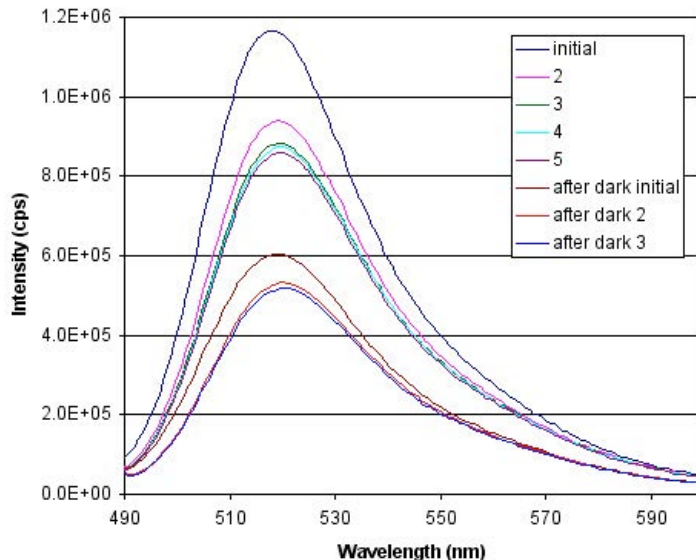


Figure 4.2.26. Fluorescence emission spectra of 1.0 mg/ml mouse IgG and anti-mouse IgG FITC labeled adsorbed to an ethanol cleaned silica slide for 30 minutes each. Legend follows graph top to bottom.

In an attempt to separate the cause of the decrease in intensity in Figure 4.2.26, a study was created where two nominally identical silica slides were coated with the pair of IgG proteins, one then being dried in darkness and the other in white light plus 485 nm light. If photobleaching is the cause of the decrease in intensity, then the sample dried in light should have a lower intensity than the sample dried in darkness. If drying is the only cause of the decrease in intensity, then there should be little or no difference between the sample emission scans. Figure 4.2.27 is the resulting emission scan after exposure to 0.1 mg/ml mouse IgG and anti-mouse IgG FITC labeled. Spectra were collected after 2, 5, 10 and 15 minutes of exposure to air. The samples were initially moist and were observed to become dry between 2 and 5 minutes. The legend in the figure is in the same order as the plot lines from top to bottom. It is clear that both drying and photobleaching decrease fluorescence intensity since the sample set exposed to light consistently has a lower intensity than the unexposed set and both decrease in intensity with drying.

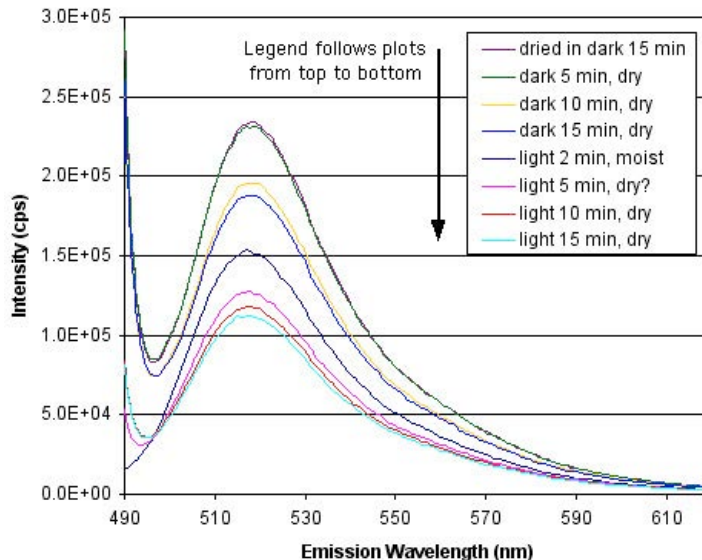


Figure 4.2.27. Fluorescence emission spectra of two silica slides with 0.1 mg/ml mouse IgG and FITC anti-mouse IgG adsorbed during drying in either light or darkness. Excited at 485 nm.

Once standards and samples were being analyzed together, it was observed that many of the samples had a higher apparent intensity than the standards, suggesting that there was more protein present in the “depleted” solutions. This being clearly inconsistent with the SDS-PAGE results, it was concluded that controls would have to be run as well as standards to account for any evaporation or binding to sample container walls. Three streptavidin standards of the same concentration 0.1 mg/ml were selected to study the history dependence of protein solution concentrations. The first standard was placed into the fluorimeter and the emission spectrum was collected. Second, a standard that was simulated to have a glass sample placed in it (henceforth referred to as a “control”) was placed into the fluorimeter and analyzed. The control sample is treated in the same manner as the sample solutions except that no glass sample had been added to the control solution. The third data collection was the second streptavidin standard. Figure 4.2.28 shows the resulting data plot with the legend being in the order of the plot lines from top to bottom, but in reverse order of how they were collected

chronologically. It is obvious that the two standards did not contain the same amount of protein, which leads one to doubt the repeatability of creating dilution series in standards. The control had a slightly lower intensity than Standard 2, but much higher than Standard 1. All of these studies helped to determine the true experimental error and the error found is applied to bar charts for binding capacities. The 2σ error in area was determined to be approximately 2 μg .

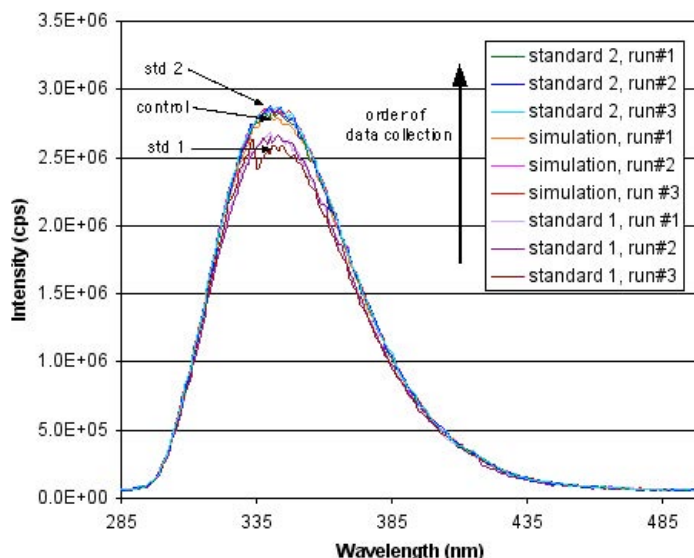


Figure 4.2.28. Fluorescence emission scan of three separate streptavidin solutions of 0.1 mg/ml concentration. Two solutions were standards and the other was created as a control. Excited at 280 nm.

Since there was such a large variation between standards run on different days (shown in Figure 4.2.29), the binding set sample fluorescence spectra were all collected in the same day. For both binding sets, only the secondary IgG solution was analyzed, specifically the anti-mouse Fc specific FITC labeled protein. For the first binding set, only the natural fluorescence of primary streptavidin was analyzed. For the second binding set, both streptavidin and the secondary protein fluorescein biotin was analyzed. The fluorescence emission of streptavidin (originally 0.01 mg/ml) adsorbed to the

Binding Set One gamut of samples is shown in Figure 4.2.30. This is the expected result, having the controls at the highest intensity, followed by the bulk samples and the standard and then the powders at the lowest intensity.

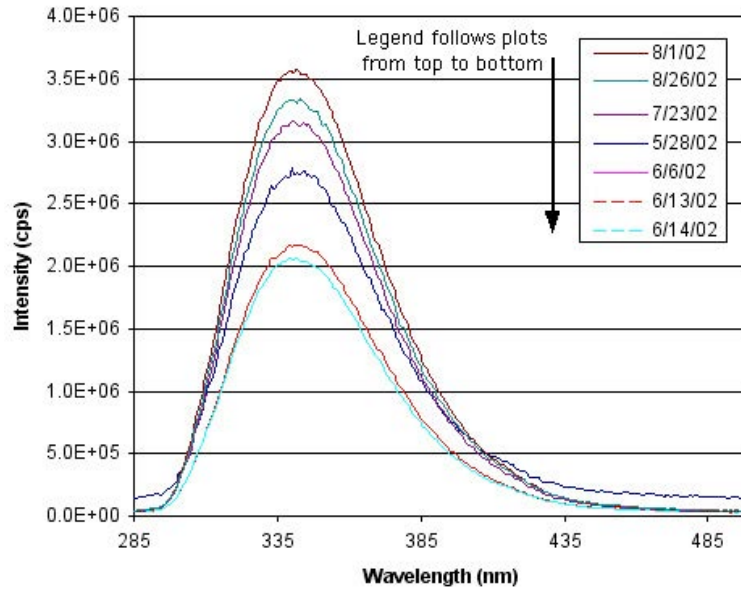


Figure 4.2.29. Fluorescence emission spectra collected on various dates for 0.1 mg/ml streptavidin protein solution. Each day is a different solution.

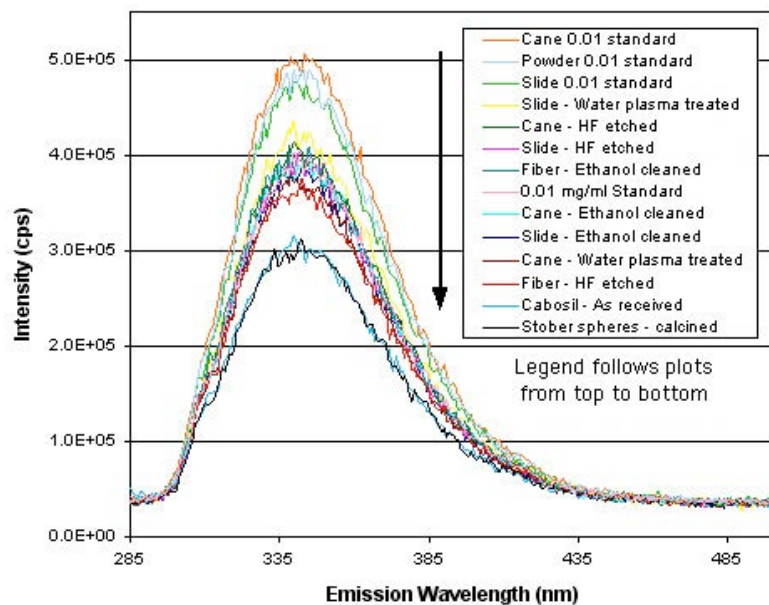


Figure 4.2.30. Fluorescence emission spectra of streptavidin depleted solutions (originally 0.01 mg/ml) from Binding Set One. Excited at 280 nm.

The other three protein concentrations resulted in data that was not as well behaved as the 0.01 mg/ml streptavidin. Figure 4.2.31 shows the fluorescence emission spectra for depleted 0.1 mg/ml streptavidin solutions after having been exposed to all samples in Binding Set One, controls and standards. In this figure the arrow points to the water plasma treated slide depleted streptavidin solution. Figure 4.2.32 shows the same for 0.01 mg/ml FITC IgG after Binding Set One samples with mouse IgG adsorbed and Figure 4.2.33 shows that for 0.1 mg/ml FITC IgG. In Figure 4.2.32, the arrow is pointing to the HF etched slide depleted FITC IgG solution as an anomalous result. This slide was later recreated and its fluorescence emission was collected. The result is shown later in the bar charts for slides. In Figure 4.2.33, the arrow points to the Cab-o-Sil® and Stöber sphere depleted FITC IgG solutions. These two powders bound much more protein than the other samples for this solution.

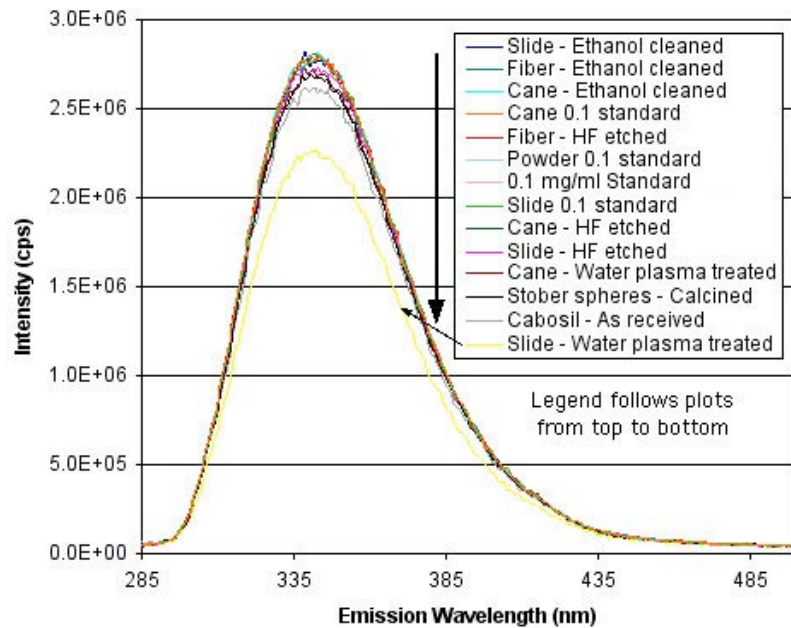


Figure 4.2.31. Fluorescence emission spectra of streptavidin depleted solutions (originally 0.1 mg/ml) from Binding Set One. Excited at 280 nm.

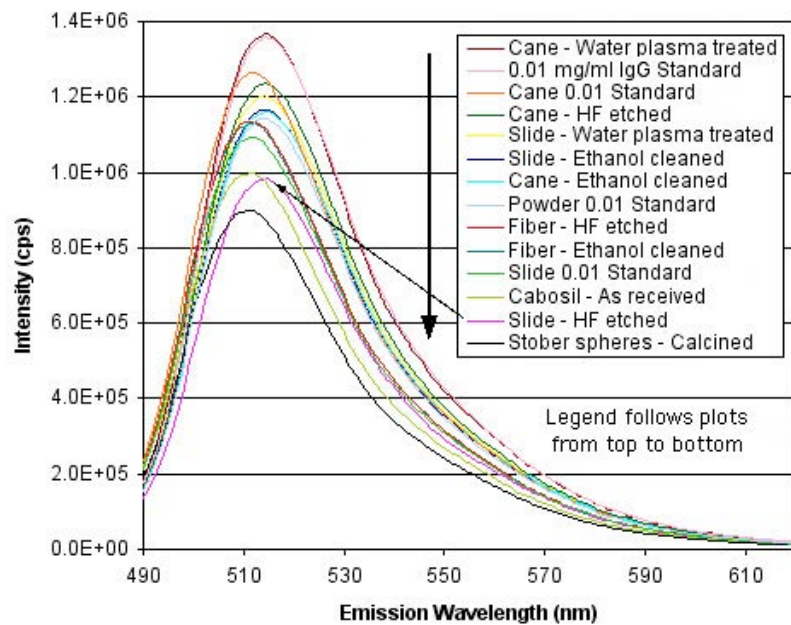


Figure 4.2.32. Fluorescence emission spectra of FITC IgG depleted solutions (originally 0.01 mg/ml) from Binding Set One. Excited at 485 nm.

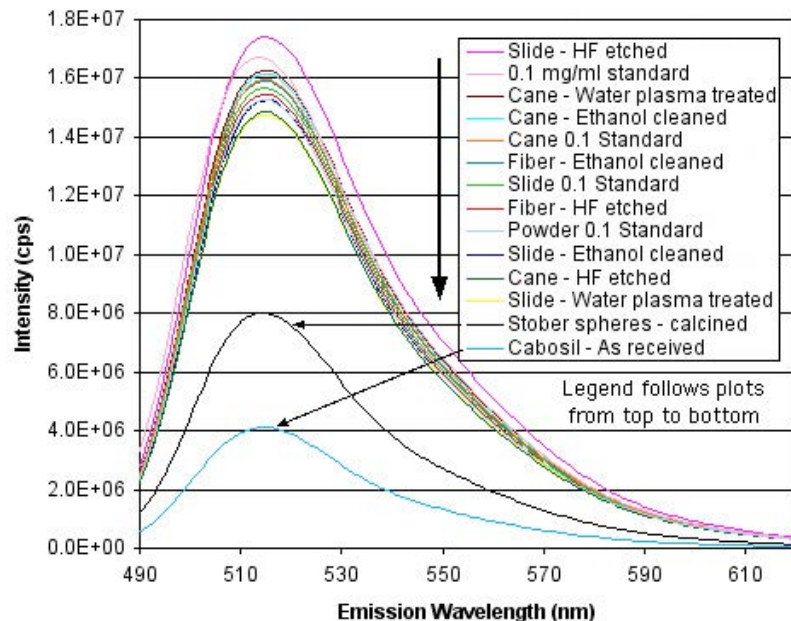


Figure 4.2.33. Fluorescence emission spectra of FITC IgG depleted solutions (originally 0.1 mg/ml) from Binding Set One. Excited at 485 nm.

The corresponding bar charts from Binding Set One separated by each silica form are shown in Figures 4.2.34 through 4.2.38. Figure 4.2.34 shows the results for the silica slides (with the recreated HF slide), Figure 4.2.35 is for the silica cane, Figure 4.2.36 is for the silica fiber, Figure 4.2.37 is for the Stöber spheres and Figure 4.2.38 is for the Cab-o-Sil®.

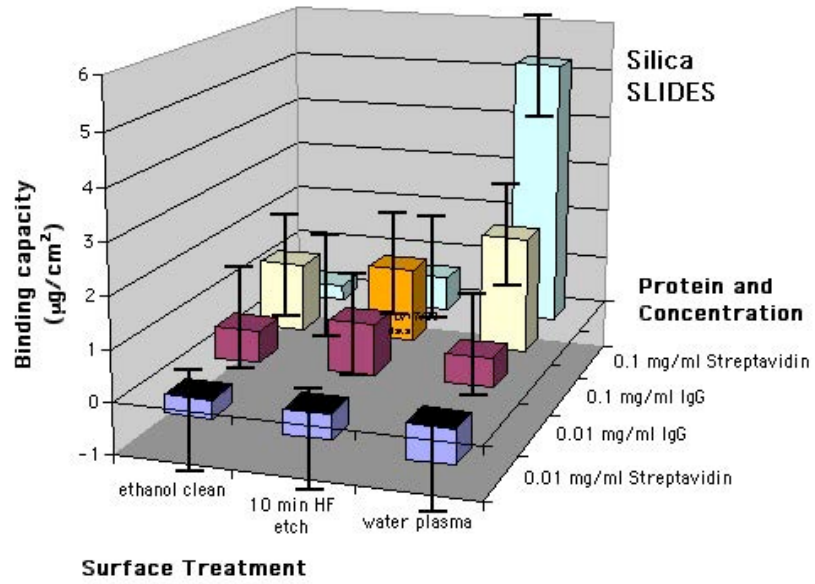


Figure 4.2.34. Binding capacity bar chart for all silica slides in Binding Set One.

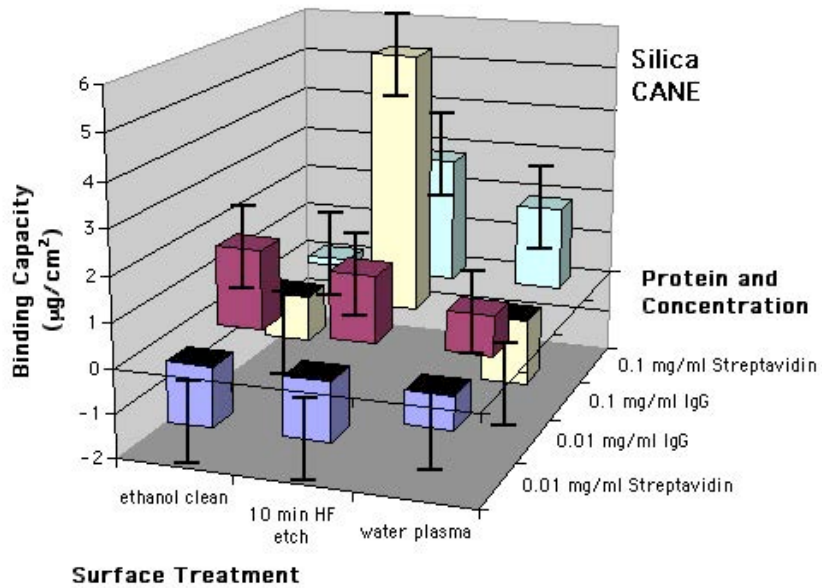


Figure 4.2.35. Binding capacity bar chart for all silica cane in Binding Set One.

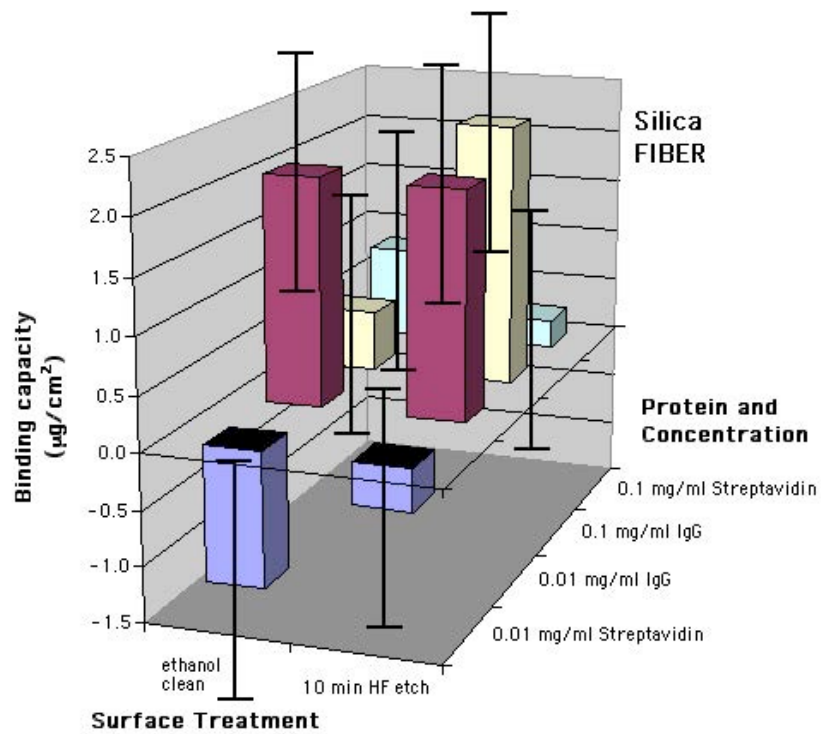


Figure 4.2.36. Binding capacity bar chart for all silica fibers in Binding Set One.

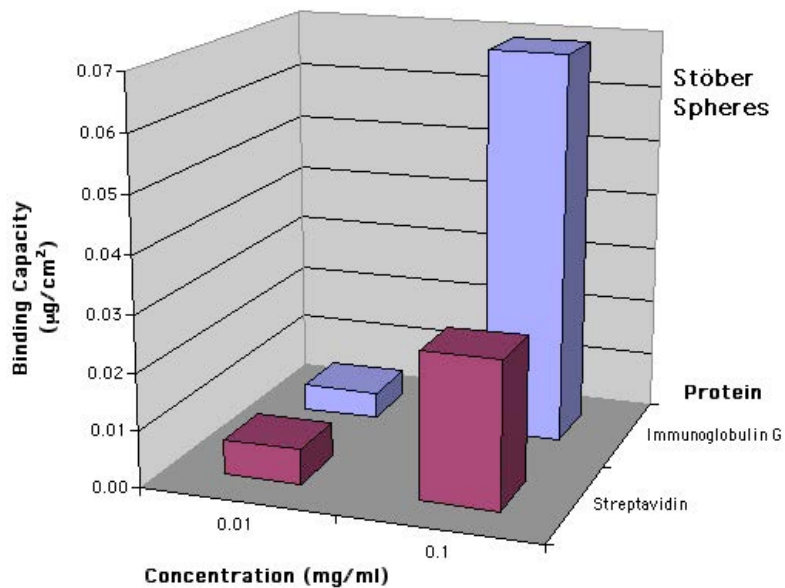


Figure 4.2.37. Binding capacity bar chart for all silica Stober spheres in Binding Set One.

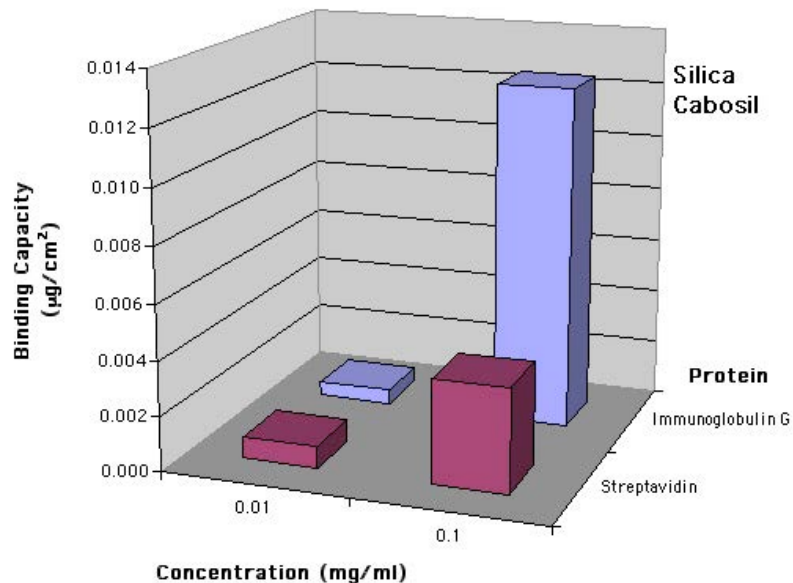


Figure 4.2.38. Binding capacity bar chart for all silica Cab-o-Sil® in Binding Set One.

To determine if there is any dependence of the fluorescence of a protein solution on its thermal history and exposure to air, a short study was conducted where five 0.01 mg/ml streptavidin standards were treated very differently. Figure 4.2.49 shows the resulting fluorescence emission spectra of these five solutions at room temperature. The spectra with the lowest intensity is of the solution that was created, never frozen, reheated to 37°C, but not opened. The next lowest band intensity is of the standard that was created, frozen, reheated to 37°C and opened at this temperature. The next two spectra, which coincide, are of the standards that were created, frozen, one reheated to 25°C and the other to 37°C, and not opened at these temperatures. The spectra with the highest band intensity is representative of the streptavidin solution that was created, frozen, reheated to 25°C and opened at this temperature. The order of entries in the legend is the same order from top to bottom as the plot lines.

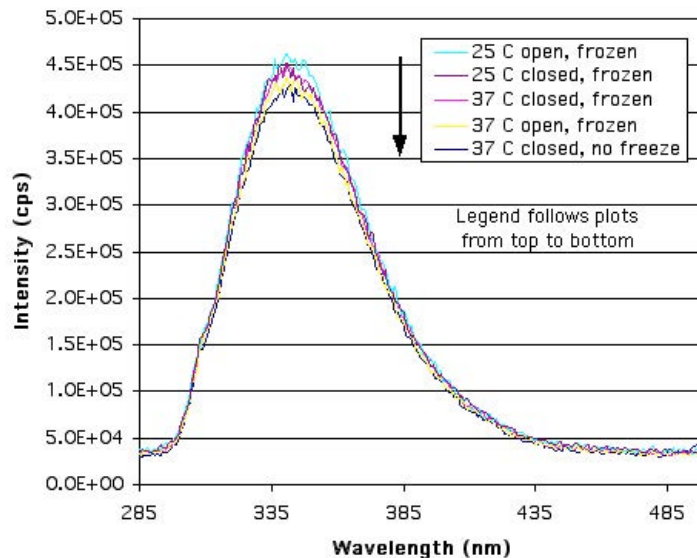


Figure 4.2.39. Fluorescence emission spectra of five 0.01 mg/ml streptavidin solutions with different thermal and air exposure histories. Excited at 280 nm.

The next study that was conducted involved investigating the pH dependence of fluorescence. Streptavidin protein solutions of 0.01 mg/ml concentration were created in 1mL aliquots and then either HCl or NaOH were added to control the pH. The pH of the solutions were 2, 4, 6, 7.4, 8, 10 and 12. Two vials of each pH were created and for each pair, one was treated as a control and the other was exposed to two pieces of silica cane. The resulting fluorescence emission spectra of the controls and depleted streptavidin solutions excited at 280 nm are shown in Figure 4.2.40. The order of entries in the legend is the same top to bottom as the order of plot lines. The streptavidin solution pH with the lowest intensity is 12 and that of the highest intensity is 2. All the others fall roughly in this general order and so it can be concluded that as pH decreases, the fluorescence intensity of streptavidin increases.

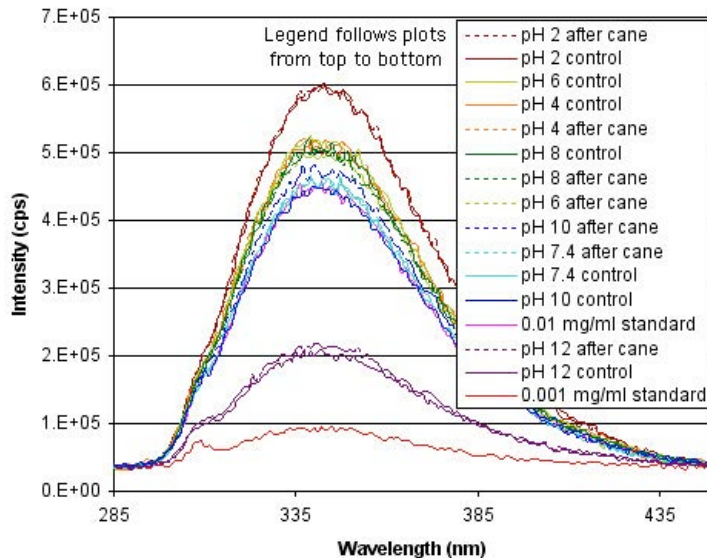


Figure 4.2.40. Fluorescence emission spectra of 0.01 mg/ml streptavidin solutions at various pHs. Half are controls and half have been exposed to silica cane.

Since the fluorescence signal of streptavidin adsorbed to a surface is too low to be detected by the fluorimeter, it was hypothesized that by stripping the proteins off the surface, the fluorescence could be measured. HF etched cane was chosen as the silica surface and two pieces of cane were placed in 0.01 mg/ml and 0.1 mg/ml protein solutions of streptavidin and the pair of IgG proteins. Figure 4.2.41 shows the emission spectra of four streptavidin standards, LSB-R and the two samples after boiling in 0.5 mL of LSB-R. As expected, the intensity of the two samples is so low that the quantity of protein cannot be calculated. Figure 4.2.42 shows the fluorescence emission spectra for the FITC IgG standards (only two shown), one LSB-R, and two samples with the pair of proteins that were all boiled in 0.5 mL of LSB-R. For both of these figures, the order of the legend follows the data plots from top to bottom. The 0.1 mg/ml mouse IgG and anti-mouse IgG coated cane produced a fluorescence that could be quantified. The amount of fluorescent protein (FITC IgG) adsorbed to this sample was approximately 1.6 μg . The other sample's intensity was too low to quantify accurately.

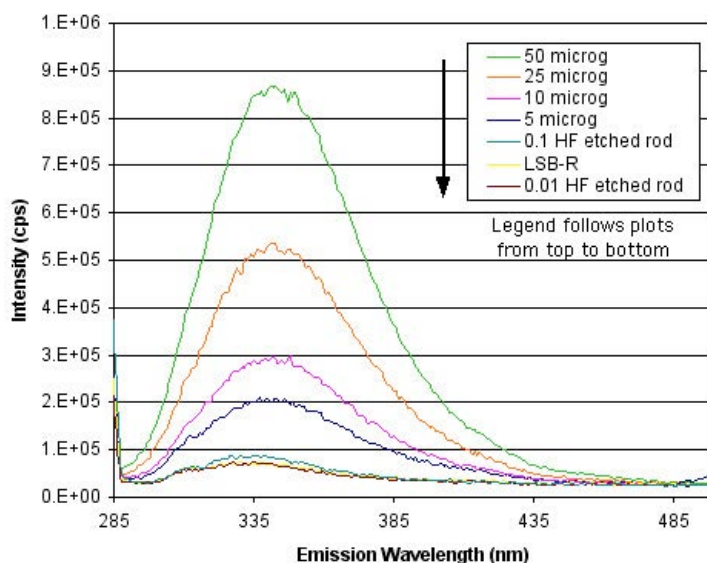


Figure 4.2.41. Fluorescence emission spectra of streptavidin protein boiled in LSB-R, as well as two HF etched cane samples with adsorbed protein.

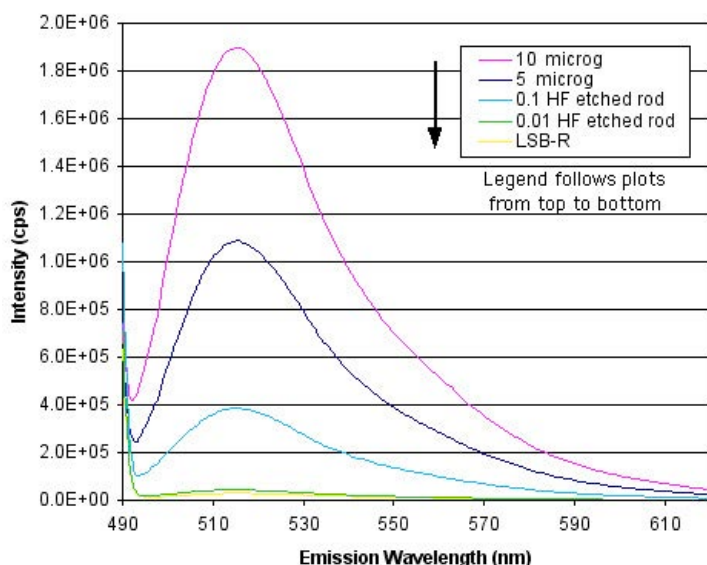


Figure 4.2.42. Fluorescence emission spectra of FITC IgG protein boiled in LSB-R, as well as two HF etched cane samples with adsorbed mouse IgG and FITC IgG.

The last set of fluorescence experiments encompassed three fluorescent proteins at two concentrations, five forms of silica, and four surface

treatments for a total of 90 fluorescence collections, not including controls or standards. This set of experiments is referred to as Binding Set Two. All of the data collections for a given protein were performed in a single sitting to prevent variation in lamp intensity and atmospheric conditions. Figure 4.2.43 shows spectra for the streptavidin depleted solutions originally 0.01 mg/ml. This figure is rather complicated, but the FiHF sample displays the highest intensity with CaWP having the lowest. After the samples, the 0.01 mg/ml standard has the next highest intensity followed by Rcctrl, Pcntrl and then Scntrl. For the powder region, SSTt shows the higher intensity with the other three powders coinciding below this. In Binding Set One, the controls had the highest intensity while in Binding Set Two they have lower intensities than the bulk samples. The correlating fluorescein biotin fluorescence intensity is shown in Figure 4.2.44.

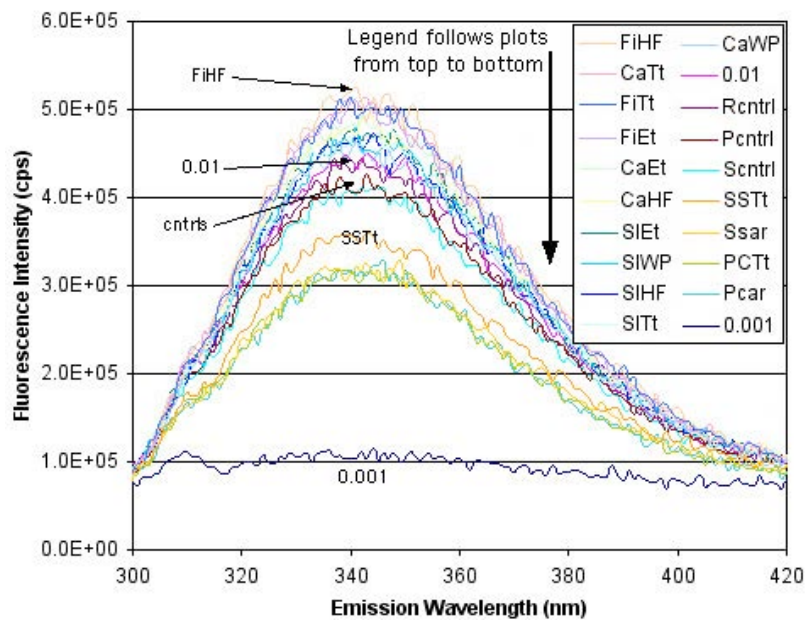


Figure 4.2.43. Fluorescence emission spectra of streptavidin depleted solutions (0.01 mg/ml) from Binding Set Two.

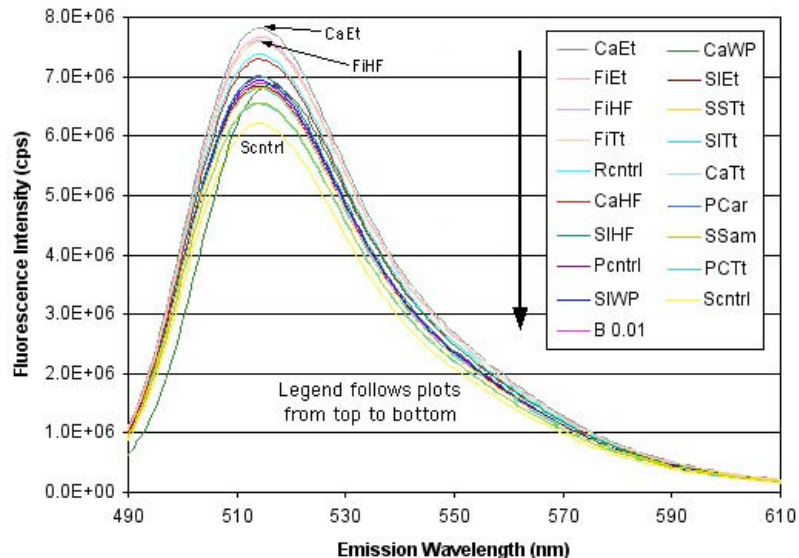


Figure 4.2.44. Fluorescence emission spectra of depleted fluorescein biotin (originally 0.01 mg/ml) after exposure to streptavidin coated samples from Binding Set Two. Excited at 485nm.

Spectra of the streptavidin and fluorescein biotin depleted solutions, originally 0.1 mg/ml, are shown in Figure 4.2.45 and 4.2.46, respectively. For the streptavidin plot all of the controls and the 0.1 mg/ml standard have the highest intensity, followed by FiTt, then the remainder of the samples, with SIHF having the lowest intensity and therefore having bound the most protein. In Figure 4.2.46, the 0.1 mg/ml standard has the highest intensity followed by both Stöber sphere samples. CaHF, SIWP, PCar and PCTt are in the group of plots of medium intensity that appear to be shifted to a lower wavelength.

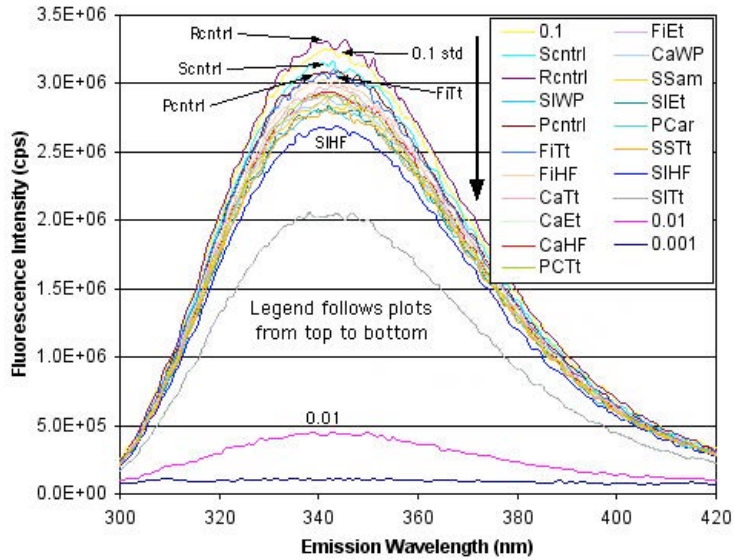


Figure 4.2.45. Fluorescence emission spectra for depleted streptavidin solution (originally 0.1 mg/ml) from Binding Set Two.

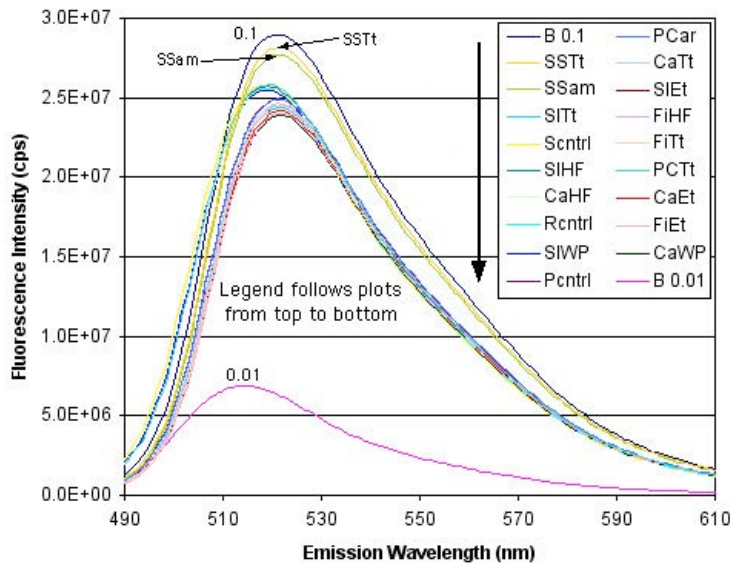


Figure 4.2.46. Fluorescence emission spectra of depleted fluorescein biotin solutions (originally 0.1 mg/ml) after exposure to streptavidin coated samples from Binding Set Two.

The FITC IgG samples from Binding Set Two did not exhibit any peak shifting like they did in Binding Set One. The samples were first surface treated, then exposed to mouse-IgG for 30 minutes, rinsed for 5 minutes with

TBS, exposed to anti-mouse IgG FITC labeled Fc specific for 30 minutes and rinsed again. The data shown in the next two figures are from the FITC depleted solutions. Figure 4.2.47 shows the resulting fluorescence emission spectra from the 0.01 mg/ml solutions and Figure 4.2.48 shows the spectra of the 0.1 mg/ml solutions from Binding Set Two. Both legends are presented in order of decreasing fluorescence intensity.

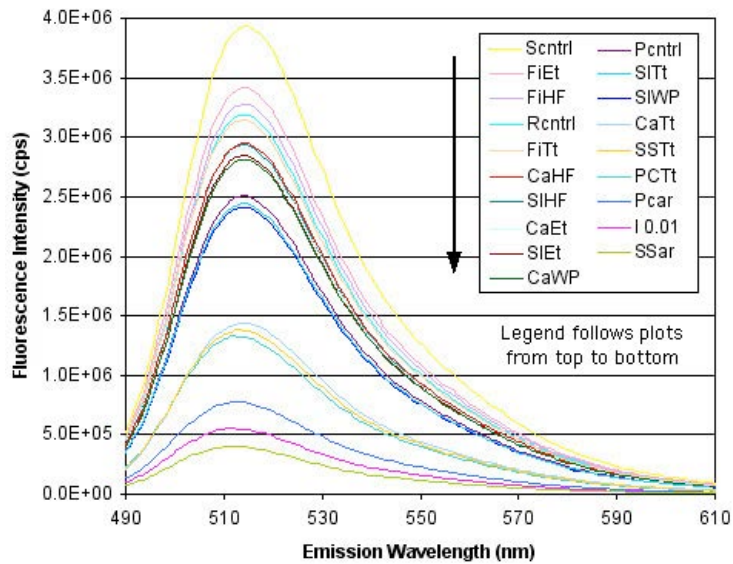


Figure 4.2.47. Fluorescence emission spectra of FITC IgG (originally 0.01 mg/ml) after exposure to mouse IgG coated samples from Binding Set Two.

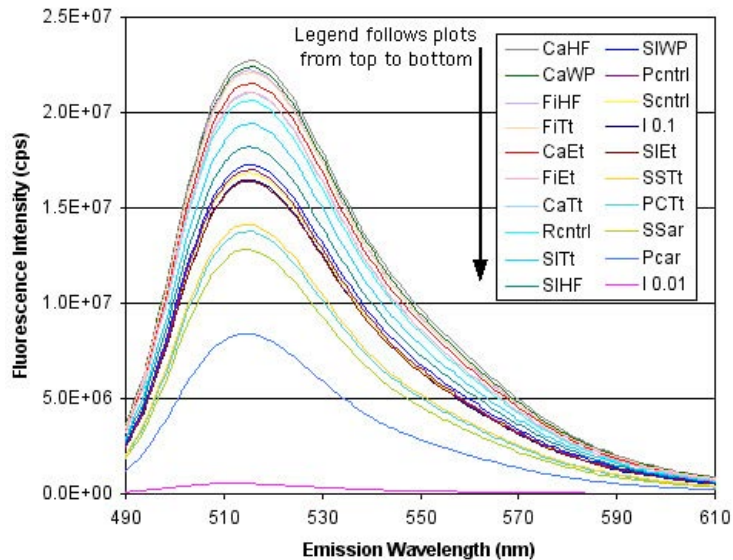


Figure 4.2.48. Fluorescence emission spectra of FITC IgG (originally 0.1 mg/ml) after exposure to mouse IgG coated samples from Binding Set Two.

For Binding Set Two, the binding amounts were calculated using the method previously described, using the control data. These amounts from all three 0.01 mg/ml solutions are compared in Table X. The binding amounts from all three 0.1 mg/ml solutions are compared in Table XI. There is not much correlation seen between the three proteins. There is an abundance of negative values because many of the sample solutions exhibited higher fluorescence than their respective controls and standards. The data presented in these two tables are calculated using the concentration found for the corresponding controls as the starting concentration. The only fairly consistently non-negative values were those representing the powder samples. If the standard concentrations are used as the starting concentrations then the data in Tables XII and XIII are the resulting binding amounts. Figures 4.2.49 through 4.2.53 show the binding capacities graphically of FITC IgG and streptavidin depleted solutions after exposure to silica slides, cane, fiber, Cab-o-Sil® and Stöber spheres, respectively.

Table X. Concentration 0.01 mg/ml Streptavidin, Biotin, and FITC IgG Binding Amount Results from Binding Set Two Using Controls as the Starting Concentrations

Sample	0.01 mg/ml Protein Binding ($\mu\text{g}/\text{cm}^2$) Using Controls		
	<i>Streptavidin</i>	<i>Biotin</i>	<i>FITC IgG</i>
SIEt	-0.6181	-0.4971	1.4918
SIHF	-0.5781	-0.7265	1.3776
SIwP	-0.5331	-0.5902	2.1227
SITt	-0.5218	-0.4587	2.1598
CaEt	-1.0609	-0.9976	1.1676
CaHF	-1.2529	0.2020	0.9008
CawP	-0.3615	0.3038	1.4175
CaTt	-1.5828	-0.5274	7.0520
FiEt	-1.3333	-0.5501	-0.8019
FIHF	-1.7272	-0.4438	-0.3573
FITt	-1.6493	-0.4503	0.2197
PCar	0.0038	0.0022	0.0113
PCTt	0.0040	0.0019	0.0082
SSam	0.0005	0.0002	0.0018
SSTt	0.0003	0.0001	0.0010

Table XI. Concentration 0.1 mg/ml Streptavidin, Biotin, and FITC IgG Binding Amount Results from Binding Set Two Using Controls as the Starting Concentrations

Sample	0.1 mg/ml Protein Binding ($\mu\text{g}/\text{cm}^2$) Using Controls		
	<i>Streptavidin</i>	<i>Biotin</i>	<i>FITC IgG</i>
SIEt	2.4216	0.4207	0.5518
SIHF	3.6743	-0.3430	-2.6451
SIwP	4.2629	-0.0229	-0.8303
SITt	9.3608	0.5509	-4.2668
CaEt	9.2974	2.4809	-4.8996
CaHF	9.6868	-0.5921	-11.0949
CawP	10.6754	3.3142	-8.9822
CaTt	8.3641	0.9743	-2.0164
FiEt	8.2451	2.4494	-1.7211
FIHF	6.1070	1.0411	-6.3020
FITt	4.9825	1.3262	-6.2223
PCar	0.0114	-0.0003	0.0652
PCTt	0.0072	-0.0025	0.0253
SSam	0.0013	-0.0020	0.0043
SSTt	0.0014	-0.0024	0.0029

Table XII. Concentration 0.01 mg/ml Streptavidin, Biotin, and FITC IgG Binding Amount Results from Binding Set Two Using Standards as the Starting Concentrations

Sample	0.01 mg/ml Protein Binding ($\mu\text{g}/\text{cm}^2$) Using Standards		
	<i>Streptavidin</i>	<i>Biotin</i>	<i>FITC IgG</i>
SIEt	-0.5114	0.0445	-3.0014
SIHF	-0.4524	-0.0883	-3.1154
SIWP	-0.4226	-0.0296	-2.5150
SITt	-0.4152	0.0826	-2.6413
CaEt	-1.6441	-2.1327	-9.5381
CaHF	-1.8361	-0.9332	-9.8050
CaWP	-0.9447	-0.8314	-9.2883
CaTt	-2.1661	-1.6626	-3.6538
FiEt	-1.8115	-1.4810	-9.5806
FIHF	-2.2054	-1.3746	-9.1360
FITt	-2.1275	-1.3812	-8.5590
PCar	0.0038	0.0018	-0.0018
PCTt	0.0040	0.0014	-0.0050
SSam	0.0005	0.0002	0.0001
SSTt	0.0003	0.00004	-0.0007

Table XIII. Concentration 0.1 mg/ml Streptavidin, Biotin, and FITC IgG Binding Amount Results from Binding Set Two Using Standards as the Starting Concentrations

Sample	0.1 mg/ml Protein Binding ($\mu\text{g}/\text{cm}^2$) Using Standards		
	<i>Streptavidin</i>	<i>Biotin</i>	<i>FITC IgG</i>
SIEt	2.9729	5.1075	0.0913
SIHF	4.2093	4.2055	-3.1890
SIWP	4.8194	4.7078	-1.3101
SITt	9.9338	5.4222	-4.7528
CaEt	6.5985	16.5305	-24.8486
CaHF	6.9879	13.4575	-31.0439
CaWP	7.9765	17.3638	-28.9312
CaTt	5.6652	15.0239	-21.9654
FiEt	6.0320	13.9701	-18.0792
FIHF	3.8939	12.5618	-22.6602
FITt	2.7695	12.8469	-22.5804
PCar	0.0165	0.0231	0.0616
PCTt	0.0122	0.0208	0.0217
SSam	0.0019	0.0010	0.0038
SSTt	0.0020	0.0006	0.0024

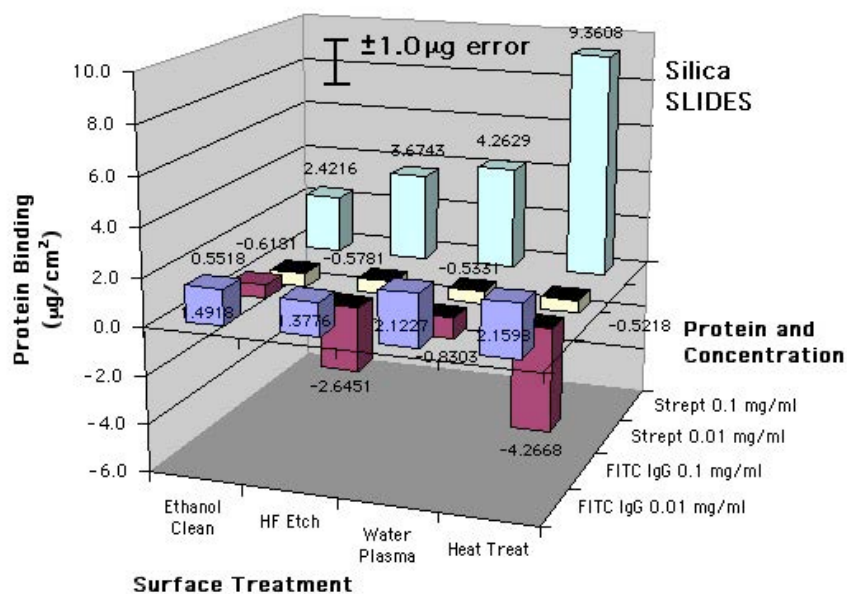


Figure 4.2.49. Binding amounts for silica slides after FITC IgG and streptavidin from Binding Set Two.

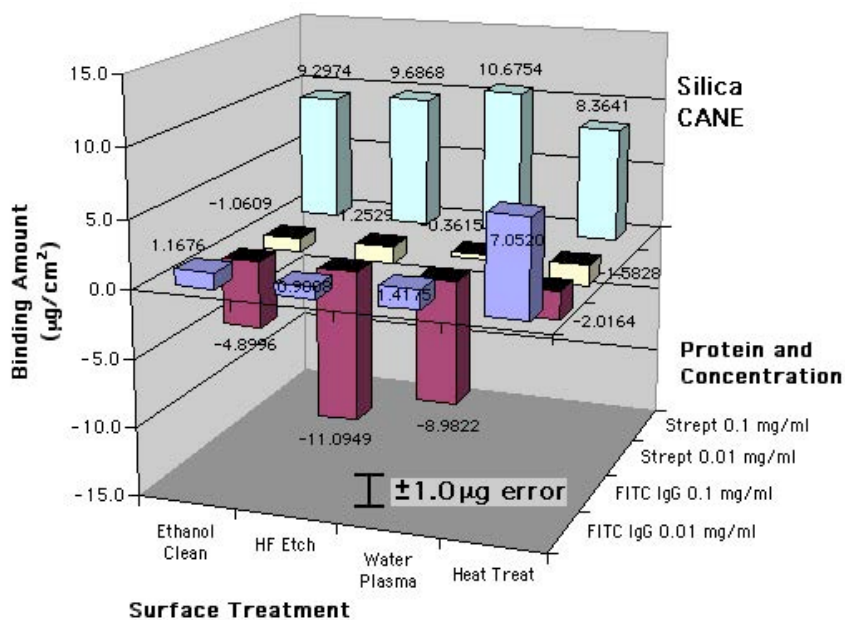


Figure 4.2.50. Binding amounts for silica cane after FITC IgG and streptavidin from Binding Set Two.

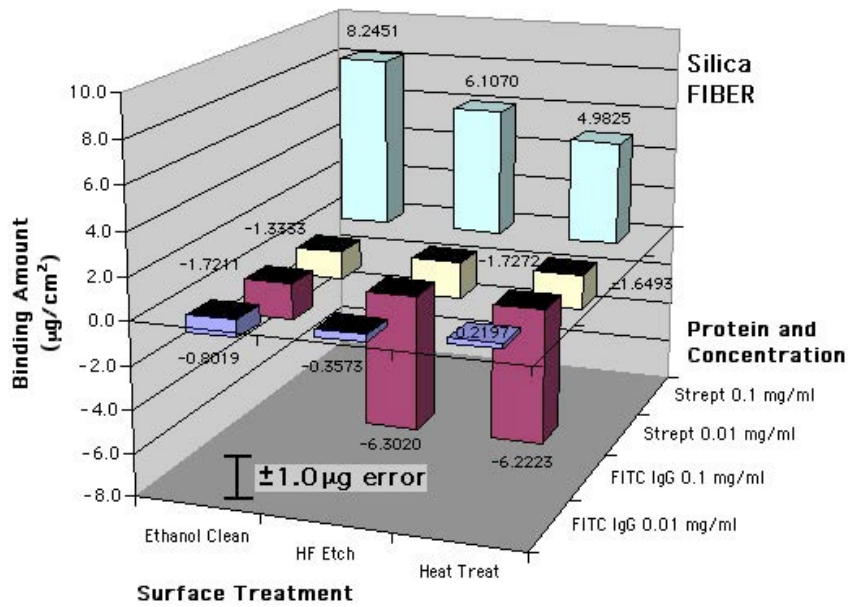


Figure 4.2.51. Binding amounts for silica fiber after FITC IgG and streptavidin from Binding Set Two.

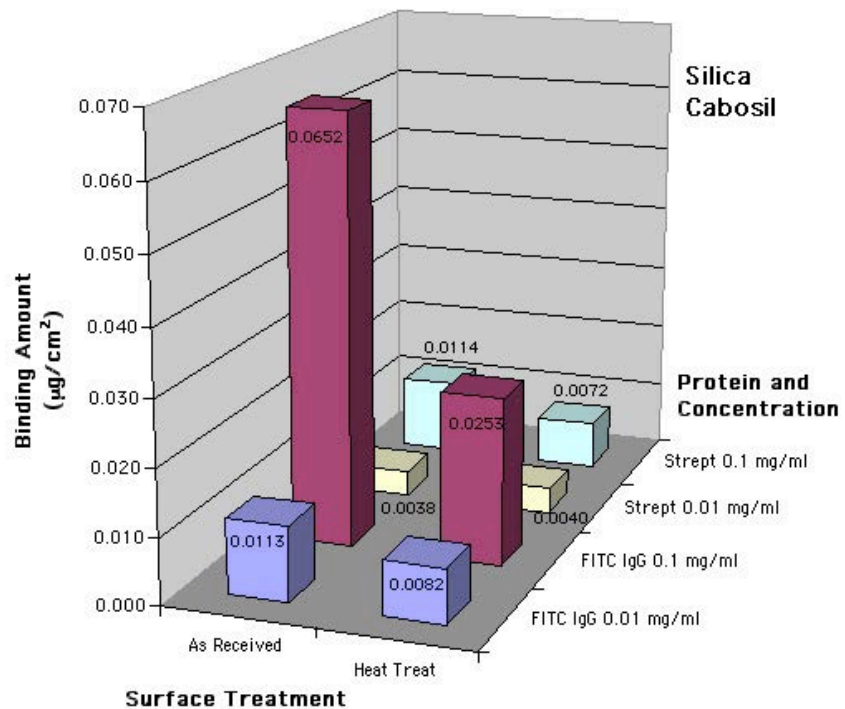


Figure 4.2.52. Binding amounts for silica Cab-o-Sil® after FITC IgG and streptavidin from Binding Set Two.

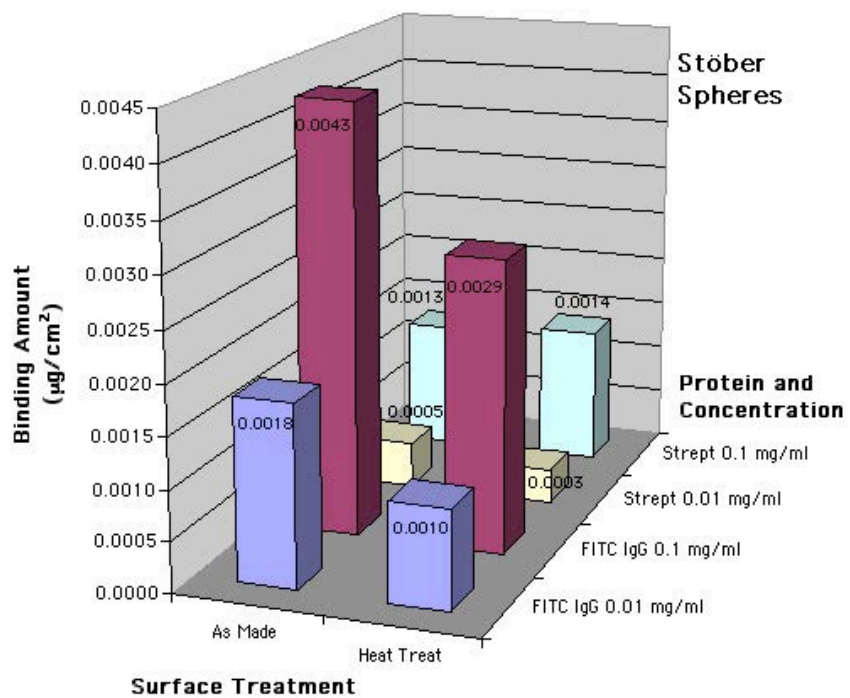


Figure 4.2.53. Binding amounts for silica Stöber spheres after FITC IgG and streptavidin from Binding Set Two.

4.3. Bicinchoninic Acid Protein Assay

The BCA protein assay technique can be used to determine the concentration of protein in a solution by measuring the absorbance of light. The absorbance, measured at 562 nm, is linear with respect to the protein concentration within the range of 5 $\mu\text{g/ml}$ to 2000 $\mu\text{g/ml}$. The BCA assay kit from Pierce includes bovine serum albumin standards of 2 mg/ml concentration. These certified standards are intended to be used to create the range of standards from which the absorbance is measured to make a linear calibration plot. This plot is then fit with a line and the unknown solution concentrations are found using the equation of the line. It is suggested by the Pierce BCA assay literature that the best results arise from using the same protein in the standards as is in the unknowns. All solutions were run in triplicate and for this study the solutions analyzed were always the primary protein solutions. All plates were analyzed in the μQuant plate reader both immediately after incubation (warm) and then after a half hour of cooling (cool). It was determined that the best curve fit arises from the analysis of warm plates.

The first assay that was performed was intended to measure mouse-IgG standards to be used for BCA assay. In addition, the 0.1 mg/ml concentration stock solution of mouse IgG was also measured. This assay utilized the BSA standards to do so and in addition depleted mouse-IgG solutions were analyzed after exposure to WP and HF cane. The results were promising and so the next analysis was done on all of the depleted solutions from binding set one using BSA as the standards. These results were fairly scattered and all of the concentrations were much higher than their original concentration. These solutions had been cycled through a few freezes and thaws and the vials had been opened a number of times, so the concentrations were certainly not representative of freshly depleted solutions.

The success of a BCA assay is highly dependent on the skill and experience of the operator loading the microtiter plate. It was observed throughout the entire set of BCA assays that the calibration curve fit became more accurate with time. The third assay measured depleted streptavidin solutions after binding to set one samples and the associated control solutions. Since the BSA standards were used to create the curve fit, the results are all offset by a factor related to the difference between BSA and streptavidin proteins and how these proteins react with the bicinchoninic acid.

Streptavidin standards were used to create the calibration curve fit for the next measurement of the depleted streptavidin solutions from binding set one. These standards were made fresh the day before the measurement in the range of 5 $\mu\text{g/ml}$ to 250 $\mu\text{g/ml}$. The same was done for fresh mouse-IgG standards, which were analyzed along with the depleted mouse-IgG solutions from binding set one. The BCA assay results for streptavidin and IgG are shown in Tables XIV and XV, respectively.

Table XIV. BCA Assay Binding Results for Depleted Streptavidin Solutions from Binding Set One

Glass Form	Surface Treatment	Concentration (mg/ml)	Binding Results ($\mu\text{g}/\text{cm}^2$)	+/- Error
Slide	ethanol clean	0.01	3.3537	1.1647
Slide	10 min HF etch	0.01	2.1379	1.1346
Slide	water plasma	0.01	2.7736	0.997
Cane	ethanol clean	0.01	-0.0326	2.4242
Cane	10 min HF etch	0.01	4.1901	1.2771
Cane	water plasma	0.01	5.4291	0.7312
Fiber	ethanol clean	0.01	6.5006	3.2019
Fiber	10 min HF etch	0.01	3.0300	1.0704
Cabosil	as-received	0.01	0.00179	0.00022
Stober	calcined	0.01	0.01037	0.00386
Slide	ethanol clean	0.1	-0.0406	1.4591
Slide	10 min HF etch	0.1	3.0209	2.4523
Slide	water plasma	0.1	2.9927	1.7923
Cane	ethanol clean	0.1	13.5647	6.0963
Cane	10 min HF etch	0.1	19.1732	5.949
Cane	water plasma	0.1	11.9017	8.0119
Fiber	ethanol clean	0.1	15.6307	4.8293
Fiber	10 min HF etch	0.1	0.5473	4.175
Cabosil	as-received	0.1	0.00365	0.00163
Stober	calcined	0.1	-0.00129	0.0122

Table XV. BCA Assay Binding Results for Depleted Mouse-IgG Solutions from Binding Set One

Glass Form	Surface Treatment	Concentration (mg/ml)	Binding Results ($\mu\text{g}/\text{cm}^2$)	+/- Error
Slide	ethanol clean	0.01	-0.3686	0.9251
Slide	10 min HF etch	0.01	0.4065	0.3941
Slide	water plasma	0.01	-1.4689	0.6305
Cane	ethanol clean	0.01	-3.0977	2.888
Cane	10 min HF etch	0.01	-14.5266	17.1438
Cane	water plasma	0.01	-3.6031	3.2978
Fiber	ethanol clean	0.01	-3.3103	2.7877
Fiber	10 min HF etch	0.01	-0.9344	2.3745
Cabosil	as-received	0.01	-0.00005	0.00048
Stober	calcined	0.01	0.00094	0.00313
Slide	ethanol clean	0.1	-6.6519	1.3984
Slide	10 min HF etch	0.1	-5.6381	1.6216
Slide	water plasma	0.1	-6.0440	2.3847
Cane	ethanol clean	0.1	-17.6895	4.9367
Cane	10 min HF etch	0.1	-21.5861	9.3271
Cane	water plasma	0.1	-20.3633	6.3639
Fiber	ethanol clean	0.1	-19.0211	6.2157
Fiber	10 min HF etch	0.1	-20.7831	5.229
Cabosil	as-received	0.1	0.00875	0.00106
Stober	calcined	0.1	0.03414	0.00652

A pH variation study was conducted as discussed in previous results sections. Streptavidin solutions of 0.01 mg/ml concentrations were made with pHs of 2, 4, 6, 7.4, 8, 10 and 12. These solutions were treated both as controls and were exposed to two pieces of ethanol cleaned cane each. The resulting concentrations from the BCA assay are highly dependent on the pH, even though the physical concentrations of the controls are all 0.01 mg/ml. Unlike the direct fluorescence relationship observed versus pH, the BCA results for the controls display a bimodal distribution with maxima occurring near pH 7.4 and pH 12. The results for the exposed samples do not follow the controls with maxima at pHs 2 and 8.

The other curiosity is the factor of correction between the certified BSA standards and the two primary proteins used in this study. A curve fit containing eight standards created for BSA had an r-squared of 0.9994. The concentrations of the mouse-IgG and streptavidin solutions investigated were 0.01 mg/ml, 0.1 mg/ml and 1.0 mg/ml. The Pierce literature published a factor of correction for IgG of 1.18, meaning that any BCA data for IgG using BSA for standards will be 1.18 times greater than it should be. This factor of 1.18 was the exact number that was found to relate the IgG values to their actual concentrations. The streptavidin concentrations had a factor of correction on average of 1.53 using BSA as standards.

The last set of BCA assays arise from the second binding set. Four assays were done due to the increase in number of samples from binding set one to binding set two. The first assay included streptavidin depleted solutions after exposure to silica slides, cane or fiber and streptavidin standards. The second assay was also for depleted streptavidin solutions after exposure to Cab-o-Sil® or Stöber spheres with streptavidin as the standards. The third assay involved mouse-IgG standards and depleted mouse-IgG solutions after exposure to silica slides, cane or fiber from binding set two. The last BCA assay was performed on mouse-IgG solutions after exposure to Cab-o-Sil® or Stöber powders with IgG standards. The results for

the BCA assays are shown on a silica form basis to compare the four protein/concentrations. Figure 4.3.1 is a bar chart of the BCA assay binding results for silica slides as a function of surface treatment and protein/concentration. Figure 4.3.2 is the bar chart binding results for silica cane. The silica fiber BCA assay results are shown in Figure 4.3.3. For these three figures there is a trend seen in the 0.01 mg/ml streptavidin line as a function of surface treatment. The streptavidin binds decreasing amounts of protein in order of ethanol clean, HF etch, water plasma treatment and heat treatment. Figures 4.3.4 and 4.3.5 are the BCA assay binding results after exposure to Cab-o-Sil® and Stöber spheres, respectively.

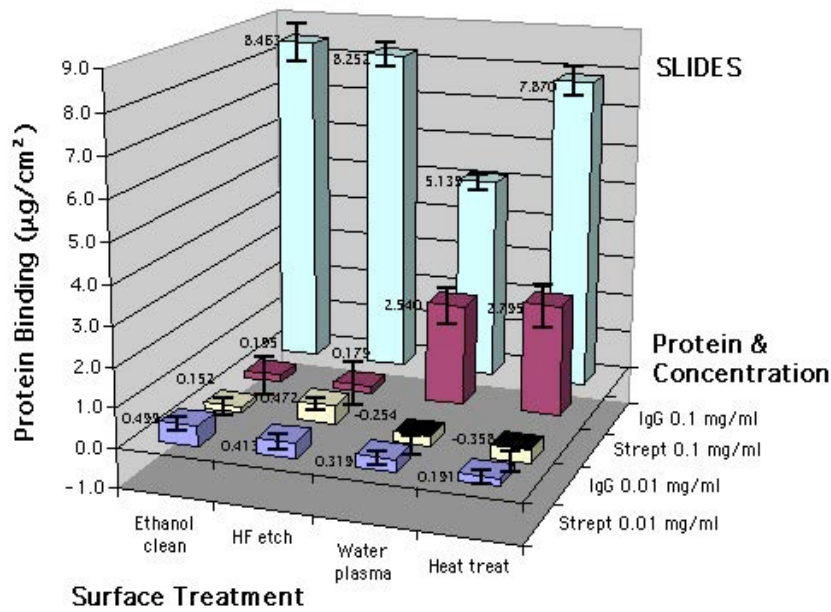


Figure 4.3.1. BCA assay binding results for silica slides from Binding Set Two using controls.

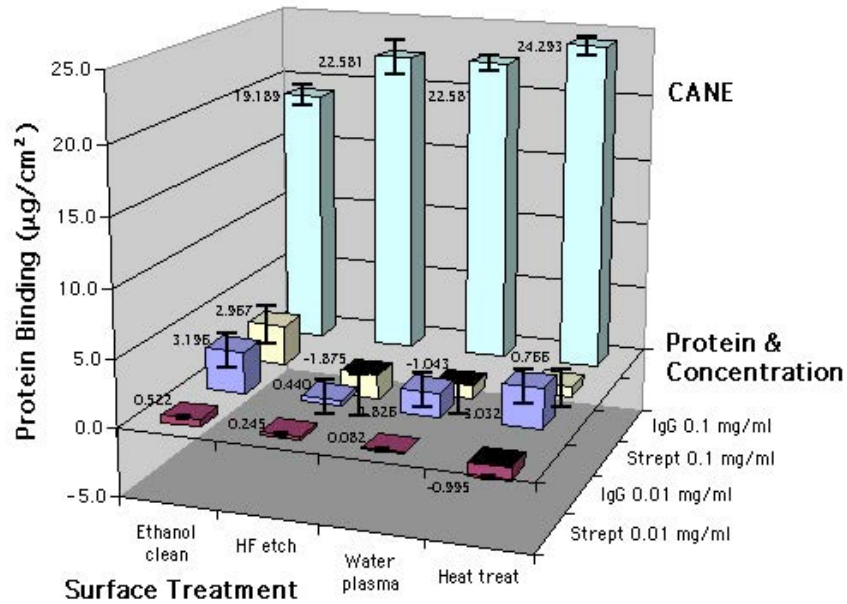


Figure 4.3.2. BCA assay binding results for silica cane from Binding Set Two using controls.

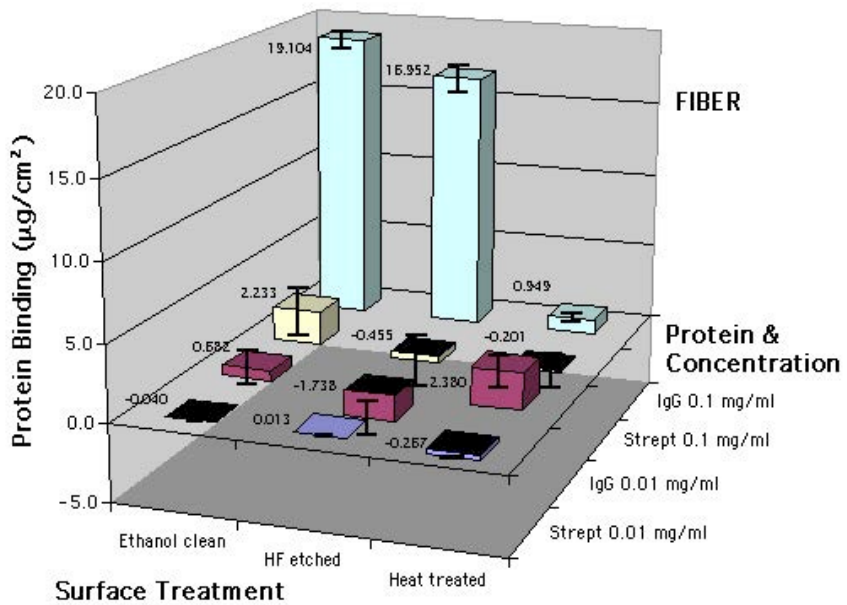


Figure 4.3.3. BCA assay binding results for silica fibers from Binding Set Two using controls.

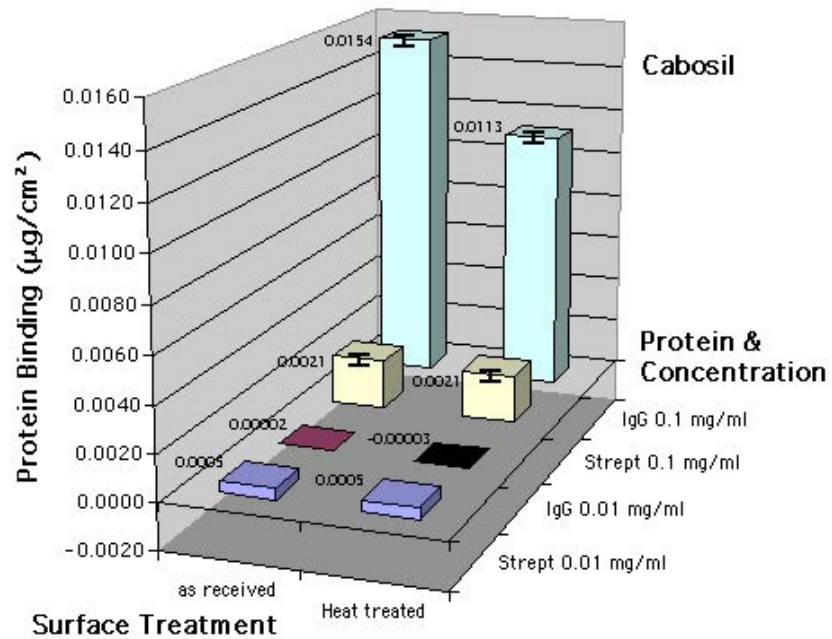


Figure 4.3.4. BCA assay binding results for fumed silica Cab-o-Sil® from Binding Set Two using controls.

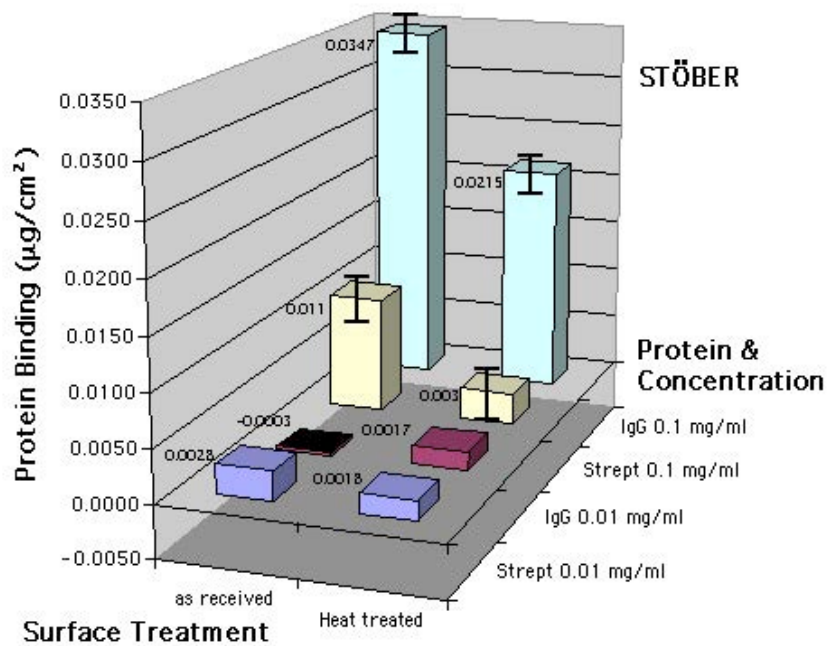


Figure 4.3.5. BCA assay binding results for Stöber microspheres from Binding Set Two using controls.

4.4. X-ray Analyses

Two X-ray techniques were briefly employed in this study. The first was a glancing incidence (GIXA) technique used to determine the protein “film” thickness on silica slides. The other technique was an adapted version of powder diffraction whereby highly absorbing plates were placed in the beam path. The sample in this case was a quartz single crystal and because the signal is so intense, the plates were used in order for the signal to be handled by the detector.

The GIXA technique compares the data collected to a model set up by the user to simulate the data. It is a tedious process to set up and try simulations because slight changes in the starting values can cause an entirely different fit to occur. The starting values and the values that are iterated during the simulation include the substrate roughness and density, the hydrated layer thickness, roughness and density and also the organic layer thickness, roughness and density. The software utilized for the simulations is called RefSim[®] and its database contains a very limited selection of organic materials. Therefore, the streptavidin proteins were represented by a CH₂ layer with a density of 1.69 g/cm³. The density for the substrate, represented by SiO₂, is much higher at 2.48 than the typical density of amorphous silica, 2.2 g/cm³, but any deviation from the set value caused the simulation not to fit at all. Figure 4.4.1 is the GIXA data for an untreated silica slide incubated with 0.01 mg/ml streptavidin protein for 30 minutes and then dried. Also shown in this figure is the simulation fit. Table XVI lists the values that create the simulation.

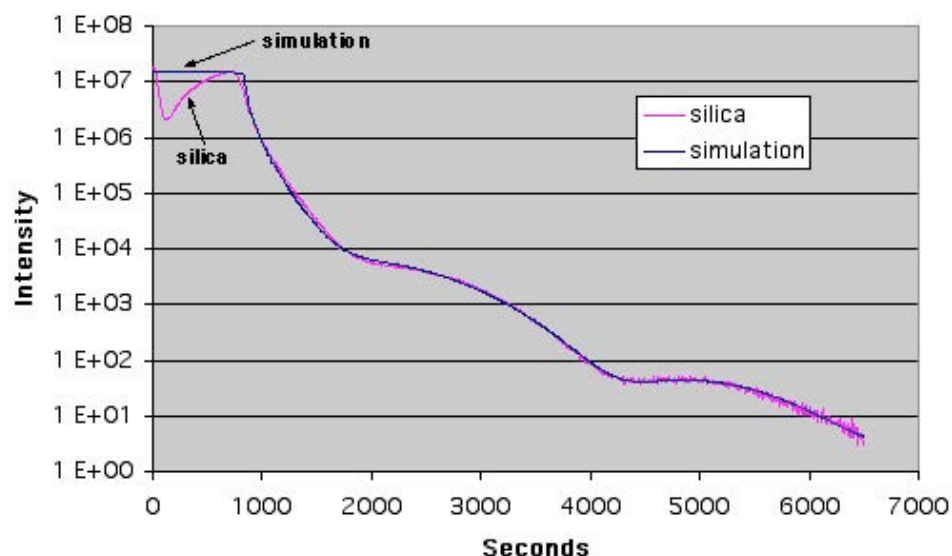


Figure 4.4.1. GIXA data for untreated silica slide coated with streptavidin protein and the simulation fit.

Table XVI. GIXA Model Values for the Data Simulation Shown in Figure 4.4.1

	Thickness (Å)	Roughness (Å)	Density (g/cc)
SiO ₂	infinite	8.37	2.48
SiOH	2.03	2.74	2.2
CH ₂	46.2	8.96	1.69

X-ray analysis was also used to determine, or rather confirm, the plane index for a single crystal natural quartz terminal. To do this, the Miller-Bravais index system of a hexagonal crystal must first be understood. Hexagonal crystals have a four index naming system, $(hkil)$, where i is the reciprocal of the fractional intercept on the third basal axis. Since the intercepts of a plane on the other two basal axes determine the intercept on the third, the value of i is redundant and is dependent on the values of h and k . Therefore, $h+k=-i$, and since i is redundant it is sometimes replaced by a dot or removed altogether. Doing this replacement though defeats the purpose for which the Miller-Bravais system was intended, to give similar

indices to similar planes. For example, if the four index representations of the side planes of a hexagonal crystal are listed it is clear that they are all related; $(10\bar{1}0)$, $(\bar{1}010)$, $(01\bar{1}0)$, $(0\bar{1}10)$, $(\bar{1}100)$, and $(1\bar{1}00)$. However, if the i index is removed, it is not obvious that these planes are related; (100) , (010) , $(\bar{1}10)$, $(\bar{1}00)$, $(0\bar{1}0)$, and $(1\bar{1}0)$.

It was this notation variation that caused much confusion because the software used to deconvolute x-ray data only gives indices in the three-index form. Figure 4.4.2 is the X-ray intensity versus 2-Theta data for the powdered crystal, the single crystal terminal and the quartz PDF from top to bottom. By comparing the 2-Theta value to the list of planes associated with 2-Theta values, it was concluded that the terminal is of the (101) crystal orientation. This (101) actually corresponds to a four-index representation of $(10\bar{1}1)$ or the $\{10\bar{1}1\}$ family for all of the terminals. Through knowing this, it is then easy to determine that the sides of the single crystal are of the $\{1\bar{1}00\}$ plane family. Both the natural terminal and the sides of the crystal were used in this study. The top graph of Figure 4.4.2 was simply to confirm that the crystal was indeed quartz.

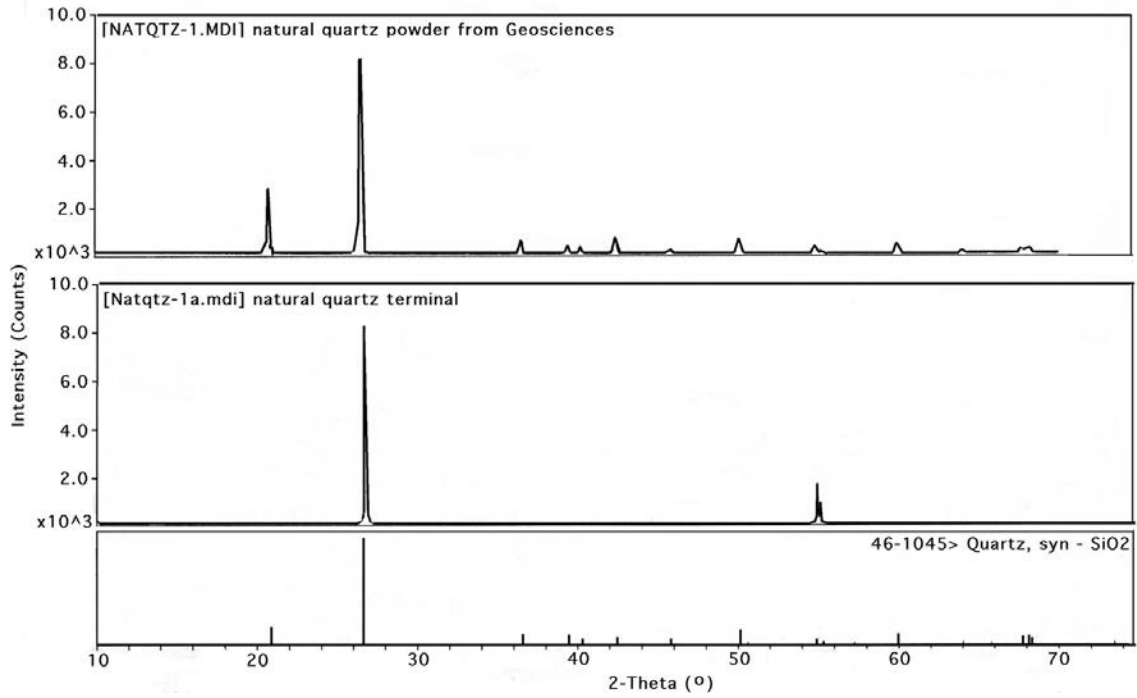


Figure 4.4.2. X-ray data for quartz crystal. Powder diffraction data (top). Single crystal diffraction of natural quartz terminal (middle). PDF of synthetic quartz (bottom).

4.5. Atomic Force Microscopy (AFM)

“Do what you can, with what you have, where you are.” - Teddy Roosevelt

AFM is one of the most powerful tools for surface analysis of glasses. It is for this reason that this technique was utilized for this study. It was possible to visually characterize the changes in a glass surface with surface treatment using AFM. In addition, it was possible to image protein agglomerations on glass surfaces, which will lead to a further understanding of the interactions of proteins with glasses. All of the images in this section and the following section (4.6) were collected at either Corning Incorporated or Digital Instruments.

Fisher’s Finest soda-lime silicate (FFSLS) slides were investigated in the early stages of this project and so they were examined with atomic force microscopy. Figure 4.5.1 is an AFM image of an as-received FFSLS slide. Light features are protrusions and dark features are depressions. Clearly visible is an organic film and the areas where the film does not cover the slide are occupied by small crystals. These small crystals are most likely debris from the formation process. The presence of the film and the processing debris was confirmed by Dr. Sanford at Erie Scientific (slide suppliers for Fisher).^{1 2001} Cleaning with isopropanol does not remove either surface contaminant. Figure 4.5.2 is an AFM image of a similar slide after it has been etched in 10% HF acid for 2 minutes. The organic film has been removed, but some of the processing debris remains. Due to the presence of these surface anomalies, soda-lime silicate slides were obtained directly from Dr. Sanford that had not been coated with the organic film. These slides are referred to as non-coated soda-lime silicate (NCSLS) or just SLS slides. Some of the NCSLS slides also had remaining processing debris on the surface,

while other NCSLS slides had been thoroughly cleaned. There was no way of determining prior to the AFM scan which slides would be free of debris.

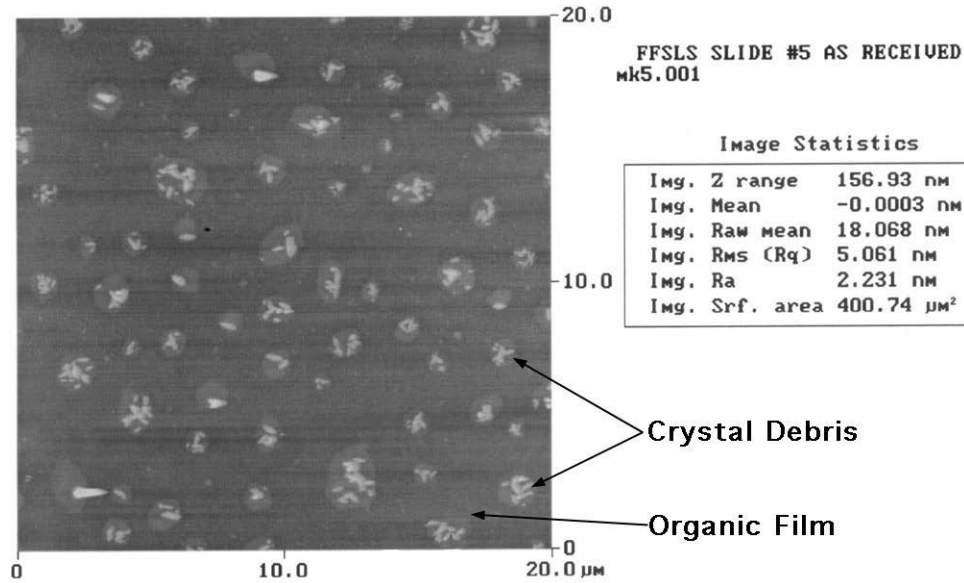


Figure 4.5.1. AFM tapping mode image of an as-received FFSLs slide showing crystal processing debris and organic film.

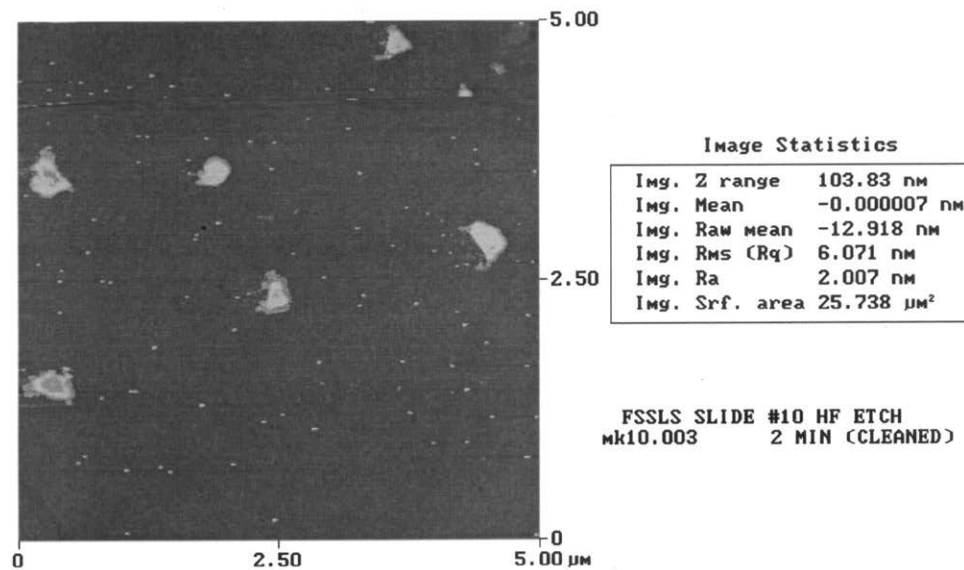


Figure 4.5.2. AFM tapping mode image of an FFSLs slide etched in HF acid for 2 minutes showing processing debris, but no surface film.

The NCSLS slides that initially had surface processing debris like the one shown in Figure 4.5.3, were not cleared of this debris after HF etching. Figure 4.5.4 is the same slide as in Figure 4.5.3, but along with a phase contrast image which shows that the debris is made of a different material than the glass. The phase contrast image is created by measuring the phase lag in the tip interaction with the surface. A softer material will interact with the tip more creating more of a phase lag. Figure 4.5.5 is an image of the same slide as in Figure 4.5.3 after etching in HF for 10 minutes. Before etching the average surface roughness for this slide was 7.374 nm and after etching the roughness was 8.435 nm. Another one of the NCSLS slides from the same box was imaged in the AFM using tapping mode and the resulting image is shown in Figure 4.5.6. This slide has no processing debris and is very smooth with an average roughness (Ra) of 1.047 nm. Figure 4.5.7 is the same slide after etching in HF for 10 minutes. As expected, this etched slide with no processing debris had a slightly higher Ra of 1.188 nm than the non-etched slide. Despite the difference in original surface roughness of the two types of NCSLS slide, exposure to HF acid for 10 minutes led to approximately a 12% increase in surface roughness. The Ra is calculated by using the following equation:

$$Ra = \frac{1}{N_L} \sum_{i=1}^{N_L} |z_i(x)| \quad (10)$$

where N_L is the number of points and $z(x)$ is the height of the point from the center line. The other roughness value, the RMS roughness or Rq is calculated from:

$$Rq = \sqrt{\frac{1}{N_L} \sum_{i=1}^{N_L} z_i^2(x)} \quad (11)$$

and is more sensitive to large features, so it has a larger value than Ra in general.

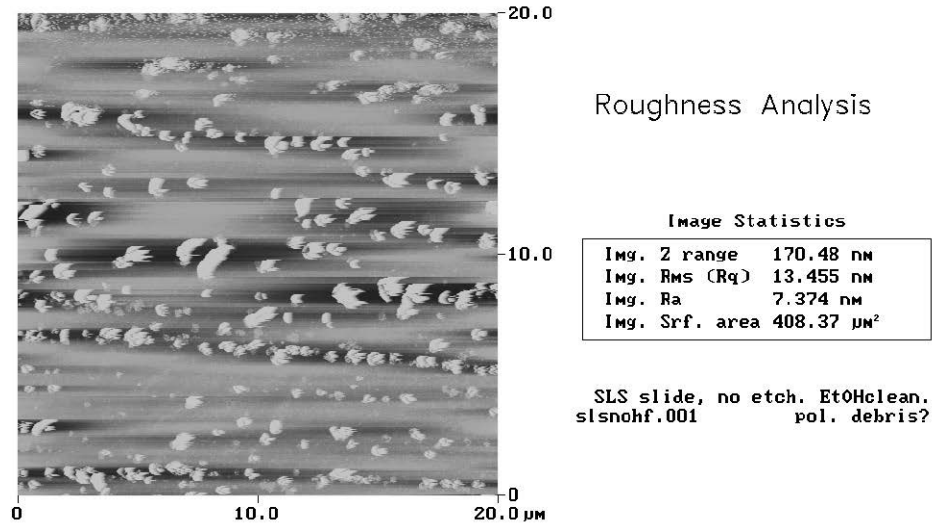


Figure 4.5.3. AFM tapping mode image of an as-received NCSLS slide showing heavy processing debris.

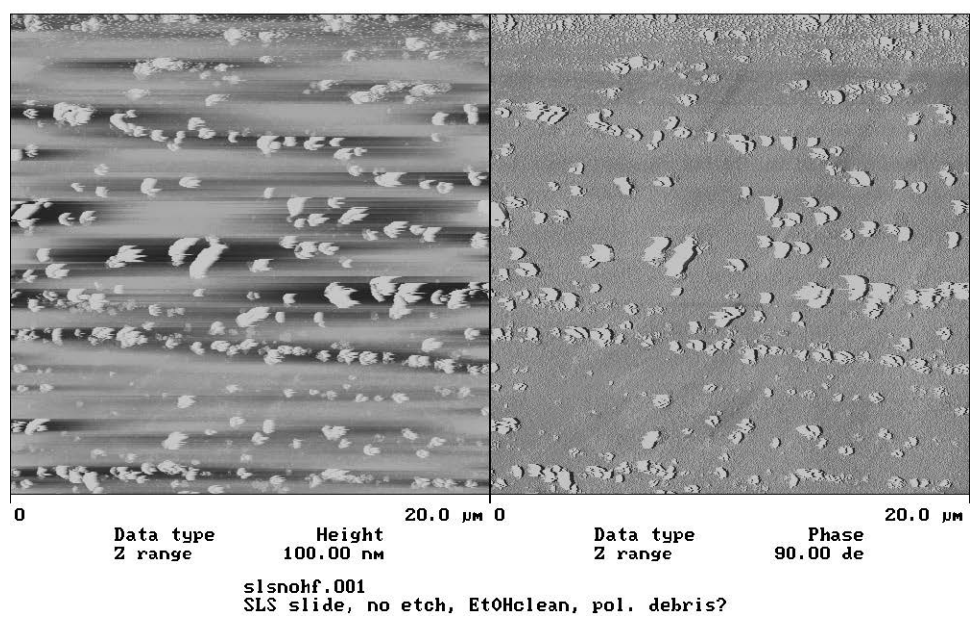


Figure 4.5.4. AFM tapping mode images of an as-received NCSLS slide. Left is topographical data and right is phase contrast data.

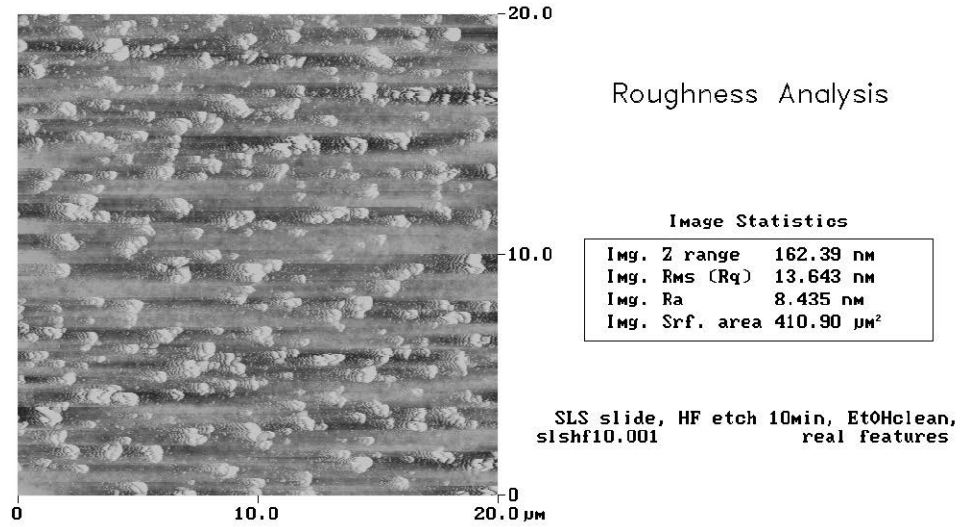
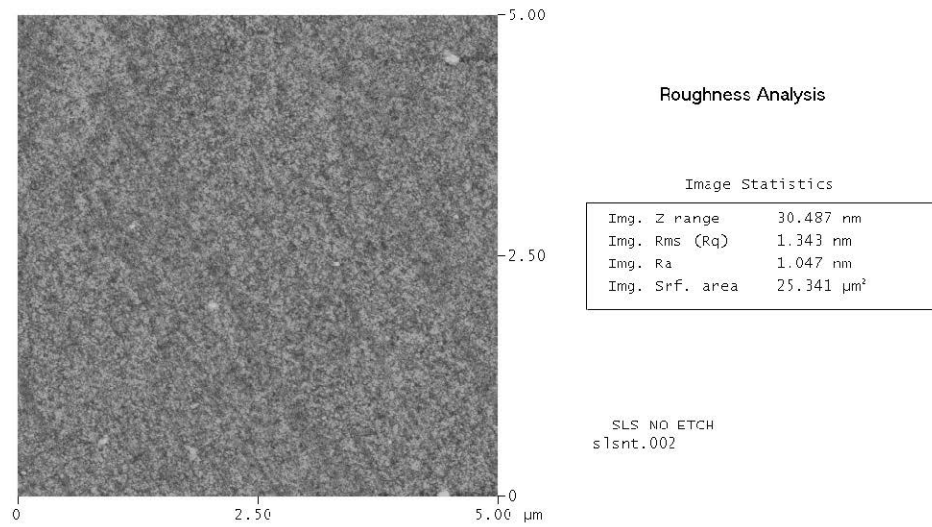


Figure 4.5.5. AFM tapping mode image of an NCSLS slide etched in HF acid for 10 minutes showing processing debris remains after etching.



4.5.6. AFM tapping mode image of another as-received NCSLS slide showing no processing debris.

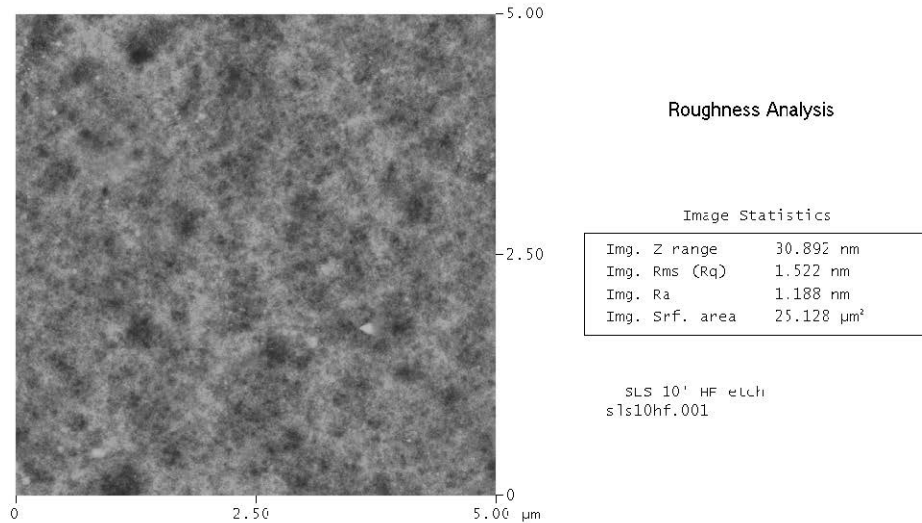


Figure 4.5.7. AFM image of an NCSLS slide etched in 10% HF acid for 10 minutes showing a slight roughening of the surface.

Once this study began to focus on silica only, SiO_2 slides were obtained and analyzed in the atomic force microscope. These slides were supplied by Quartz Scientific. An AFM image of slides after having been cleaned with ethanol is shown in Figure 4.5.8 with the roughness analysis. The average roughness of these slides is extremely low at 0.597 nm and 0.606 nm. These same slides were etched in 10% HF acid for 2 minutes or 10 minutes and imaged in tapping mode. The resulting topographical dual image is shown in Figure 4.5.9 along with the roughness analysis. The Ra of the 2-minute etched slide is increased to 1.236 nm from 0.597 nm. The Ra of the 10 min etched slide is increased to 2.944 nm from 0.606 nm. For the 2-minute etch in HF the scratches and pits are enhanced on the surface and after 10 minutes of etching the silica is changed on the structural scale, meaning that scratches and pits are no longer easily distinguished from overall surface roughness. The average roughness of the untreated silica slides is fairly consistent from slide to slide, but the Ra of the SLS slides varies as much as $\pm 75\%$ of the average. Figure 4.5.10 is a composite of four AFM images

showing the Ra of untreated silica and SLS as well as the Ra of silica and SLS having been etched in HF for 2 minutes. The Ra is for the image acquired and so this value is dependent on the sampling area. All four images are the same scan size of 5 microns. Again, after 2 minutes of etching in HF the silica slide has an enhancement of scratches and pits, while the SLS slide is etched on the structural level. The size of the feature no longer has an effect on the etching rate after 10 minutes.

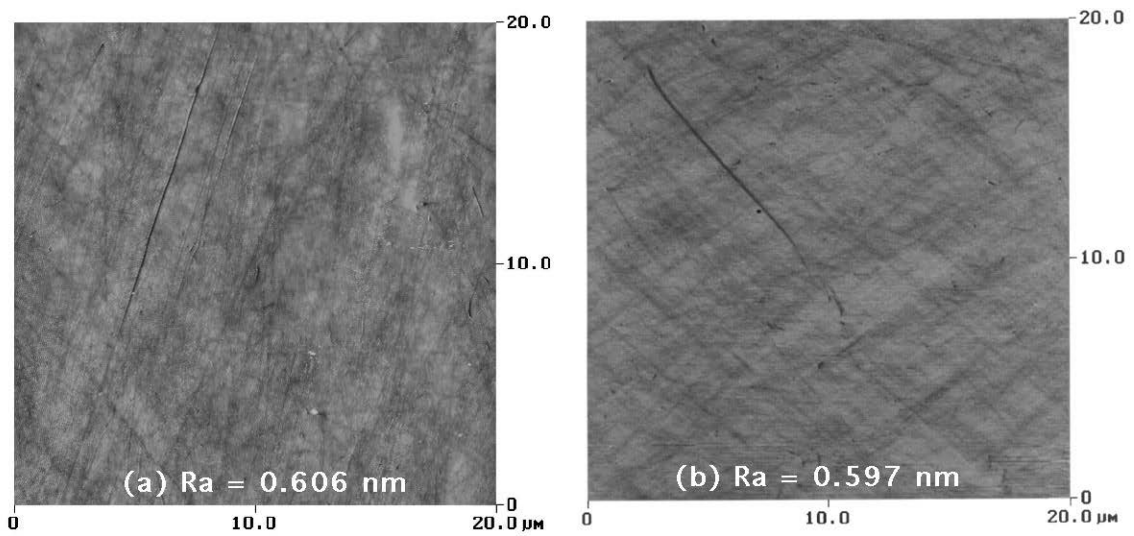


Figure 4.5.8. AFM tapping mode image of two silica glass slides having been cleaned with ethanol.

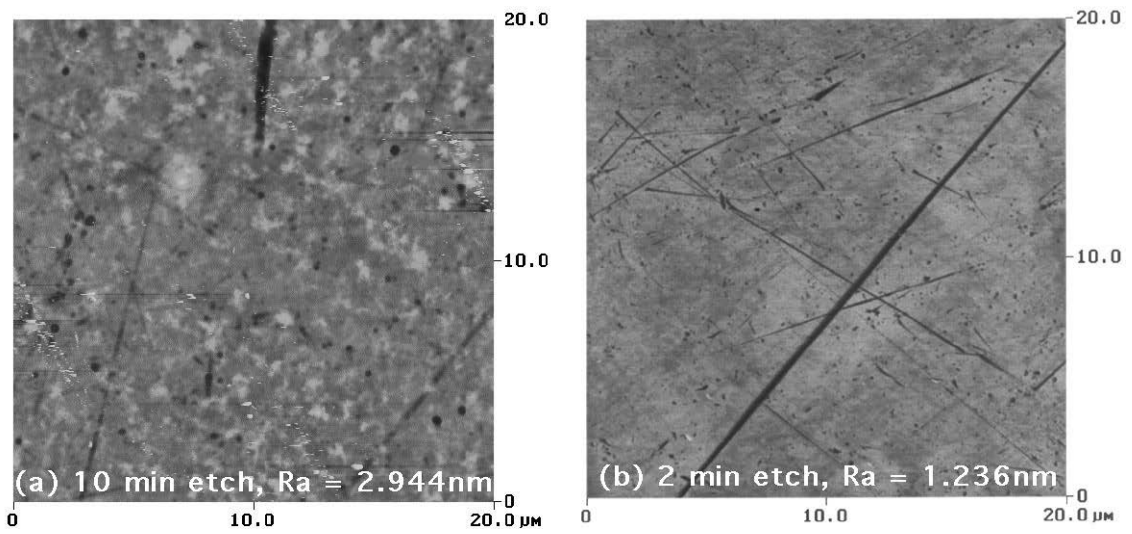


Figure 4.5.9. AFM tapping mode image of a silica glass slide etched in 10% HF acid for (a) 10 minutes and (b) 2 minutes.

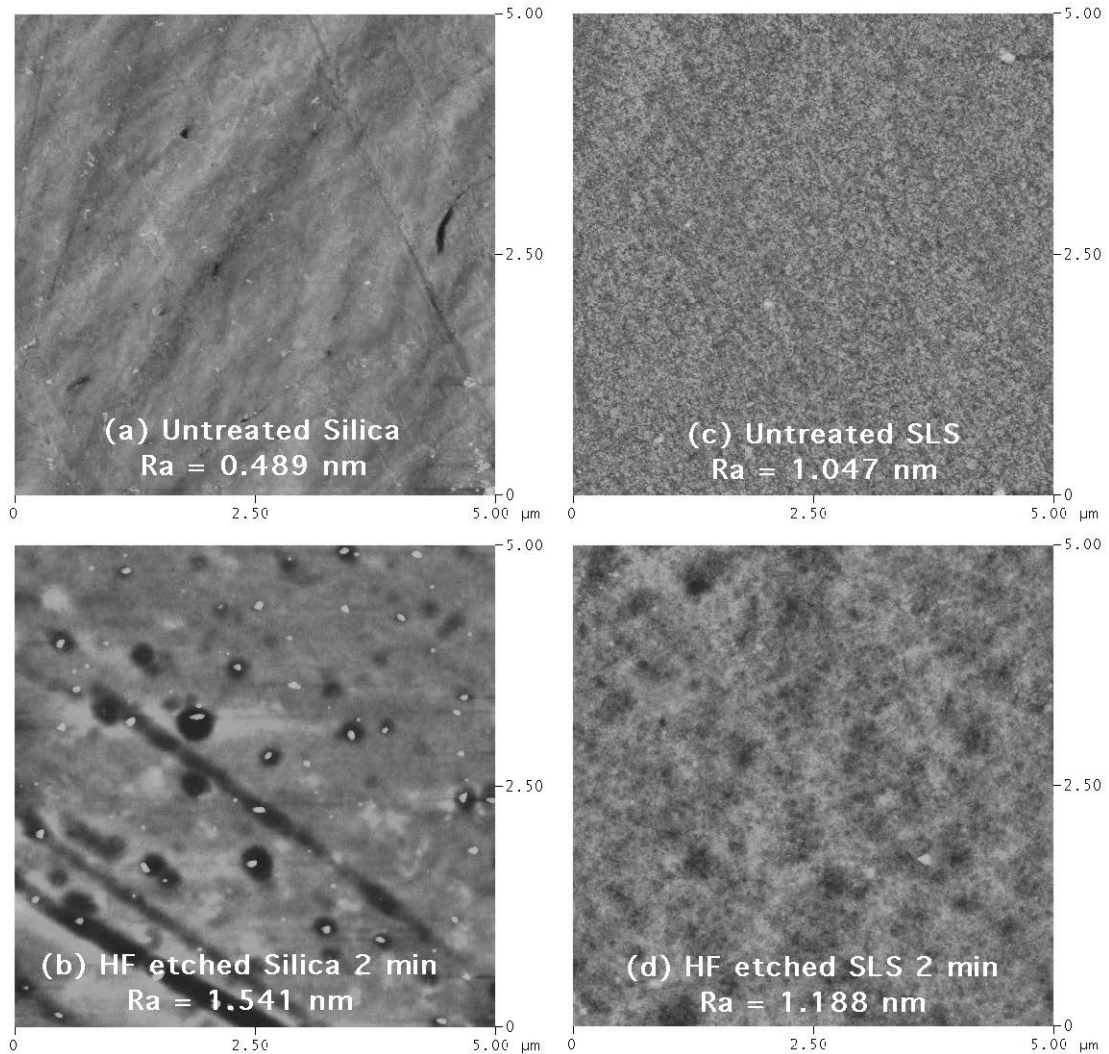


Figure 4.5.10. AFM tapping mode images of silica and SLS slides. (a) untreated silica, (b) 2 min HF etched silica, (c) untreated SLS, and (d) 2 min HF etched SLS.

A 3-dimensional image comparison of an untreated SLS slide and a slide etched in HF acid for 2 minutes is shown in Figure 4.5.11. The Ra of this untreated SLS slide at a scan size of 2 microns was calculated to be 0.275 nm. This untreated Ra is much lower than the Ra's obtained from larger area scans. The Ra of the etched SLS slide was 2.828 nm. Due to the large discrepancy between SLS slide roughness', it cannot be claimed that the scan size effects the calculated Ra for SLS slides.

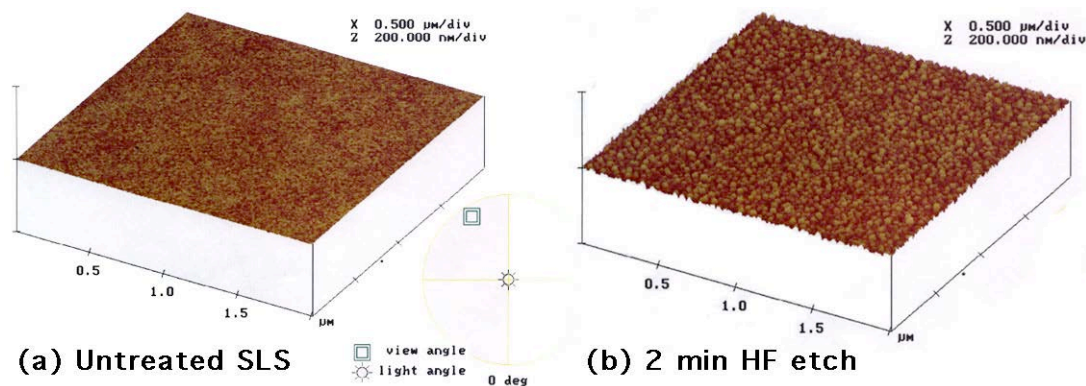


Figure 4.5.11. 3-D AFM tapping mode images of SLS slides (a) untreated and (b) etched in HF acid for 2 minutes.

The Ra dependency on the scan size is however illustrated in Figure 4.5.12. This figure is a 1-micron scan AFM image of the same slide shown in Figure 4.5.10.b. The Ra for this image is only 0.560 nm, where the larger 5-micron scan gave an Ra of 1.541 nm. This suggests that for the silica slides there are features on the order of between 1 and 5 microns, which is clearly observed by examining Figure 4.5.10.b more closely.

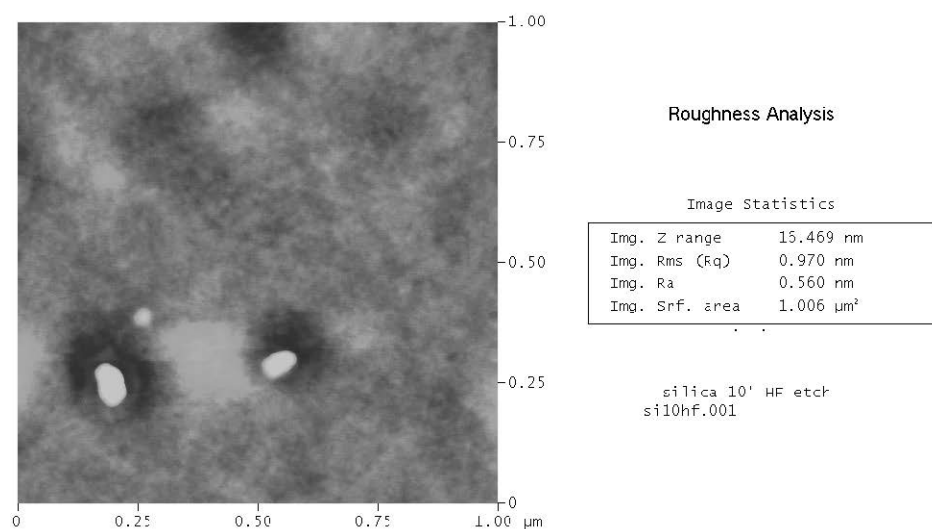


Figure 4.5.12. AFM tapping mode image of a silica slide etched in 10% HF acid for 10 minutes.

The next silica slide surface treatment that was examined with atomic force microscopy was the water plasma. The topographical image for a slide treated with water plasma for 10 minutes is shown in Figure 4.5.13. The scale bar to the right of the image in Figure 4.5.13 is the shading guide for the features on the surface. Light features are protrusions and dark features are depressions. The corresponding section analysis, shown in Figure 4.5.14, takes a line cross section of the image and plots the topography. There are small well-defined surface features observed on the slides after a water plasma treatment. The “before” condition of the surface can be taken as that represented by Figure 4.5.8. This contamination is generally found to settle in scratches, align on the surface and also exist randomly. Figure 4.5.15 is a dual topography and phase contrast image of another such 10-minute water plasma treated silica slide. The phase contrast image confirms that the surface contamination is a different material than the glass. The lighter features indicate a phase with lower density than the glass. A SLS glass slide was given a 5-minute water plasma treatment and the contamination from the treatment is again observed as well as the original polishing debris. An AFM image of this slide is shown in Figure 4.5.16.

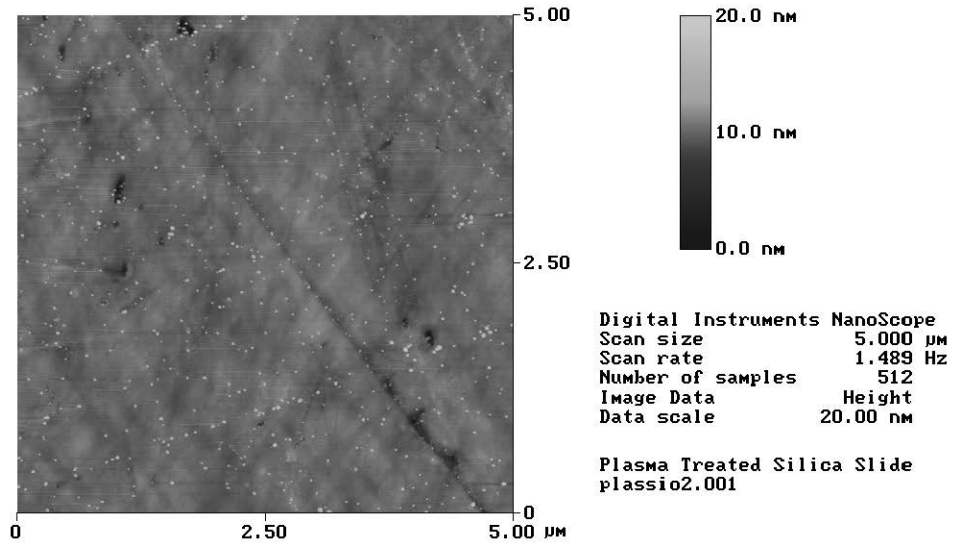


Figure 4.5.13. AFM tapping mode topographical image of a 10-minute water plasma treated silica slide.

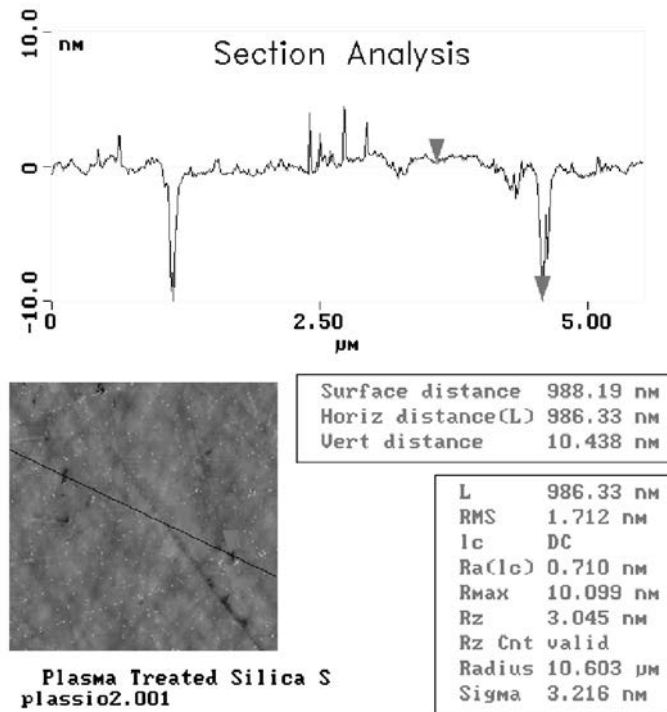


Figure 4.5.14. Section analysis of the line drawn in the lower left-hand image.

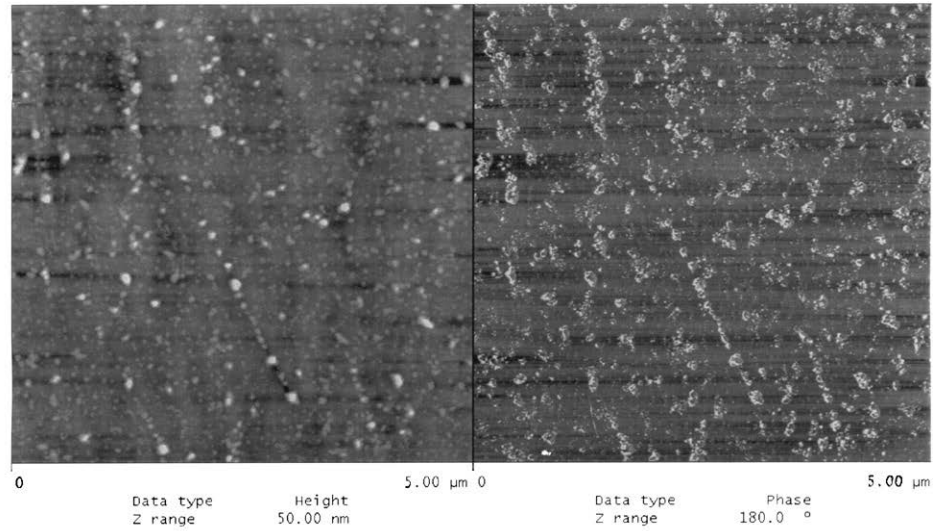


Figure 4.5.15. AFM topographical (left) and phase contrast (right) image of a 10-minute water plasma treated SLS slide.

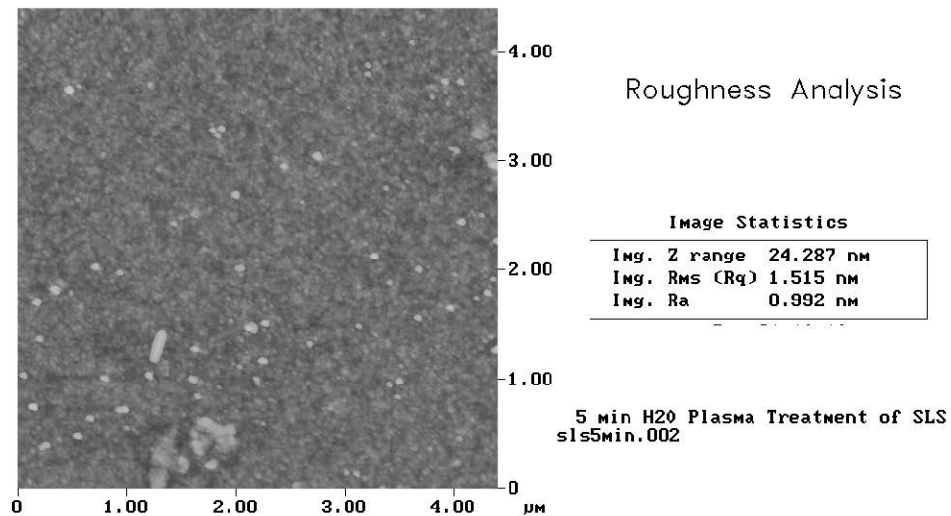


Figure 4.5.16. AFM image of a SLS slide after a water plasma treatment for 5 minutes.

The natural quartz terminal was also evaluated using the atomic force microscope. The terminal is crystal face $(10\bar{1}1)$ and there are steps in this plane as is evidenced in Figure 4.5.17. The image roughness statistics also shown in this figure indicate that the terminal is considerably more rough than any of the slides used in this study. Figure 4.5.18 shows these steps

more clearly as appearing as cracks in the quartz terminal surface. There are also geometrical indentations that appear frequently across the quartz terminal. Figure 4.5.19 shows a topographical AFM image of one of these depressions, which appear to be rectangular in shape and a few hundred nanometers in depth. Figure 4.5.20 is a 3-dimensional representation of the same depression. Figure 4.5.21 shows the section analysis of another depression and this analysis shows that the first step in the depression is approximately 200 nm with the second step being another 122 nm at the bottom. The depression is also approximately 16 microns across in the direction of the line denoting the section analysis.

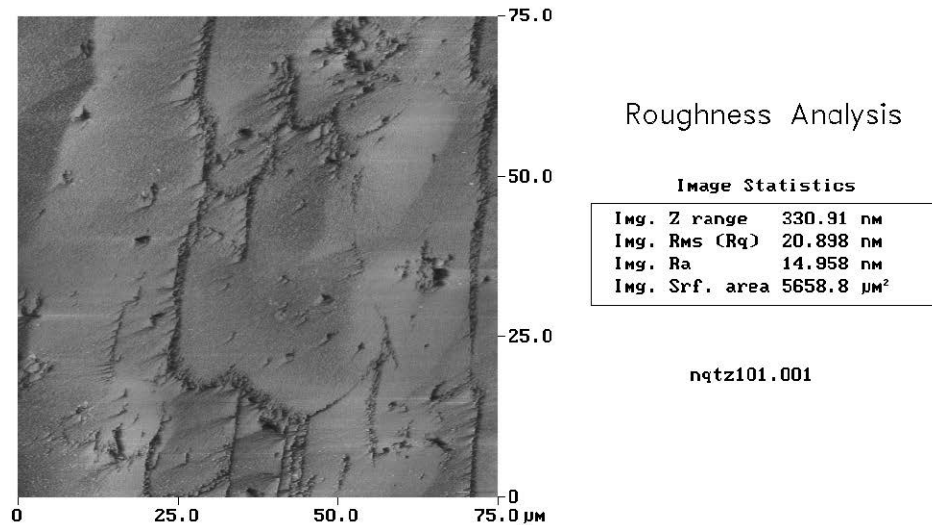


Figure 4.5.17. AFM tapping mode image of the natural quartz single crystal terminal with roughness analysis.

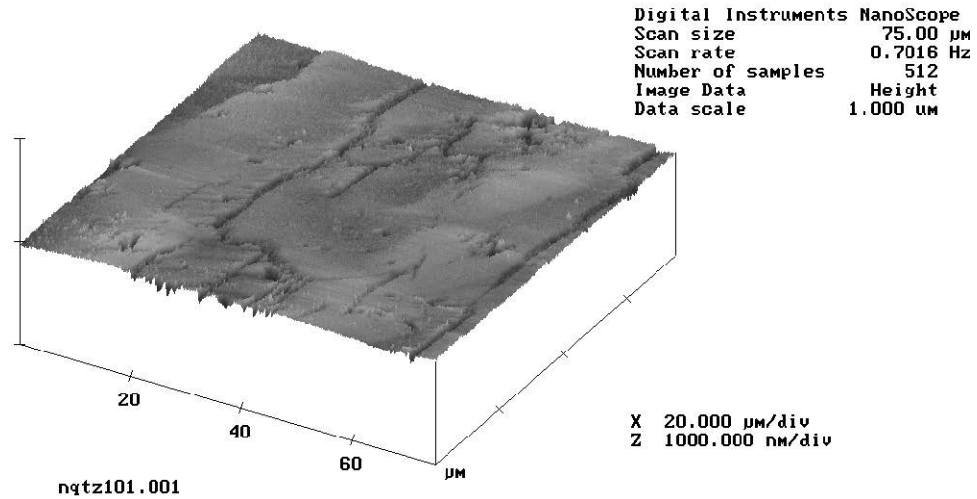


Figure 4.5.18. 3-dimensional AFM tapping mode image of the natural quartz single crystal terminal showing planar steps.

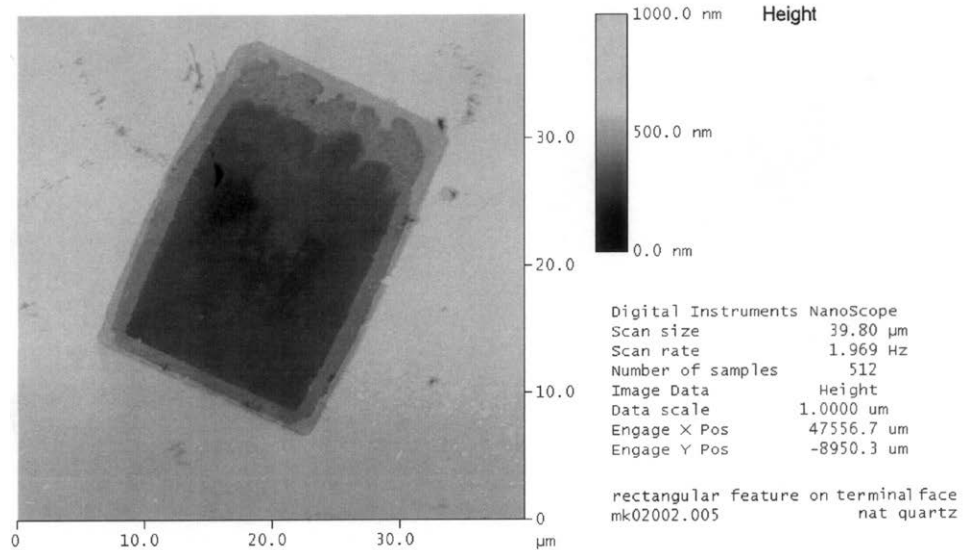


Figure 4.5.19. AFM topographical image with height scale bar showing a rectangular depression on the natural quartz single crystal terminal.

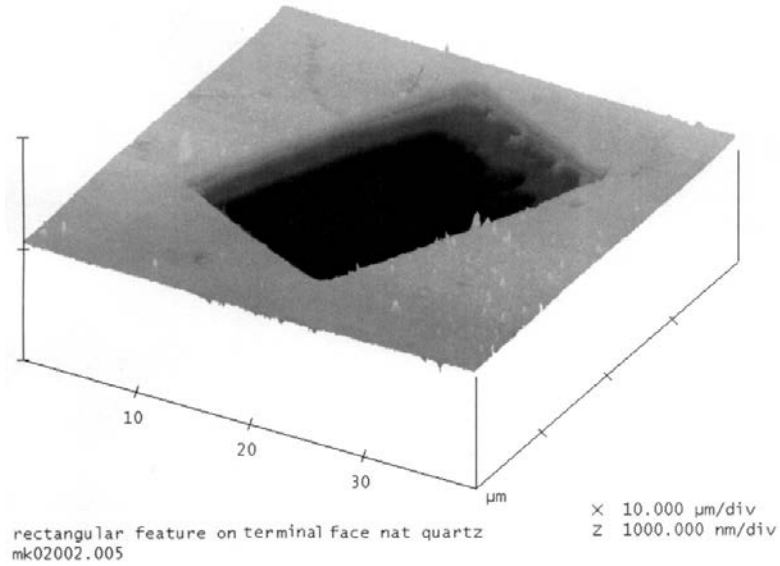


Figure 4.5.20. 3-dimensional AFM tapping mode image of the rectangular feature on natural quartz single crystal terminal.

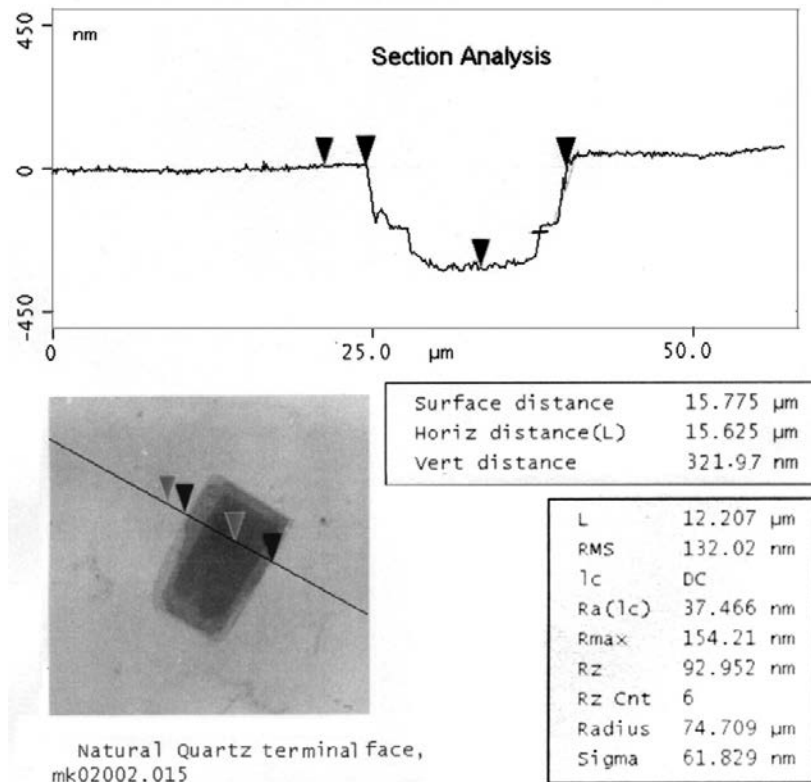


Figure 4.5.21. AFM section analysis of a second rectangular feature on the natural quartz single crystal terminal.

The bottom of the rectangular features were imaged at a higher magnification, namely at a 5 micron and 1 micron scan sizes. Figure 4.5.22 is the 5-micron topographical image and Figure 4.5.23 is the 1-micron dual topography and phase contrast image. The features observed in both of these images are approximately 80-100 nanometers in size. Figure 4.5.23, specifically the phase image on the right shows a much more detailed image of the surface. This suggests that while the topography may not change as drastically, the surface chemistry does. Again, the surface roughness is evident and is clearly seen in the 3-dimensional image of the 5-micron scan shown in Figure 4.5.24.

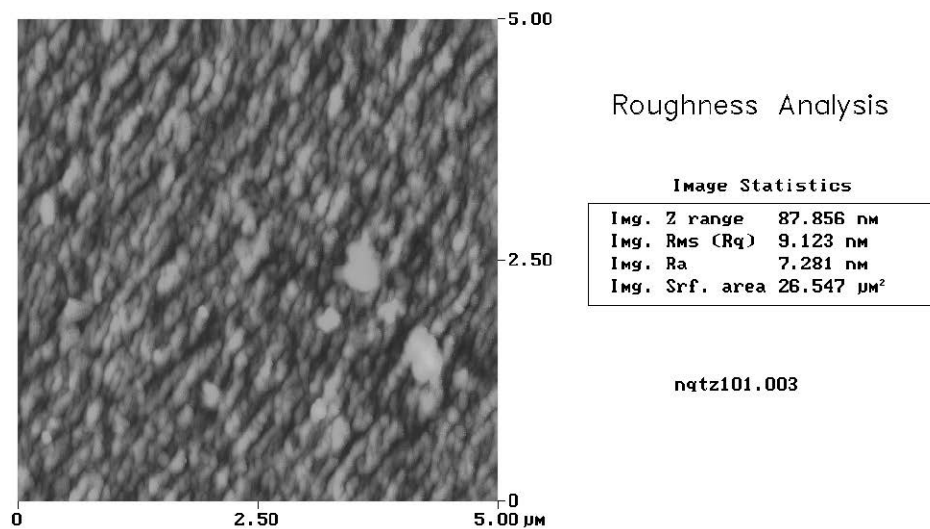


Figure 4.5.22. AFM tapping mode image of natural quartz single crystal terminal at a 5-micron scan size with roughness analysis.

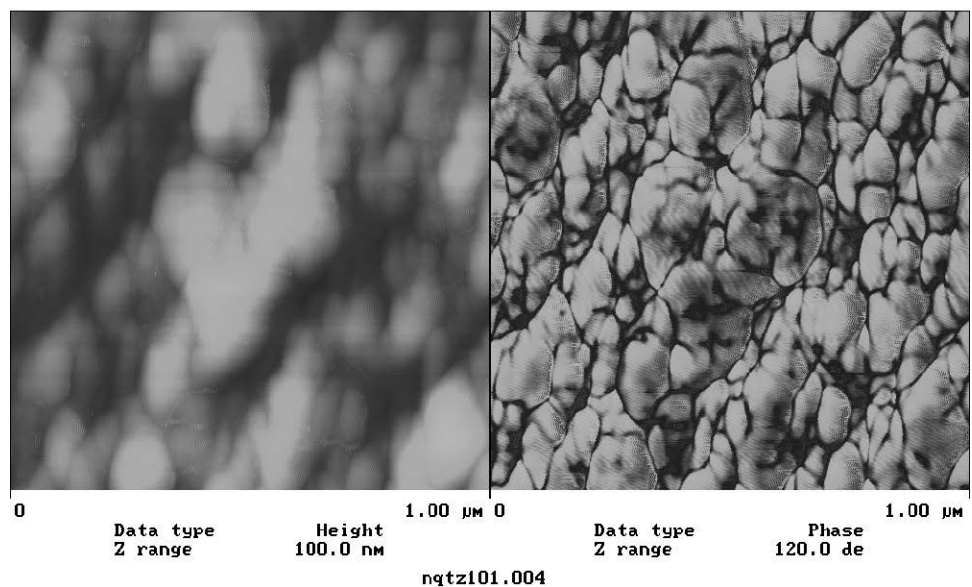


Figure 4.5.23. AFM topographical (left) and phase contrast (right) images for a 1-micron scan of the natural quartz single crystal terminal.

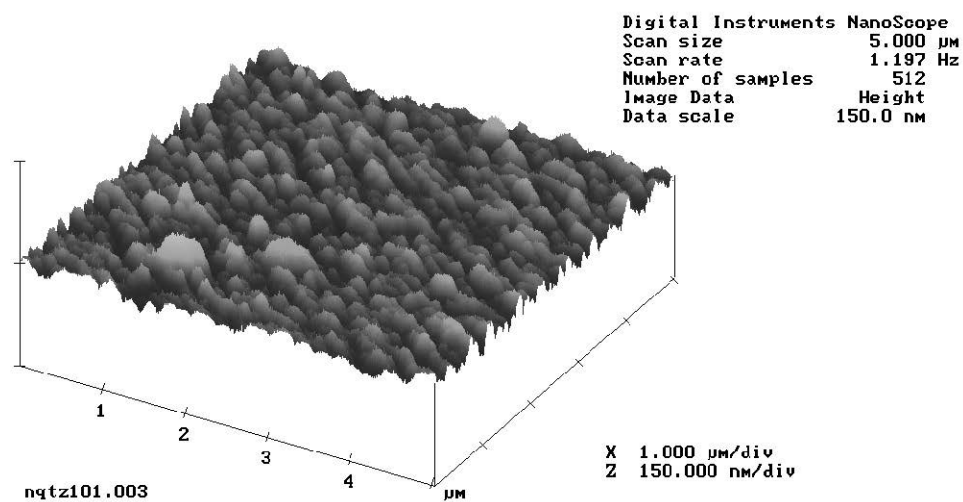


Figure 4.5.24. 3-dimensional AFM tapping mode image of the natural quartz single crystal terminal at a 5-micron scan size.

The non-flat glass surfaces were also investigated as well as a few of the surface treatments applied to these glasses. Ethanol cleaned silica fiber and HF etched silica fiber were imaged using atomic force microscopy. Figure 4.5.25 is a 3-dimensional image of a 2-micron scan of ethanol cleaned fiber. Large bumps are observed on the fiber surface as well as very subtle ripples around the circumference. Figure 4.5.26 shows a 1-micron scan of an ethanol cleaned fiber displaying a circular feature that is slightly raised from the rest of the surface. This fiber was also etched in HF acid for 10 minutes and imaged with AFM. Figure 4.5.27 shows a 2-micron topographical scan of this fiber surface. Cavities on the order of 300-500 nm are clearly observed all over the surface exhibiting the damage caused by HF etching of this glass. Figure 4.5.28 is the same image as in 4.5.27, except that the 3-dimensional representation gives a clear picture of the severity of the surface damage caused by HF etching.

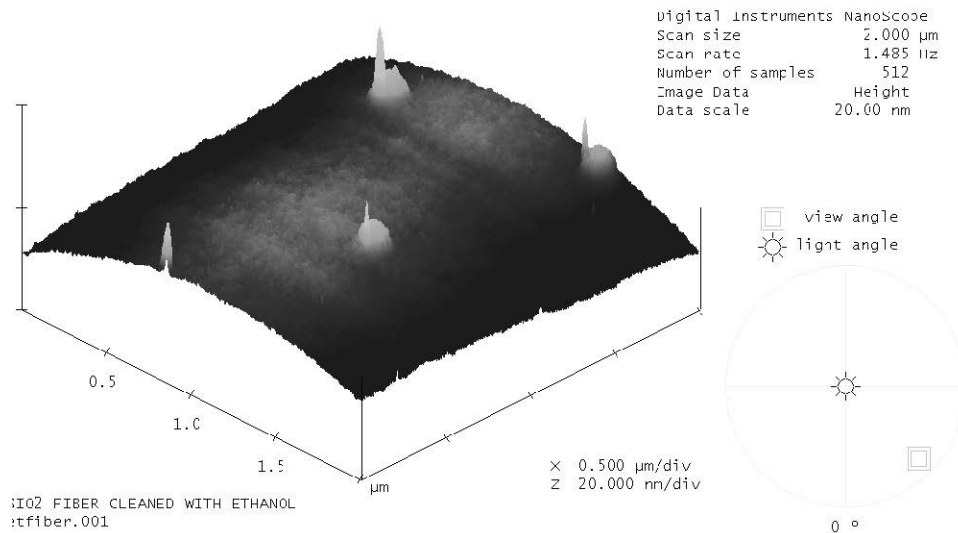


Figure 4.5.25. 3-dimensional AFM tapping mode image of an ethanol cleaned silica fiber surface.

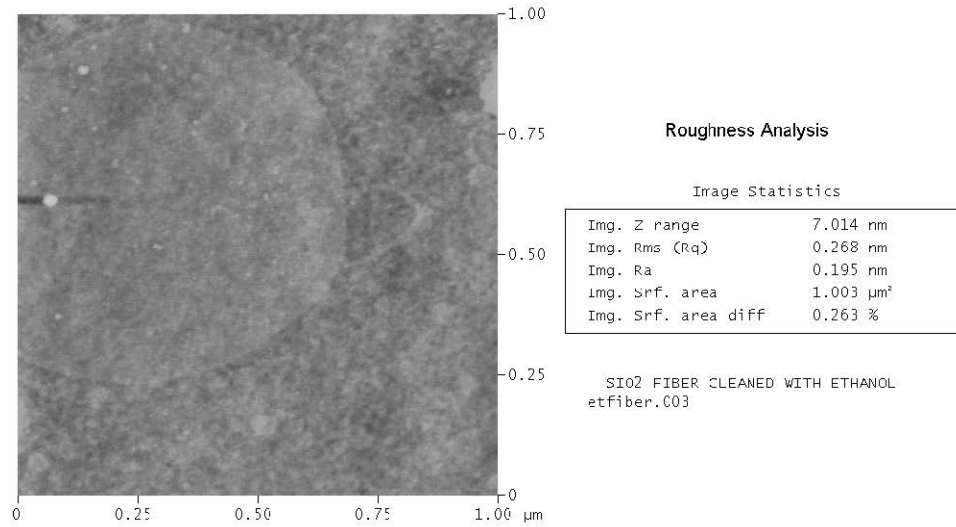


Figure 4.5.26. AFM tapping mode image of a 1-micron section of an ethanol cleaned fiber surface with roughness analysis.

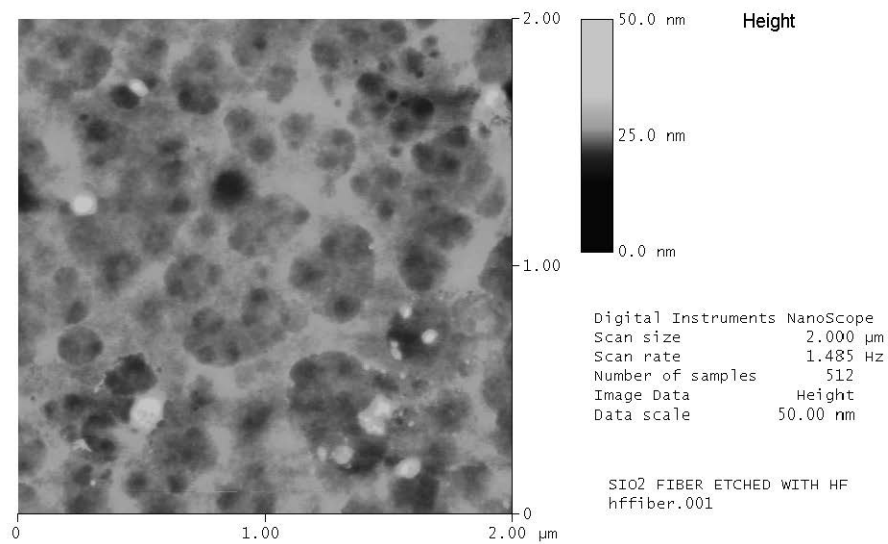


Figure 4.5.27. AFM topographical tapping mode image of a 10-minute HF etched fiber surface with height scale bar.

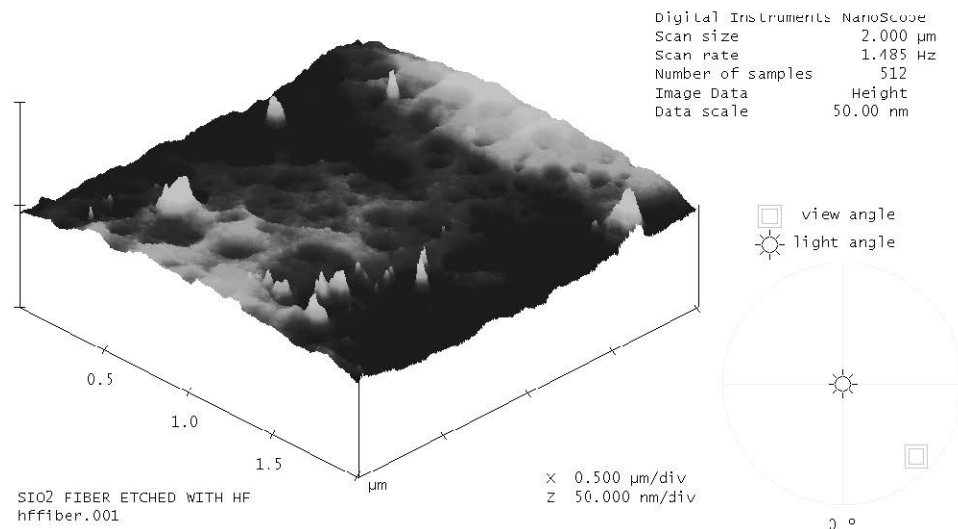


Figure 4.5.28. 3-dimensional AFM tapping mode image of a 10-minute HF etched fiber surface.

Since it is possible to image large biological molecules such as DNA easily with the AFM, it was investigated whether proteins could be imaged on the glass surfaces.² Training was obtained at Veeco/Digital Instruments Metrology Lab in Philadelphia for fluid cell tapping. Fluid cell tapping is required to image a protein in its native state, since proteins need to be in a buffered solution to sustain their natural conformation. But first, dried proteins were imaged on glass surfaces. Streptavidin was adsorbed onto an ethanol cleaned silica slide, allowed to dry, and then the slide was imaged using tapping mode AFM. Figure 4.5.29 is a topographical representation of streptavidin adsorbed to an ethanol cleaned silica slide. The white features observed were not seen on the ethanol cleaned silica slides and so it can be deduced that these features represent protein agglomerations. The features are approximately 100-200 nm, which is much larger than the size of an individual protein and so it is assumed that these features are agglomerations.

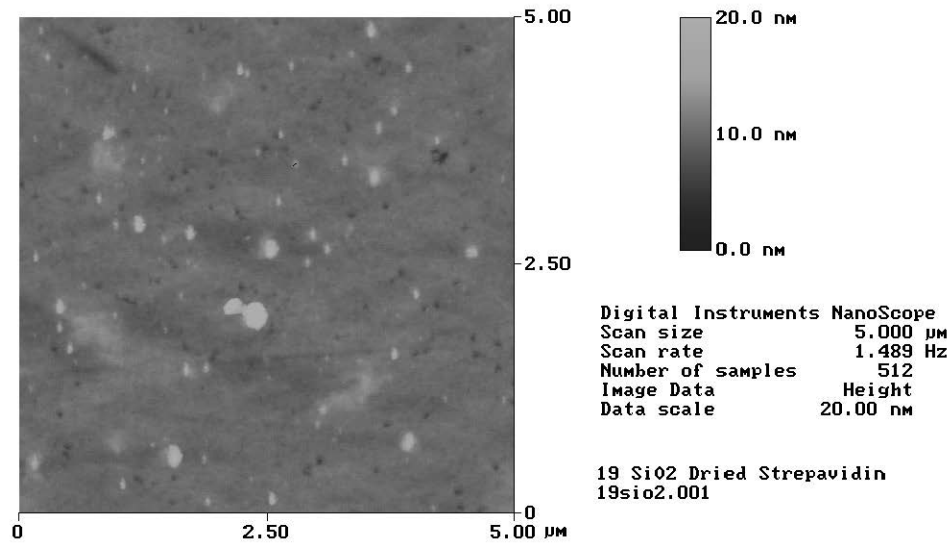


Figure 4.5.29. AFM tapping mode topographical image of dried streptavidin protein adsorbed to an ethanol cleaned silica slide.

A solution of streptavidin was placed in the fluid cell on a freshly cleaved mica surface to be sure no surface impurities were present. Figure 4.5.30 is a section analysis of streptavidin on mica. It appears that there are streptavidin agglomerations that are 14 nm in diameter. A phase image was taken as well as a topographical image of a slightly different area of streptavidin solution on mica. The resulting image is shown in Figure 4.5.31. The dark areas on the phase image on the right show that the tip interacts differently with the protruding features in the topographical image on the left.

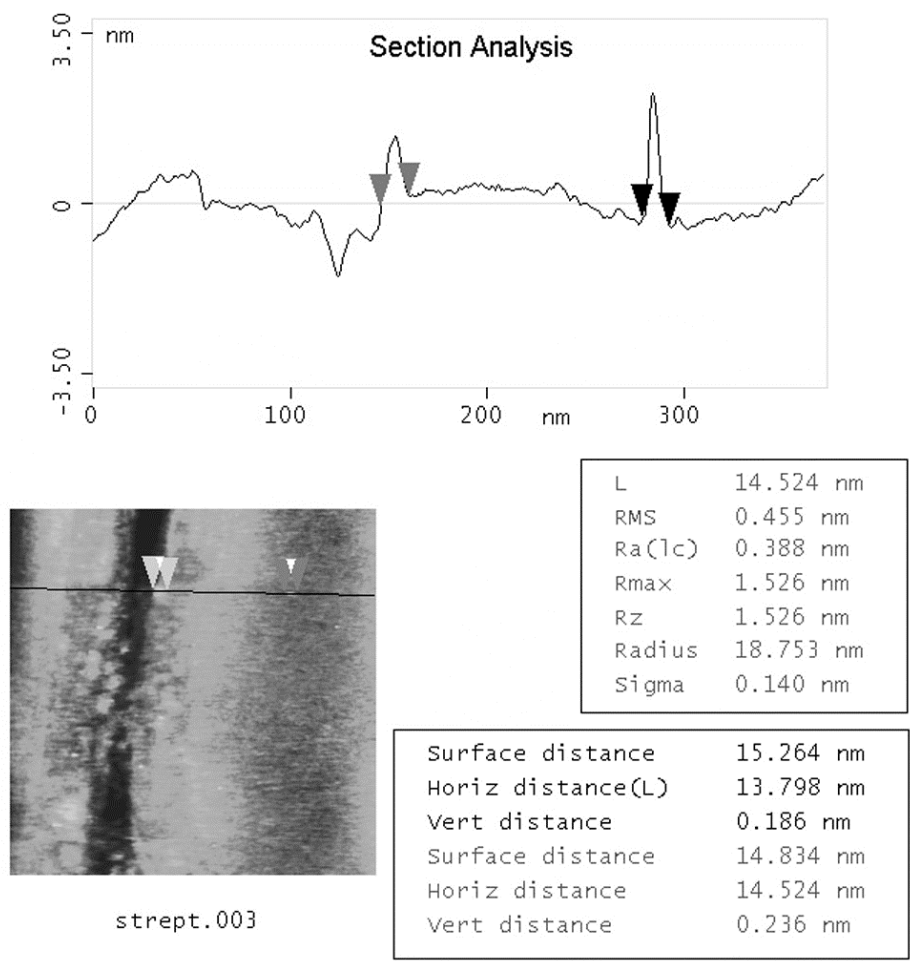


Figure 4.5.30. Section analysis of streptavidin on mica imaged using fluid cell tapping mode.

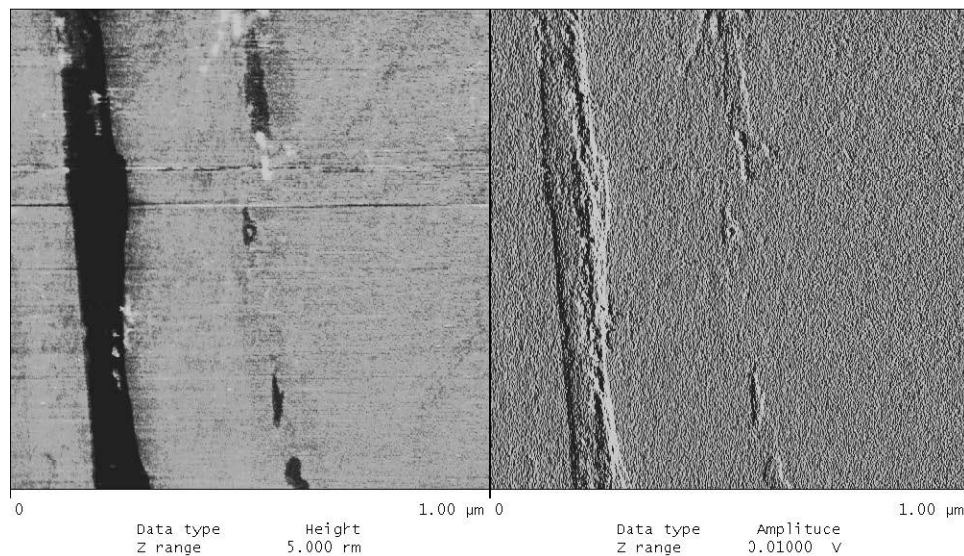


Figure 4.5.31. Fluid cell tapping topographical image (left) and phase contrast image (right) of streptavidin on mica.

An HF etched silica slide surface was imaged in air and also in a streptavidin solution using a fluid cell. Figure 4.5.32 shows the resulting images in (a) and (b), respectively. The two images are very different suggesting that the 40-50 nm features in (b) are indeed protein agglomerations. An ethanol cleaned cane was imaged with tapping mode AFM and is shown in Figure 4.5.33. Surface impurities are observed on this surface on the order of 100 nm and smaller. Figure 4.5.34 shows a 500 nm tapping mode scan of the surface roughness inherent in the silica cane. Mouse IgG was adsorbed onto this sample and imaged. Figure 4.5.35 shows a 10-micron scan of mouse-IgG adsorbed and dried on an ethanol cleaned cane. This image shows dried salt crystals from the tris-buffered saline in which the protein is dissolved and also bump-like features measuring ~500 nm in diameter. Figure 4.5.36 is a 5-micron scan of the same sample. This image shows three different sized subclasses of protein agglomeration. The smallest of the three sizes of agglomerations is shown in Figure 4.5.37. This 1-micron scan shows mouse-IgG agglomerations approximately 100 nm in size. The next higher magnification of mouse-IgG adsorbed onto cane is a 250

nm scan size AFM tapping mode image shown in Figure 4.5.38. Individual IgG proteins are approximately 160 Angstroms in the longest dimension and so single proteins are not distinguishable in this image. Figure 4.5.39 is another 5-micron scan of IgG on cane, but this image is in an area where no salt crystals had grown. In comparing Figures 4.5.33 and 4.5.39, of the ethanol cleaned cane and the ethanol cleaned cane with adsorbed mouse-IgG, one easily sees a difference in surface features.

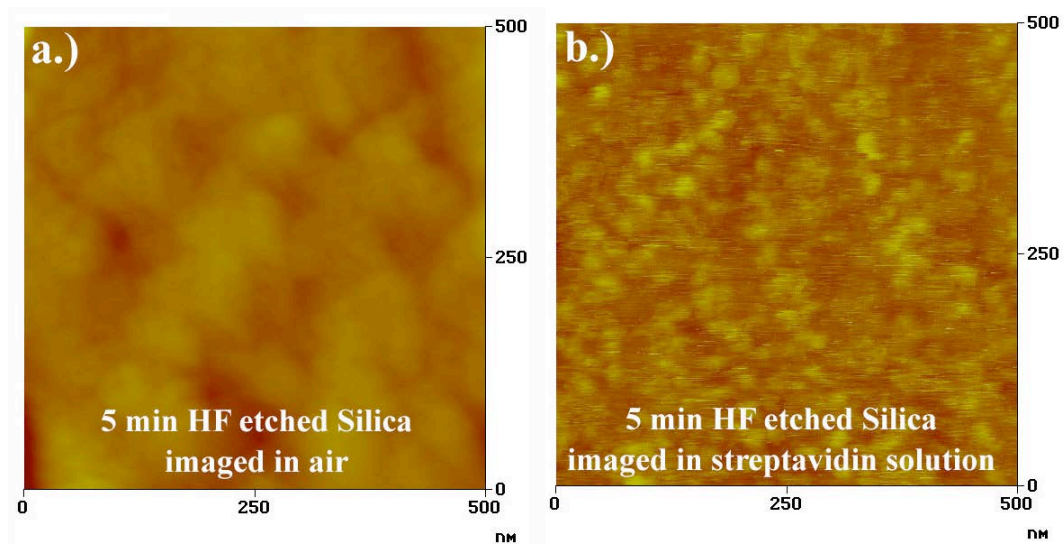


Figure 4.5.32. AFM tapping mode images of a HF etched silica slide in (a) air and (b) using a fluid cell under a streptavidin solution.

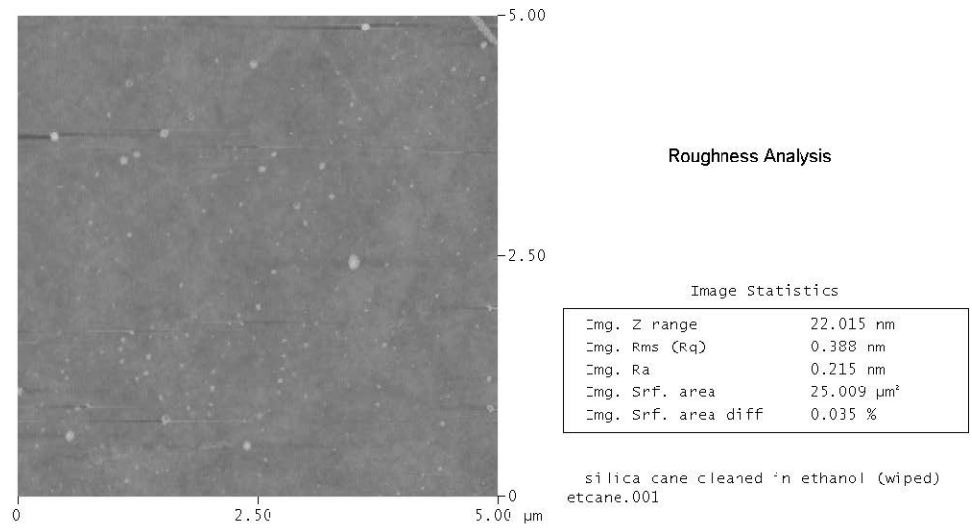


Figure 4.5.33. AFM tapping mode 5-micron image of cane cleaned with ethanol.

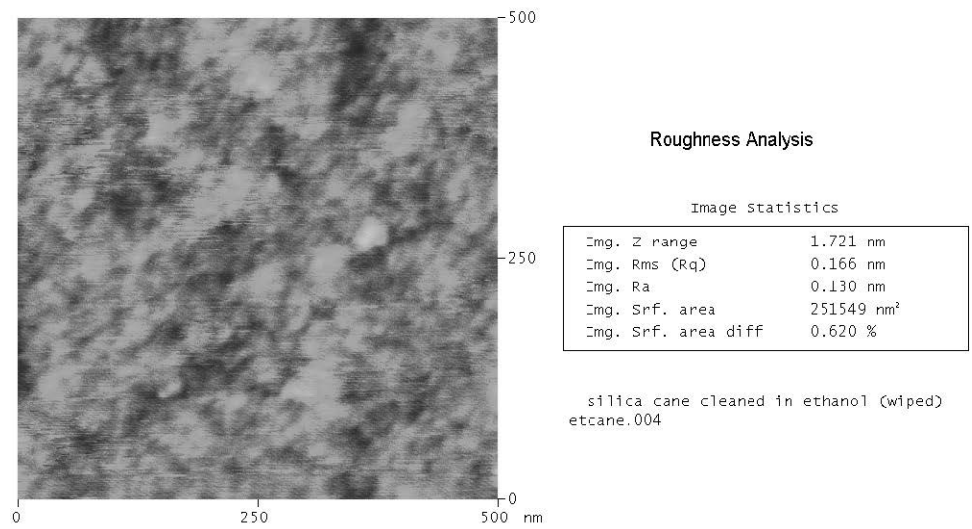


Figure 4.5.34. AFM tapping mode 500 nm image of cane cleaned with ethanol.

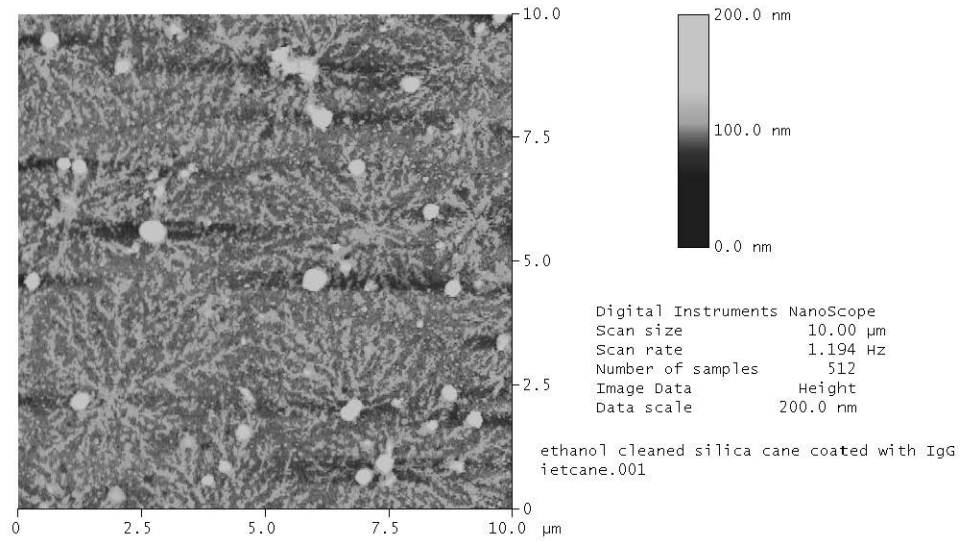


Figure 4.5.35. AFM tapping mode 10-micron image of dried adsorbed mouse IgG on an ethanol cleaned cane.

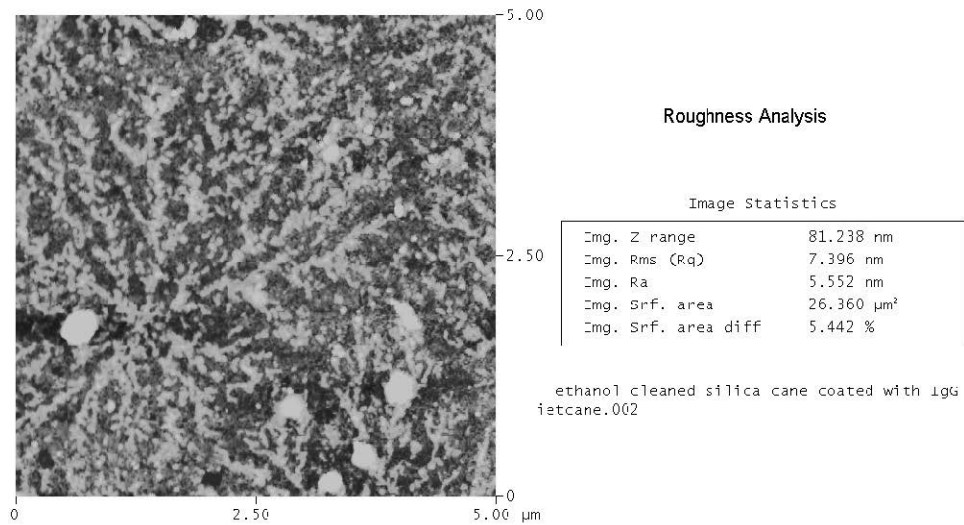


Figure 4.5.36. AFM tapping mode 5-micron image of dried adsorbed mouse-IgG on ethanol cleaned silica cane.

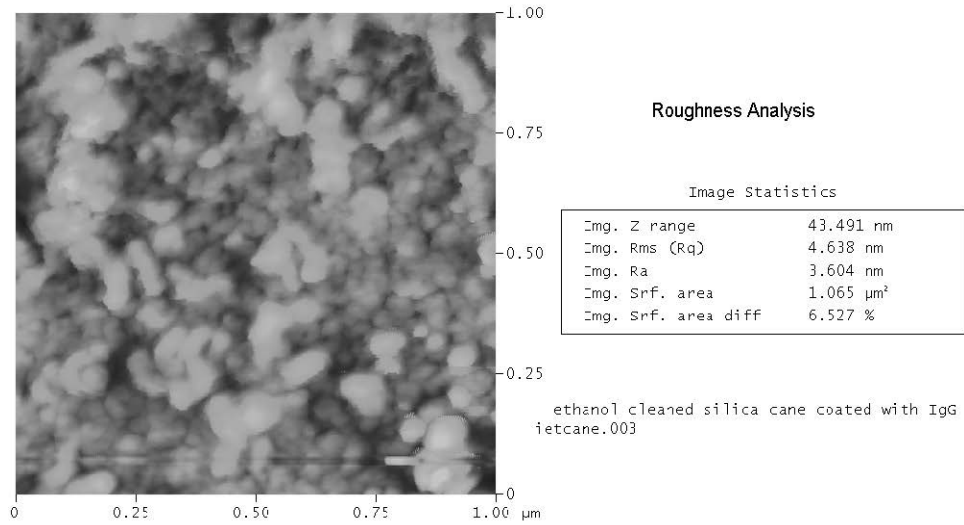


Figure 4.5.37. AFM tapping mode 1-micron image of the small agglomerations of mouse-IgG on ethanol cleaned cane.

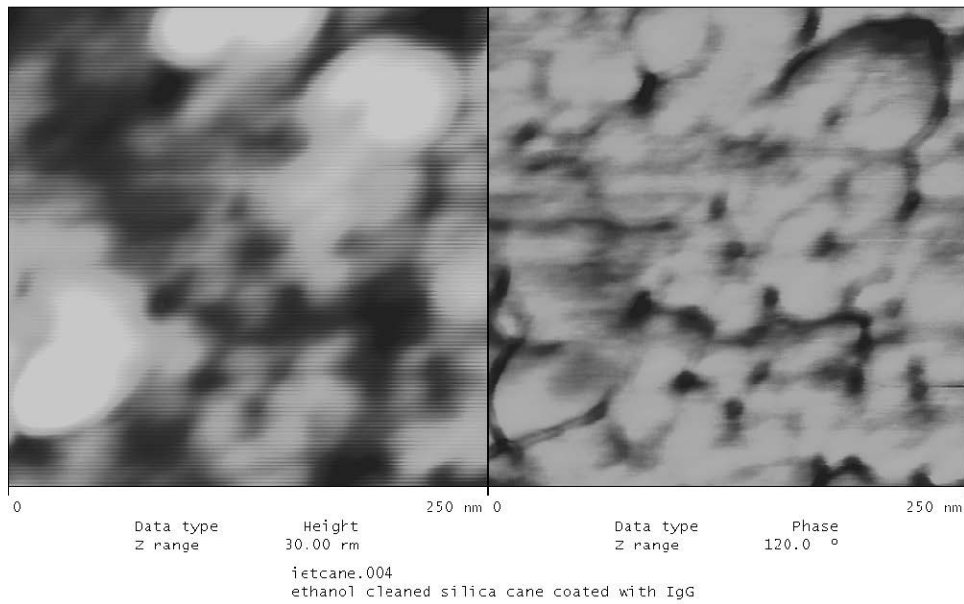


Figure 4.5.38. A 250 nm AFM topographical (left) and phase contrast image (right) of mouse-IgG adsorbed onto ethanol cleaned silica cane.

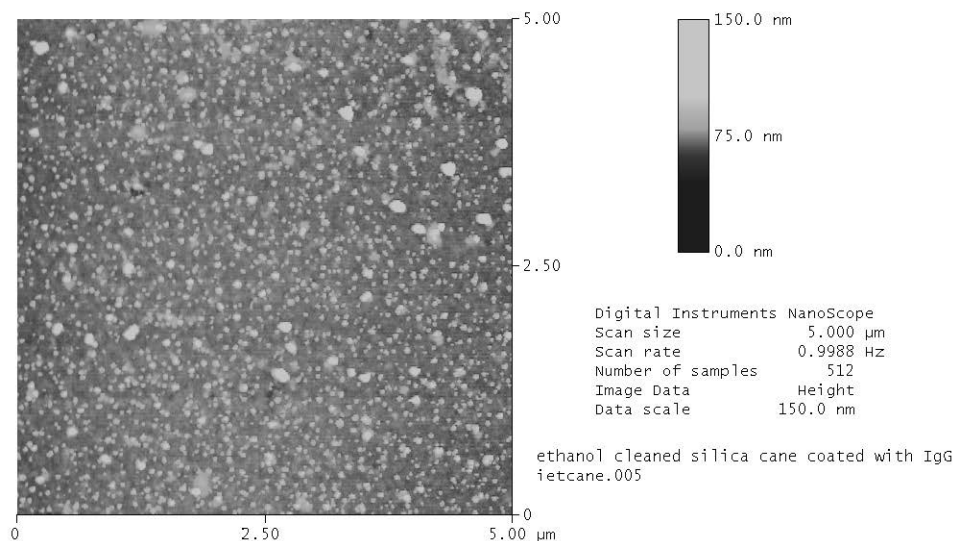


Figure 4.5.39. AFM tapping mode, 5-micron scan of a non-salt crystal area on IgG-coated ethanol-cleaned cane.

Streptavidin was also adsorbed to ethanol cleaned cane, allowed to dry, and then imaged using tapping mode AFM. Figure 4.5.40 shows a 5-micron scan of such a sample. Again 180-200 nm features are observed where they were not observed in a plain ethanol cleaned silica cane. Figure 4.5.41 is a dual 1-micron topographical and phase contrast image of streptavidin adsorbed to silica cane. This phase image clearly shows a difference in the composition of the coinciding topographical features. The phase image features are also finer than the topographical image features, but in the topography, one can almost see small black dots inside the white lumps. Figure 4.5.42 is a higher magnification dual scan of the streptavidin on cane and these black dots are more clearly observed in the topographical image. It is then noted that these black dots correspond to the features of the phase contrast image. The black dot indicates a depression in the feature and the white dots of the phase image indicate a material of a different nature than the glass. These features are undoubtedly streptavidin protein agglomerations of 30-50 nm in size.

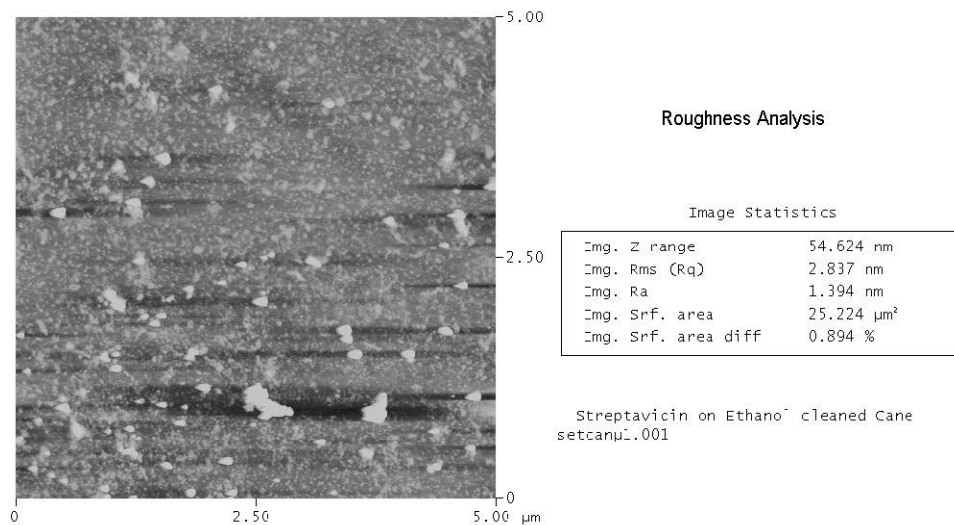


Figure 4.5.40. AFM tapping mode 5-micron image of adsorbed and dried streptavidin on ethanol cleaned silica cane.

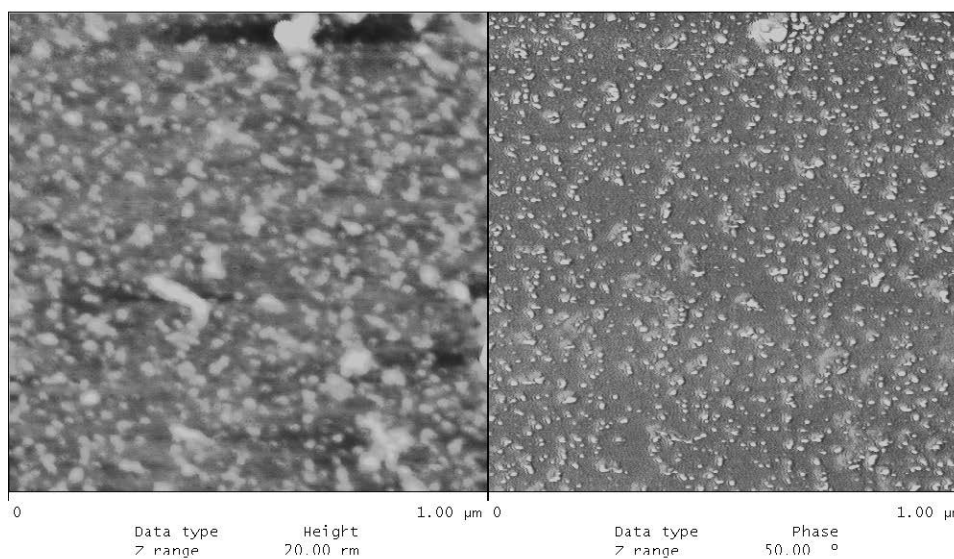


Figure 4.5.41. A 1-micron AFM topographical (left) and phase contrast (right) image of streptavidin adsorbed to ethanol cleaned silica cane.

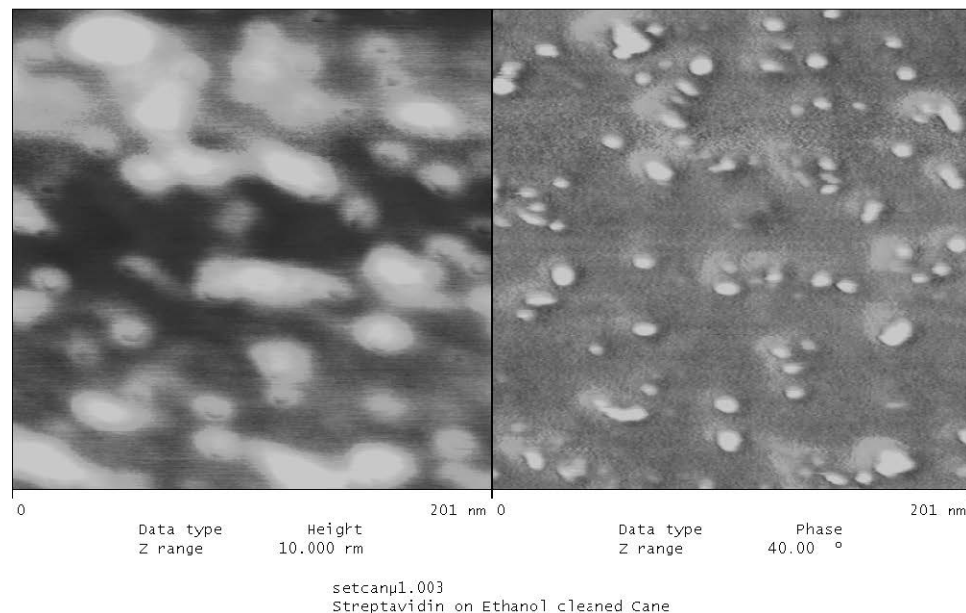


Figure 4.5.42. A 200 nm tapping mode AFM topographical (left) and phase contrast (right) image of streptavidin adsorbed to ethanol cleaned silica cane.

Silica cane was also HF etched and imaged. This cane was then exposed to both mouse-IgG and streptavidin separately and imaged with the AFM again. A 5-micron scan of HF etched silica cane is shown in Figure 4.5.43. The surface is roughened slightly over an ethanol cleaned cane. A 500-nm scan shows the surface roughness more clearly and this is shown in Figure 4.5.44. Mouse IgG was then adsorbed to the HF etched cane, dried, and imaged using tapping mode. Figure 4.5.45 shows a 5-micron scan of this sample. In comparing Figure 4.5.43 with 4.5.45, one observes that the IgG gives an even coating to the sample, which has the appearance of smoothing the previously rough HF etched surface. Figure 4.5.46 is a 1-micron scan of the same sample showing the round 100 nm features that are most likely agglomerations of IgG protein. Streptavidin was adsorbed onto HF etched silica cane, allowed to dry, and then imaged using tapping mode AFM. Figure 4.5.47 shows streptavidin on HF etched cane and here shows only two levels of protein size agglomeration. There are large 100-200 nm round agglomerations and smaller 30-50 nm size features. The small features are

more clearly observed in Figure 4.5.48, a 500-nm image with both topography and phase contrast. The phase contrast again allows the softer protein material to be viewed as separate from the topography. Figure 4.5.49 is a section analysis of a 1-micron scan of streptavidin on HF etched silica cane. This analysis provides the evidence that the small features are approximately 30 nm in size, but only ~2.3 nm in height.

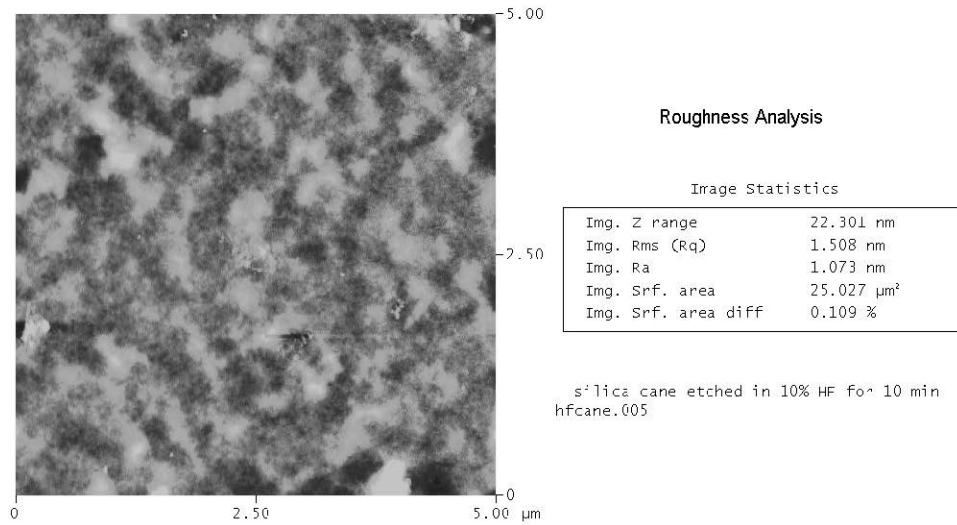


Figure 4.5.43. AFM tapping mode 5-micron image of a silica cane etched in HF for 10 minutes.

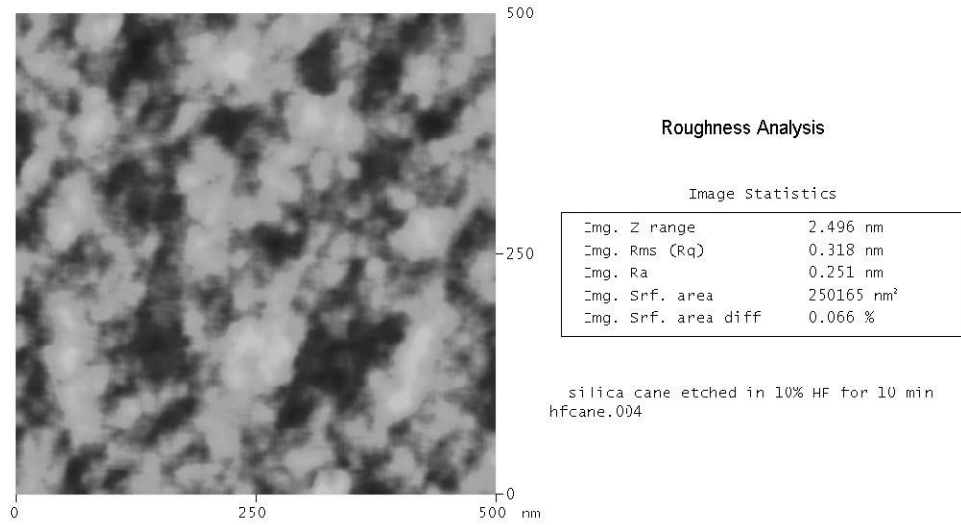


Figure 4.5.44. AFM tapping mode 500-nm image of HF etched silica cane.

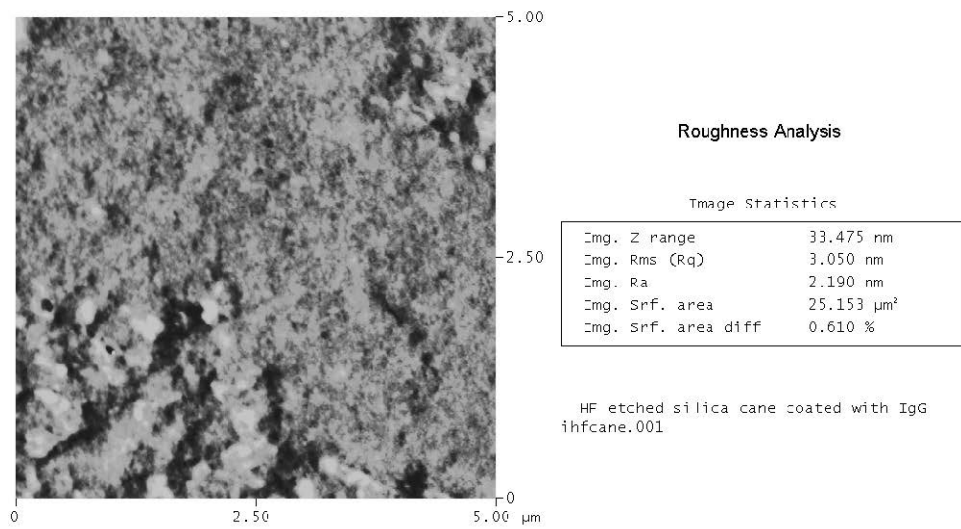


Figure 4.5.45. AFM tapping mode 5-micron image of mouse-IgG adsorbed onto HF etched silica cane.

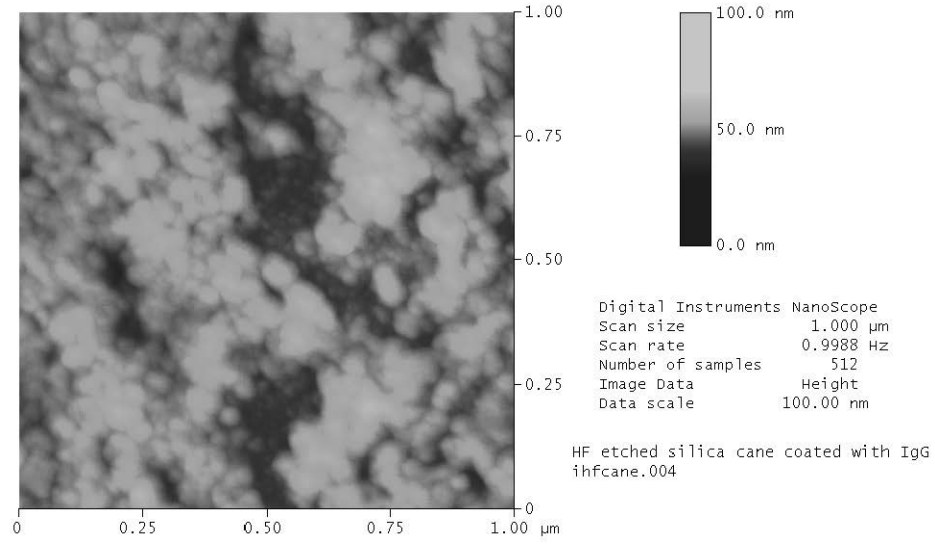


Figure 4.5.46. AFM tapping mode 1-micron image of mouse-IgG adsorbed onto HF etched silica cane.

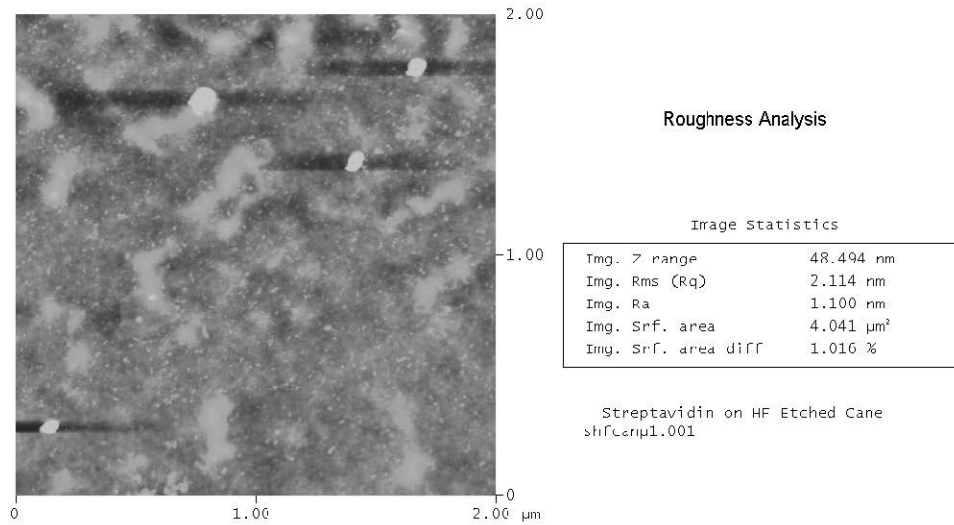


Figure 4.5.47. AFM tapping mode 2-micron image of streptavidin adsorbed onto HF etched silica cane.

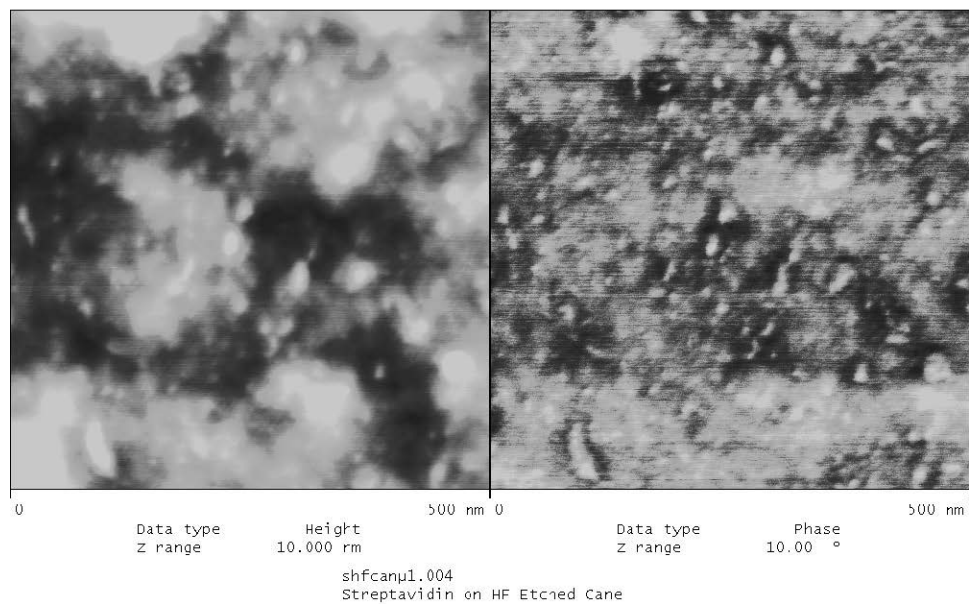


Figure 4.5.48. A topographical (left) and phase contrast (right) image of streptavidin adsorbed to HF etched silica cane.

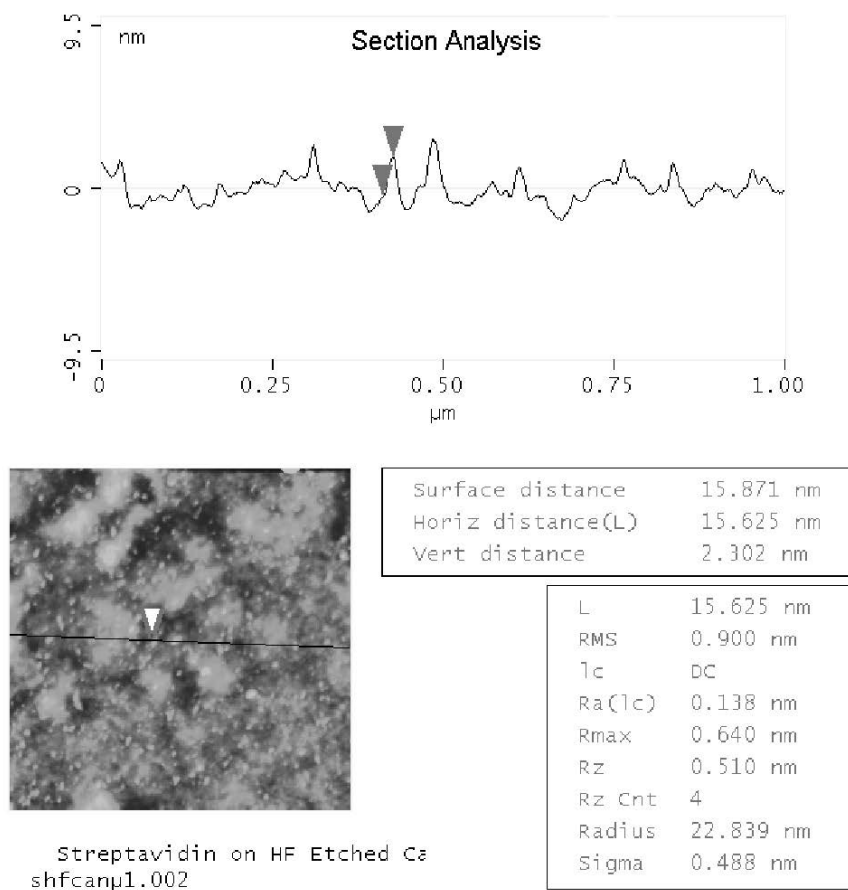


Figure 4.5.49. AFM 1-micron section analysis of streptavidin adsorbed onto HF etched silica cane showing the height and diameter of the small protein agglomerations.

Silica cane was treated in a water plasma RF microwave for 10 minutes. These cane were imaged as is using tapping mode AFM and were also exposed to mouse-IgG, dried and then imaged. Figure 4.5.50 shows a 5-micron scan of water plasma treated silica cane. A generous coating of particles is clearly evident. These surface features were seen on water plasma coated silica slides as discussed previously. The features are approximately 50-60 nm in diameter. The variation in the height of these particles is shown in the 3-dimensional 1-micron image of the water plasma treated cane in Figure 4.5.51. The height of these particles varies between 1 to 5 nm. Figure 4.5.52 shows the dual topographical and phase contrast

image of the same sample. The phase image indicates that the surface impurities interact with the AFM tip differently than the glass surface. Figure 4.5.53 is a 500 nm scan of the same sample showing more definitely the width of the features consistently being near 50 nm. The mouse-IgG was adsorbed to the water plasma treated cane and Figure 4.5.54 shows the dried protein on the surface. The appearance of the surface is very different from the previous images. The protein most likely binds to the surface features and branches between them.

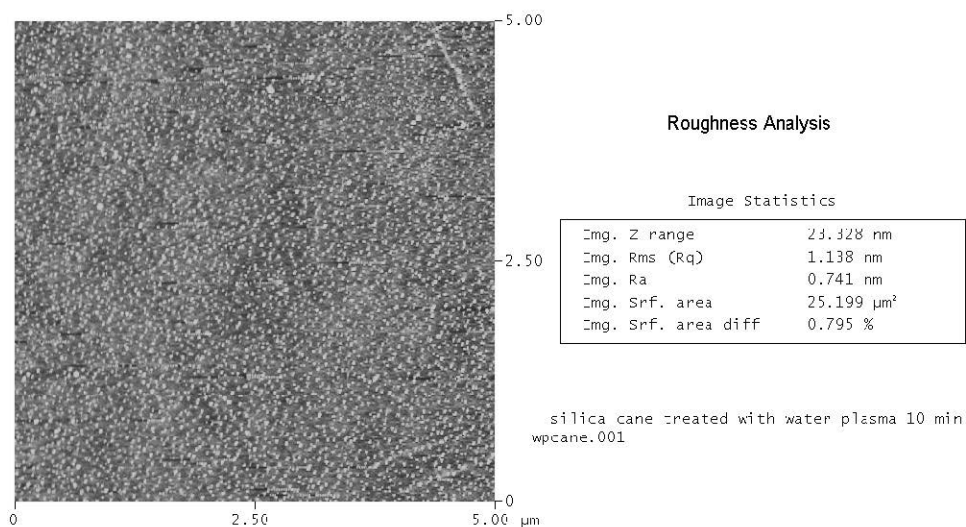


Figure 4.5.50. AFM tapping mode 5-micron image of water plasma treated silica cane.

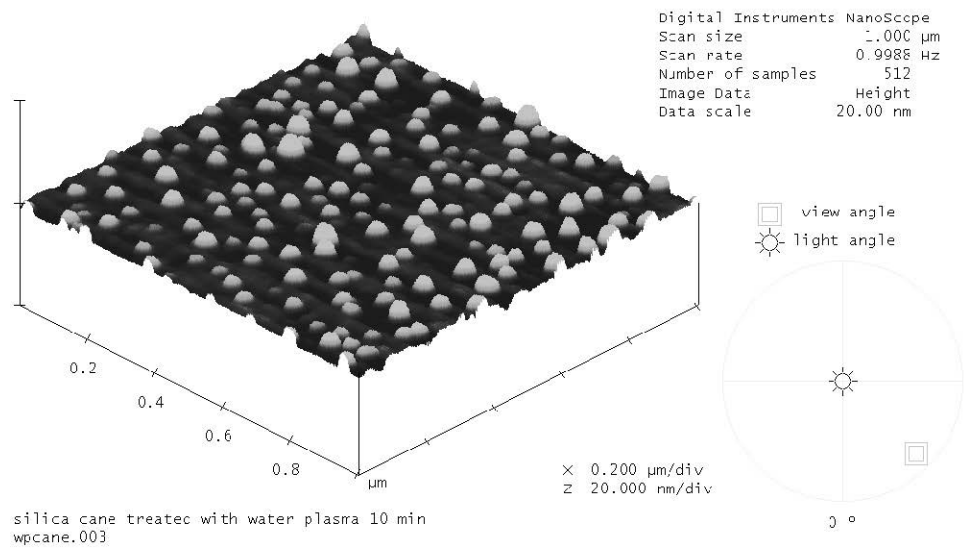


Figure 4.5.51. 3-dimensional AFM tapping mode 1-micron image of water plasma treated silica cane clearly showing surface impurities.

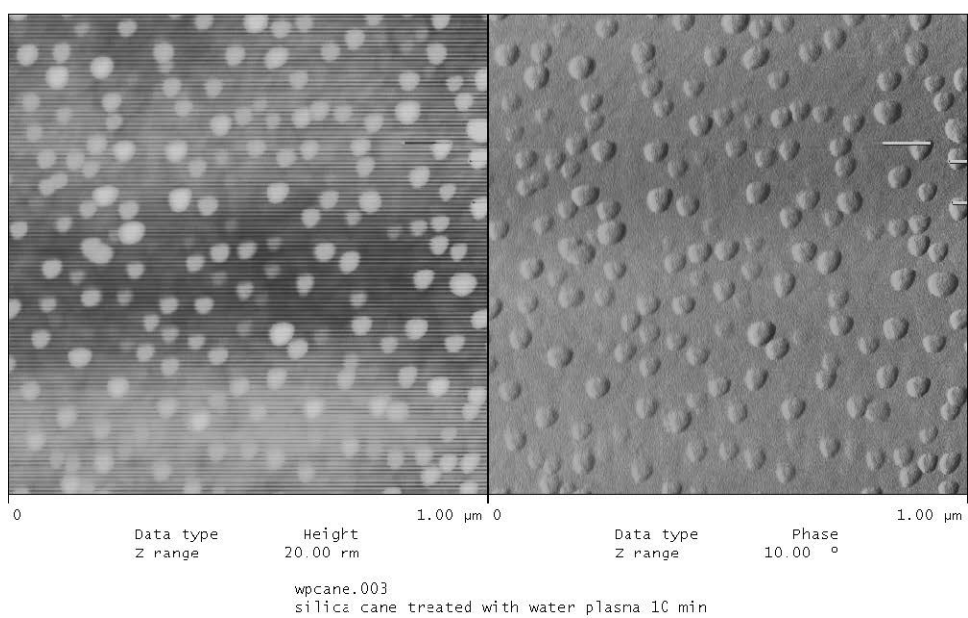


Figure 4.5.52. Dual topographical (left) and phase contrast (right) image of water plasma treated silica cane.

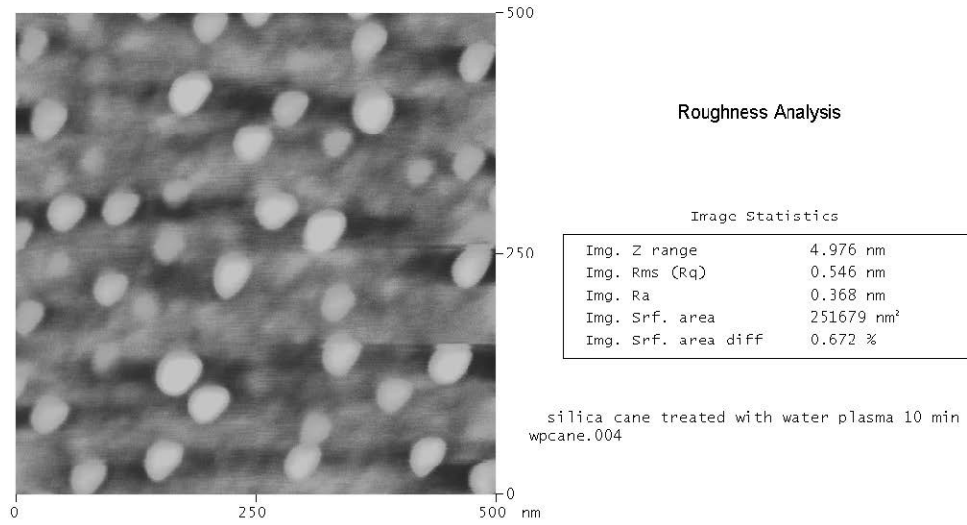


Figure 4.5.53. AFM tapping mode 500 nm image of water plasma treated silica cane.

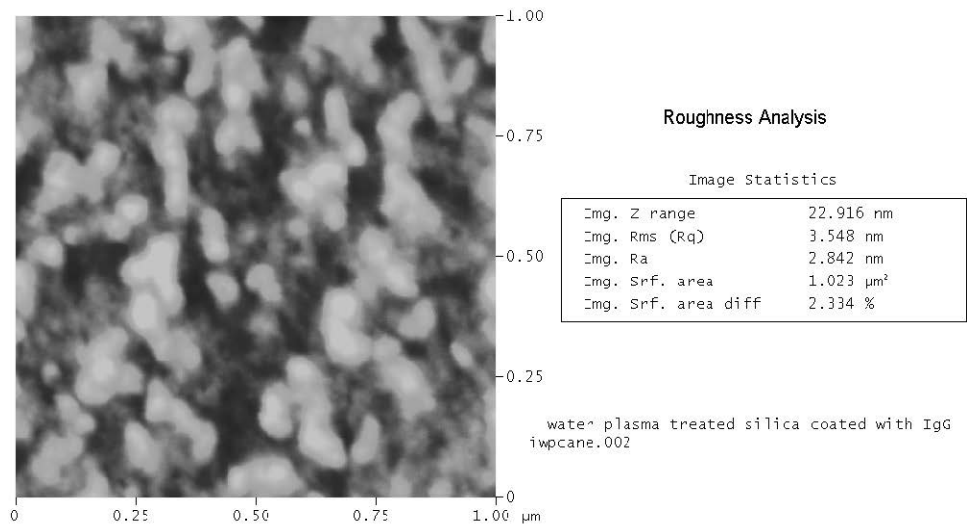


Figure 4.5.54. AFM tapping mode 1-micron image of mouse-IgG adsorbed to water plasma silica cane.

4.5.1. AFM References

1. P. Sanford, Erie Scientific Company, Portsmouth, NH, June, 2001, Private Communication.
2. A. L. Weisenhorn, M. Egger, F. Ohnesorge, S. A. C. Gould, S. P. Heyn, H. G. Hansma, R. L. Sinsheimer, H. E. Gaub, and P. K. Hansma, "Molecular-Resolution Images of Langmuir-Blodgett Films and DNA by Atomic Force Microscopy," *Langmuir*, **7** [1] 8-12 (1991).